

# Numerical Methods for the Multi-Physical Analysis of Long Span Cable-Stayed Bridges

DISSERTATION

zur Erlangung des akademischen Grades

Doktor-Ingenieur (**Dr.-Ing.**)

an der Fakultät Bauingenieurwesen

der

**Bauhaus-Universität Weimar**

vorgelegt von

M.Sc. **Nazim Abdul Nariman**

geboren am 15 Februar 1971 in Kirkuk - Irak

(Interner Doktorand)

Weimar, November 2, 2017

Mentor:

Prof. Dr.-Ing. Timon Rabczuk, Bauhaus-Universität Weimar

Gutachter:

Prof. Dr. Ir. Magd Abdel Wahab, Ghent University, Belgium

Prof. Dr. rer. nat. Tom Lahmer, Bauhaus-Universität Weimar



This work is dedicated to:

The souls of my beloved **mother** and **father**

&

To my loyal wife (**Heero**) and dearest sons (**Revan**) and (**Avyar**)

## Acknowledgements

First of all, I thank my **God** who granted me the strength and the determination to complete my doctorate study at Bauhaus Universität-Weimar in Germany.

I am deeply indebted to my dear supervisor Prof. Dr.-Ing.**Timon Rabczuk**, for his constant support, valuable advice and guidance. Actually without his encouragement and understanding of many obstacles encountered during my PhD study, it would have been nearly impossible to continue and complete.

I would also like to give a special thanks to Prof. Dr.-Ing.**Guido Morgenthal** for providing a wealth of helpful advice and guidance related to the area of wind effects on long span bridges and validation process.

My grateful thanks are also to Prof. Dr. rer. nat. **Tom Lahmer** for his recommendations regarding the field of sensitivity analysis.

I owe my most sincere gratitude to my wife **Heero** and sons **Revan** and **Avyar** for enduring so much and remaining alone for a long time so that to support me.

Lastly, I would like to thank Dr.-Ing. **Mohammed Msekh** for assisting me in many directions during my study in Weimar, I am grateful to him.



**Nazim Abdul Nariman**

Weimar, September 23, 2016

## Ehrenwörtliche Erklärung

Ich erkläre hiermit ehrenwörtlich, dass ich die vorliegende Arbeit ohne unzulässige Hilfe Dritter und ohne Benutzung anderer als der angegebenen Hilfsmittel angefertigt habe. Die aus anderen Quellen direkt oder indirekt übernommenen Daten und Konzepte sind unter Angaben der Quellen gekennzeichnet.

Weitere Personen waren an der inhaltlich-materiellen Erstellung der vorliegenden Arbeit nicht beteiligt. Insbesondere habe ich hierfür nicht die entgeltliche Hilfe von Vermittlungs- bzw. Beratungsdiensten (Promotionsberater oder anderer Personen) in Anspruch genommen. Niemand hat von mir unmittelbar oder mittelbar geldwerte Leistungen für Arbeiten erhalten, die im Zusammenhang mit dem Inhalt der vorgelegten Dissertation stehen.

Die Arbeit wurde bisher weder im In- noch im Ausland in gleicher oder ähnlicher Form einer anderen Prüfungsbehörde vorgelegt.

Ich versichere ehrenwörtlich, dass ich nach bestem Wissen die reine Wahrheit gesagt und nichts verschwiegen habe.

A handwritten signature in blue ink, consisting of a horizontal line with a stylized, upward-pointing flourish above it.

**Nazim Abdul Nariman**

Weimar, September 23, 2016

This dissertation has been constructed supporting on the following published papers:

- 1- Nariman N. A. (2017). **Thermal Fluid-Structure Interaction and Coupled Thermal-Stress Analysis in a Cable Stayed Bridge Exposed to Fire.** *Frontiers of Structural and Civil Engineering*, doi:10.1007/s11709-017-0452-4.
- 2- Nariman N. A. (2017). **Kinetic Energy Based Model Assessment and Sensitivity Analysis of Vortex Induced Vibration of Segmental Bridge Decks.** *Frontiers of Structural and Civil Engineering*, 11(4), 480-501.
- 3- Nariman N. A. (2017). **Aerodynamic Stability Parameters Optimization and Global Sensitivity Analysis for a Cable Stayed Bridge.** *KSCE Journal of Civil Engineering*, 21(5), 1866-1881.
- 4- Nariman N. A. (2017). **Control Efficiency Optimization and Sobol's Sensitivity Indices of MTMDs Design Parameters for Buffeting and Flutter Vibrations in a Cable Stayed Bridge.** *Frontiers of Structural and Civil Engineering*, 11(1), 66-89.
- 5- Nariman N. A. (2017). **A Novel Structural Modification to Eliminate the Early Coupling between Bending and Torsional Mode Shapes in a Cable Stayed Bridge.** *Frontiers of Structural and Civil Engineering*, 11(2), 131-142.
- 6- Nariman N. A. (2016). **Influence of Fluid-Structure Interaction on Vortex Induced Vibration and Lock-in Phenomena in Long Span Bridges.** *Frontiers of Structural and Civil Engineering*, 10(4), 363-384.



## Abstract

The main categories of wind effects on long span bridge decks are buffeting, flutter, vortex-induced vibrations (VIV) which are often critical for the safety and serviceability of the structure. With the rapid increase of bridge spans, research on controlling wind-induced vibrations of long span bridges has been a problem of great concern. The developments of vibration control theories have led to the wide use of tuned mass dampers (TMDs) which has been proven to be effective for suppressing these vibrations both analytically and experimentally. Fire incidents are also of special interest in the stability and safety of long span bridges due to significant role of the complex phenomenon through triple interaction between the deck with the incoming wind flow and the thermal boundary of the surrounding air.

This work begins with analyzing the buffeting response and flutter instability of three dimensional computational structural dynamics (CSD) models of a cable stayed bridge due to strong wind excitations using ABAQUS finite element commercial software. Optimization and global sensitivity analysis are utilized to target the vertical and torsional vibrations of the segmental deck through considering three aerodynamic parameters (wind attack angle, deck streamlined length and viscous damping of the stay cables). The numerical simulations results in conjunction with the frequency analysis results emphasized the existence of these vibrations and further theoretical studies are possible with a high level of accuracy. Model validation is performed by comparing the results of lift and moment coefficients between the created CSD models and two benchmarks from the literature (flat plate theory) and flat plate by (Xavier and co-authors) which resulted in very good agreements between them. Optimum values of the parameters have been identified. Global sensitivity analysis based on Monte Carlo sampling method was utilized to formulate the surrogate models and calculate the sensitivity indices. The rational effect and the role of each parameter on the aerodynamic stability of the structure were calculated and efficient insight has been constructed for the stability of the long span bridge.

2D computational fluid dynamics (CFD) models of the decks are created with the support of MATLAB codes to simulate and analyze the vortex shedding and VIV of the deck. Three aerodynamic parameters (wind speed, deck streamlined length and dynamic viscosity of the air) are dedicated to study their effects on the kinetic energy of the system and the vortices shapes and patterns. Two benchmarks from the literature (Von Karman) and (Dyrbye and Hansen) are used to validate the numerical simulations of the vortex shedding for the CFD models. A good consent between the results was detected. Latin hypercube experimental



method is dedicated to generate the surrogate models for the kinetic energy of the system and the generated lift forces. Variance based sensitivity analysis is utilized to calculate the main sensitivity indices and the interaction orders for each parameter. The kinetic energy approach performed very well in revealing the rational effect and the role of each parameter in the generation of vortex shedding and predicting the early VIV and the critical wind speed.

Both one-way fluid-structure interaction (one-way FSI) simulations and two-way fluid-structure interaction (two-way FSI) co-simulations for the 2D models of the deck are executed to calculate the shedding frequencies for the associated wind speeds in the lock-in region in addition to the lift and drag coefficients. Validation is executed with the results of (Simiu and Scanlan) and the results of flat plate theory compiled by (Munson and co-authors) respectively. High levels of agreements between all the results were detected. A decrease in the critical wind speed and the shedding frequencies considering (two-way FSI) was identified compared to those obtained in the (one-way FSI). The results from the (two-way FSI) approach predicted appreciable decrease in the lift and drag forces as well as prediction of earlier VIV for lower critical wind speeds and lock-in regions which exist at lower natural frequencies of the system. These conclusions help the designers to efficiently plan and consider for the design and safety of the long span bridge before and after construction.

Multiple tuned mass dampers (MTMDs) system has been applied in the three dimensional CSD models of the cable stayed bridge to analyze their control efficiency in suppressing both wind -induced vertical and torsional vibrations of the deck by optimizing three design parameters (mass ratio, frequency ratio and damping ratio) for the (TMDs) supporting on actual field data and minimax optimization technique in addition to MATLAB codes and Fast Fourier Transform technique. The optimum values of each parameter were identified and validated with two benchmarks from the literature, first with (Wang and co-authors) and then with (Lin and co-authors). The validation procedure detected a good agreement between the results. Box-Behnken experimental method is dedicated to formulate the surrogate models to represent the control efficiency of the vertical and torsional vibrations. Sobol's sensitivity indices are calculated for the design parameters in addition to their interaction orders. The optimization results revealed better performance of the MTMDs in controlling both the vertical and the torsional vibrations for higher mode shapes. Furthermore, the calculated rational effect of each design parameter facilitates to increase the control efficiency of the MTMDs in conjunction with the support of the surrogate models which simplifies the process of analysis for vibration control to a great extent.

A novel structural modification approach has been adopted to eliminate the early coupling between the bending and torsional mode shapes of the cable stayed bridge. Two lateral steel

beams are added to the middle span of the structure. Frequency analysis is dedicated to obtain the natural frequencies of the first eight mode shapes of vibrations before and after the structural modification. Numerical simulations of wind excitations are conducted for the 3D model of the cable stayed bridge. Both vertical and torsional displacements are calculated at the mid span of the deck to analyze the bending and the torsional stiffness of the system before and after the structural modification. The results of the frequency analysis after applying lateral steel beams declared that the coupling between the vertical and torsional mode shapes of vibrations has been removed to larger natural frequencies magnitudes and higher rare critical wind speeds with a high factor of safety.

Finally, thermal fluid-structure interaction (TFSI) and coupled thermal-stress analysis are utilized to identify the effects of transient and steady state heat-transfer on the VIV and fatigue of the deck due to fire incidents. Numerical simulations of TFSI models of the deck are dedicated to calculate the lift and drag forces in addition to determining the lock-in regions once using FSI models and another using TFSI models. Vorticity and thermal fields of three fire scenarios are simulated and analyzed. The benchmark of (Simiu and Scanlan) is used to validate the TFSI models, where a good agreement was manifested between the two results. Extended finite element method (XFEM) is adopted to create 3D models of the cable stayed bridge to simulate the fatigue of the deck considering three fire scenarios. The benchmark of (Choi and Shin) is used to validate the damaged models of the deck in which a good coincide was seen between them. The results revealed that the TFSI models and the coupled thermal-stress models are significant in detecting earlier vortex induced vibration and lock-in regions in addition to predicting damages and fatigue of the deck and identifying the role of wind-induced vibrations in speeding up the damage generation and the collapse of the structure in critical situations.



# Contents

<b>Contents</b> .....	xii
<b>List of Figures</b> .....	xviii
<b>List of Tables</b> .....	xxiv
<b>Nomenclature</b> .....	xxv
<b>1 Introduction</b> .....	1
1.1 Background.....	1
1.2 State of The Art.....	5
1.3 Literature Review.....	6
1.4 Aim and Objectives of Work.....	8
1.5 Methodology.....	9
1.6 Dissertation Outline .....	12
<b>2 Aerodynamic Stability of Long Span Bridges</b> .....	16
2.1 Vertical and Torsional Vibrations .....	16
2.2 Aerodynamic Stability Parameters.....	17
2.2.1 Wind Attack Angle.....	17
2.2.2 Deck Section.....	18
2.2.3 Viscous Damping of Stay Cables.....	18
2.3 Equation of Motion.....	19
2.3.1 Aerodynamic Forces and Moment.....	20
2.4 Finite Element Model.....	21
2.4.1 Mesh Convergence.....	22
2.4.2 Wind Load.....	23
2.4.3 Frequency Analysis.....	24
2.4.4 Results of Mode Shapes.....	24
2.4.5 Simulation of The Mode Shapes.....	25
2.5 Aerodynamic Instability Analysis.....	26
2.5.1 Results of Vertical Vibrations.....	26
2.5.2 Results of Torsional Vibrations.....	27

2.5.3	Simulation of Aerodynamic Instability.....	27
2.6	Aerodynamic Parameters Optimization .....	29
2.6.1	Results of Wind Attack Angle Effect .....	30
2.6.2	Results of Deck Streamlined Length Effect .....	31
2.6.3	Results of Stay Cables Viscous Damping Effect.....	32
2.7	Validation of The FE Models.....	33
2.7.1	Flat Plate Theory Benchmark .....	33
2.7.2	Flat Plate Model (Xavier and Co-authors) Benchmark .....	34
2.8	Sensitivity Analysis.....	35
2.9	Experimental Design.....	35
2.9.1	Monte Carlo Sampling.....	36
2.9.2	Probability Distribution.....	36
2.9.3	Response Surface Methodology.....	37
2.9.4	Sobol’s Sensitivity Indices.....	38
2.9.5	Results and Discussion of The Surrogate Models.....	39
2.9.6	Results and Discussion of The Sensitivity Indices.....	43
2.9.7	Convergence of The Results.....	44
<b>3</b>	<b>Kinetic Energy Based Model Assessment.....</b>	<b>47</b>
3.1	Von Karman Vortex Street .....	47
3.2	VIV Parameters.....	48
3.2.1	Reynolds Number.....	48
3.2.2	Deck Shape.....	49
3.2.3	Dynamic Viscosity of Air.....	49
3.3	Vortex Shedding Phenomenon in Bridges.....	50
3.4	Finite Element Model.....	51
3.4.1	Mesh Convergence.....	53
3.5	Results of Vorticity and Kinetic Energy.....	55
3.5.1	Wind Speed Effect.....	55
3.5.2	Deck Streamlined Length Effect.....	58
3.5.3	Dynamic Viscosity of Air Effect.....	60
3.6	Validation of 2D-CFD Models.....	62
3.6.1	Von Karman Benchmark.....	62

3.6.2	Dyrbye and Hansen Benchmark.....	63
3.7	Sensitivity Analysis.....	64
3.7.1	Latin Hypercube Sampling.....	64
3.8	Surrogate Model Results and Discussion.....	65
3.9	Sensitivity Analysis Results and Discussion.....	69
3.9.1	Convergence of The Results.....	69
<b>4</b>	<b>Fluid-Structure Interaction and Lock-In Phenomenon.....</b>	<b>73</b>
4.1	Vortex Induced Vibration (VIV).....	73
4.2	Fluid-Structure Interaction (FSI).....	74
4.2.1	One-Way FSI.....	74
4.2.2	Two-Way FSI.....	75
4.3	Finite Element Models.....	76
4.3.1	Boundary Conditions .....	78
4.4	Results and Discussion.....	79
4.4.1	Vortex Shedding Simulation.....	79
4.4.2	Lift Forces.....	81
4.4.3	Drag Forces.....	83
4.4.4	Kinetic Energy.....	86
4.4.5	Lock-In Phenomenon.....	86
4.4.6	Lift Coefficient.....	88
4.4.7	Drag Coefficient.....	89
4.4.8	Reynolds Number.....	90
4.4.9	Strouhal Number.....	90
4.5	Validation of The FSI Models.....	92
4.5.1	Simiu and Scnlan Benchmark.....	92
4.5.2	Flat Plate Model (Munson and Co-authors) Benchmark .....	93
<b>5</b>	<b>Control Efficiency Optimization of Multiple Tuned Mass Dampers.....</b>	<b>95</b>
5.1	Tuned Mass Damper (TMD).....	95
5.1.1	Energy Dissipation Mechanism.....	96
5.2	Multiple Tuned Mass Dampers (MTMDs).....	96
5.3	Concept of TMD Using Two-Mass System.....	97
5.4	Equation of Motion.....	99

5.5	Finite Element Model of The TMD.....	102
5.5.1	Mode Shapes Analysis.....	103
5.6	Optimization of TMD Parameters.....	106
5.6.1	Optimum Mass Ratio.....	106
5.6.2	Results and Discussion.....	107
5.6.3	Simulation of The Models.....	109
5.6.4	Optimum Frequency Ratio.....	109
5.6.5	Results and Discussion.....	110
5.6.6	Optimum Damping Ratio.....	112
5.6.7	Results and Discussion.....	113
5.7	Validation of The TMDs Models.....	114
5.7.1	Wang and Co-authors Benchmark.....	115
5.7.2	Lin and Co-authors Benchmark.....	116
5.8	Global Sensitivity Analysis.....	116
5.9	Box-Behnken Sampling Method.....	117
5.9.1	Surrogate Models Results.....	119
5.9.2	Sensitivity Indices Results and Discussion.....	120
5.9.3	Convergence of The Results.....	122
<b>6</b>	<b>Novel Structural Modification.....</b>	<b>125</b>
6.1	Flutter Wind Speed.....	125
6.2	Flutter Analysis.....	125
6.3	Finite Element Model After Modification.....	127
6.3.1	Structural Modification and Mode Shapes.....	129
6.3.2	Results of Vertical Displacements.....	132
6.3.3	Results of Torsional Displacements.....	132
6.4	Results of Control Efficiency.....	133
<b>7</b>	<b>Thermal Fluid-Structure Interaction and Coupled Thermal-Stress Analysis</b>	
	<b>Due to Fire.....</b>	<b>135</b>
7.1	Standard Temperature-Time Fire Curve .....	135
7.2	Heat-Transfer Analysis .....	136
7.2.1	Thermal Analysis of a Cable Stayed Bridge .....	137
7.2.2	Heat-Transfer Theory .....	137

7.2.3	Thermal Boundary Conditions .....	138
7.3	Thermal Fluid-Structure Interaction .....	138
7.3.1	Governing Equations .....	139
7.3.2	Fluid Model .....	139
7.3.3	Solid Model .....	140
7.4	Finite Element Model of TFSI .....	140
7.4.1	Fire Scenarios.....	142
7.4.2	Results of TFSI-Models Simulations.....	143
7.4.3	Results of Lift and Drag Forces-FSI-Models.....	144
7.4.4	Results of Lift and Drag Forces-TFSI-Models.....	146
7.4.5	Results of Lock-in Phenomenon .....	148
7.5	Validation of TFSI-Models.....	150
7.6	Coupled Thermal-Stress Analysis.....	150
7.6.1	Thermal Cracking and Spalling of Concrete .....	151
7.6.2	Finite Element Model of Coupled Thermal-Stress .....	152
7.6.3	Results of Deck Displacements .....	153
7.6.4	Extended Finite Element Method .....	155
7.6.5	Results of Cracking and Spalling of The Deck.....	157
7.7	Validation of Coupled Thermal - Stress Models.....	160
<b>8</b>	<b>Conclusions and Recommendations for Further Research.....</b>	<b>162</b>
8.1	Conclusions.....	162
8.2	Recommendations for Further Researches .....	166
	<b>Appendix A.....</b>	<b>168</b>
A.1	Mesh Convergence.....	168
A.2	Surrogate Models Equations for Vertical and Torsional Responses (MATLAB Codes).....	168
A.3	Lift Force and Aerodynamic Parameters.....	169
A.4	Surrogate Models Equations for Kinetic Energy and Lift Force (MATLAB Codes)....	170
A.5	Effect of TMD's Design Parameters on Vertical and Torsional Responses .....	170
A.6	Surrogate Models Equations for Vertical and Torsional Control Efficiencies (MATLAB Codes).....	172
	<b>References.....</b>	<b>173</b>





# List of Figures

2.1	Vertical and torsional motions of the deck.....	16
2.2	Aerodynamic characterization of a section.....	18
2.3	Sag of a stay cable and viscous damping.....	19
2.4	Mesh convergence considering four mode shapes of vibrations.....	22
2.5	Wind speed fluctuation time history.....	23
2.6	Wind pressure and the FE model.....	23
2.7	Eight mode shapes of vibrations (Frequency Analysis).....	25
2.8	Time history of vertical vibration at mid-span center of the deck.....	26
2.9	Time history of flutter vibration at mid-span edges of the deck.....	27
2.10	Eight simulations of vibration in the cable stayed bridge model.....	28
2.11	Wind attack angle effect on the vertical displacement of the deck .....	30
2.12	Wind attack angle effect on the torsional displacement of the deck.....	30
2.13	Deck streamlined length effect on the vertical displacement of the deck.....	31
2.14	Deck streamlined length effect on the torsional displacement of the deck.....	31
2.15	Viscous damping of stay cables effect on the vertical displacement of the deck.....	32
2.16	Viscous damping of stay cables effect on the torsional displacement of the deck.....	33
2.17	Lift coefficient $C_L$ with wind attack angle validation.....	34
2.18	Moment coefficient $C_m$ with wind attack angle validation.....	34
2.19	Coefficient of determination between actual and predicted vertical displacement.....	40
2.20	Response surface plot showing effect of <b>X1</b> and <b>X2</b> on the predicted vertical displacement.....	40
2.21	Response surface plot showing effect of <b>X1</b> and <b>X3</b> on the predicted vertical displacement.....	41
2.22	Response surface plot showing effect of <b>X2</b> and <b>X3</b> on the predicted vertical displacement.....	41
2.23	Coefficient of determination between actual and predicted torsional displacement.....	41
2.24	Response surface plot showing effect of <b>X1</b> and <b>X2</b> on the predicted torsional displacement.....	42
2.25	Response surface plot showing effect of <b>X1</b> and <b>X3</b> on the predicted torsional displacement.....	42
2.26	Response surface plot showing effect of <b>X2</b> and <b>X3</b> on the predicted torsional displacement.....	42

2.27	Convergence of sensitivity indices-Vertical displacement.....	44
2.28	Convergence of sensitivity indices-Torsional displacement.....	45
3.1	Karman-Bernard's (Von Karman) vortex street.....	47
3.2	Vortex Street for a bluff body (Dyrbye and Hansen, 1999).....	48
3.3	Dynamic viscosity of air versus temperature.....	50
3.4	Schematic flow around a stationary bridge deck.....	51
3.5	Deck model dimensions.....	52
3.6	Flow domain size in CFD.....	52
3.7	Vortex shedding-Mesh size 28074 elements.....	53
3.8	Vortex shedding-Mesh size 9943 elements.....	53
3.9	Vortex shedding- Mesh size 7724 elements.....	54
3.10	Vortex shedding-Mesh size 6202 elements.....	54
3.11	Vortex shedding-Mesh size 5317 elements.....	54
3.12	Vortex shedding-Velocity field-V=0.5 m/s.....	55
3.13	Vortex shedding-Vorticity field-V=0.5 m/s.....	55
3.14	Vortex shedding-Velocity field-V=12.5 m/s.....	56
3.15	Vortex shedding-Vorticity field-V=12.5 m/s.....	56
3.16	Vortex shedding-Velocity field-V=25 m/s.....	56
3.17	Vortex shedding-Vorticity field-V=25 m/s.....	56
3.18	Wind speed V = 0.5 m/s and the kinetic energy of the system.....	57
3.19	Wind speed V = 12.5 m/s and the kinetic energy of the system.....	57
3.20	Wind speed V = 25 m/s and the kinetic energy of the system.....	58
3.21	Effect of wind speed on the kinetic energy of the system.....	58
3.22	Vortex shedding-Velocity field-Deck streamlined length L = 0 m.....	59
3.23	Vortex shedding-Velocity field-Deck streamlined length L = 1 m.....	59
3.24	Vortex shedding-Velocity field-Deck streamlined length L = 2 m.....	59
3.25	Effect of deck streamlined length on the kinetic energy of the system.....	60
3.26	Vortex shedding-Velocity field-Air dynamic viscosity $\mu=1.632E-5$ .....	61
3.27	Vortex shedding-Velocity field-Air dynamic viscosity $\mu=1.757E-5$ .....	61
3.28	Vortex shedding-Velocity field-Air dynamic viscosity $\mu=1.882E-5$ .....	61
3.29	Effect of air dynamic viscosity on the kinetic energy of the system.....	62

3.30	Wind speed and ratio of two vortices rows central distance to one row vortices central distance validation.....	63
3.31	Wind speed and one row vortices central distance validation.....	64
3.32	Coefficient of determination between actual and predicted kinetic energy.....	66
3.33	Response surface plot showing effect of <b>X1</b> and <b>X2</b> on the predicted kinetic energy.....	66
3.34	Response surface plot showing effect of <b>X1</b> and <b>X3</b> on the predicted kinetic energy.....	66
3.35	Response surface plot showing effect of <b>X2</b> and <b>X3</b> on the predicted kinetic energy.....	67
3.36	Coefficient of determination between actual and predicted lift force.....	67
3.37	Response surface plot showing effect of <b>X1</b> and <b>X2</b> on the predicted lift force.....	68
3.38	Response surface plot showing effect of <b>X1</b> and <b>X3</b> on the predicted lift force.....	68
3.39	Response surface plot showing effect of <b>X2</b> and <b>X3</b> on the predicted lift force.....	68
3.40	Convergence of sensitivity indices-Kinetic energy.....	70
3.41	Convergence of sensitivity indices-Lift force.....	71
4.1.a	Deck model dimensions.....	77
4.1.b	Flow domain size.....	77
4.1.c	The CSD model .....	77
4.2	Domains and fluid–structure interaction boundary conditions.....	78
4.3.a	CFD mesh size-9943 elements.....	79
4.3.b	CSD mesh size-357 elements.....	79
4.4	Vortex shedding one-way V=1 m/s.....	80
4.5	Vortex shedding two-way V=1 m/s.....	80
4.6	Vortex shedding one-way V=10 m/s.....	80
4.7	Vortex shedding two-way V=10 m/s.....	80
4.8	Vortex shedding one-way V=15 m/s.....	81
4.9	Vortex shedding two-way V=15 m/s.....	81
4.10	Time history of lift forces V=1 m/s.....	81
4.11	Time history of lift forces V=5 m/s.....	82
4.12	Time history of lift forces V=10 m/s.....	82
4.13	Time history of lift forces V=15 m/s.....	83
4.14	Time history of drag forces V=1 m/s.....	84
4.15	Time history of drag forces V=5 m/s.....	84

4.16	Time history of drag forces $V=10$ m/s.....	85
4.17	Time history of drag forces $V=15$ m/s.....	85
4.18	Time history of the simulations kinetic energy.....	86
4.19	Vortex shedding at Lock-in region.....	87
4.20	Wind speed versus Vortex shedding frequency - Lock-In phenomenon.....	88
4.21	Reynolds number versus lift coefficient.....	89
4.22	Reynolds number versus drag coefficient.....	89
4.23	Reynolds number versus Strouhal number.....	91
4.24	Wind speed versus Vortex shedding frequency- Lock-in phenomenon validation.....	92
4.25	Reynolds number versus drag coefficient validation.....	93
5.1	TMD attached to the primary mass.....	98
5.2	Location of TMDs for suppressing a- Vertical vibration and b- Torsional vibration .....	100
5.3	Positioning the TMDs.....	102
5.4	Wind speed fluctuation profile.....	103
5.5	Eight mode shapes of vibrations.....	104
5.6	Power spectral densities of vertical and torsional displacements at the mid span.....	105
5.7	TMD mass ratio effect on the vertical vibration.....	107
5.8	TMD mass ratio effect on torsional vibration.....	108
5.9	TMDs mass ratio effect on vertical and torsional vibrations.....	109
5.10	TMD frequency ratio effect on the vertical vibration.....	111
5.11	TMD frequency ratio effect on torsional vibration.....	112
5.12	TMD damping ratio effect on the vertical vibration.....	113
5.13	TMD damping ratio effect on the torsional vibration.....	114
5.14	Validation for TMDs mass ratio effect on the vertical vibration of the deck.....	115
5.15	Validation for TMDs damping ratio effect on the vertical vibration of the deck.....	116
5.16	Box-Behnken experimental design.....	117
5.17	Coefficient of determination-Vertical vibration control efficiency.....	120
5.18	Coefficient of determination-Torsional vibration control efficiency.....	120
5.19	Convergence of sensitivity indices-Vertical vibration control efficiency.....	122
5.20	Convergence of sensitivity indices-Torsional vibration control efficiency.....	123

6.1	Wind induced forces (lift and drag) and moment in the deck.....	126
6.2	Finite element model before structural modification.....	128
6.3	Finite element model after structural modification.....	128
6.4	Wind speed fluctuation time history.....	128
6.5	Sixteen mode shapes of vibrations before and after structural modification.....	131
6.6	Time history of vertical vibrations at center of the deck mid-span.....	132
6.7	Time history of torsional vibrations at outer edges of the deck mid-span.....	133
7.1	ISO 834 Standard temp - Time fire curve.....	135
7.2	The heat- transfer process of a segmental bridge deck exposed to fire.....	137
7.3	Deck TFSI-model dimensions.....	141
7.4.a	Segmental deck exposed to fire scenarios-Fire scenario 1.....	142
7.4.b	Segmental deck exposed to fire scenarios-Fire scenario 2.....	142
7.4.c	Segmental deck exposed to fire scenarios-Fire scenario 3.....	142
7.5.a	TFSI-Models-Fire scenarios-Fire scenario 1-Vorticity field .....	144
7.5.b	TFSI-Models-Fire scenarios- Fire scenario 1-Temperature field.....	144
7.5.c	TFSI-Models-Fire scenarios-Fire scenario 2-Vorticity field.....	144
7.5.d	TFSI-Models-Fire scenarios-Fire scenario 2-Temperature field.....	144
7.5.e	TFSI-Models-Fire scenarios-Fire scenario 3-Vorticity field.....	144
7.5.f	TFSI-Models-Fire scenarios-Fire scenario 3-Temperature field.....	144
7.6.a	Lift and drag forces-FSI models- No Fire.....	145
7.6.b	Lift and drag forces-FSI models-Fire scenario1.....	145
7.6.c	Lift and drag forces-FSI models-Fire scenario 2.....	145
7.6.d	Lift and drag forces-FSI models-Fire scenario 3.....	145
7.7.a	Lift and drag forces-TFSI models-No Fire.....	147
7.7.b	Lift and drag forces-TFSI models-Fire scenario1.....	147
7.7.c	Lift and drag forces-TFSI models-Fire scenario 2.....	147
7.7.d	Lift and drag forces-TFSI models-Fire scenario 3.....	147
7.8	Lock-in Phenomenon - TFSI and FSI models .....	149
7.9	Lock-in TFSI-models validation .....	150
7.10	Finite element 3D model of the cable stayed bridge.....	152

7.11	Horizontal displacement .....	154
7.12	Vertical displacement.....	154
7.13	Angular displacement .....	154
7.14	Enriching shape functions of node 2 and node 3.....	156
7.15	Crack in 3D by two level set functions $\Phi$ and $\Psi$ .....	156
7.16	Maximum principal stress - Fire scenario 1- Without XFEM damage simulation .....	157
7.17	Maximum principal stress - Fire scenario 1- With XFEM damage simulation.....	157
7.18	Maximum principal stress - Fire scenario 2- Without XFEM damage simulation .....	158
7.19	Maximum principal stress - Fire scenario 2- With XFEM damage simulation .....	158
7.20	Maximum principal stress - Fire scenario 3- Without XFEM damage simulation .....	159
7.21	Maximum principal stress - Fire scenario 3- With XFEM damage simulation .....	159
A.1	Mesh convergence for mode shapes of vibrations.....	168
A.3.1	Effect of wind speed on the generated lift force in the deck.....	169
A.3.2	Effect of deck streamlined length on the generated lift force in the deck.....	169
A.3.3	Effect of air dynamic viscosity on the generated lift force in the deck.....	169
A.5.1	Effect of TMD mass ratio on the vertical vibration of the deck.....	170
A.5.2	Effect of TMD mass ratio on the torsional vibration of the deck.....	170
A.5.3	Effect of TMD frequency ratio on the vertical vibration of the deck.....	171
A.5.4	Effect of TMD frequency ratio on the torsional vibration of the deck.....	171
A.5.5	Effect of TMD damping ratio on the vertical vibration of the deck.....	171
A.5.6	Effect of TMD damping ratio on the torsional vibration of the deck.....	172

# List of Tables

2.1	Material properties .....	22
2.2	Modes and frequencies.....	24
2.3	Aerodynamic parameters and range values.....	29
2.4	Results of lift and moment coefficients for ABAQUS FE model and two benchmarks.....	33
2.5	Range values and probability distributions for the aerodynamic parameters.....	36
2.6	Sensitivity indices of the aerodynamic parameters.....	43
3.1	Validation with Von Karman benchmark.....	63
3.2	Validation with Dyrbye and Hansen benchmark.....	64
3.3	Sensitivity indices.....	70
4.1	Reynolds number versus lift and drag coefficients for multiple wind velocities.....	90
4.2	Strouhal number versus vortex shedding frequency for multiple wind velocities.....	91
5.1	Vibration modes data.....	103
5.2	Parameters of TMDs for multiple mass ratios.....	106
5.3	Vertical vibration control efficiency-Mass ratio .....	107
5.4	Torsional vibration control efficiency-Mass ratio .....	108
5.5	Parameters of the TMD for multiple frequency ratios .....	110
5.6	Vertical vibration control efficiency-Frequency ratio.....	111
5.7	Torsional vibration control efficiency-Frequency ratio.....	112
5.8	Parameters of the TMD for multiple damping ratios .....	112
5.9	Vertical vibration control efficiency-Damping ratio.....	113
5.10	Torsional vibration control efficiency-Damping ratio .....	114
5.11	The level of variables chosen for the Box-Behnken design.....	118
5.12	Box-Behnken design with coded and actual values for three size fractions .....	119
5.13	Sensitivity indices.....	121
6.1	Mode shapes and frequencies.....	129
7.1	Lock-in data for TFSI and FSI models .....	149
7.2	Mode shapes and frequencies.....	153



# Nomenclature

## Abbreviations

FE	Finite Element
VIV	Vortex Induced Vibration
B.C	Boundary Condition
CSD	Computational Structural Dynamics
CFD	Computational Fluid Dynamics
FSI	Fluid-Structure Interaction
TMDs	Tuned Mass Dampers
MTMDs	Multiple Tuned Mass Dampers
FFT	Fast Fourier Transform
PSD	Power Spectral Density
TFSI	Thermal Fluid-Structure Interaction
XFEM	Extended Finite Element Method

## Aerodynamic Stability Parameters

$E_{eq}$	Equivalent modulus of elasticity
$E_c$	Effective modulus of elasticity
$A_c$	Cross sectional area
$l_c$	Horizontal projected length of the stay cable
$w$	Weight of the stay cable per unit length
$T$	Tension in the stay cable
$\mathbf{D}(t)$	Nodal displacement vector
$\dot{\mathbf{D}}(t)$	Nodal speed vector
$\ddot{\mathbf{D}}(t)$	Nodal acceleration vector
$\mathbf{M}$	Mass matrix
$\mathbf{C}$	Damping matrix
$\mathbf{K}$	Stiffness matrix
$\mathbf{F}^s$	Self excited force vector
$\mathbf{F}^b$	Buffeting force vector

$\bar{C}_{Fx}$	Mean force coefficient along x – axis
$\bar{C}_{Fy}$	Mean force coefficient along y – axis
$\bar{F}_x$	Mean force along x – axis
$\bar{F}_y$	Mean force along y – axis
$B$	Characteristic dimension
$\rho$	Density of air
$\bar{U}_z$	Mean wind speed along deck height
$\bar{F}_D$	Mean drag force
$\bar{F}_L$	Mean lift force
$\bar{M}$	Mean moment
$\bar{C}_D$	Mean drag force coefficient
$\bar{C}_L$	Mean lift force coefficient
$\bar{C}_M$	Mean moment coefficient
$\bar{y}$	Mean of $y_i$ values
$N$	Number of simulations
$V(y)$	Variance of $y_i$ values
$\beta_0, \beta_i, \beta_{ii}, \beta_{ij}$	Regression parameters
$D$	Design matrix
$\epsilon$	Random error
$X'$	Transpose of matrix $X$
$V(Y)$	Total variance of model output
$S_i$	First order sensitivity index
$S_{ij}$	Second order sensitivity index
$S_{Ti}$	Total sensitivity index
$R^2$	Coefficient of determination

### **Kinetic Energy Based Model Assessment**

$\Gamma$	Strength of vorticity
$u_K$	Speed of vortices
$h_K$	Distance between the rows (Von Karman)
$b_K$	Distance between the vortices in a row (Von Karman)
$\bar{H}_K$	Mean value of induced horizontal force per unit length
$q$	Kinetic pressure

$h$	Height of deck
$C_{HK}$	Horizontal force coefficient
$U$	Wind flow speed
$V_K$	Fluctuating across – wind force per unit length
$C_{VK}$	Vertical force coefficient
$f_s$	Vortex shedding frequency
$U_1$	Speed of vortices (Dyrbye and Hansen)
$l_v$	Distance between the vortices (Dyrbye and Hansen)
$d$	Height of the bluff body (Dyrbye and Hansen)
$Re$	Reynolds number
$\mu$	Dynamic viscosity of air
$Ke$	Kinetic energy of the system
$L$	Deck streamlined length

### **Fluid-Structure Interaction and Lock-in Phenomenon**

$S_t$	Strouhal number
$L_S$	Across wind force (Simiu and Scanlan)
$C_{LS}$ , $Y_1$ , $Y_2$ , and $\varepsilon$	Experimental parameters
$K_{st}$	Strouhal reduced frequency
$M_s$	Structural mass matrix
$D_s$	Structural damping matrix
$K_s$	Structural stiffness matrix
$F_s$	Applied force vector
$u$	Nodal displacement vector
$\dot{u}$	Velocity of the structure vector
$\ddot{u}$	Acceleration of the structure vector
$C_L$	Lift force coefficient
$C_D$	Drag force coefficient

### **Control Efficiency Optimization of MTMDs**

$\mu$	Mass ratio for dampers
$m_d$	Mass of the damper
$m$	Mass of the primary mass
$\dot{u}_d$	Velocity of the damper

$\dot{u}$	Velocity of the primary mass
$\ddot{u}_d$	Acceleration of the damper
$\ddot{u}$	Acceleration of the primary mass
$w_d$	Natural circular frequency of the damper
$w$	Natural circular frequency of the primary mass
$\xi_d$	Damping ratio of the damper
$\xi$	Damping ratio of the primary mass
$c_d$	Damping coefficient of the damper
$c$	Damping coefficient of the primary mass
$k_d$	Stiffness of the damper
$k$	Stiffness of the primary mass
$p$	Sinusoidal excitation
$u_d$	Response of the damper
$u$	Response of the primary mass
$\hat{u}_d$	Displacement amplitude of the damper
$\hat{u}$	Displacement amplitude of the primary mass
$\delta$	Phase shift
$\xi_e$	Equivalent damping ratio
$\mathbf{u}_s$	Vector of absolute displacement of the main structure
$u_{t1}$	Absolute displacement of TMD1
$u_{t2}$	Absolute displacement of TMD2
$\mathbf{x}_s$	Vector of generalized coordinate displacement the of main structure
$x_{t1}$	Generalized displacement of TMD1
$x_{t2}$	Generalized displacement of TMD2
$\Phi_n$	An $n$ th natural mode shape of the main structure without TMD
$f_{d,opt}$	Optimum frequency ratio parameter of the TMD
$\xi_{d,opt}$	Optimum damping ratio parameter of the TMD
$z$	Factor number
$c_p$	Replicate number of the central point
$y$	Predicted response
$\beta_0$	Model constant
$x_1, x_2, x_3$	Independent variables

$\beta_1, \beta_2, \beta_3$	Linear coefficients
$\beta_{12}, \beta_{13}, \beta_{23}$	Cross product coefficients
$\beta_{11}, \beta_{22}, \beta_{33}$	Quadratic coefficients

### **Novel Structural Modification**

$\mathbf{y}$	Displacement vector
$v$	Horizontal degree of freedom
$w$	Vertical degree of freedom
$\varphi_x$	Rotational degree of freedom
$\mathbf{f}_z$	Aeroelastic force matrix
$B$	Deck width
$\rho$	Air density
$V$	Wind speed
$K$	Reduced frequency
$\omega$	Response frequency
$A_i^*, H_i^*, P_i^* (i = 1, \dots, 6)$	Experimental flutter derivatives
$\mathbf{K}_z$	Aeroelastic stiffness matrix
$\mathbf{C}_z$	Damping matrix
$\Phi$	Modal matrix
$\mu, G$	Complex values
$\theta$	Structural damping
$\gamma$	Damping frequency

### **Thermal Fluid-Structure Interaction and Coupled Thermal-Stress Analysis Due to Fire**

$T_c$	Temperature of fluid in celsius
$t$	Time
$q_c$	Convective heat flux
$h_c$	Convection coefficient
$T_s$	Surface temperature
$T_a$	Ambient temperature
$q_r$	Radiation heat flux
$\phi$	Shape factor
$\epsilon_s$	Emissivity of surface

$\epsilon_a$	Emissivity of Ambient
$\sigma$	Stephan – Boltzmann's constant
$h_{net}$	Net heat flux
$k$	Isotropic thermal conductivity coefficient
$\rho$	Density
$c$	Specific heat of the material
$n$	Normal to the surface
$h$	Heat – transfer coefficient
$h_r$	Thermal irradiation
$q$	Boundary heat exchange per unit area
$v$	Velocity of the fluid
$m$	Momentum
$E$	Energy per unit volume
$\tau_v$	Viscous shear stress tensor
$Re$	Reynolds number
$Pr$	Prandtl number
$\Omega_2$	Solid domain
$\psi_s$	Temperature of the solid
$\psi_r$	Temperature rate
$Q$	Heating source
$\dot{H}(\psi)$	Temperature dependent conductivity
$h_s(\psi)$	Specific heat capacity
$\bar{c}$	Forced convection of the fluid
$\psi_\infty^4$	Bulk temperature
$u^h(X)$	Discretization of the displacement field in 1D
$N_j(X)$	Shape functions of the nodes $N_j$
$N_j(X)H(f(X))$	Enriched shape functions of the nodes $N_j$



# Chapter 1

## Introduction

### 1.1 Background

Long span bridges are vulnerable to many types of vibrations when subjected to wind buffeting action due to their slenderness, high flexibility, low structural damping and lightweight. Therefore their safety and serviceability are often critical due to wind-induced vibrations. Buffeting action is a type of vibration motion induced by turbulent wind. The natural wind is not steady but has a turbulent characteristic, so the wind fluctuations in the vertical and horizontal directions are random in space, and thus the wind pressures along the bridges are random in time and space. The coupled mode of vibrations which is resulting from the deck-stay cables interaction at lower modes of vibrations is dominant and critical case. The buffeting responses of the long span bridges increase and become more notable when increasing the bridge span and the deck width. The internal forces and the displacements resulted from buffeting responses are growing more apparent when the wind speed is high. As a result many serious effects are arising such as fatigue of the structural components and in critical cases result in the failure of the structure. The Tacoma incident is the best example case of a wind induced failure. However significant numbers of bridges have experienced extreme responses which were of sufficiently large amplitudes to be considered at serious condition. Aerodynamic effect is the most important aspect of this type of vibration and the greatest aerodynamic effect is caused by flutter. The flutter stability of bridge structures is due to the critical wind speed. When flutter occurs, the wind forces change continuously due to structural displacements, while the wind alters the stiffness and structural damping of the system. When the free span of a bridge increases, the aerodynamic instability increases. The critical wind speed would step down due to the resulting reduced torsional stiffness particularly and the reduced bending stiffness. When the structural damping becomes very low, a small oscillation would be amplified until the structural failure [Simiu and Scanlan, 1996; Diana *et al.*, 1998; Lin *et al.*, 2000; Chen *et al.*, 2001; Chen and Cai, 2003; Chen *et al.*, 2004; Valdebenito and Aparicio, 2006; Al-Assaf, 2006; Ubertini, 2008; Starossek and Aslan, 2008; Janjic, 2010; Kwon, 2010; Patil, 2010; Van Vu. *et al.*, 2011; Keerthana *et al.*, 2011; Kvamstad, 2011; Odden and Skyvulstad, 2012; Huang *et al.*, 2012; Qin *et al.*, 2013; Mohammadi, 2013; Flamand *et al.*, 2014; Xu, 2013; Xie *et al.*, 2014; Xu *et al.*, 2014].

When the aeroelastic interaction between the wind and the long span bridges is generated, the flutter and the torsional instabilities can take place at certain wind speeds. The vibrational



## 1.1 Background

---

response of long span bridges is affected by many structural characteristics like mass, stiffness and energy dissipation mechanisms [Ding and Lee, 2000; Man, 2004; He *et al.*, 2008; Ge and Xiang, 2008; Vairo, 2010; Zhang Xi, 2012; Shin *et al.*, 2014]. Recently many slender long span bridges have been constructed without taking in consideration the both the bending and torsional stiffness, which resulted in wide displacements especially at the mid span of the deck with probabilities of aeroelastic instability and structural failure. The extra sensitivity of long span cable supported bridges due to wind excitation is related to the very low structural damping in the coupled modes of vibrations widely below 1% and even less than this value in the vibration modes associated with cable vibrations. Flutter and torsional instabilities force limits on the length increase of long span cable supported bridges which can be avoided by better aerodynamic design of the deck or by the use of vibration control methods [Jones and Spartz, 1990; Pacheco *et al.*, 1993; Cheng, 1999; Su *et al.*, 2003; Fujino *et al.*, 2010; Wang *et al.*, 2013; Phan and Nguyen, 2013; Xiong *et al.*, 2014; Preumont *et al.*, 2015; Kusano, 2015; Haque, 2015; Bakis *et al.*, 2016].

Vortex induced vibration (VIV) which is one of the wind-induced vibrations, is predominantly decisive for the security and serviceability of these structures. The segmental bridge decks are being selected supporting on many factors like structural and economic characteristics, where the essential shape of the deck is not requisite to be aerodynamically efficient optimally. Due to this fact, long span bridges are overwhelmingly undergo VIV [Frandsen, 2004; Sarwar and Ishihara, 2010; Wu and Kareem, 2012; Fujino and Siringoringo, 2013]. Several research studies on the geometries and the vortex shedding mechanisms from bluff bodies have been conducted. Presently the deck cross sections are designed between bluff bodies and streamlined, for example the Tsing Lung Bridge in Hong Kong. The wind flow in the wake region of a bluff body such as segmental bridge decks is described by vortices which are shed from its trailing edge continuously at a particular frequency, where they are often attributed to Karman vortices. The shape and the pattern of the vortices are occasionally referred to Karman Street [Kiviluoma, 2001; Nicoli, 2008; Edvardsen, 2010; Patil, 2010; Asyikin, 2012; Dahl, 2013]. These vortices are shed from the bridge deck continuously regardless of the wind speed magnitude. The shedding eddies have frequencies varying linearly with the wind speed since the Strouhal number is stable mostly. When the shedding frequency is matching the frequency of particular mode of vibration of the structure, either vertical or torsional, the resonance might occur as a result the lock-in of the bridge oscillation starts. Within particular limits and if the wind speed continues to increase, the shedding frequency of the vortices keeps unaltered. This situation is named synchronization domain. In a certain case where the ambit of the wind velocities is wide, this might cause fatigue, discomforts or failure depending on the oscillations amplitude [Zhang *et al.*, 2004;

## 1.1 Background

---

Diana *et al.*, 2006; Irwin, 2008; Fariduzzaman *et al.*, 2008; Zhang, 2012; Flamand *et al.*, 2013; Belloli *et al.*, 2014; Grouthier *et al.*, 2014]. Various shapes and patterns of vortex shedding exist. These depend on the shape of the deck, diverse vortex shedding mechanisms and Reynolds number (Re). The vortex shedding mechanism might be totally different relying on the shape of the deck cross section. The main reason of VIV in a long span bridge is referred to structural low damping and structural slenderness. This truth is approved in the case of Rio-Niteroi Bridge in Rio de Janeiro which has manifested vortex shedding vibrations even at weak wind speed of 14 m/s, where this event was not counted for in the design stage. VIV can be reduced through selecting suitable cross sections and shapes for bridge decks [Blackburn and Henderson, 1996; Schewe and Larsen, 1998; Larsen and Walther, 1998; Xie *et al.*, 2011; Lopes *et al.*, 2006; Tang *et al.*, 2008; Chen *et al.*, 2014]. The aerodynamic behavior and the damping of the bridge decks are affected and altered by the vortex shedding pattern and the shape of the vortices. As a result, the deck reaction is affected. The vortex shedding pattern and the shape of the vortices are affected by the frequency and the amplitude of the oscillations. Hence, the study of the vortices shape and the vortex shedding pattern helps to comprehend the relationship between the vortex shedding patterns and the structural response at various Reynolds numbers [Bosch and Dhall, 2008; Liu *et al.*, 2012; Corriols and Morgenthal, 2012; Bosman, 2012; Abdi *et al.*, 2012; Hansen *et al.*, 2013, Borna *et al.*, 2013].

VIV is a strong fluid-structure interaction (FSI) phenomenon. The application of FSI concept in the vibration of long span bridges is a sensitive and important step in understanding the actual behavior of the structure during vibration resulted from a wind excitation. The VIV of the deck is a type of vibration results from the FSI between the wind and the deck of the bridge. When a bridge deck is excited by a wind, it starts to oscillate in the in-line and the cross-flow directions. The in-line oscillation often takes place at twice the frequency of the cross-flow oscillation, and it is very small compared to the cross-flow oscillation. Therefore it is not important in the majority of the engineering applications. When the cross-flow oscillation amplitude of the deck is large enough, the FSI enhances and increases the strength of the vortices or the mean drag forces on the deck. In the same time, the motion of the deck will alter the phase, sequence and the vortices pattern in the wake region. The application of fluid-structure coupling using numerical simulations is a complicated problem. It does result in arising difficulties related to the fluid and the structure simulations in addition to coupling of these two systems which is a hard process. These difficulties resulted from the coupling process depends highly on the physical properties of the problem which is under simulation [Simiu and Scanlan, 1996; Selvam *et al.*, 1998; Dowell and Hall 2001; Onate and Garcia, 2001; Frandsen, 2004; Liaw, 2005; Chakrabarti, 2005; Vazquez, 2007; Badia and Codina,

## 1.1 Background

---

2007; Forster, 2007; Bourdier, 2008; Farshidianfar and Zanganeh, 2009; Razzaq *et al.*, 2010; Schmucker *et al.*, 2010; Peng and Chen, 2012; Raja, 2012; Sarkic, 2014].

Fast increase of bridge spans led to undertake research on controlling wind-induced vibration in long span bridges. Many research efforts have been done to improve aerodynamic stabilities and to suppress excessive buffeting vibrations in long span bridges both at the construction and at service time. The solution for the buffeting and flutter vibrations control in long-span bridges is mainly related to the use of passive devices, dynamic energy absorbers such as tuned mass dampers (TMDs), which have been studied to mitigate serious dynamic buffeting vibration or to enhance the flutter stability of long span bridges. These control devices that are called dynamic energy absorbers, dissipate external energy through supplying damping to the designated mode shapes of vibrations [Lin *et al.*, 1999; Din and Lee, 2000; Pourzeynali and Esteki, 2009; Chen, 2010]. Increasing the lengths of the bridge span and adopting slender decks tend to make the frequencies of the mode shapes of vibrations close to each other, which results in increasing the modal coupling effects via aero-elastic effects in strong wind cases. The effects of modal coupling resulted from a strong wind may lead to a significant additional component to the buffeting vibration of each certain mode, compared with the modal coupling effects resulted from a weak wind. There is a limitation imposed on the application of TMD because it is effective in suppressing vibrations in one mode only, usually it is the first mode. Furthermore, a TMD is efficient in a narrow frequency range only, this exactly when it is tuned to a certain natural frequency of the structural system and it doesn't act efficiently if the system manifests many narrow natural frequencies [Tang, 1997; Kubo, 2004; Starossek and Aslan, 2007; Ubertini *et al.*, 2015].

The application of thermal fluid-structure interaction (TFSI) is very important regarding the safety and stability of long span due to fire incidents. It enables a profound analysis about triple interaction between the bridge deck, forthcoming wind and the thermal boundary of the air. Regarding TFSI, in Addition to the fluid domain and the structural domain, a thermal domain is considered. Many environmental thermal effects such as fire, solar radiation and the air temperature have significant impact on bridges. The continuous change of temperatures in their structural elements may result in nonlinear thermal stresses that affect their performance significantly. Generally, fire incidents are caused by smashing of vehicles and combust of fuel on or under the bridges. The variation in the structural temperature and its distribution in bridges lead to displacements, deformations, potentially extreme stresses, cracks and in serious cases of fire might lead to structural collapse. Fires that are originated by gasoline are considered most dangerous than building fires because they are distinguished by a rapid heating rate and very high temperature. Regarding these types of fires, very high

## 1.2 State of The Art

---

temperatures will be acquired during the first few minutes [Baba *et al.*, 1988; Potgieter and Gamble, 1989; Bennetts and Moinuddin, 2009; Paya-Zaforteza and Garlock, 2012; Garlock *et al.*, 2012; Grilli *et al.*, 2012; Zhou and Yi, 2013; Peris-Sayol *et al.*, 2014; Braxtan *et al.*, 2015; Zhou *et al.*, 2016; Kodur and Agrawal, 2016; Schumacher, 2016]. A bridge fire took place in Birmingham, USA in 2002 due to collide of a diesel tanker with one of the Piers. The fire finished after 45 minutes of burning 142,000 liters of diesel approximately. The location of the fire was under the bridge and a part was unexposed. Due to non-regular exposure, the bridge collapsed partially. The MacArthur Maze Bridge in USA in 2007, partially failed due to truck incident with one of the support columns resulted in combustion of 32, 600 liters of gasoline for more than two hours [Choi, 2008; Giuliani *et al.*, 2012; Wright *et al.*, 2013; Alos-Moya *et al.*, 2014].

## 1.2 State of The Art

The up to date studies regarding wind-induced vibrations and especially the aerodynamic stability of long span cable supported bridges have covered the effect of many aerodynamic parameters on the overall structural damping which is responsible of the safety and serviceability of the structure. Theoretical analysis using finite element method and experimental analysis utilizing wind tunnel test have been adopted to enhance the design of the structure against this problem in particular the deck. But the vibration problem in these structures has not been solved totally. It is has been proofed that the coupled mode of vibrations is the dominant which is resulting from the deck-stay cables interaction at lower modes of vibrations due to associated and nearby wind excitations.

The previous studies were mostly supporting on the results of Reynolds number (Re) and Strouhal number (St) to analyze the VIV of the deck and in the same time without considering important parameters that have uncertain effects on this type of vibration. The influence of the (FSI) in the analysis of VIV has achieved important and active results but it still needs to be thoroughly studied, in addition to its role on predicting the lock-in phenomena and critical wind speed.

The most of previous researches have studied the application of active and passive devices to control vibrations in the long span bridges such as multiple tuned mass dampers (MTMDs) to optimize the design parameters considering the first lower natural frequencies of the long span bridges, in the same time the performance of the MTMDs system is still limited and hasn't controlled the horizontal, vertical and torsional vibrations of the deck totally.

Up to date researches have concentrated on the heat- transfer in the structural elements of bridges and analyzed their failure due to fire incidents and thermal environmental effects.

### 1.3 Literature Review

---

Numerical simulations were utilized to model the actual damaged members of the bridges supporting on standard temperature-time curve of Eurocode1. These researches haven't covered the effect of transient heat-transfer due to fire incidents on the behavior of long span bridges during wind excitations regarding VIV and lock-in phenomenon. They haven't considered the thermal effect mechanism on the generation of lock-in phenomena in addition to the role of thermal effects in speeding up the fatigue and failure of the bridge along with the incoming critical wind speeds.

### 1.3 Literature Review

Previous studies in the field of wind-induced vibrations have been conducted to study the problem theoretically and practically so that to identify the solutions to control or at least to suppress the vibrations and eliminate their serious effects on the performance and safety of the long span bridges. The following is a short summary of many studies and the findings of the previous works.

[Ma *et al.*, 2010] investigated the aerodynamic behavior of the Sutong Bridge. They presented the main results of wind tunnel tests on a sectional model and the full aeroelastic models of the Sutong Bridge. They discovered that both the lift and moment coefficients are increasing from (-1 to 0.5) and (-0.2 to 0.1) respectively with the increase of the turbulent wind attack angle between ( $-10^\circ$  to  $10^\circ$ ). [Xavier *et al.*, 2015] studied experimentally the effect of wind attack angle on the generation of lift and drag forces and pitching moment in a flat plate with multiple aspect ratios excited by a turbulent wind in the wind tunnel test. The results of the lift and the moment coefficients were supported on the range of wind attack angle between ( $0$  to  $90^\circ$ ). The lift coefficient and moment coefficient values were (-0.12 to 0.01) and (-0.01 to 0.01) respectively, which is an indicator that increasing the wind attack angle will increase the generated lift force and moment in the flat plate. [Abdel-Aziz and Attia, 2008] conducted numerical analysis on four bridge deck sections using ANSYS software, they calculated the effect of wind attack angle on the lift and moment coefficients for the bridge deck section. The range of turbulent wind attack angle was between ( $-10^\circ$  to  $10^\circ$ ), in the other hand the calculated lift coefficient was (-0.65 to 0.2) and the calculated moment coefficient was (-0.065 to 0.1). The results affirm the increase of lift force and pitching moment in the bridge deck model.

An analytical study concerning the stability of the vortex patterns in a wake of a stationary rectangular cylindrical body was carried out by Von Karman and Rubach, 1911. Based on the two dimensional potential flow theory and assuming that the fluid is irrotational except in

### 1.3 Literature Review

---

concentrated vortices, it was shown that the vortex pattern is stable, if the vortices are organized in unsymmetrical double row pattern. [Dyrbye and Hansen, 1999] have derived the vortex shedding frequency of a non-vibrating bluff body where the time between the vortices at each side is equal to the distance divided by the speed of the vortices. The distance between the vortices must be proportional to the width of the body.

[Munson *et al.*, 2002] studied the character of the drag coefficient as a function of Reynolds number for objects with various degrees of streamlining, from a flat plate normal to the upstream flow to a flat plate parallel to the flow (two-dimensional), where this value is related to the cross flow oscillation of the body. They calculated the value of the drag coefficient for a flat plate parallel to the flow which is simulating the bridge deck subjected to a wind flow, this value's range was (0.08-0.0075) for the Reynolds number range ( $0.2 \cdot 10^6 - 2.3 \cdot 10^6$ ).

Many researchers have studied the application of TMD system in long span bridges. [Jain *et al.*, 1998] analyzed the effects of modal damping on bridge performance of aero-elasticity. It was found that supplemental damping provided through appropriate external dampers could certainly increase the flutter stability and reduce the buffeting response of long span bridges. [Nobuto *et al.*, 1988] made a study on flutter control using a couple of TMDs, and the numerical example indicated its efficiency. On this basis, a more advanced parametric study was performed by [Gu *et al.*, 1998] through a theoretical analysis and a wind tunnel test on the Tiger-gate Bridge model. [Lin *et al.*, 2000] studied the effect of TMD system in the reduction of torsional and vertical responses of suspension bridges subjected to wind loading. The important parameters involved are the natural frequency ratio and the mass ratio of damping device to the structure. They used a TMD system with two degrees of freedom, vertical and torsional. They obtained a TMD mass ratio of 2 % for getting a reduction of 25 % and 33 % in vertical and torsional responses of the bridges, respectively. Considerable effort has been directed towards the reduction of the mass ratio to an acceptable level, say less than 1%. Weight penalty and precise tuning of frequency are major considerations in their application. [Wang *et al.*, 2014] studied the optimum control of buffeting displacement in the Sutong Bridge using multiple tuned mass dampers (MTMDs). They discovered that the mass ratio and damping ratio parameters have a significant effect in controlling the vertical vibration of the deck. They obtained a mass ratio of 2% reduces 29% and a damping ratio of 3% reduces 27.5% of the vertical response of the Sutong Bridge [Kubo, 2004; Yang, 2008; Pourzeynali and Esteki, 2009; Chen, 2010]. Since the structural damping of long span bridges is very low, the applications of dashpots and frictional dampers have become an important need to increase the damping of the structure against multiple types of vibrations, such as tuned mass damper (TMD) which are mechanical dampers are modally tuned and applied at critical locations in the long span bridges to increase the structural damping of the structure [Petersen,

## 1.4 Aim and Objectives of Work

---

2001]. Sealed tuned liquid column gas damper is another device used to increase the structural damping of long span bridges which is consisted of gas spring effect consideration especially when the vibrations are occurring in low frequency range [Ziegler and Amiri, 2013]. Electromechanical actuator bearing energy conversion characteristics is another innovative device is used to damp the vibrations in long span bridges. The work of this device is similar to piezoelectric device, where efficient design of this device can lead to optimally damping vibrations of the system and energy harvesting abilities [Caruso *et al.*, 2009].

[Dotrepe *et al.*, 2006] used the developed SAFIR code at the University of Liege to implement numerical analysis for the collapse of Vivegnis Bridge. The incident happened when a fire broke out due to explosion of a gas pipe. A room temperature was considered to generate their model so that to validate it with the measurements. They performed a transient heat-transfer structural analysis supporting on the hydrocarbon temperature-time data of Eurocode1-1-2. The mode of failure and the time needed in the numerical simulation exhibited a good agreement with the actual data of the bridge collapse. [Kodur *et al.*, 2013] discussed the effects of fire incident on a bridge. They stated that the fire effect on bridges girder requires especial modeling as compared to the effect of fire on a building beam. They considered the data for the variation of heat-transfer parameters along the depth of the beam. The analysis of the results showed that when the girder depth increases, the web, flange and the slab of the girder are subject to lower radiation effects. [Zhou *et al.*, 2016] searched the temperature distribution of the Humber suspension Bridge in UK. They utilized numerical simulation for the box girder in addition to field measurements by considering multiple wind velocity to determine the thermal initial boundary conditions. They performed a transient heat-transfer and they investigated the vertical and horizontal temperature differences for the box girder. Then results of the temperature data at different regions and different times were in good agreement with the measured data, where a significant result was detected for the horizontal temperature variation in the box girder.

## 1.4 Aim and Objectives of Work

The work in this dissertation aims to:

- 1- Applying proficient numerical modeling methodologies to study and analyze the effect of wind-induced vibrations in a cable stayed bridge and to assess the behavior of the structure under the excitations of critical wind speeds and lock-in phenomenon which is responsible of generating many types of vibrations, aerodynamic instabilities and seriously affecting the safety and serviceability of the structural system by considering both computational structural

## 1.5 Methodology

---

dynamics (CSD) and computational fluid dynamics (CFD) models in addition to fluid-structure interaction (FSI) concept in the numerical simulations.

2- Constructing surrogate models for the responses of the cable stayed bridge regarding vertical and torsional vibrations of the segmental deck by the support of many active and famous methods of sampling methods which help the designers and researchers to predict the response of the system against all types of wind-induced vibrations easily and rapidly to a great extent of accuracy by considering the global effects of many aerodynamic parameters that are directly and indirectly involve in the process.

3- Predicting the role and rational effect of each utilized aerodynamic parameter on the structural response which can be used to verify the results from the experimental analysis from wind tunnel test by adopting regression analysis and variance-based global sensitivity analysis.

4- Optimizing the control efficiency of the multiple tuned mass dampers (MTMDs) system which is used to suppress and accommodate the vertical and torsional vibrations of the segmental deck by the use of minimax technique and Sobol's sensitivity indices considering three design parameters of TMDs.

5- Modifying the design of the segmental deck and the structural system so that to eliminate the danger of early coupling between the vertical and torsional mode shapes which has been proofed to be the reason beyond the negative structural damping and the possible collapse of the structure in critical wind speed situations.

6- Identifying the effect of fire incidents on the VIV and early lock-in phenomenon in addition to the detection of damages and fatigue of the segmental deck. Also to find out the coupled role of both wind-induced vibrations and fire scenarios on earlier damage generation and collapse of the structure by considering both transient heat-transfer and steady state heat-transfer through utilizing thermal fluid-structure interaction (TFSI) concept and coupled thermal-stress analysis in addition to extended finite element method (XFEM) analysis for crack propagation.

## 1.5 Methodology

To achieve the mentioned objectives, this work comprises of various stages.

1-Initially, 3D models of a long span cable stayed bridge are created using ABAQUS finite element software. A strong wind with a speed of 47 m/s and duration of 30 seconds is dedicated for numerical simulations. The wind fluctuation data is adopted supporting on exact



## 1.5 Methodology

---

field data from the literature. Then mesh convergence analysis is conducted to identify the most suitable and accurate models. Frequency analysis is performed and the first eight mode shapes of vibrations in the range of (0.242 -0.813) Hz are utilized to identify the dominant mode shapes of vibrations. Optimization of three aerodynamic parameters (wind attack angle, deck streamlined length and stay cables viscous damping) is conducted to calculate the optimum values regarding suppression of vertical and torsional vibrations of the segmental deck. Validation is performed supporting on the benchmark of flat plate theory for lift coefficient and the benchmark of flat plate model by Xavier and co-authors for moment coefficient. Global sensitivity analysis supporting on Monte Carlo sampling method is conducted to calculate the sensitivity indices of each parameter to find out the role and rational effect of each parameter in suppressing the deck vibrations, where surrogate models are constructed and convergence process for the number of samples used in the analysis is performed.

2- 2D-CFD models for the segmental deck of the cable stayed bridge are generated in ABAQUS supporting on mesh convergence for the wind flow domain so that to simulate the vortex shedding accurately. The numerical simulations of wind flow cases are with duration of 100 seconds and  $0^\circ$  attack angle supporting on both non-turbulent and turbulent flow situations by using the Spalart-Allmaras turbulence model for the latter. Kinetic energy of the system and the shapes and patterns of the vortices are based on to detect the roles of three aerodynamic parameters (wind speed, deck streamlined length and dynamic viscosity of the air) on the generation of vortex shedding and VIV. The CFD models are validated using the benchmark of Von Karman and the benchmark of Dyrbye and Hansen for vortices shapes and patterns. Variance based sensitivity analysis is performed supporting on Latin Hypercube sampling method to construct the surrogate models to identify the role and rational effect of each parameter on the kinetic energy of the system and the lift forces. Convergence analysis is conducted to identify the suitable number of samples for sensitivity analysis.

3- CFD models of the deck for one-way FSI approach and both CSD and CFD models of the deck for two-way FSI approach are generated in ABAQUS to run co-simulations for the wind flow with duration of 100 seconds and  $0^\circ$  attack angle so that to simulate and analyze the effect of FSI on the VIV and lock-in phenomenon by targeting the lift and drag forces in addition to kinetic energy as criteria of comparison supporting on a range of wind speed cases falls between (1-15) m/s. Validation of the FSI models performed basing on the benchmark of Simiu and Scanlan for lock-in phenomenon and based on the benchmark of Munson and co-authors for the drag coefficient related to a flat plate model.

## 1.5 Methodology

---

4- 3D models of the MTMDs are created in ABAQUS and they are attached to the slab of the segmental deck in the 3D model of the cable stayed bridge inside the hollows in three rows at the mid span and they are distributed symmetrically in both x and z directions. The dimensions of a single TMD is (4\*4\*0.24) m made of steel. A strong wind excitation with a speed of 54 m/s with 25° attack angle supporting on field data from the literature and a previously prepared excitation frequency is dedicated in the numerical simulations for duration of 30 seconds. Frequency analysis is performed, and twenty mode shapes of vibrations in the range of (0.242-1.631) Hz are considered so that to examine the control efficiency of the MTMDs in suppressing the vertical and torsional vibrations of the deck at higher mode shapes. Optimization of three design parameters (mass ratio, frequency ratio and damping ratio) is conducted using minimax technique so that to identify the optimum values. The results of the optimum values are validated using the benchmark of Wang and co-authors regarding both mass ratio effect on the vertical vibration control efficiency and damping ratio effect on vertical vibration control efficiency and using the benchmark of Lin and co-authors regarding mass ratio effect on the vertical vibration control efficiency. The calculated optimum values are utilized to start global sensitivity analysis supporting on fifteen samples from Box-Behnken sampling method to construct the surrogate models, then the rational effect and role of each design parameter are calculated for the vertical and torsional control efficiencies using Sobol's sensitivity indices.

5- In order to eliminate the early coupling between the vertical and torsional mode shapes of vibrations, a structural modification is adopted. Two lateral steel beams with 146 m length and cross section dimensions (10\*0.5) m at the pylons location and (5\*0.5) m at the mid span are created and added to the original 3D model of the cable stayed bridge model at both sides of the mid span. The wind speed in the numerical simulations is 54 m/s with 30 seconds duration. Frequency analysis after modification is performed for the first eight mode shapes of vibrations so that to compare the new mode shapes with the original mode shapes before the structural modification. The vertical and torsional displacements of the deck due to the wind excitations are calculated at the mid span of the deck to identify the effect of the structural modification on the vertical and torsional vibrations control efficiency.

6- CFD and CSD models of the segmental deck are created in ABAQUS to run numerical simulations for the TFSI analysis considering three fire scenarios (above, below and at one side) of the deck. Standard ISO 834 fire time-temperature data is used to apply the transient heat-transfer to a duration of 100 seconds in conjunction with wind flow analysis with a speed of 6 m/s to simulate and analyze the vortex shedding and both the lift and drag forces and a speed range between (1-15) m/s to simulate and analyze the lock-in phenomenon depending on the critical scenario case detected for lift and drag forces. A comparison process is

## 1.6 Dissertation Outline

---

conducted between the results of TFSI models and FSI models so that to identify the effect of thermal boundary of three fire scenarios on the results. Validation of the TFSI models is performed considering the benchmark of Simiu and Scanlan for lock-in phenomenon. A steady state heat-transfer analysis with duration of 1200 seconds is conducted to run numerical simulations of coupled thermal-stress for the 3D model of the cable stayed bridge with the same fire scenarios and the same standard ISO 834 fire data. Vertical, horizontal and angular displacements are calculated at the mid span of the deck where an area of (22\*20) m of the deck is dedicated for the fired region. The damaged models including cracks and spalling of the concrete are identified supporting on maximum principal stress through utilizing XFEM analysis. The damaged models are validated using the benchmark of Choi and Shin for the damaged zone of a reinforced concrete beam.

## 1.6 Dissertation Outline

Chapter 1, comprises of an introduction to the main subject of the dissertation and a literature review including a short summary of many previous works in that area, in addition to the aim and the scope of the work summarizing the targets that are planned to be achieved. Furthermore, the methodology of the present work is outlined, and the final section is related to the outline of the dissertation, where short descriptions about each chapter of the dissertation are listed.

Chapter 2, focuses on buffeting response and flutter instability of a cable stayed bridge model created using ABAQUS finite element program. Numerical simulations of wind excitations are conducted in conjunction with the frequency analysis to optimize three aerodynamic parameters (wind attack angle, deck streamlined length and stay cables viscous damping). Validation process is performed considering two benchmarks from the literature (flat plate theory and flat plate by Xavier and co-authors). Optimum values of the adopted aerodynamic parameters are being identified and discussed. Sobol's sensitivity indices which is a method of global sensitivity analysis is adopted to calculate the roles and rational effects of each parameter supporting on Monte Carlo sampling method to formulate the surrogate model for the response of the structural system for both vertical and torsional vibrations of the deck.

In Chapter 3, simulations and analysis of vortex shedding and vortex induced vibration VIV due to wind excitation are studied and assessed considering 2D models of segmental bridge decks basing on kinetic energy of the system using CFD models (stationary position) generated by ABAQUS program and with the support of MATLAB codes. Three parameters (wind speed, deck streamlined length and dynamic viscosity of the air) are dedicated to study

and discuss their effects on the kinetic energy of the system in addition to the shapes and patterns of the vortices. Two benchmarks from the literature (Von Karman) and (Dyrbye and Hansen) are considered to validate the vortex shedding aspects for the CFD models. Latin hypercube experimental method is dedicated to generate the surrogate models for the kinetic energy of the system and the generated lift forces. Variance based sensitivity analysis is utilized to calculate the roles and rational effects of each parameter on the kinetic energy of the system and the lift forces through finding the main sensitivity indices and the interaction orders for each parameter.

In Chapter 4, deck models of a cable stayed bridge are generated in ABAQUS, once using only CFD model (one-way fluid-structure interaction) and another by using both the CFD model and the CSD model together (two-way fluid-structure interaction) in a co-simulation. Shedding frequencies for the associated wind velocities in the lock-in region are calculated, in addition to calculating the lift and the drag coefficients for the two approaches. Validation is performed for the results with two benchmarks from the literature (lock-in phenomenon by Simiu and Scanlan) and the (flat plate theory by Munson and co-authors). The results of the critical wind velocity and the shedding frequencies addition to the lift and drag forces considering both two-way and one-way approaches which are related to the prediction of earlier VIV and lower critical wind speeds are thoroughly discussed.

In Chapter 5, optimization of three design parameters (mass ratio, frequency ratio and damping ratio) of multiple tuned mass dampers MTMDs which are applied for the cable stayed bridge model excited by a strong wind are studied by dedicating minimax optimization technique. ABAQUS program is utilized to run numerical simulations with the support of MATLAB codes and Fast Fourier Transform FFT technique. The optimum values of these three parameters are calculated and discussed in detail. Validation of the optimum results is being performed supporting on two benchmarks from the literature (Wang and co-authors) and (Lin and co-authors). Box-Behnken sampling method is dedicated to formulate the surrogate models to represent the control efficiency of the vertical and the torsional vibrations. Sobol's sensitivity indices are calculated for each design parameter in addition to their interaction orders to identify and detect the roles and rational effects of the design parameters on the vertical and torsional control efficiencies of the MTMDs.

In Chapter 6, a novel structural modification approach is adopted to increase the bending and torsional stiffness of the cable stayed bridge model generated using ABAQUS program. Two lateral steel beams are added to the middle span of the structure. Frequency analysis is dedicated to obtain the natural frequencies of the first eight mode shapes of vibrations before and after the structural modification approach. Numerical simulations of wind excitation are

## 1.6 Dissertation Outline

---

conducted for the 3D model of the cable stayed bridge with duration of 30 seconds supporting on real data of a strong wind from the literature. Both vertical and torsional displacements are calculated at the mid span of the deck to analyze both the bending and the torsional stiffness of the system before and after the structural modification. The results of the frequency analysis before and after applying lateral steel beams in addition to the coupling between the vertical and torsional mode shapes are discussed in relation with the safety of the structure.

In Chapter 7, thermal fluid structure-interaction (TFSI) and coupled thermal-stress analysis are utilized to identify the effects of transient and steady-state heat-transfer on the vortex induced vibration and fatigue of a segmental bridge deck due to fire incidents. Numerical simulations of TFSI models of a segmental bridge deck are dedicated to calculate the lift and drag forces in addition to the lock-in regions. Simiu and Scanlan benchmark is used to validate the TFSI models. Extended finite element method (XFEM) is adopted to create 3D models of the cable stayed bridge to simulate the fatigue of the deck due to three fire scenarios. Choi and Shin benchmark is used to validate the damaged models of the deck in which a good coincide was seen between them. The results revealed that TFSI models and thermal-stress models are significant in detecting earlier vortex induced vibration and lock-in regions in addition to predicting damages and fatigue of the deck due to fire incidents.

Chapter 8, includes the main conclusions which have been framed as a sequence of the present work. Further research recommendations for the future are listed and detailed so that to enhance and improve the current results through dedicating additional methods and techniques.



# Chapter 2

## Aerodynamic Stability of Long Span Bridges

### 2.1 Vertical and Torsional Vibrations

Three main factors are considered to be the basic supports for the buffeting responses of long span bridges, the intensity of the wind turbulence, the natural frequencies and the shape of the structure [Chunhua and Haifan, 2000 and Xiao *et al.*, 2012], where long span bridges with low natural frequencies or small deck widths are particularly exposed to flutter instability. The combination of buffeting and flutter can be the cause of large aerodynamic instabilities because of high vibrations amplitude. These aerodynamic instabilities generate negative aerodynamic damping and rapidly building up severe torsional and vertical vibrations resulting in the collapse of the structure shortly. The safety of the cable supported long span bridges usually is not related to buffeting, but it just causes discomfort for the users of these types of structures and fatigue of the structural elements [Chowdhury, 2004; Stærdahl *et al.*, 2008; Shuxian 2009]. **Figure 2.1** shows only the vertical and the torsional motions of a bridge deck due to buffeting, where these two types of motions are the axis of this study.

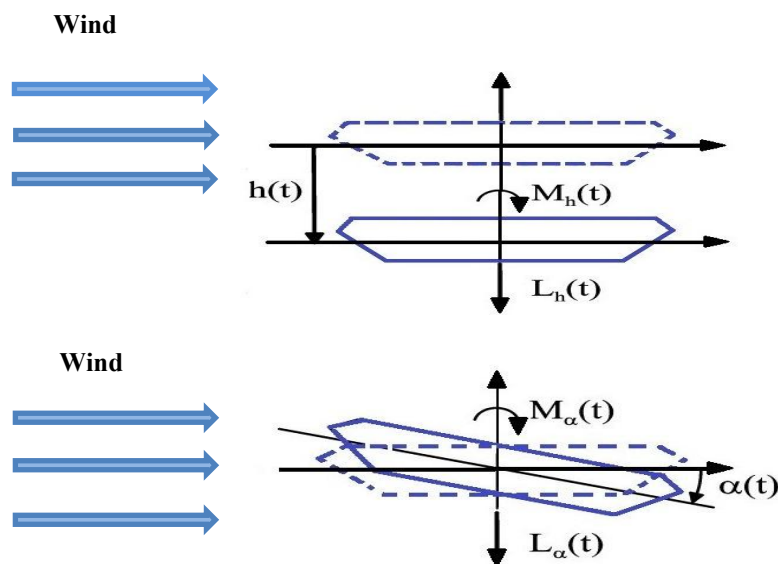


**Figure 2.1** Vertical and torsional motions of the deck

## 2.2 Aerodynamic Stability Parameters

---

Particular care should be dedicated to flutter, where one of the main issues of the designers of long span cable supported bridges is the collapse possibility due to tragic flutter. Efficient and adequate information are needed for the probability of failure because of flutter, as it was the reason of failure in Tacoma narrow Bridge in 1940. The critical wind speed resulted in this accident was 42 mph. This critical wind speed resulted in vertical motion which was the reason of developing tardiness between the opposite sides of the bridge providing a side to side twisting motion.

The aerodynamic stability and modification of long span cable stayed bridge is necessary to be sophisticated [Matsumoto *et al.*, 1995 and Diana *et al.*, 1998]. Up to date understanding of bridge aerodynamic behavior and improved response prediction is a must to investigate the aerodynamic stability plans. The importance of coupling between the modes of vibration in the case of estimating the buffeting response, especially at situations of higher wind velocities is an important task, and the coupling between flutter and buffeting issues has been classified [Jain *et al.*, 1996; Wilde and Fujino, 1998; Katsuchi *et al.*, 1999]. Several cases of analytical outputs of multimode flutter analyses of long span cable supported bridges mark the complicated aerodynamic coupling due to nearly spaced natural frequencies and 3D mode shapes. Moreover, flutter multimode coupling is not always originated by symmetric torsional mode [Agar, 1989; Chen, 2004; Ge and Xiang, 2008].

## 2.2 Aerodynamic Stability Parameters

### 2.2.1 Wind Attack Angle

Two types of wind flows, laminar and turbulent are both the cases of dynamic vibration in long span cable stayed bridges. The cause of buffeting is due to unsteady wind loading on the structure because of speed fluctuation of the oncoming wind. Wind turbulence is a strong factor that affects the aerodynamic behavior of the structure [Haan, 2000; Bartoli *et al.*, 2008; Xu *et al.*, 2014; Zhang *et al.*, 2016]. Bridge decks are subjected to large amplitudes of vibration because of turbulent high speed winds, in which large fluctuation of immediate angle of attack may result in aerodynamic nonlinearities that are considered to be critical for the safety of the structure. To model both buffeting and flutter vibrations, considering the effects of prompt angle of attack is a must, where this factor is obviously the source of high buffeting responses of the long span cable supported bridges [Diana *et al.*, 1998 and Ding *et al.*, 2000].



### 2.2.2 Deck Section

Due to increase in the length of the bridge span, these types of structures are turning more flexible, consequently this property entails the study of bluff body aerodynamics regarding the flutter instability of the bridge deck. The shapes of bridge decks have complex cross sections, so wind tunnel test is an important solution to define the aerodynamic derivatives, and it is largely important to select efficient deck models to avoid flutter instability [Scanlan, 1977; Bartoli *et al.*, 2008; Kusano *et al.*, 2014].

Bluff bodies, such as bridge decks are aerodynamically classified into three section types basing on the characteristics of the wind flow created supporting on zero angle of wind attack [Fransos, 2008 and Dahl, 2013] (see **Figure 2.2**). These sections are Streamlined sections such as Messina Bridge and Normandy Bridge, Bluff sections like Tacoma Narrow Bridge and Lions Gate Bridge and finally Semi streamlined sections for example Great Belt East Bridge and Tataru Bridge.

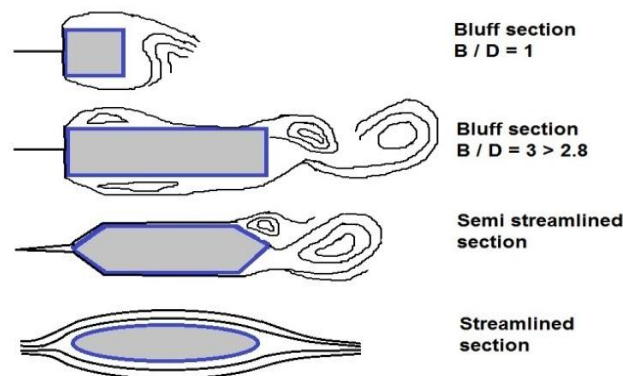


**Figure 2.2** Aerodynamic characterization of a section

### 2.2.3 Viscous Damping of Stay Cables

The stay cables are considered the main structural elements of long span cable stayed bridges. Due to flexible, relative small mass and highly low damping, stay cables are exposed to large amplitude vibrations by wind excitation. These vibrations can be the cause of stay cables fatigue and eventual decrease of their service life, [Soltane *et al.*, 2010]. The sag of a stay cable occurs with a catenary shape because of its weight and tensile force (**Figure 2.3**).

The sagging of the stay cables should be considered when a single straight cable element is used to represent the stay cable. The tensile stiffness of the stay cable is assumed to be elastically ideal. Furthermore, the bending stiffness, compressive and shear stiffness are

## 2.3 Equation of Motion

negligible. The nonlinearity of the cable sagging can be simulated supporting on the stay cable equivalent modulus of elasticity  $E_{eq}$  (see Equation (2.1)).

$$E_{eq} = \frac{E_c}{1 + \frac{(wl_c)^2 A_c E_c}{12T^3}} \quad (2.1)$$

where  $E_c$ ,  $A_c$  and  $l_c$  are the effective modulus of elasticity, the cross-sectional area and the horizontal projected length of the stay cable, respectively;  $w$  is the weight of the stay cable per unit length;  $T$  is the tension in the stay cable. In global analysis of cable stayed bridges, one common practice is to model each cable as a single truss element with an equivalent modulus to allow for sag [Liu and Wang, 2012; Liu *et al.*, 2012; Sardesai and Desai, 2013]. The element stiffness matrix in local coordinates for such a cable element can be written as:

$$k_c = \frac{A_c E_{eq}}{l_c} \begin{bmatrix} 1 & 0 & -1 & 0 \\ 0 & 0 & 0 & 0 \\ -1 & 0 & 1 & 0 \\ 0 & 0 & 0 & 0 \end{bmatrix} \quad (2.2)$$

Under the excitation of a wind, the stay cable vibrates due to energy dissipation results in damping effect of the stay cables. It is a fact that the damping of a stay cable is too low (0.005-0.01) and its vibration cannot be avoided. Hence, instruments such as viscous dampers with certain characteristics could be used to mitigate the vibration [Xu *et al.*, 2014].

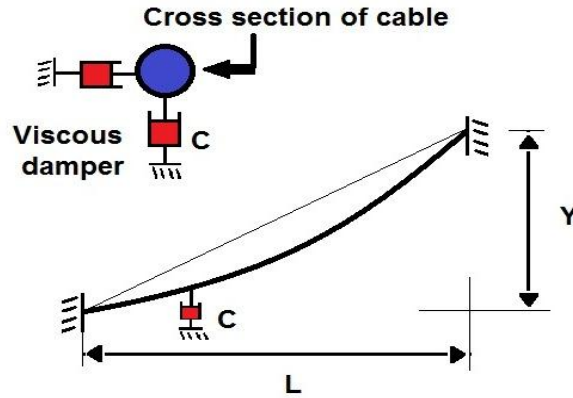


Figure 2.3 Sag of a stay cable and viscous damping

## 2.3 Equation of Motion

The effect of flutter implicates nonlinear aerodynamic behavior, so it has been plausible in many examples to deal with the problem as linear analytical methods. Whereas the

## 2.3 Equation of Motion

---

justification for this deal is that structural response is generally treated as linear elastic and following exponentially modification of the sinusoidal oscillation. The separation between the stable and the unstable systems is conducted by a primary condition that may be treated as to have small amplitude to start it [Simiu and Scanlan, 1996 and Al-Assaf, 2006].

The equation of motion of a cable stayed bridge subjected to wind excitations, referred to the global coordinate system, can be stated in a matrix form as follows:

$$\mathbf{M}\ddot{\mathbf{D}}(\mathbf{t}) + \mathbf{C}\dot{\mathbf{D}}(\mathbf{t}) + \mathbf{K}\mathbf{D}(\mathbf{t}) = \mathbf{F}^s(\mathbf{t}) + \mathbf{F}^b(\mathbf{t}) \quad (2.3)$$

where  $\mathbf{D}(\mathbf{t})$ : is the nodal displacement vector,  $\dot{\mathbf{D}}(\mathbf{t})$  and  $\ddot{\mathbf{D}}(\mathbf{t})$  are the vectors of the nodal speed and acceleration, respectively.  $\mathbf{M}$ ,  $\mathbf{C}$  and  $\mathbf{K}$  are the matrices of mass, damping and stiffness, respectively,  $\mathbf{F}^s$  is the self-excited force vector,  $\mathbf{F}^b$  is the buffeting force vector. In the flutter analysis, the buffeting force is not included in **Equation (2.3)** because flutter is related to the aerodynamic damping and stiffness that are induced by the self-excited force only [Chen *et al.*, 2000; Chen *et al.*, 2001; Chen, 2006; Chen *et al.*, 2009; Andrienne, 2012; Chen, 2012; Huang *et al.*, 2012].

### 2.3.1 Aerodynamic Forces and Moment

The vibration of bridge deck generally implicates torsional deformation of the deck, and a relevant excitation technique for which there is a solution which is a direct analysis. Aerodynamic forces are coupling together vertical and torsional natural modes of vibrations. Flat plate theory is used as a base for the analytical solution, where this provides good results even for many practical box girder deck sections, such as Severn Bridge which is the frontier example [Maguire and Wyatt, 2002].

The forces per unit length  $F_x$  and  $F_y$  along the fixed body axes ( $x$ -axis and  $y$ -axis respectively) are computed using the measured pressures. The mean force coefficients in  $x$  and  $y$  directions are obtained as given below:

$$\bar{C}_{Fx} = \frac{\bar{F}_x}{B \left( \frac{1}{2} \rho \bar{U}_z^2 \right)} \quad (2.4)$$

$$\bar{C}_{Fy} = \frac{\bar{F}_y}{B \left( \frac{1}{2} \rho \bar{U}_z^2 \right)} \quad (2.5)$$

where  $\bar{C}_{Fx}$  and  $\bar{C}_{Fy}$  are mean force coefficient along  $x$  and  $y$  axes and  $B$  is the characteristic dimension which is taken as the height of the bridge section. The resultant of the aerodynamic

## 2.4 Finite Element Model

---

forces experienced by a structure subjected to wind action can be resolved into drag  $F_D$ , (along- wind) force acting in the direction of the mean wind and lift  $F_L$ , (across- wind) force acting perpendicular to the direction of the mean wind. By resolving  $F_x$  and  $F_y$  in the direction of wind and perpendicular to the direction of wind, the drag force  $F_D$  and the lift force  $F_L$ , respectively are obtained. Forces along drag and lift directions are computed based on the equations given below [Ricciardelli *et al.*, 2002 and Nelson, 2011]:

$$\bar{C}_D = \frac{\bar{F}_D}{0.5\rho\bar{U}_z^2B} \quad (2.6)$$

$$\bar{C}_L = \frac{\bar{F}_L}{0.5\rho\bar{U}_z^2B} \quad (2.7)$$

The wind induced moments are the effects resulting from the normal forces on the bridge surface at top and bottom multiplied by their lever arms and integrated over the entire surface. Moment coefficient is computed from:

$$\bar{C}_M = \frac{\bar{M}}{0.5\rho\bar{U}_z^2B^2} \quad (2.8)$$

where  $\bar{C}_D$  ,  $\bar{C}_L$  and  $\bar{C}_M$  are mean drag, lift force and moment coefficients, respectively,  $0.5\rho\bar{U}_z^2$  is the reference pressure at deck height  $z$ , due to mean wind speed  $\bar{U}_z$  and  $\rho$  is the density of air [Chen *et al.*, 2001; Ge and Xiang, 2009; Ma *et al.*, 2010; Keerthana *et al.*, 2011].

## 2.4 Finite Element Model

A cable stayed bridge model is created in ABAQUS with 324 m length and 22 m width, the main parts of the bridge is the deck which consists of connected reinforced concrete deck segments with 2.6 m height. Four reinforced concrete pylons with square shapes 4\*4 m dimensions and 103 m height, and 80 stay cables are connecting the deck to the pylons in a fan shape arrangement (see **Figure 2.6**). Each cable is with cross section area 0.00785 m<sup>2</sup>. The main steel bar diameter is 0.06 m and the diameter of the temperature steel bars in addition to the stirrups are 0.04 m. The boundary condition of the deck is fixed in one side and free for longitudinal translation in the other side. The pylons are fixed at the bottom and each two pylons are connected by six reinforced concrete ties with 4\*4 m dimensions and 22 m length. The stay cables equivalent Young's modulus of elasticity has been used to approximate the sagging occurrence in the cables because it was modeled as truss elements (see **Table 2.1**).

## 2.4 Finite Element Model

**Table 2.1**

Material properties

Material	Mass density Kg/m <sup>3</sup>	Young's modulus of Elasticity Pa	Poisson's ratio
High strength concrete	2643	3.10E+10	0.25
Steel bar	7800	2.00E+11	0.30
Stay cable	9438	1.65E+11	0.30

The deck is modeled as (C3D10: A10-quadratic tetrahedron) elements, pylons and ties are modeled as (C3D8R: An 8 node linear brick reduced integration hourglass control) elements, the reinforcing steel bars are modeled as (B31: A 2- node linear beam in space) elements and the stay cables are modeled as (T3D2: A 2- node linear 3D truss) elements.

### 2.4.1 Mesh Convergence

Sufficiently refined mesh is important to make sure that the results obtained from ABAQUS simulations are suitable. Coarse meshes can yield inaccurate results in analyses using implicit or explicit methods. The numerical solutions of the models will tend toward a unique value as the mesh is refined. The mesh will be converged when additional mesh refinement produces a negligible change in the results. Mesh convergence was performed supporting on the results of the natural frequencies for eight mode shapes of vibrations. A uniform mesh refinement was considered with equal element size for each element type, where the results are calculated 14 times. The mesh convergence obviously starts with constant path approximately from 250000 elements (see **Figure 2.4**).

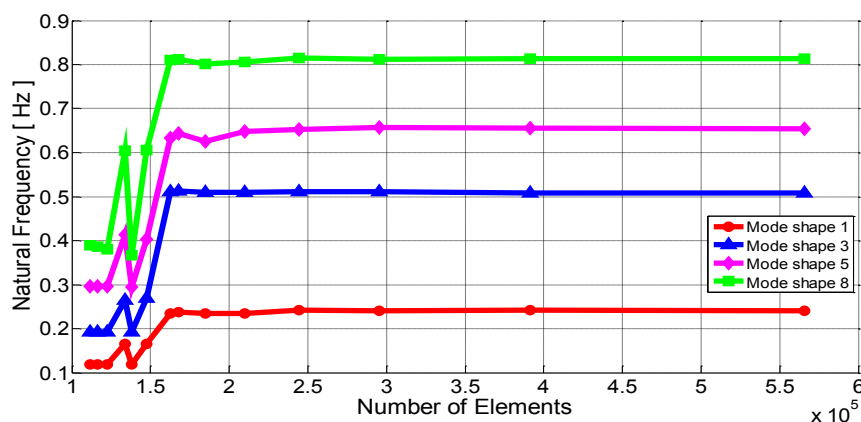


**Figure 2.4** Mesh convergence considering four mode shapes of vibrations

## 2.4 Finite Element Model

To create the model of the cable stayed bridge, the total of 391577 elements were used consisting of (10872-C3D8R elements, 108125-C3D10 elements, 6088-T3D2 elements and 266492-B31 elements) which fall in the convergence region with finer mesh size.

### 2.4.2 Wind Load

A strong wind with design speed of 47 m/s has been dedicated in the numerical simulations, and the frequency of the excitation is arranged to produce vertical and torsional vibration modes in the frequency ranges fall between the first eight mode shapes of vibrations of the cable stayed bridge. The wind pressure assigned in the simulations is with duration of 30 seconds (see **Figure 2.5**). The wind fluctuation data has been prepared depending on exact data from the literature in addition to modification of the excitation frequency [Wang *et al.*, 2010].

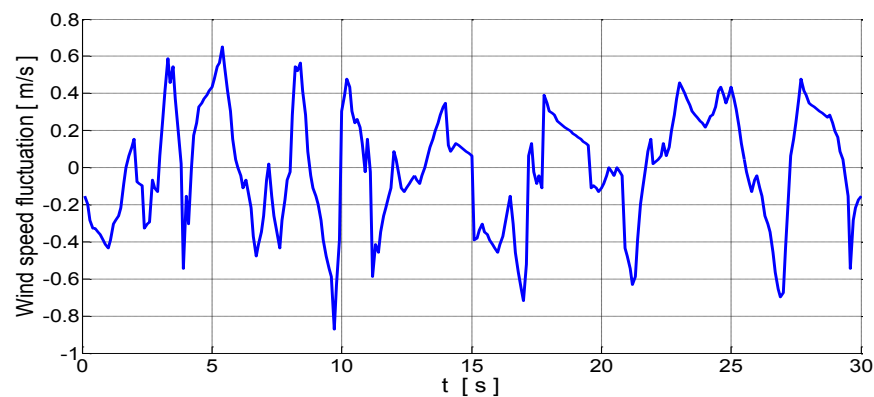


**Figure 2.5** Wind speed fluctuation time history

The cable stayed bridge model is divided into five regions over its height by taking in account the wind pressure variation due to elevation from the ground. The wind pressure is designed to excite the cable stayed bridge model perpendicular to the longitudinal axis without skewedness. The wind forces (lift and drag) and moment are assigned to the cable stayed bridge regions as pressure values supporting on the level of each region along the height (see **Figure 2.6**).

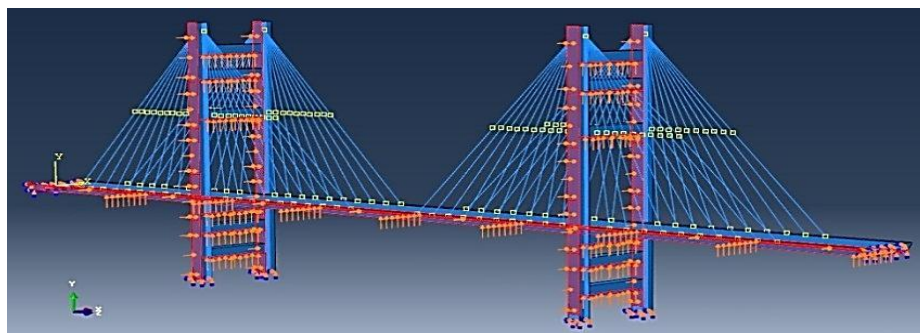


**Figure 2.6** Wind pressure and the FE model

## 2.4 Finite Element Model

---

### 2.4.3 Frequency Analysis

To analyze the predicted types of vibrations of the cable stayed bridge model, frequency analysis is conducted using ABAQUS FE program. The mode shapes of vibrations are being calculated so that to identify the dominant mode shapes of vibrations and to confirm the occurrence of vertical and torsional vibrations in the deck. The mode shapes of vibrations with low frequencies are more prone to occur than the rest mode shapes with high frequencies due to the nature of the actual winds except the situations of strong winds.

### 2.4.4 Results of Mode Shapes

The first 8 mode shapes of vibrations have been obtained, the type of vibration and the related frequency were determined for each mode shape. The first 4 mode shapes are vertical vibrations modes and their frequencies are 0.242 Hz, 0.347 Hz, 0.509 Hz and 0.613 Hz respectively (see **Table 2.2**).

**Table 2.2**

Modes and frequencies

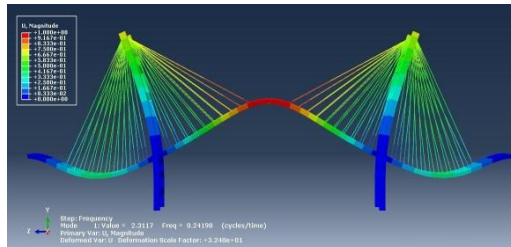
Mode shape	Type	Eigenvalue	Frequency ( Hz )
1	Vertical	2.311	0.242
2	Vertical	4.764	0.347
3	Vertical	10.248	0.509
4	Vertical	14.842	0.613
5	Lateral –Torsional	16.941	0.655
6	Vertical – Torsional	23.817	0.776
7	Torsional	24.612	0.789
8	Vertical	26.131	0.813

The fifth and sixth mode shapes are coupled lateral torsional and vertical torsional vibrations with frequencies 0.655 Hz and 0.776 Hz respectively. While in the seventh and eighth mode shapes are torsional and vertical vibrations respectively.

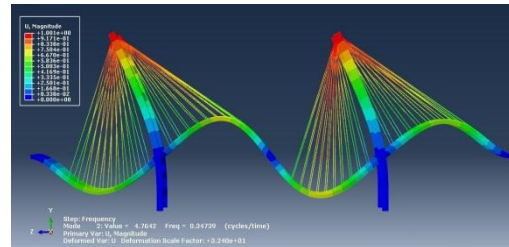
## 2.4 Finite Element Model

### 2.4.5 Simulation of The Mode Shapes

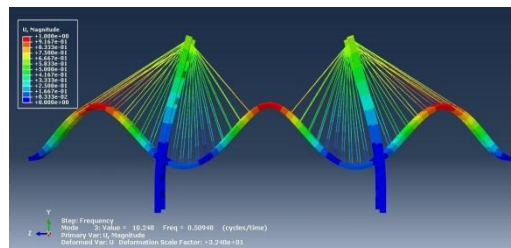
The simulations of the eight mode shapes of the cable stayed bridge model frequency analysis in **Figure 2.7** are simulating the type of the predicted vibrations that can be expected for the wind excitation.



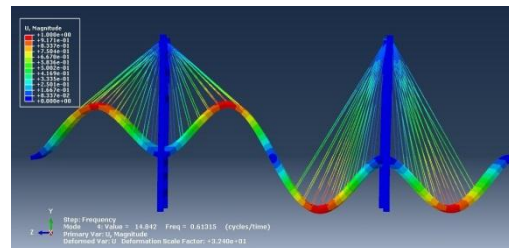
Mode shape 1



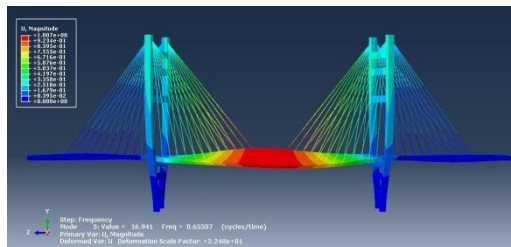
Mode shape 2



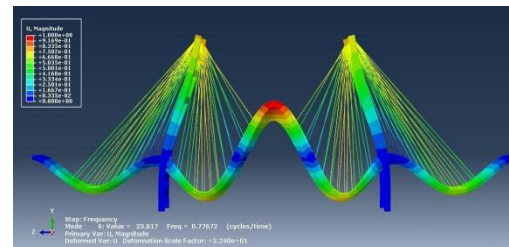
Mode shape 3



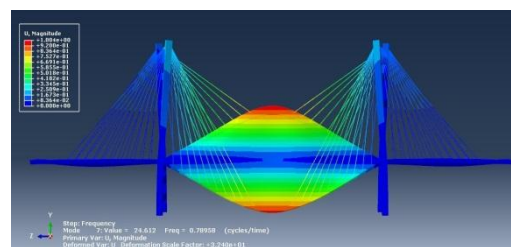
Mode shape 4



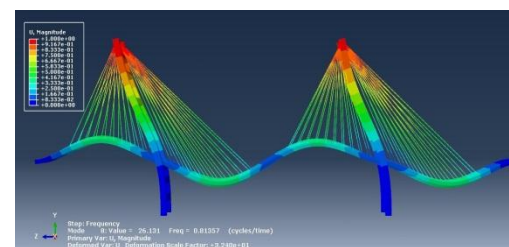
Mode shape 5



Mode shape 6



Mode shape 7



Mode shape 8

**Figure 2.7** Eight mode shapes of vibrations (Frequency Analysis)



## 2.5 Aerodynamic Instability Analysis

---

The displacements are shown obviously and the colors are representing the magnitude of the displacements in each point on the cable stayed bridge structure. The scale factor has been magnified automatically by ABAQUS so that to thoroughly express on the type of vibrations and their effect on the structural response.

## 2.5 Aerodynamic Instability Analysis

A strong wind excitation on the cable stayed bridge is modeled with duration of 30 seconds. The selected case for the aerodynamic parameters is the situation where the wind attack angle value is  $30^\circ$ , the deck streamlined length is 1.14 m and the stay cables viscous damping is 0.0086 N.s/m. Numerical simulation is conducted for this model and data are collected for the buffeting response and flutter instability of the structural model.

### 2.5.1 Results of Vertical Vibrations

The vertical displacements at the mid span center of the deck are varying with time during 30 seconds of the numerical simulation. The first 7 seconds, the displacements do not exceed 0.008 m, but after that region the deck starts to vibrate stronger, and the vertical displacement of the deck reaches 0.03 cm. This is an indication that the vertical buffeting deck response exists and the frequency of the vibration is 0.5 Hz approximately calculated using the graph of the vertical displacement time history of the deck center to calculate the number of the cycles per time (see **Figure 2.8**). As a result it is realized that the third vertical mode shape of vibration is dominant in this case where the natural frequency of this mode is 0.509 Hz.

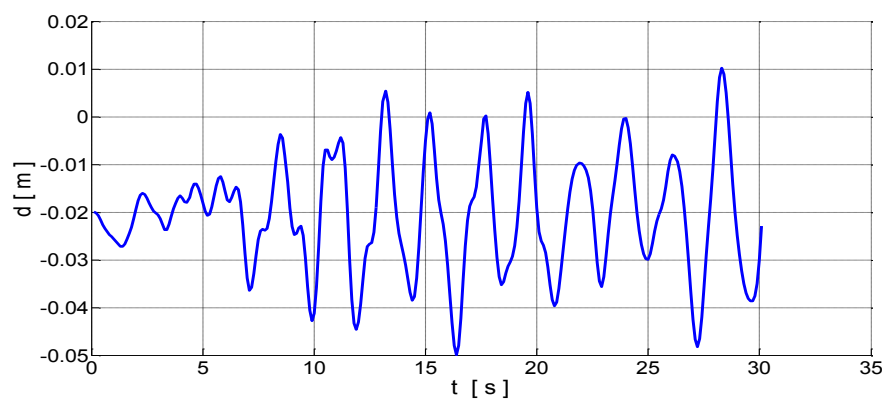


**Figure 2.8** Time history of vertical vibration at mid-span center of the deck

## 2.5 Aerodynamic Instability Analysis

### 2.5.2 Results of Torsional Vibrations

The torsional displacements at the mid span outer edges of the deck are varying with time during 30 seconds of the numerical simulation. The first 8 seconds, the displacements do not exceed 0.023 m which means that flutter is not obvious, but after that area the deck starts to flutter rapidly every 1 second with a maximum torsional displacement of 0.05 m till 27 seconds of the numerical simulation. This is an indication that the torsional flutter of the deck exists and the frequency of the vibration is 0.72 Hz approximately calculated using the graph of the vertical displacement time history of the deck left edge to calculate the number of the cycles per time (see **Figure 2.9**). This certifies that the sixth coupled vertical-torsional mode shape of vibration is dominant in this case where the natural frequency of this mode is 0.776 Hz.

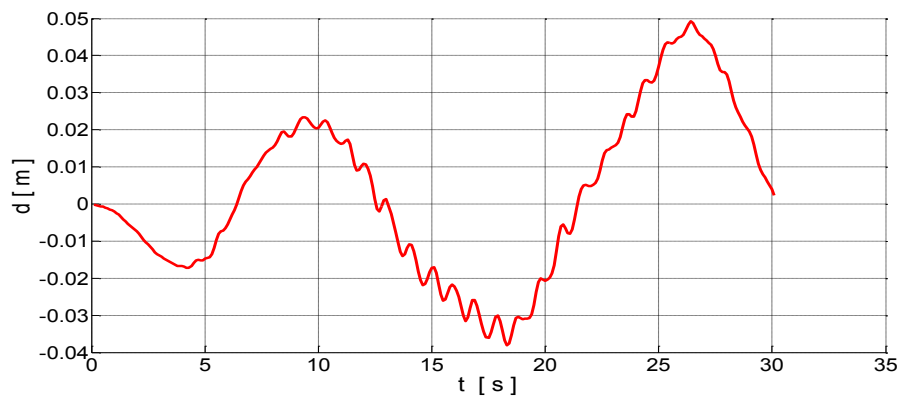
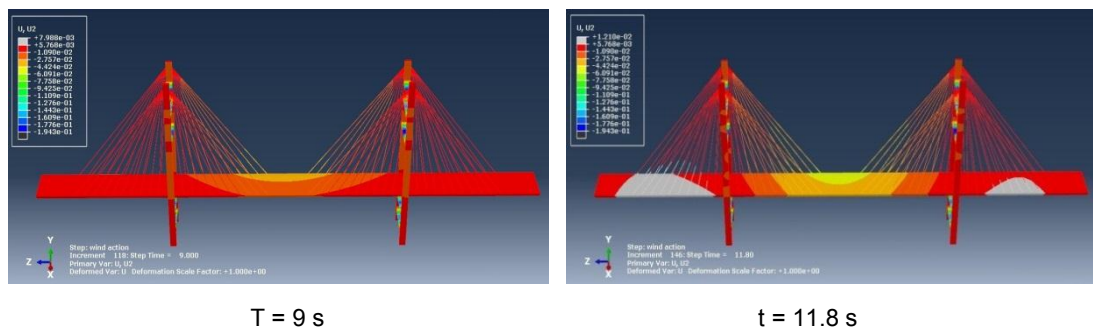


**Figure 2.9** Time history of flutter vibration at mid-span edges of the deck

### 2.5.3 Simulation of Aerodynamic Instability

To confirm the existence of aerodynamic instability in the cable stayed bridge model excited by a strong wind, the following eight figures of the numerical simulation which have been detailed in previous section, are being discussed (see **Figure 2.10**).



## 2.5 Aerodynamic Instability Analysis

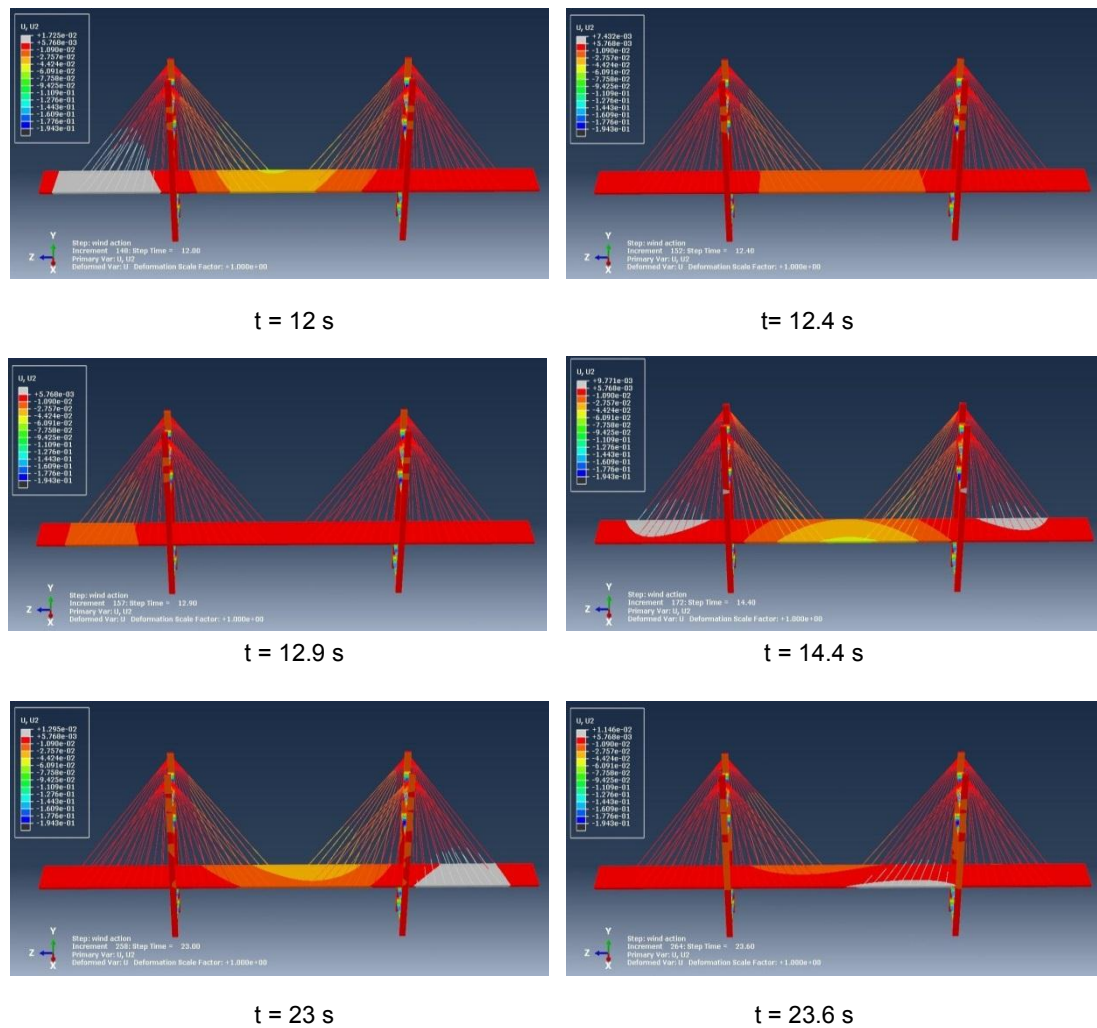


**Figure 2.10** Eight simulations of vibration in the cable stayed bridge model

The first simulation at time 9 seconds shows the generation of torsional vibration in the middle part of the deck only, where the colors are indicating this fact due to graduation of colors in one edge only. The second simulation at time 11.8 seconds displays the additional generation of torsional vibration in the left and right parts of the deck. The third simulation at time 12 seconds indicates the occurrence of vertical vibration in the left part (regular distribution of color) beside the torsional vibration of the center part of the deck. The fourth simulation at time 12.4 seconds proves the generation of vertical vibration of the center part of the deck only (regular distribution of the color). The fifth simulation at time 12.9 seconds exhibits the generation of vertical vibration at the left part of the deck. The sixth simulation at time 14.4 seconds shows up occurrence of torsional vibrations in all parts of the deck like the situation of the second simulation but in the opposite side. The seventh simulation at time 23 seconds features the generation of torsional vibration in the center part and vertical vibration in right part of the deck like the third simulation but in the opposite side. Finally the eighth simulation at time 23.6 seconds reveals the occurrence of a different torsional

## 2.6 Aerodynamic Parameters Optimization

---

vibration between the right and left sides of the center part of the deck. This is a firm fact on that the buffeting vertical response and the flutter torsional instability of the deck pour into the fact of existence of aerodynamic instability of the cable stayed bridge due to strong wind excitation.

## 2.6 Aerodynamic Parameters Optimization

Three aerodynamic parameters are utilized to realize their effects on the vertical vibration and the torsional vibration of the deck in a cable stayed bridge model. Optimization of these parameters is conducted to identify the optimum values that are taking part in the aerodynamic stability of the cable stayed bridge, this by decreasing both the buffeting response and the flutter instability of the structure. The first aerodynamic parameter (wind attack angle) is the source of fluctuation of wind excitation that generates the buffeting response in the cable stayed bridge directly, and the second aerodynamic parameter (deck streamlined length) is responsible of the generation of both vertical and torsional vibration of the deck due to vortex shedding incidence, and the third aerodynamic parameter (stay cables viscous damping) is related to the control of the stay cables oscillation which takes part in the aerodynamic stability of the cable stayed bridge. (Table 2.3) shows the range values of each aerodynamic parameter.

**Table 2.3**

Aerodynamic parameters and range values

<b>Aerodynamic parameter</b>	<b>First value</b>	<b>Second value</b>	<b>Third value</b>
Wind attack angle (°)	0	22.5	45
Deck streamlined length (m)	0	1	2
Stay cables viscous damping ( N.s /m )	0.005	0.0075	0.01

In order to evaluate the effects of the three aerodynamic parameters on the vertical and torsional vibrations of deck, nine models are utilized for the optimization process. Three cases for each aerodynamic parameter are considered, and ABAQUS numerical simulations are being adopted for the wind excitation on the cable stayed bridge model for a duration of 30 seconds.

## 2.6 Aerodynamic Parameters Optimization

### 2.6.1 Results of Wind Attack Angle Effect

When increasing the wind attack angle parameter in the FE model three times, starting from  $0^\circ$ ,  $22.5^\circ$  and  $45^\circ$ , the displacement at the center of the deck mid-span will increase in a linear way approximately to higher values. The effect of this parameter starts to appear from the beginning of the wind excitation and continues in the same pattern till the end of the 30 seconds of the numerical simulation, where the maximum displacement at the center of the deck mid span reaches 0.04 m after 16 seconds for the wind attack angle of  $45^\circ$  and for wind attack angle  $22.5^\circ$  reaches 0.03 m, but for wind attack angle  $0^\circ$  is 0.02 m (see **Figure 2.11**). This behavior means that increasing the wind attack angle will increase the vertical vibration of the deck. While increasing this parameter from  $0^\circ$ ,  $22.5^\circ$  and  $45^\circ$  will increase the flutter displacement of the deck (outer edges) reaching to 0.042 m for wind attack angle  $45^\circ$  and reaches 0.05 m both for wind attack angles  $22.5^\circ$  and  $0^\circ$  after 27 seconds of the wind excitation. The speed of repeated fluttering of the deck starts obviously after 8 seconds and continues till 27 seconds of the numerical simulation and the speed of the flutter occurrence increases with the increase of the wind attack angle (see **Figure 2.12**).

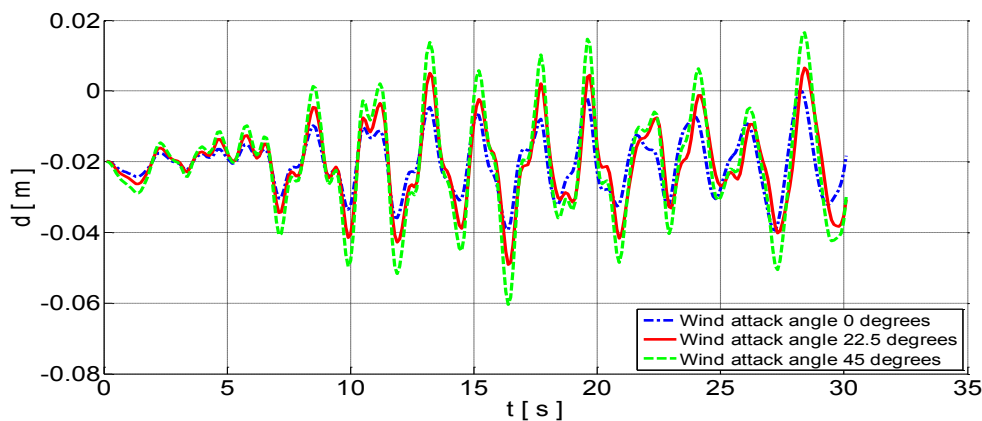


**Figure 2.11** Wind attack angle effect on the vertical displacement of the deck

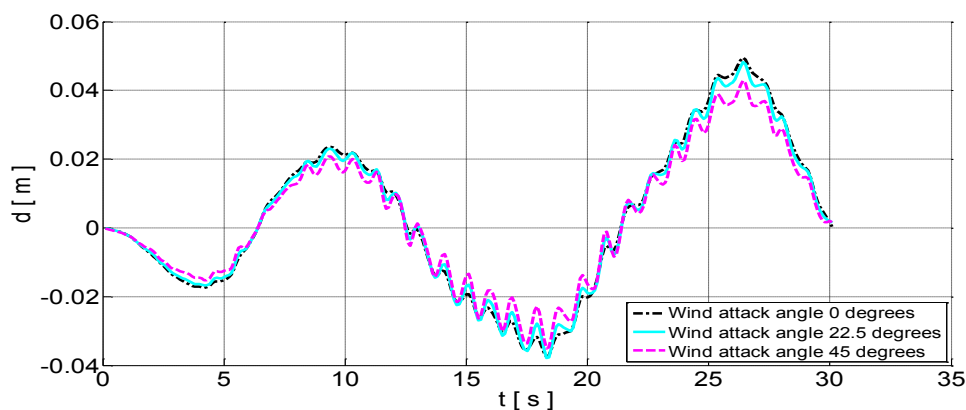


**Figure 2.12** Wind attack angle effect on the torsional displacement of the deck

## 2.6 Aerodynamic Parameters Optimization

### 2.6.2 Results of Deck Streamlined Length Effect

Increasing the deck streamlined length parameter in the FE model three times, starting from 0.0 m, 1.0 m and 2.0 m, the displacement at the center of the deck mid-span will decrease to lower values. The effect of this parameter starts to appear after 7 seconds of the wind excitation and continues in the same pattern till the end of the 30 seconds of the numerical simulation. The maximum displacement at the center of the deck mid span reaches 0.0275 m after 28 seconds for the deck streamlined length of 0.0 m and for deck streamlined length 1.0 m reaches 0.0225 m, but for deck streamlined length 2.0 m is 0.02 m (see **Figure 2.13**). This is an indication that adopting streamlined sections for the deck will decrease the vertical vibration of the deck. While increasing this parameter from 0.0 m, 1.0 m and 2.0 m will have a very small non appreciable effect on the flutter displacement of the deck reaching to 0.05 m for all cases approximately after 27 seconds of the wind excitation. The speed of repeated fluttering of the deck starts obviously when after 8 seconds and continues till 27 seconds of the numerical simulation as for wind attack angle cases, and the speed of the flutter occurrence stays stable when increasing the deck streamlined length (see **Figure 2.14**).

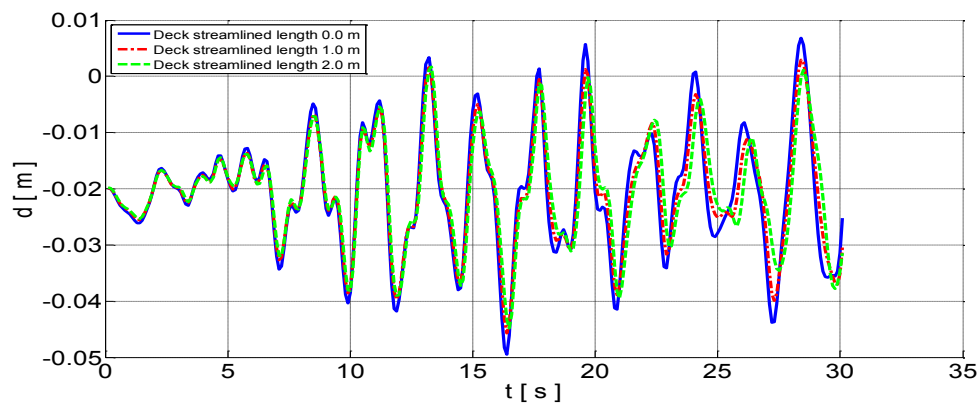


**Figure 2.13** Deck streamlined length effect on the vertical displacement of the deck

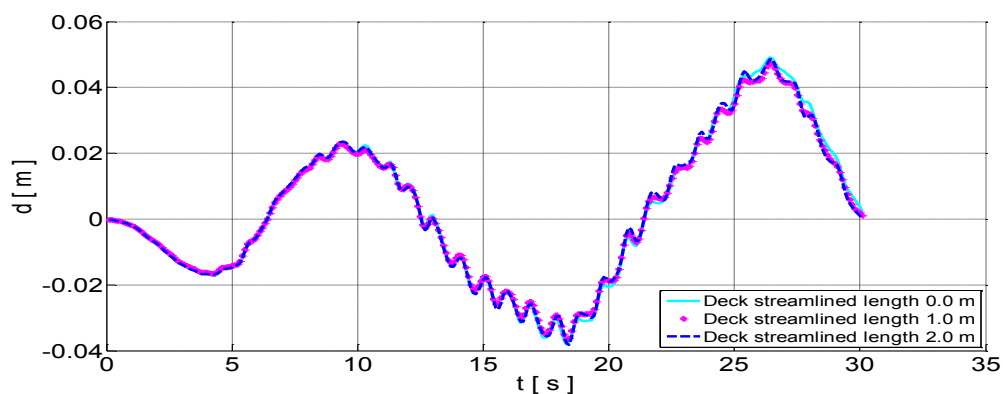


**Figure 2.14** Deck streamlined length effect on the torsional displacement of the deck

### 2.6.3 Results of Stay Cables Viscous Damping Effect

This time when increasing the stay cables viscous damping in the FE model three times, starting from 0.005, 0.0075 and 0.01, the displacement at the center of the deck mid-span will decrease in a small range with irregular pattern. The effect of this parameter starts to appear after 6 seconds of the wind excitation and continues in the different patterns from a stable to increasing and decreasing again during the 30 seconds of the numerical simulation. The maximum displacement at the center of the deck mid span reaches 0.032 after 19 seconds for the stay cables viscous damping of 0.0075 N.s/m and for stay cables viscous damping 0.005 N.s/m reaches 0.025, but for stay cables viscous damping 0.01 N.s/m is 0.025 too (see **Figure 2.15**). A nonlinear behavior exists due to variation of the stay cables viscous damping values in relation with the vertical vibrations of the deck.

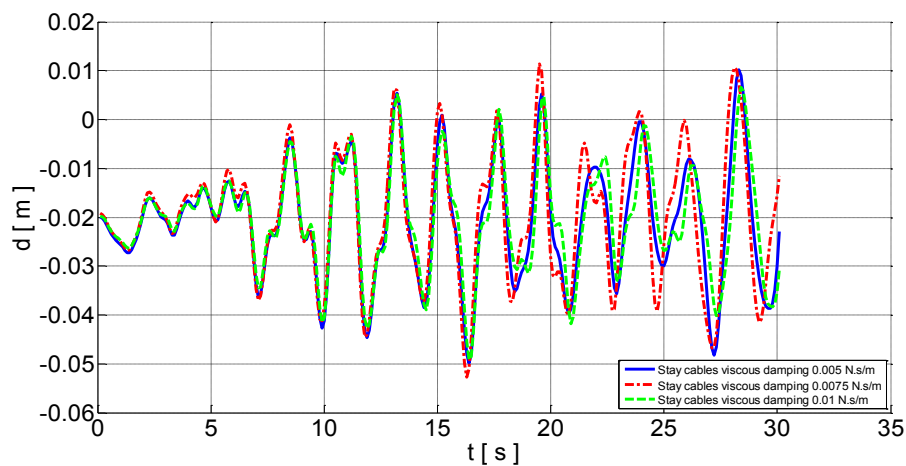


**Figure 2.15** Viscous damping of stay cables effect on the vertical displacement of the deck

Considering torsional vibration of the deck, when increasing this parameter from 0.005 to 0.0075 and to 0.01 will have a very small non appreciable effect on the flutter displacement of the deck for all cases but just for a period of time between 23-28 seconds reaching to maximum 0.0475 m for both 0.005 and 0.01 cases approximately and becomes 0.0425m for 0.0075 case. The speed of repeated fluttering of the deck starts obviously after 8 seconds and continues till 27 seconds of the numerical simulation, and the speed of the flutter occurrence increases with the increase of the stay cables viscous damping (see **Figure 2.16**).

## 2.7 Validation of The FE Models

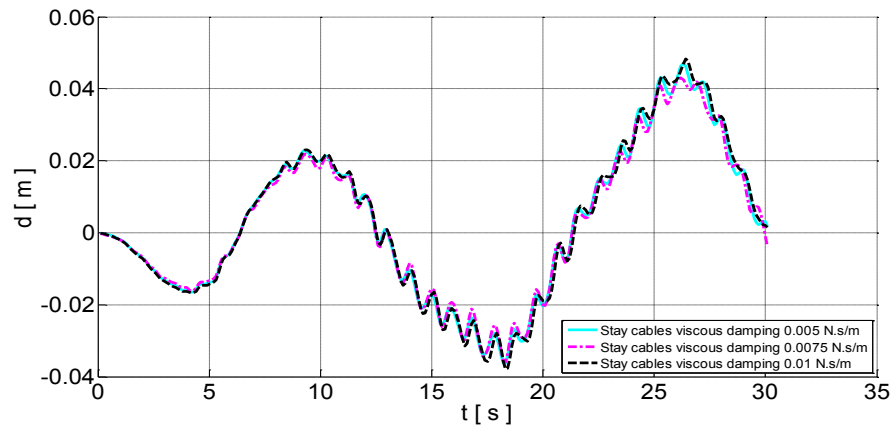


**Figure 2.16** Viscous damping of stay cables effect on the torsional displacement of the deck

## 2.7 Validation of The FE Models

The lift and moment coefficients calculated for the deck models are validated with two benchmarks from the latest literature. First benchmark is the results obtained from the flat plate theory and the second benchmark is the results of the flat plate model collected from experiments done by (Xavier et al. 2015). (Table 2.4) shows the data of the lift coefficient  $C_L$  and moment coefficient  $C_M$  for the two benchmarks and the numerical analysis results calculated from the ABAQUS FE models.

**Table 2.4**

Results of lift and moment coefficients for ABAQUS FE model and two benchmarks

	FE model	Flat plate theory	FE model	Flat plate (Xavier)
Angle of attack	$C_L$	$C_L$	$C_M$	$C_M$
0°	0.070	0.000	-0.0013	-0.0015
4°	0.480	0.450	0.0078	0.0080
8°	0.640	0.700	0.0154	0.0140
12°	0.660	0.740	0.0305	0.0280
16°	0.620	0.680	0.0266	0.0250

### 2.7.1 Flat Plate Theory Benchmark



## 2.7 Validation of The FE Models

There is a very good agreement between the results of the lift coefficient  $C_L$  for the FE model and the flat plate theory in relation with multiple wind attack angle cases as shown in **Figure 2.17**.

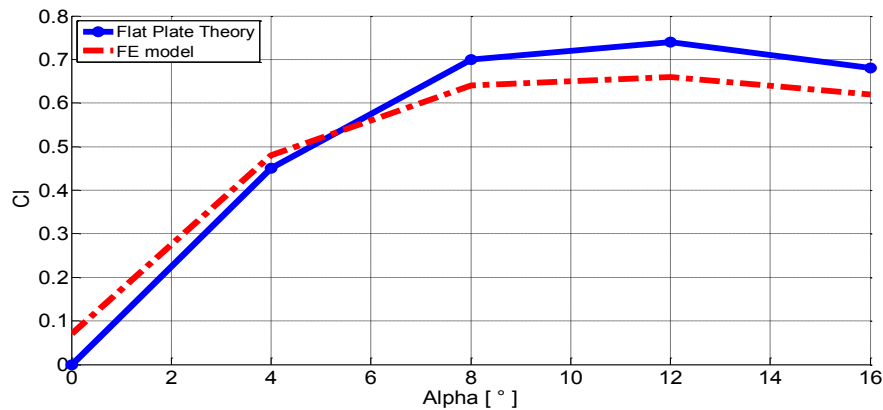


**Figure 2.17** Lift coefficient  $C_L$  with wind attack angle validation

where the curves of the data for the two approaches are in a coinciding pattern starting from  $0^\circ$ -  $16^\circ$  of wind attack angle. There is a small difference in lift coefficient value between them which is not exceeding 0.1 for the maximum situation for the wind attack angle of  $12^\circ$ .

### 2.7.2 Flat Plate Model (Xavier and Co-authors) Benchmark

The comparison between the results of the moment coefficient  $C_M$  for the FE model and the results of the flat plate model experiment done by by Xavier and co-authors for the wind attack angle cases is pointing to a good agreement between them. The two curves are coinciding to a good extent in the range of  $0^\circ$ - $16^\circ$  of wind attach angle and the maximum difference in moment coefficient is 0.0025 at the situation of  $12^\circ$  wind attach angle (see **Figure 2.18**).

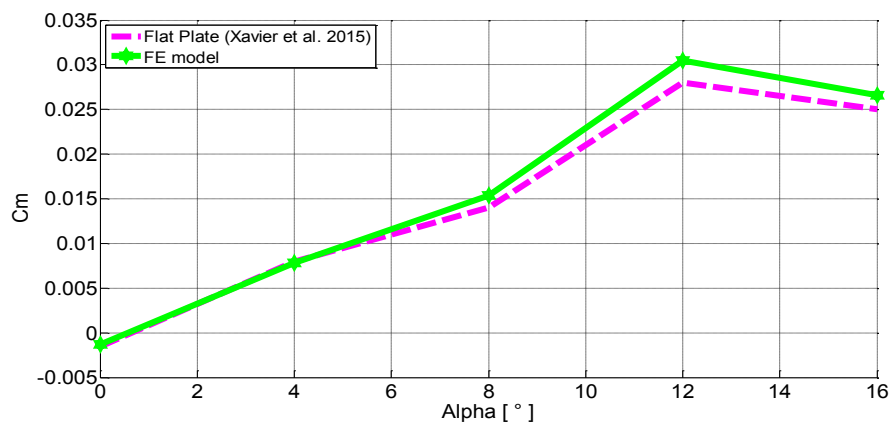


**Figure 2.18** Moment coefficient  $C_m$  with wind attack angle validation

### 2.8 Sensitivity Analysis

Sensitivity analysis is the study of how the uncertainty in the output of the model can be handed out to various sources of input, or it attributes to the identification of individual donation and various origins of uncertain inputs to the uncertainty in the output of a model [Saltelli *et al.*, 2000; Saltelli, 2004; Saltelli *et al.*, 2008; Keitel *et al.*, 2011]. There are two sorts of sensitivity analysis methods: local sensitivity analysis and global sensitivity analysis. Local sensitivity analysis methods calculate or convergent the local response of the model outputs through modifying input parameters or individual parameters with other parameters at nominal values in the hyperspace of the input parameter. In the other hand, global sensitivity analysis estimates the effects of input variations on the outputs in the total permitted ranges of the input space [Confalonieri *et al.*, 2010; Tong, 2010; Zhan *et al.*, 2013; Baroni and Tarantola, 2014].

Analyses involve the consideration of models of the form:  $\mathbf{y} = f(\mathbf{x})$  where  $\mathbf{y} = [y_1, y_2, \dots, y_n]$  is a vector of analysis result and  $\mathbf{x} = [x_1, x_2, \dots, x_n]$  is a vector of imprecisely known analysis inputs. In general the model  $f$  can be quite large and involved (e.g., a system of nonlinear partial differential equations requiring numerical solution or possibly a sequence of complex, linked models as is the case in a probabilistic risk assessment for a nuclear power plant or a performance assessment for a radioactive waste disposal facility the vector  $\mathbf{y}$  of analysis results can be of high dimension and complex structure (e.g., the elements of  $\mathbf{y}$  might be several hundred temporarily or spatially dependent functions); and the vector  $\mathbf{x}$  of analysis inputs can also be of high dimension and complex structure e.g., several hundred variables, with some variables corresponding to physical properties of the system under study and other variables corresponding to parameters in probability distributions or perhaps to designators for alternative models. The uncertainty in the elements of  $\mathbf{x}$  is characterized by a sequence of probability distributions.  $D_1, D_2, \dots, D_{n_x}$ , where  $D_j$  is a probability distribution characterizing the uncertainty in  $x_j$ . [Saltelli, 2004; Storlie and Helton, 2008; Wainwright *et al.*, 2014].

### 2.9 Experimental Design

Experimental design is widely used to control the effects of parameters in many problems. The use of this method decreases the number of experiments, using time and material resources. Furthermore, the experimental errors are minimized and the analysis performed on the results is easily realized. Utilizing experimental design, the statistical methods measure

## 2.9 Experimental Design

---

the effects of change that are resulting from operating parameters and their mutual interactions on the process.

### 2.9.1 Monte Carlo Sampling

Monte Carlo simulation is a type of simulation that relies on repeated random sampling and statistical analysis to compute the results. This method of simulation is very closely related to random experiments, experiments for which the specific result is not known in advance. In this context, Monte Carlo simulation can be considered as a methodical way of doing so-called what-if analysis. Monte Carlo techniques are commonly used to perform uncertainty and sensitivity analysis. A key element of Monte Carlo method is the sampling of input parameters for the simulation, where the goal is to explore the entire input space with a reasonable sample size  $N$ . The sample size determines the computational cost of the analysis. The unbiased mean and variance of the model output can be calculated by the following equations:

$$\bar{y} = \frac{1}{N} \sum_{i=1}^N y_i \quad (2.9)$$

$$V(y) = \frac{1}{N-1} \sum_{i=1}^N (y_i - \bar{y})^2 \quad (2.10)$$

where  $\bar{y}$  and  $V(y)$  are the mean and the variance of the  $y_i$  values.

The mean and the variance resulting from the sample and calculated with these two equations are uncertain [Saltelli *et al.*, 2008; Raychaudhuri, 2008; Burhenne *et al.*, 2011].

### 2.9.2 Probability Distribution

The probability distributions of the input parameters **X1**, **X2** and **X3** which are wind attack angle, deck streamlined length and the stay cables viscous damping respectively have been assumed to be normal or Gaussian distributions and have been accomplished using MATLAB codes (see **Table 2.5**) so that to use them to construct the sample based on Monte Carlo sampling method.

**Table 2.5**

Range values and probability distributions for the aerodynamic parameters

Input parameter	Name	Probability distribution
<b>X1</b>	Wind Attack Angle	Normal
<b>X2</b>	Deck streamlined Length	Normal
<b>X3</b>	Stay Cables Viscous Damping	Normal

## 2.9 Experimental Design

---

The aerodynamic parameters **X1**, **X2** and **X3** are arranged in samples according to the Monte Carlo sampling method. These samples are used to determine the predicted vertical and torsional displacements both at the center and outer edges of the deck mid-span respectively, so that to formulate the surrogate models for upcoming sensitivity analysis.

### 2.9.3 Response Surface Methodology

Response surface methodology is a set of statistical and mathematical methods being used for the analysis and modeling of many problems in the engineering field. The main purpose of this methodology is to optimize the response surface which is being influenced by various parameters. This methodology quantifies the relationship between the obtained response surfaces and the controllable input parameters.

If all variables are assumed to be measurable, the response surface can be expressed as follows:

$$y = f(x_1, x_2, x_3, \dots, x_k) \quad (2.11)$$

where  $y$  is the answer of the system, and  $x_i$  the variables of action called factors. The goal is to optimize the response variable  $y$ . It is assumed that the independent variables are continuous and controllable by experiments with negligible errors. It is required to find a suitable approximation for the true functional relationship between independent variables and the response surface. Two important models are utilized in response surface methodology, the first-degree model which is represented as follows:

$$y = \beta_0 + \sum_{i=1}^k \beta_i x_i + \epsilon \quad (2.12)$$

and the second-degree model is formulated in the following equation:

$$y = \beta_0 + \sum_{i=1}^k \beta_i x_i + \sum_{i=1}^k \beta_{ii} x_i^2 + \sum_{i=1}^{k-1} \sum_{j=2}^k \beta_{ij} x_i x_j + \epsilon \quad (2.13)$$

where  $x_1, x_2, \dots, x_k$  are the input factors which influence the response  $y$ ;  $\beta_0, \beta_i (i = 1, 2, \dots, k), \beta_{ii} (i = 1, 2, \dots, k), \beta_{ij} (i = 1, 2, \dots, k; j = 1, 2, \dots, k)$  are unknown parameters and  $\epsilon$  is a random error. The  $\beta$  coefficients are obtained by the least square method.

a series of  $n$  experiments should first be carried out, in each of which the response  $y$  is measured (or observed) for specified settings of the control variables. The totality of these

## 2.9 Experimental Design

---

settings constitutes the so-called response surface design, or just design, which can be represented by a matrix, denoted by  $\mathbf{D}$ , of order  $n \times k$  called the design matrix,

$$\mathbf{D} = \begin{pmatrix} x_{11} & x_{12} & \cdot & \cdot & \cdot & x_{1k} \\ x_{21} & x_{22} & \cdot & \cdot & \cdot & x_{2k} \\ \cdot & \cdot & \cdot & \cdot & \cdot & \cdot \\ \cdot & \cdot & \cdot & \cdot & \cdot & \cdot \\ \cdot & \cdot & \cdot & \cdot & \cdot & \cdot \\ x_{n1} & x_{n2} & \cdot & \cdot & \cdot & x_{nk} \end{pmatrix} \quad (2.14)$$

where  $x_{ui}$  denotes the  $u$  th design setting of  $x_i$  ( $i = 1, 2, \dots, k; u = 1, 2, \dots, n$ ). Each row of  $D$  represents a point, referred to as a design point, in a  $k$  -dimensional Euclidean space. Let  $y_u$  denote the response value obtained as a result of applying the  $u$  th setting of  $x$ , namely  $x_u = (x_{u1}, x_{u2}, \dots, x_{uk})$ , ( $u = 1, 2, \dots, n$ ).

In general:

$$\mathbf{Y} = \mathbf{X}\boldsymbol{\beta} + \boldsymbol{\epsilon} \quad (2.15)$$

where  $\mathbf{Y} = (y_1, y_2, \dots, y_n)$  which is defined as a matrix of measured values,  $\mathbf{X}$  is a matrix of independent variables of order  $n \times p$  whose  $u$  th row is  $f'(x_u)$ , and  $\boldsymbol{\epsilon} = (\epsilon_1, \epsilon_2, \dots, \epsilon_n)$ . Note that the first column of  $\mathbf{X}$  is the column of ones  $1_n$ .

Assuming that  $\boldsymbol{\epsilon}$  has a zero mean, the so called ordinary least-squares estimator of  $\boldsymbol{\beta}$  is:

$$\boldsymbol{\beta} = (\mathbf{X}'\mathbf{X})^{-1} \mathbf{X}'\mathbf{Y} \quad (2.16)$$

where  $\mathbf{X}'$  is the transpose of the matrix  $\mathbf{X}$  and  $(\mathbf{X}'\mathbf{X})^{-1}$  is the inverse of the matrix  $\mathbf{X}'\mathbf{X}$  [Gunaraj and Murugan, 1999; Annadurai *et al.*, 2004; Kwak, 2005; Aslan and Cebeci, 2007; Amenaghawon *et al.*, 2013].

### 2.9.4 Sobol's Sensitivity Indices

Sobol's indices are a global sensitivity measures which determine the contribution of each parameter (or group of parameters) to the variance of the output. The usual Sobol's sensitivity indices include the main and total effects for each parameter, but the method can also provide specific interaction terms [Glen and Isaacs, 2012]. It uses a variance ratio to estimate the importance of parameters. This method is based on the partitioning of the total variance of model output  $V(Y)$  using the following equation:

$$V(Y) = \sum_{i=1}^n V_i + \sum_{i \leq j \leq n} V_{ij} \dots + \sum_{i \leq \dots \leq n} V_{1, \dots, n} \quad (2.17)$$

## 2.9 Experimental Design

---

where  $V_i$  represent the first order effect for each parameter  $X_i$  ( $V_i = V[E(Y|X_i)]$ ) and  $V_{ij} = V(E(Y|X_i, X_j)) - V_i - V_j$  to  $V_{1, \dots, n}$  is the interactions among  $n$  parameters. The first-order sensitivity index  $S_i$  can be calculated by:

$$S_i = \frac{V_i}{V(Y)} - \frac{V[E(Y|X_i)]}{V(Y)} \quad (2.18)$$

where  $V[E(Y|X_i)]$  is the variance of the expected value of  $Y$  when conditioning with respect to  $X_i$ , and  $V(Y)$  is the unconditional variance of  $Y$ .

and the second-order sensitivity index  $S_{ij}$  can be calculated by:

$$S_{ij} = \frac{V_{ij}}{V(Y)} - \frac{V[E(Y|X_i, X_j)] - V_i - V_j}{V(Y)} \quad (2.19)$$

In general, the total sensitivity index  $S_{Ti}$  can be defined as [Homma and Saltelli, 1996; Saltelli and Tarantola, 2002; Saltelli and Annoni, 2010]:

$$S_{Ti} = \frac{E(V(Y|X_{\sim i}))}{V(Y)} \quad (2.20)$$

where the subscript  $\sim i$  refers to all of the inputs except input  $i$ , Also the total sensitivity index  $S_{Ti}$  can be written as:

$$S_{Ti} = 1 - \frac{V(E(Y|X_{\sim i}))}{V(Y)} \quad (2.21)$$

where  $V(E(Y|X_{\sim i}))$  is the variance of the expected value of  $Y$  when conditioning with respect to all parameters except for  $X_i$ .

Due to parameter interaction  $S_{Ti}$  of a parameter increases, therefore  $\sum S_{Ti} \geq 1$  will always hold. The difference  $S_{Ti} - S_i$  is a measure of how much  $X_i$  interacts with other input parameters.

The index  $S_i$  is therefore a measure of the exclusive influence of input parameter  $X_i$ . If the sum of all  $S_i$  is close to one, the model is additive with respect to its variances and no remarkable interactions between the parameters seem to exist [Nossent *et al.*, 2011; Keitel *et al.*, 2011; Zhan *et al.*, 2013; Baroni and Tarantola, 2014; Zhang *et al.*, 2015].

### 2.9.5 Results and Discussion of The Surrogate Models

The regression coefficients calculated both for vertical and torsional actual displacements supported on Monte Carlo experimental method, and in order to formulate the surrogate models for the predicted vertical and torsional displacements, 400 samples were used considering convergence process between the sensitivity indices. Quadratic and interaction

## 2.9 Experimental Design

terms were used to construct the surrogate model for the case of vertical displacement at the center of the deck mid-span. The calculated coefficient of determination  $R^2$  between the actual and the predicted vertical displacements was 98.12% (see **Figure 2.19**) which is an excellent representation of the predicted vertical displacement, which means that just 1.88% of the system response still unexplained.

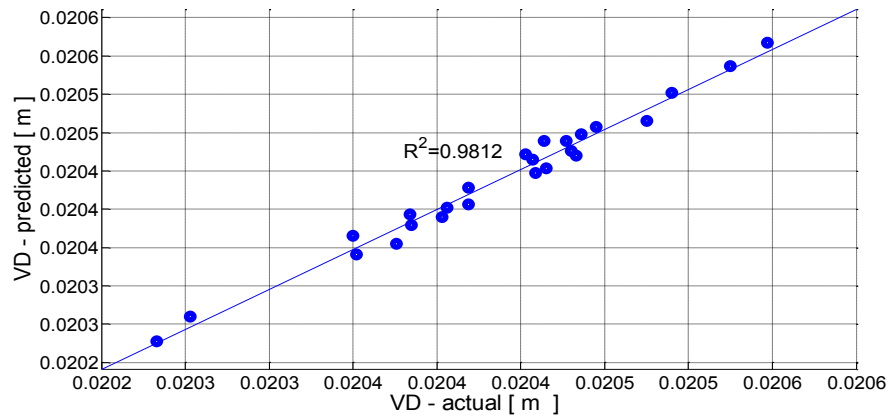


**Figure 2.19** Coefficient of determination between actual and predicted vertical displacement

The following response surface plots in **Figure 2.20**, **Figure 2.21** and **Figure 2.22** which have been generated using MATLAB codes, are the relation between each two aerodynamic parameters  $X1X2$ ,  $X1X3$ ,  $X2X3$  and the predicted vertical displacement at the center of the deck mid span.

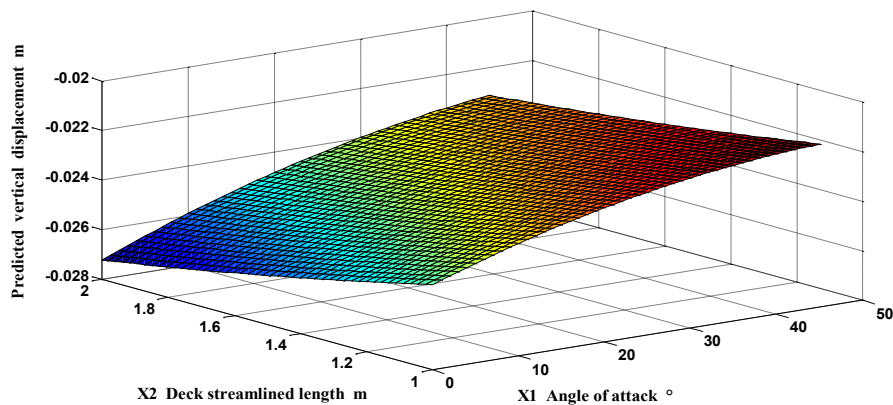


**Figure 2.20** Response surface plot showing effect of  $X1$  and  $X2$  on the predicted vertical displacement

## 2.9 Experimental Design

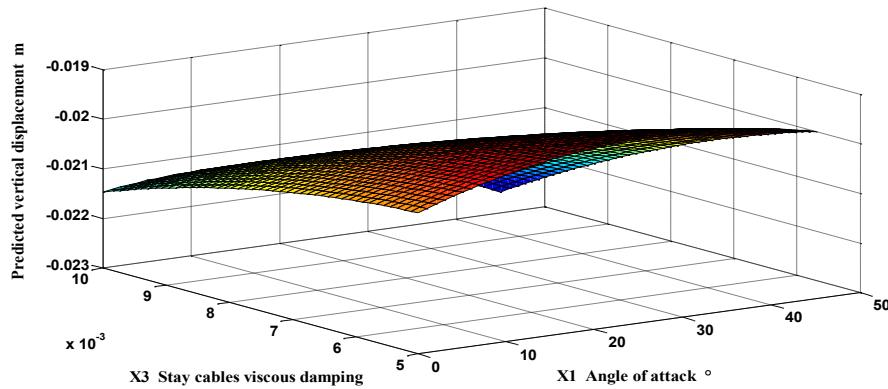


**Figure 2.21** Response surface plot showing effect of **X1** and **X3** on the predicted vertical displacement

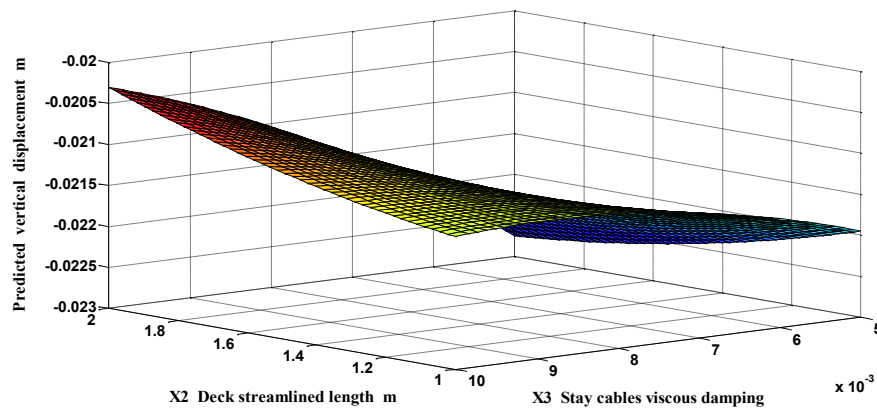


**Figure 2.22** Response surface plot showing effect of **X2** and **X3** on the predicted vertical displacement

Quadratic and interaction terms were used to build the surrogate model to calculate the torsional displacement at the outer edges of the deck mid-span. The coefficient of determination  $R^2$  calculated between the actual and the predicted torsional displacements was  $R^2 = 97.50\%$  which is a very good approximation for the prediction of torsional displacement that only 2.50% of the system response remains unexplained (see **Figure 2.23**).

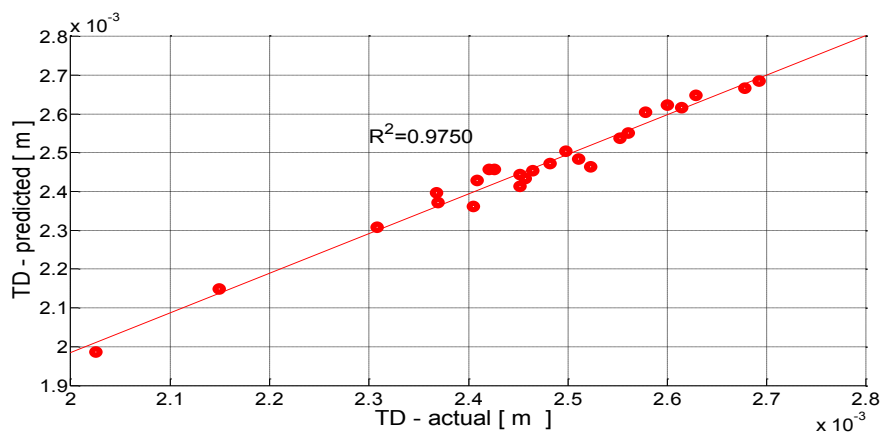


**Figure 2.23** Coefficient of determination between actual and predicted torsional displacement



## 2.9 Experimental Design

The following response surface plots express on the relation between each two aerodynamic parameters  $X1X2$ ,  $X1X3$ ,  $X2X3$  and the predicted torsional displacement at the outer edges of the deck mid span is shown in **Figure 2.24**, **Figure 2.25** and **Figure 2.26** which have been generated using MATLAB codes.

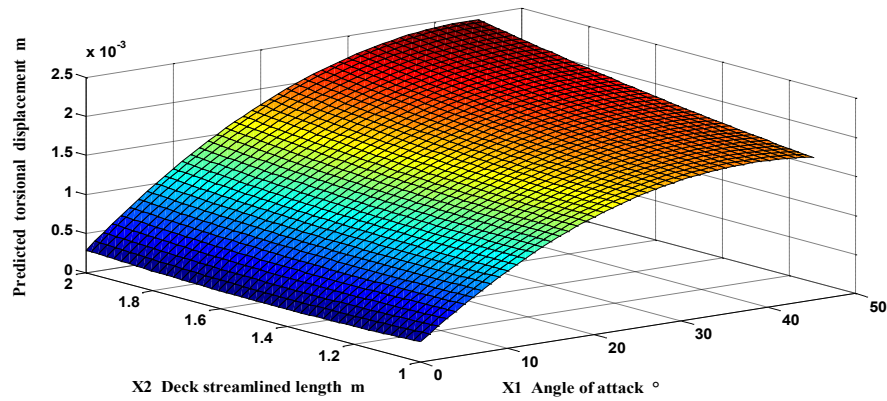


**Figure 2.24** Response surface plot showing effect of  $X1$  and  $X2$  on the predicted torsional displacement

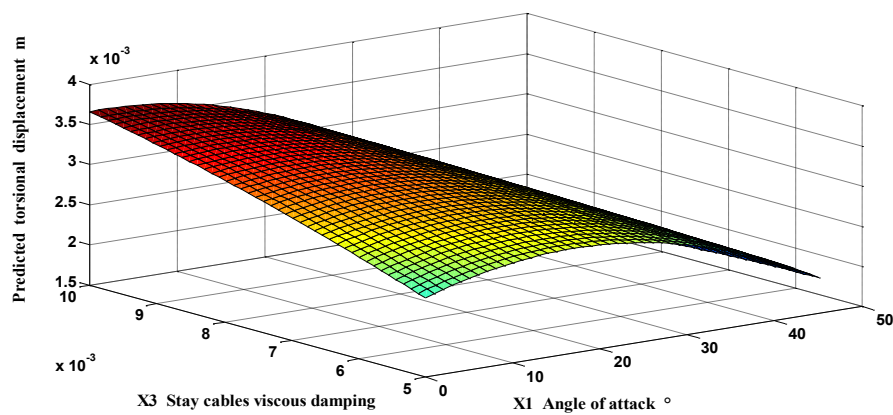


**Figure 2.25** Response surface plot showing effect of  $X1$  and  $X3$  on the predicted torsional displacement

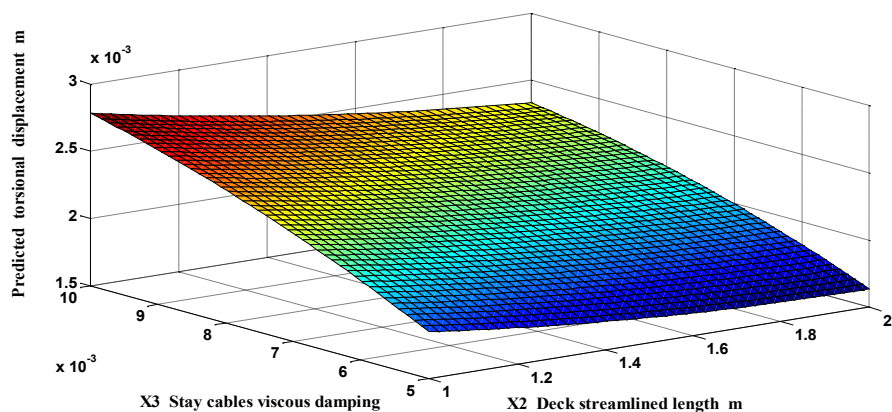


**Figure 2.26** Response surface plot showing effect of  $X2$  and  $X3$  on the predicted torsional displacement

## 2.9 Experimental Design

### 2.9.6 Results and Discussion of The Sensitivity Indices

The main orders of sensitivity indices for each aerodynamic parameter in addition to their interaction orders were calculated considering the convergence results which recommended using 400 samples to calculate both the vertical displacement and torsional displacement at the center and the outer edges of the mid span of the cable stayed bridge model respectively (see **Figure 2.27** and **Figure 2.28**). Supporting on the calculated results, the total sensitivity indices for each aerodynamic parameter have been calculated (see **Table 2.6**).

**Table 2.6**

Sensitivity indices of the aerodynamic parameters

Sensitivity indices	Vertical displacement	Torsional displacement
first order <b>X1</b>	0.682520	0.557385
first order <b>X2</b>	0.154241	0.236873
first order <b>X3</b>	0.129080	0.205698
<b>sum of first orders</b>	<b>0.965841</b>	<b>0.999956</b>
interaction between <b>X1</b> and <b>X2</b>	0.011241	0.000107
interaction between <b>X1</b> and <b>X3</b>	0.008712	0.000044
interaction between <b>X2</b> and <b>X3</b>	0.000537	0.000082
total order of <b>X1</b>	0.702473	0.557536
total order of <b>X2</b>	0.166019	0.237062
total order of <b>X3</b>	0.138329	0.205824
<b>sum of total orders</b>	<b>1.006821</b>	<b>1.000422</b>

In relation with the vertical displacement, the total order sensitivity index of aerodynamic parameter (wind attack angle) is 0.7024, this value is bigger than the total order sensitivity index of aerodynamic parameter (deck streamlined length) **X2** which is 0.1660, also it is bigger than the total order sensitivity index of aerodynamic parameter (stay cables viscous damping) **X3** which is 0.1383, this means that the vertical displacement is 70.24% due to variation in the wind attack angle, and it is 16.60% due to the variation in the deck streamlined length. Also it is 13.83% due to the variation in the stay cables viscous damping. While the interaction index between the aerodynamic parameters **X1** and **X2** is 0.0112 and between **X1** and **X3** is 0.0087, while between **X2** and **X3** is 0.0005, which means that there is

## 2.9 Experimental Design

a small interaction between the aerodynamic factors taking part in the variation of the vertical displacement of the deck at the center of the mid span.

While considering the torsional displacement, the total order sensitivity index of **X1** is 0.5575, which is the biggest aerodynamic parameter which is bigger twice of the total order sensitivity index of **X2** which is 0.2370 approximately, also it is bigger twice the total order sensitivity index of **X3** which is 0.2058 approximately, this means that the torsional displacement is dependable 55.75% on the wind attack angle variation, while it is 23.70% due to the deck streamlined length variation, and it is 20.58% due to the variation in stay cables viscous damping. While the interaction index between **X1** and **X2** is 0.0001 and between **X1** and **X3** is 0.0000, in the other hand, between **X2** and **X3** is 0.0000 too, this proves that the surrogate model is additive approximately which means that there is no interaction between aerodynamic parameters take part in the variation of the torsional displacement of the deck at the outer edges of the mid span.

### 2.9.7 Convergence of The Results

The process of global sensitivity analysis supporting on Sobol's sensitivity indices requires certain or adequate samples of experiments to find out the predicted effect of the aerodynamic parameters on the response of the system. The most efficient number of samples is being identified through the convergence of the sum of first orders and total sensitivity indices of the aerodynamic parameters. All the sensitivity indices (first orders, interaction orders and total orders) for each aerodynamic parameter have been calculated using m MATLAB codes. Two outputs have been utilized in the process of converges, the vertical displacement and torsional displacement. **Figure 2.27** and **Figure 2.28** show the relation between the number of samples and the sum of first orders sensitivity indices, in the same time between the number of samples and the sum of total sensitivity indices of the three aerodynamic parameters.

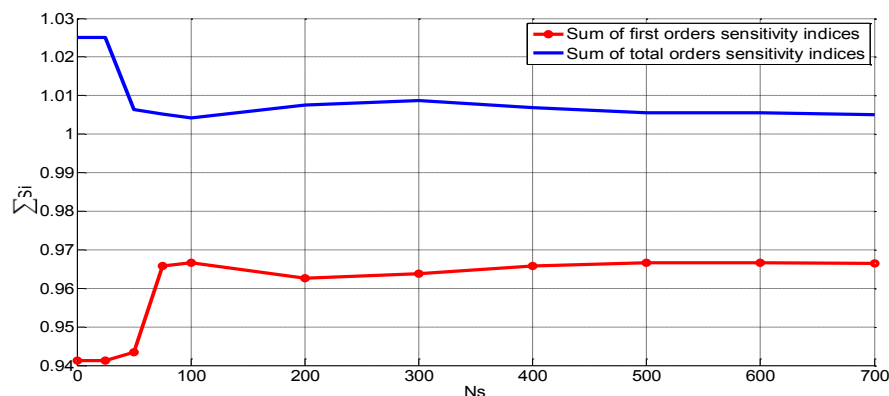


**Figure 2.27** Convergence of sensitivity indices –Vertical displacement

## 2.9 Experimental Design

---

For the case of vertical displacement (see **Figure 2.27**), the two curves of the sum of first orders and total orders of sensitivity indices at the beginning are not coinciding to reach convergence till 400 samples. After this stage the two curves are starting to converge at the 400 number of samples, where the two curves continue to remain in a stable position after many times of changing the number of samples.

Also for the torsional displacement (see **Figure 2.28**) the two curves are reaching convergence at 400 samples too, and the coinciding pattern continues.

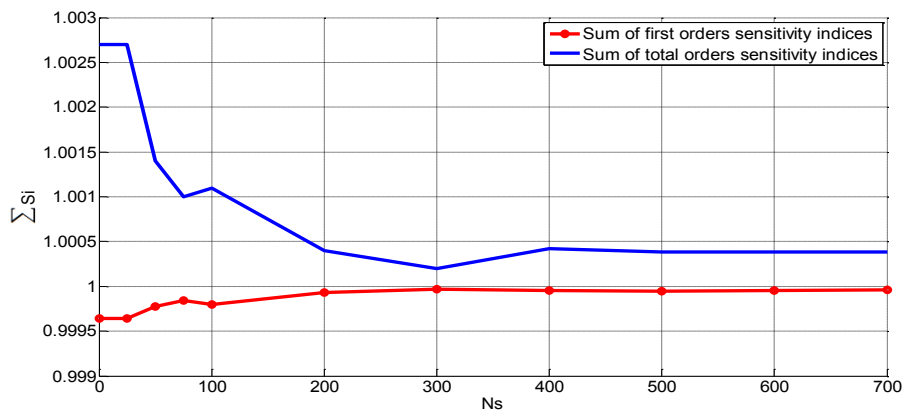


**Figure 2.28** Convergence of sensitivity indices –Torsional displacement

The convergence results of the two cases necessitate utilizing 400 samples of experiments to efficiently get the predicted rational effects of each aerodynamic parameter on both the variation of the vertical displacement and torsional displacement.



# Chapter 3

## Kinetic Energy Based Model Assessment

### 3.1 Von Karman Vortex Street

Attempts have been made to obtain analytical expressions for the fluctuating lift force experienced by the bluff cylinder owing to the ideal Karman-Benard vortex trail (see **Figure 3.1**). The stable configuration of vortices possesses the relations:  $h_K/b_K = \pi^{-1} \operatorname{arccosh} \sqrt{2} \approx 0.281$  and  $|\Gamma| = \sqrt{8} u_K b_K$ , where  $\Gamma$  is the strength of vorticity for a concentrated vortex.  $u_K$  is the speed of the vortices,  $b_K$  is the distance between the vortices in a row and  $h_K$  is the distance between the rows.

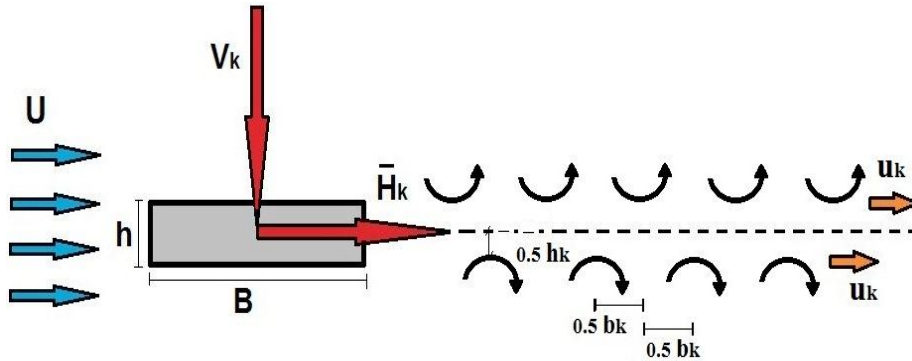


**Figure 3.1** Karman-Bernard's (Von Karman) vortex street

Furthermore, it was shown that the vortex trail induces almost steady drag force to the body given by the following formula:

$$\bar{H}_K = qh C_{HK} \quad (3.1)$$

in which  $\bar{H}_K$  is the mean value of the induced horizontal force per unit length,  $q$  is the kinetic pressure and the associated force coefficient  $C_{HK}$  is expressed as:

$$C_{HK} = \frac{2\Gamma}{U^2 h} \frac{h_K}{b_K} (U - 2u_K) + \frac{\Gamma^2}{\pi U^2 h b_K} \quad (3.2)$$

Considering infinite vortex trail and circular cross-section, Chen found that:

$$V_K = \rho u_K \Gamma = qh C_{VK} \quad (3.3)$$

## 3.2 VIV Parameters

where

$$C_{VK} = \left( \frac{\Gamma}{U b_K} \right)^2 \frac{b_K}{h} \tanh \frac{\pi h_K}{b_K} \quad (3.4)$$

$V_K$  is the fluctuating across-wind force per unit length and  $C_{VK}$  is the associated aerodynamic exciting coefficient. The aeroelastic actions can be considered in **Equation (3.2)** and **Equation (3.4)** by noting that the spacing between the vortex row  $h_K$ , and thus the induced forces, can alter, if the cross-section performs across-wind oscillations. In general, analytical formulations for the aerodynamic exciting coefficients are dependent on the approximations assumed for the near-wake behind the body. The vibrations generated by vortex shedding usually occur in slender structures with low damping. The vibrations occur if the vortex shedding frequency coincides with or come close to the natural frequency of the structure. The vortex shedding frequency  $f_s$  of a non-vibrating body can be derived as suggested by [Dyrbye and Hansen, 1999] see **Figure 3.2**. The time between the vortices at each side is equal to the distance  $lv$  divided by the speed of the vortices  $U_1$ . The frequency is the inverse of the period, giving that  $f_s = U_1/lv$ . The distance between the vortices  $lv$ , must be proportional to the structure width  $d$ , since this is the only relevant length.

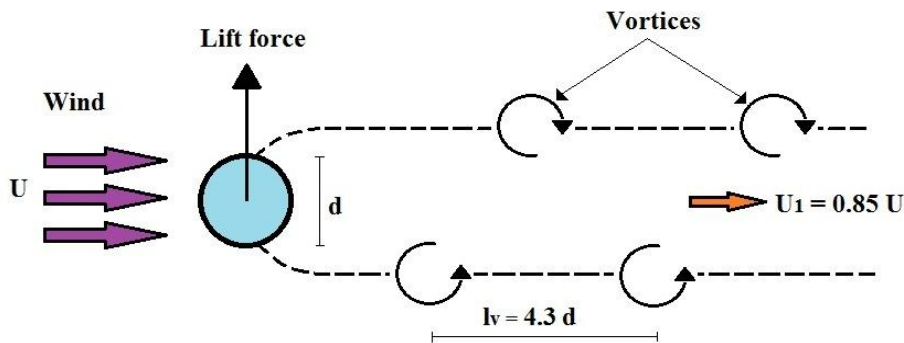


**Figure 3.2** Vortex Street for a bluff body (Dyrbye and Hansen, 1999)

## 3.2 VIV Parameters

### 3.2.1 Reynolds Number

Reynolds number is a dimensionless number that describes the flow around smooth bluff bodies such as a bridge deck. It is the ratio between the inertia forces and viscous forces:

$$Re = \frac{DU}{\nu} \quad (3.5)$$

## 3.2 VIV Parameters

---

in which  $D$  is the diameter of the cylinder,  $U$  is the flow speed and  $\nu$  is the kinematic viscosity of the fluid. Flow regimes are obtained as the result of many changes of the Reynolds number. The changes of the Reynolds number generate separation of flows in the wake region of the bluff body, which are called vortices. At low values of Reynolds number ( $Re < 5$ ), there no separation occurs. When Reynolds number is further increased, the separation starts to occur and becomes unstable and initiates the phenomenon named vortex shedding at particular frequency. The main parameter of Reynolds number is the wind speed that is directly related to the generation of VIV by affecting the kinetic energy of the flow system that is the source of vortex shedding [Schewe and Larsen, 1998; Kazutoshi *et al.*, 2007; Irwin, 2008; Asyikin, 2012; Wu and Kareem, 2012; Sutardi, 2014].

### 3.2.2 Deck Shape

The deck shape of a bridge is essential to be in such a way to enhance the aerodynamic behavior and to reduce the tendency to vortex shedding. [Bienkiewicz, 1987] studied various cross section samples and [Nagao *et al.*, 1993] studied the ratios of width and the height of box girders and many shapes of fairing. The results of these studies concluded that the best streamlined deck shape involves better aerodynamic stability of the structure. While [Wardlaw *et al.*, 1983] discovered that the turbulence can suppress the vortex shedding. [Noda *et al.*, 2009] displayed the role of the leading edge of the bottom deck separation on the lift force at a certain Reynolds number. However, there are other flow features, like top deck leading edge separation and bottom deck trailing separation that their aerodynamic behavior are still not clear [Larsen and Walther, 1998; Lin *et al.*, 2005; Gosteev *et al.*, 2014; Haque *et al.*, 2016].

### 3.2.3 Dynamic Viscosity of Air

Vortex shedding has an important relation with the dynamic viscosity of air, so it is essential to consider this parameter in the study of vortex shedding patterns and vortices shapes. The contact between the air particles and the deck surface has adhesion force that creates the boundary layer. However, because of air mass, it undergoes inertial effect according to Newton's law and Navier-Stokes equations. The link between the inertial forces and the viscous forces is specified by Reynolds number. The boundary layer separation point explains the deck behavior submerged in the wind flow. A deck shape with a surface with high curvature, the separation point modifies with respect to Reynolds number, which is the source of diverse effects related to vortex shedding [Jurado *et al.*, 2012 and Meinhardt *et al.*, 2014]. The dynamic viscosity of air represents the resistance of the air to shearing wind flows. This parameter has values that vary linearly with the variation of temperature (see **Figure 3.3**).



### 3.3 Vortex Shedding Phenomenon in Bridges

---

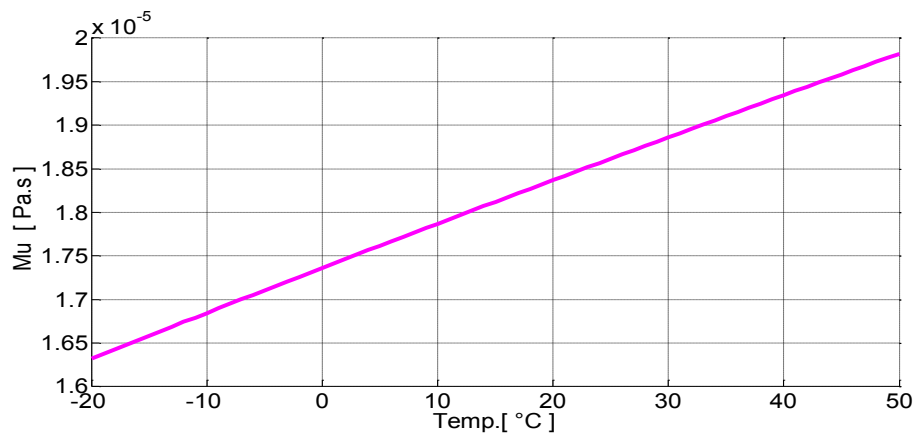


Figure 3.3 Dynamic viscosity of air versus temperature

### 3.3 Vortex Shedding Phenomenon in Bridges

When a bridge deck is subjected to a wind flow perpendicularly, the wind would be retarded when it is with contact with the deck surface and boundary layer being composed. This boundary layer at some parts of the deck, trends to separate from the deck. The separation of the boundary layer generates a force on the deck and pressure on the windward part and suction at leeward part. As a result, vortices would be formed which alters the distribution of pressure on the bridge deck surface leading to structural deflections of the deck. These vortices might not be symmetric around the deck. Hence diverse lifting forces are generated around the deck. The motion of the deck would be transverse to the direction of the incoming wind. When the shedding frequency of vortices matches the natural frequency of the bridge, resonance oscillations will occur predominantly. The amplitude of the oscillations relies on the system damping and the fluctuation of the wind. These oscillations might reach lock-in region, consequently result in dangerous extension and failure due to fatigue [Zhang *et al.*, 2004; Diana *et al.*, 2006; Flamand *et al.*, 2013; Belloli *et al.*, 2014; Grouthier *et al.*, 2014; Meinhardt *et al.*, 2014].

Due to fluctuation of wind and variation with respect to time and elevation, the frequency of vortex shedding is not remaining stable for a long time. As a result, bridges are not apt to everyday wind excitation. In a critical case, when the wind is unusually stable and long lasting, vortex shedding can result in vertical motion of the deck with amplitude up to decimeters, where the duration of wind excitation in this case ranges between several minutes and some hours. The amplitude of oscillations is an important case that is concerning the users' comfort, especially when it reaches noticeable level and when the fatigue of the

### 3.4 Finite Element Model

---

structural elements is expected. A principal sketch of the phenomenon can be seen in **Figure 3.4**.

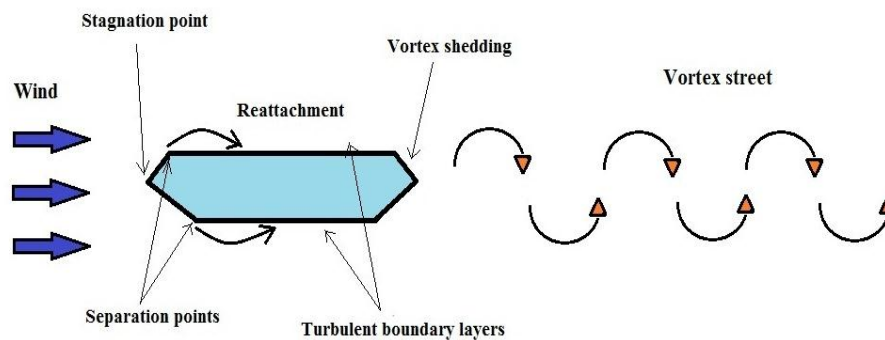


**Figure 3.4** Schematic flow around a stationary bridge deck

A wind flow around asymmetric bluff body like a bridge deck will affect the periodic vortex shedding or even suppress it. The motion of the deck which is periodic in nature may occur when the shedding frequency of the vortices is close to natural frequency of the bridge. The vortex induce vibrations can be averted by assigning the frequencies of the generated vortices be widely far from the natural frequency of the bridge. This step can be done by changing the geometry of the bridge structure or altering the natural frequencies in the design stage or after construction. Strouhal number is the most critical parameter in the subject of vortex shedding, which links between the shedding frequencies of the vortices, buff body diameter and flow speed. Due to nonlinearity in the bridge structures and aerodynamic force Simiu and Scanlan, 1996 suggested a synthesis sample to take into account the nonlinear influence [Marin, 2003; Dol *et al.*, 2008; Stevens and Simonsen, 2008; Andrienne, 2012; Flamand *et al.*, 2014].

### 3.4 Finite Element Model

The bridge segmental deck model is generated in ABAQUS-CFD in 2D model with dimensions 2.6 m height and total width of 22 m as shown in **Figure 3.5**, the thickness is 2 m. The flow domain size is 140 m length and 40 m height, the position of the deck model in the flow domain should be in a position so that to facilitate a proper area to show the vortex shedding in the downstream **Figure 3.6**, in addition to an appropriate area above and under the deck model to show the boundary layers around the deck with the separation points.

### 3.4 Finite Element Model

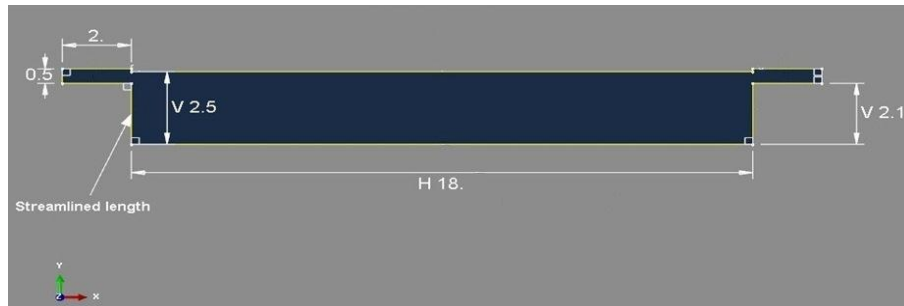


Figure 3.5 Deck model dimensions

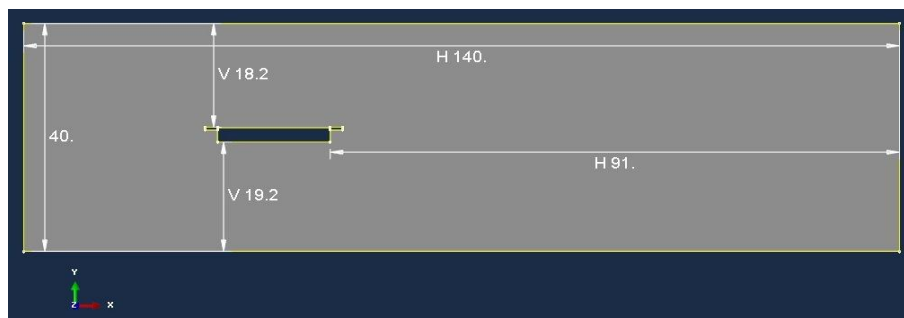


Figure 3.6 Flow domain size in CFD

The air density is assigned  $1.29 \text{ kg/m}^3$  and the dynamic viscosity of the air is assigned between the range ( $1.6321\text{E-}05$  -  $1.9821\text{E-}05$ ) Pa.s depending on the temperature between ( $-20$ )  $^{\circ}\text{C}$  and ( $50$ )  $^{\circ}\text{C}$  (see **Figure 3.3**). The model part is meshed using CFD element fluid family with FC3D8: A-8 node linear fluid brick. The deck wall assigned with 0.4 element size and the flow domain with 1 element size. A flow step with 100 seconds duration is created to simulate the vortex shedding. Spalart- Allmaras turbulence model has been used in this analysis for turbulent flow situations. Four boundary conditions are defined for the model, fluid boundary B.C for the inlet flow and far fields assigning the air speed value in the horizontal direction only (zero attack angle) and the other two directions with zero magnitudes, fluid B.C for the outlet flow assigning zero pressure, fluid B.C for the front and back of the flow model with zero speed magnitude for the third direction perpendicular to the model (z- direction) and non-slip fluid B.C for the wall condition of the deck. A job is created and the results are analyzed depending on the case if the model needs to be assigned model turbulence or not, this is to be done by checking the time history of the kinetic energy dissipated, where if the plot is oscillating randomly this means that the model needs to activate the model turbulence in the flow step, as a result this indicates necessity of predefining a fluid turbulence in the initial step. Commonly a very large number of Reynolds number indicates the need for a turbulence model.

### 3.4 Finite Element Model

#### 3.4.1 Mesh Convergence

The vortex shedding in the flow domain at the downstream of the deck in the velocity field depends on the mesh size around the deck and the downstream so that to facilitate a better simulation for the boundary layers and separation regions, in addition to the vortex shedding periodically. **Figure 3.7** shows the velocity field of the result with mesh size 28074 elements where the vortex shedding is not simulated correctly compared to the actual phenomenon, the vortices shedding is not in an asymmetric style, this is due to very fine mesh size around the deck model.

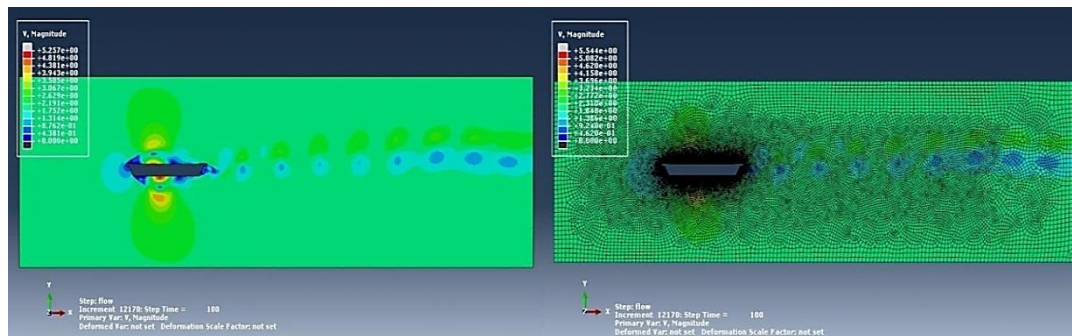


**Figure 3.7** Vortex shedding – Mesh size 28074 elements

The vortex shedding simulation in **Figure 3.8** with mesh size 9943 elements is the best simulation of the actual phenomenon, this is because the vortices shed is in an asymmetric form and the shedding is near the trail of the deck at the wake region, and it worthy that the mesh size in this case is appropriate, while the vortex shedding simulated in the model in **Figure 3.9** with mesh size 7724 elements is simulated in a weak style because the shedding of vortices is relatively far from the trail of the deck despite the asymmetric style, and this indicates that the mesh size is not suitable.

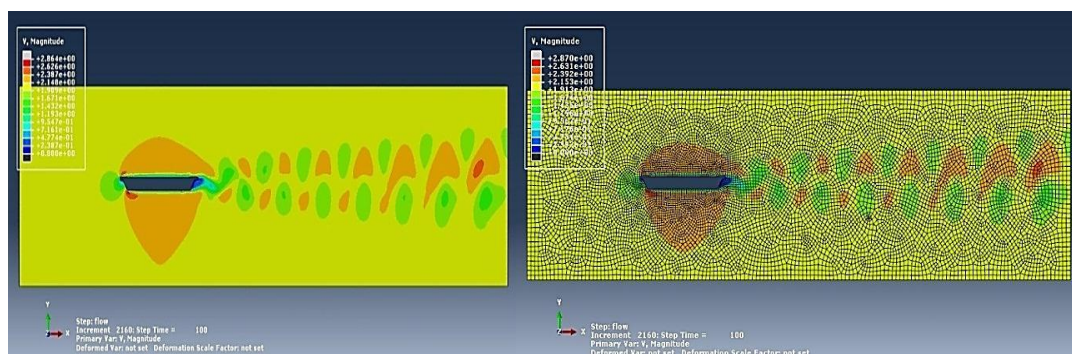


**Figure 3.8** Vortex shedding – Mesh size 9943 elements

### 3.4 Finite Element Model

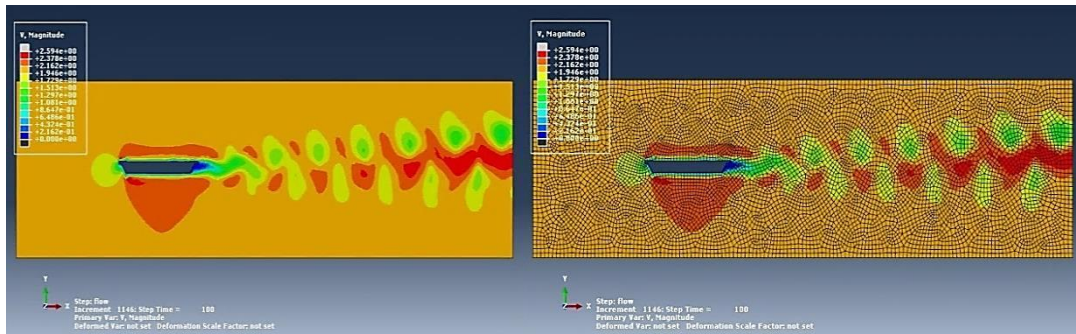


Figure 3.9 Vortex shedding – Mesh size 7724 elements

The models in **Figure 3.10** and **Figure 3.11** with mesh sizes 6202 and 5317 elements simultaneously are not showing the vortex shedding at all due to the coarse mesh sizes of the models. They look like to have a very large Reynolds number especially high speed magnitude of the wind flow. As a result the mesh size of 9943 elements would be utilized to mesh the CFD model.

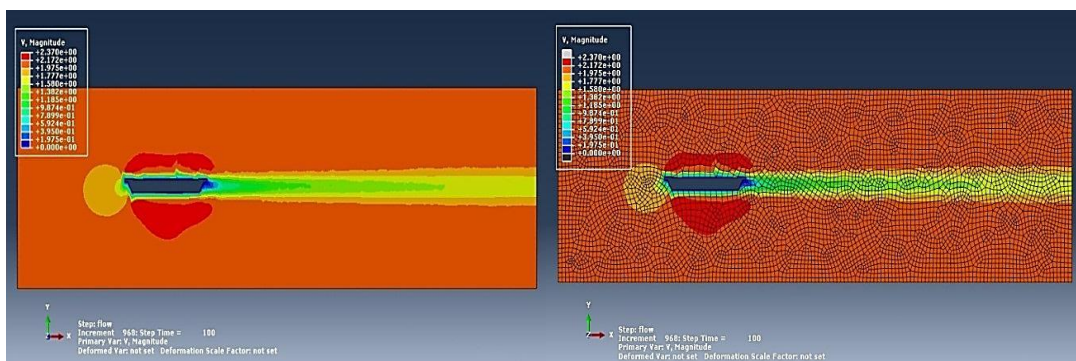


Figure 3.10 Vortex shedding – Mesh size 6202 elements

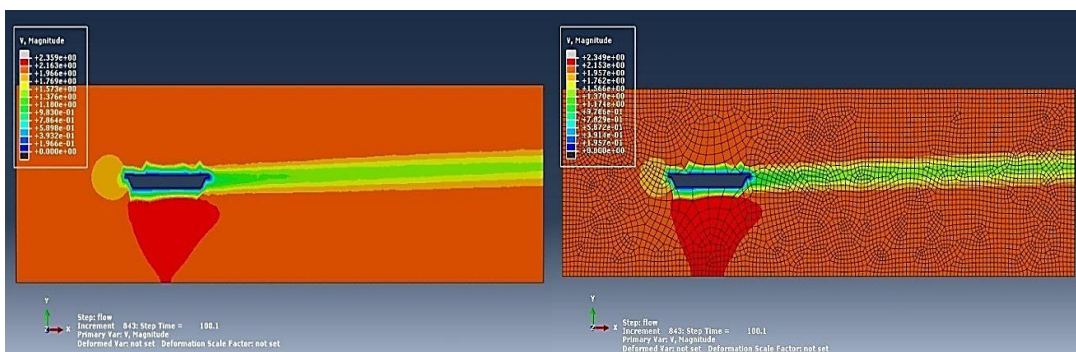


Figure 3.11 Vortex shedding – Mesh size 5317 elements



## 3.5 Results of Vorticity and Kinetic Energy

### 3.5.1 Wind Speed Effect

When the wind speed parameter denoted by **X1** increases, the vortex shedding in the downstream of the deck is obviously being better generated and regulated in shape and the frequency of shedding increases. When the wind speed  $V=0.5$  m/s, the vortex shedding is in the way to generate and the vortices are simply shedding but without regular style (see **Figure 3.12**). The vorticity field of this case shows the wind flow around the deck and the start of vortex shedding in the wake region (see **Figure 3.13**). When the wind speed increases to  $V=12.5$  m/s, the vortex shedding appears very well and the asymmetric pattern of the vortices can be seen very well (see **Figure 3.14**) with bigger frequency of shedding. The vortices shape and style in this case are bigger and wider than the previous case (see **Figure 3.15**). While when the wind speed reaches  $V=25$  m/s, the vortex shedding can be seen more organized with bigger frequency of shedding (see **Figure 3.16**). The vorticity field shows bigger vortices and different style of shedding (see **Figure 3.17**). All these cases indicate that increasing the wind speed will help to better generate the vortex shedding in the wake region, also the shape and the pattern of the vortices change to different style and the frequency of shedding increases, where this will enhance starting the vibration of the deck.

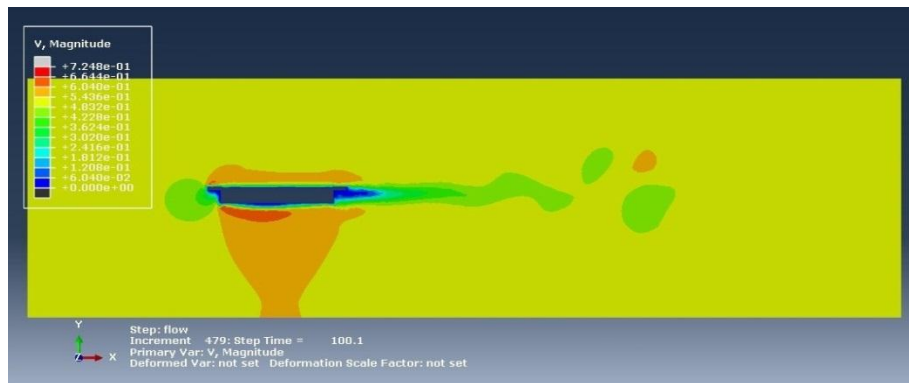


Figure 3.12 Vortex shedding - Velocity field -  $V=0.5$  m/s

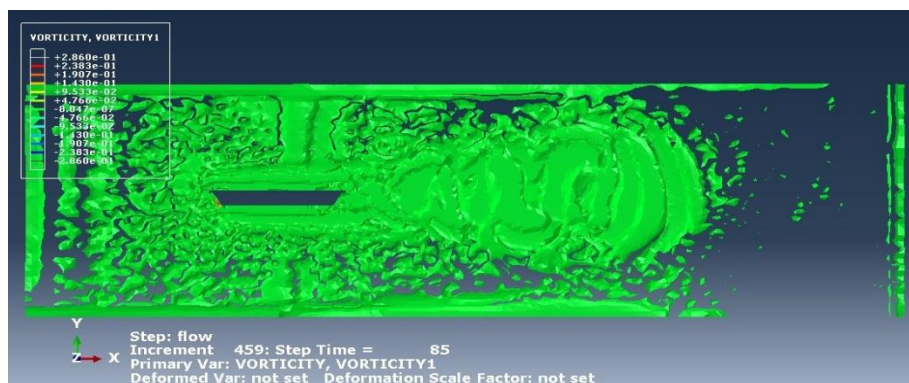


Figure 3.13 Vortex shedding - Vorticity field -  $V=0.5$  m/s

### 3.5 Results of Vorticity and Kinetic Energy

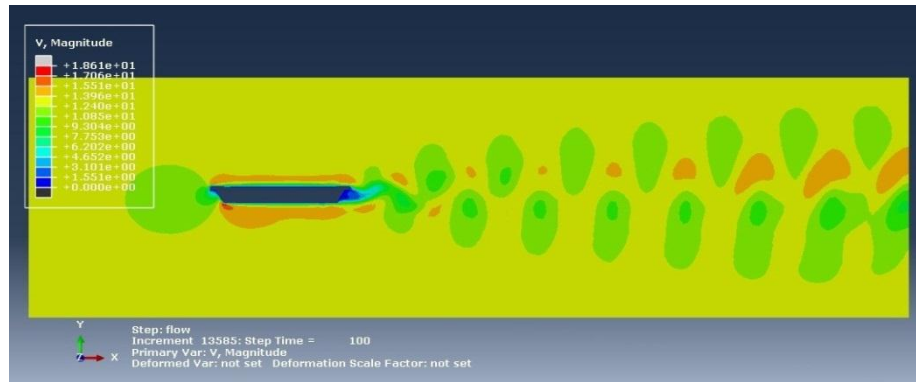


Figure 3.14 Vortex shedding - Velocity field -  $V=12.5$  m/s

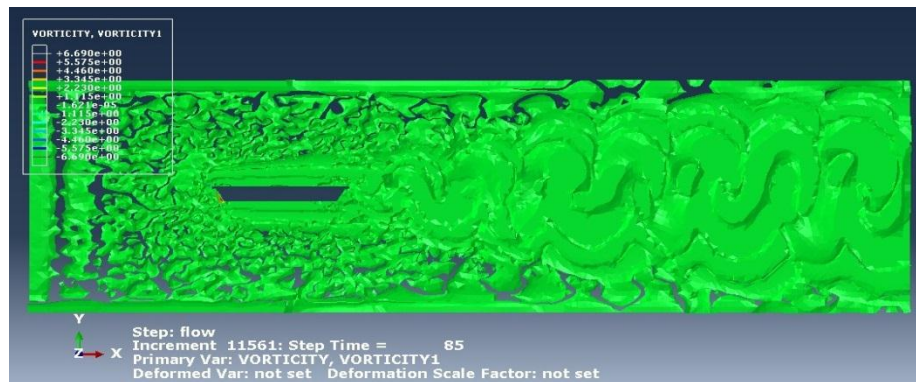


Figure 3.15 Vortex shedding - Vorticity field -  $V=12.5$  m/s

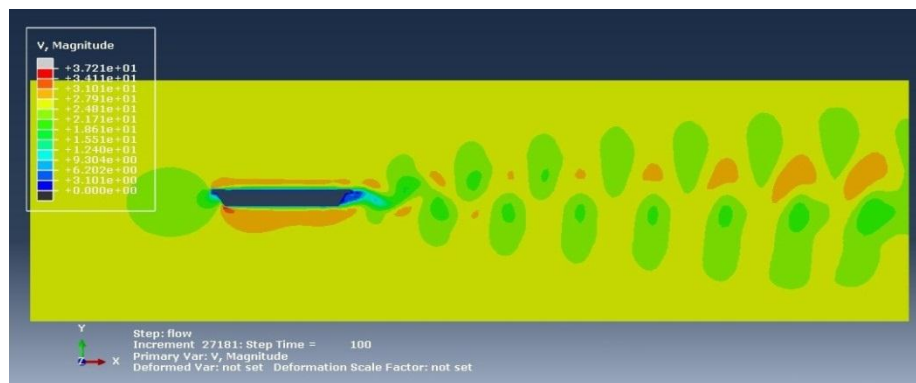


Figure 3.16 Vortex shedding - Velocity field -  $V=25$  m/s

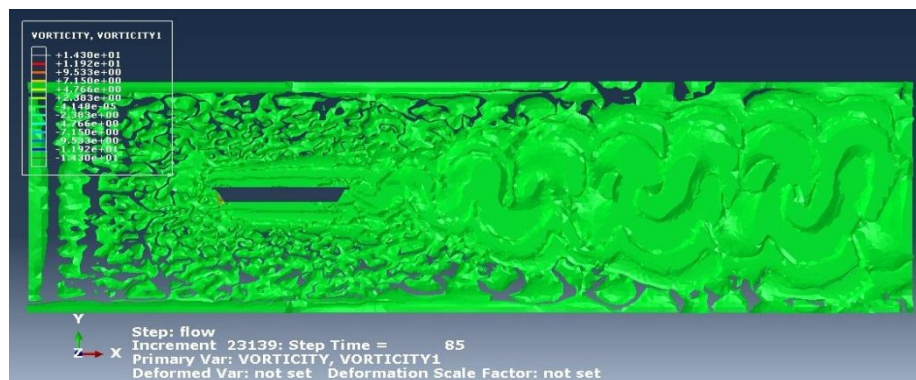
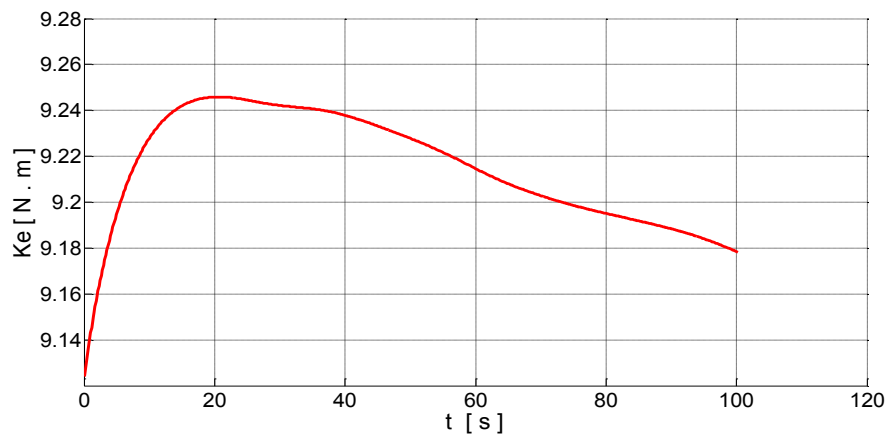


Figure 3.17 Vortex shedding - Vorticity field -  $V=25$  m/s

### 3.5 Results of Vorticity and Kinetic Energy

Regarding the kinetic energy of the system, when the wind speed increases, the kinetic energy increases in a nonlinear way. When the wind speed is  $V = 0.5$  m/s, the kinetic energy starts increasing till 18 seconds from the simulation, and after that it starts to decrease in a semi linear way due to energy dissipation due to generation of very simple vortex shedding that can be seen in **Figure 3.18**. While for wind speed  $V = 12.5$  m/s, the kinetic energy increases till 2 seconds from the simulation and suddenly drops down till 7 seconds from the simulation and again starts to rise until 13 seconds with an oscillatory style in the same time decreasing to a stable oscillatory position starting from 20 seconds from the simulation till the end indicating the start of the deck vibration with a certain frequency (see **Figure 3.19**). Furthermore, when the wind speed is higher  $V = 25$  m/s, the kinetic energy increases highly in the same way as previous case of  $V = 12.5$  m/s, but the sudden drop and sudden rise start in earlier position in the same time with a greater frequency of oscillation (see **Figure 3.20**). The overall comparison between the three kinetic energy cases can be seen in **Figure 3.21**.



**Figure 3.18** Wind speed  $V = 0.5$  m/s and the kinetic energy of the system

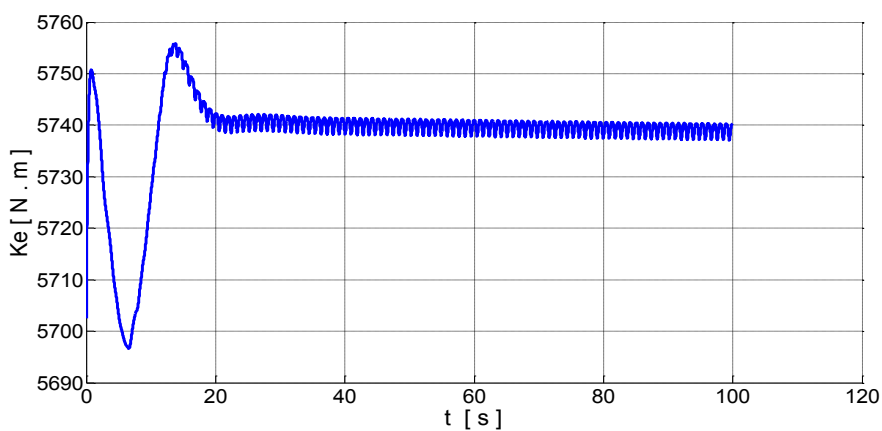


**Figure 3.19** Wind speed  $V = 12.5$  m/s and the kinetic energy of the system



### 3.5 Results of Vorticity and Kinetic Energy

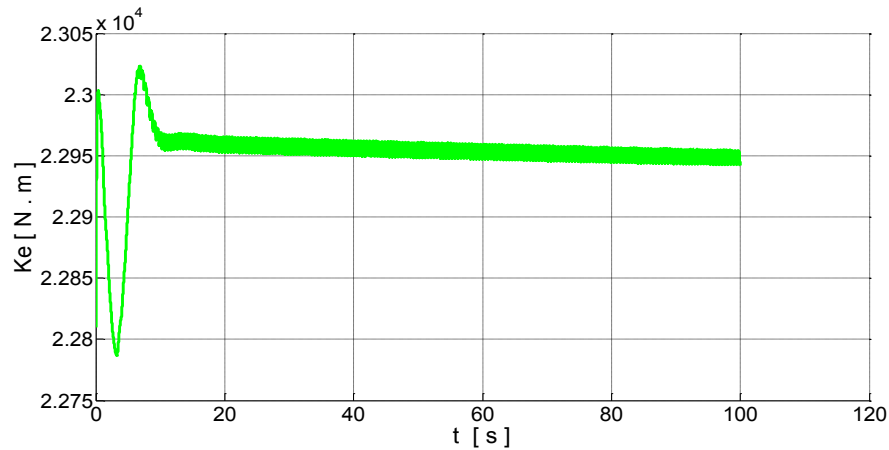


Figure 3.20 Wind speed  $V = 25$  m/s and the kinetic energy of the system

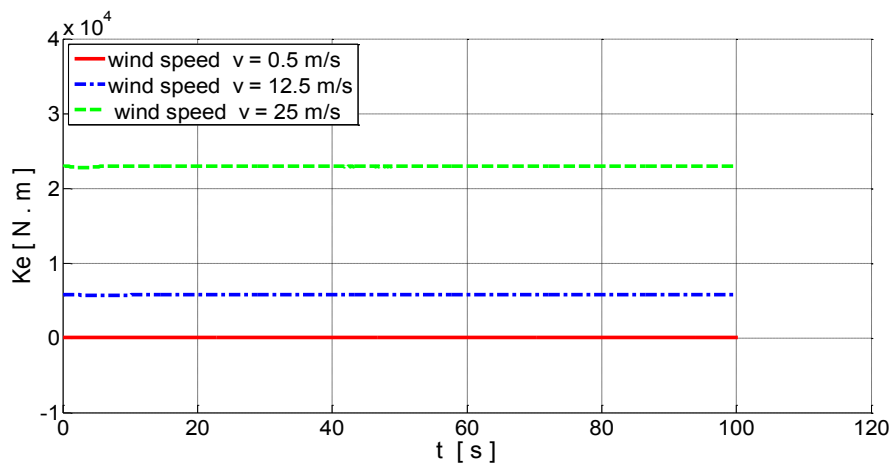


Figure 3.21 Effect of wind speed on the kinetic energy of the system

#### 3.5.2 Deck Streamlined Length Effect

The input parameter **X2** is the deck streamlined length. When the wind speed is constant and just this length is changed, many situations of vortex shedding from the wake region and vortices shapes and patterns are recognized. When this length  $L = 0$  m, the vortex shedding is generated in an primary establishing pattern showing the two rows of the asymmetric rows of the vortices (see **Figure 3.22**), but when the length  $L = 1$  m, the vortex shedding modifies to better shape and pattern of vortices in the two rows and the vortex trail can be recognized and seen better (see **Figure 3.23**). While when this length  $L = 2$  m, the vortex shedding disappears and the vortices shape and pattern are destroyed (see **Figure 3.24**).

### 3.5 Results of Vorticity and Kinetic Energy

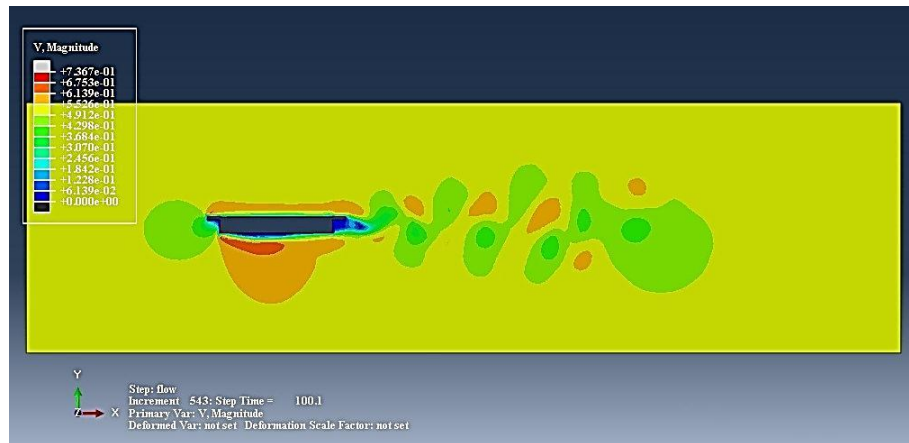


Figure 3.22 Vortex shedding - Velocity field - Deck streamlined length  $L = 0$  m

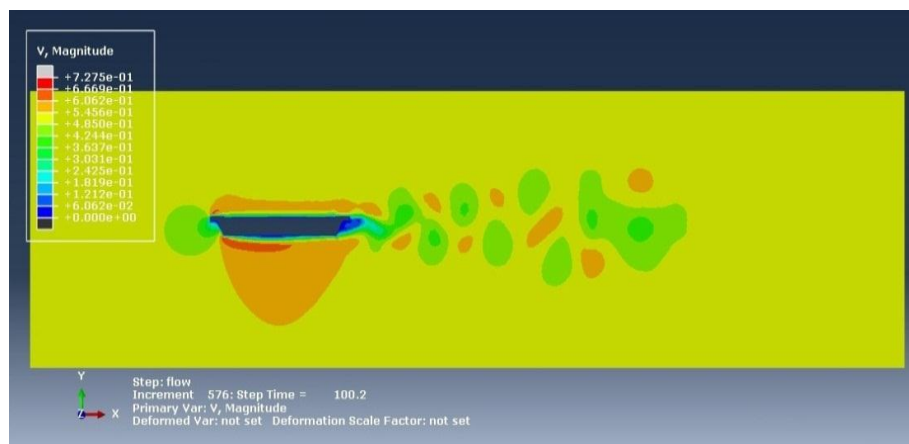


Figure 3.23 Vortex shedding - Velocity field - Deck streamlined length  $L = 1$  m

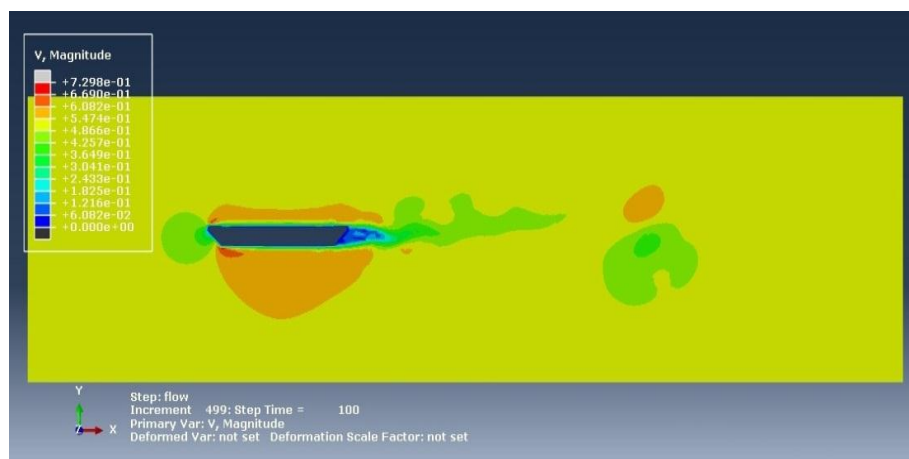


Figure 3.24 Vortex shedding - Velocity field - Deck streamlined length  $L = 2$  m

This means that a certain streamlined shape of the deck helps to avoid the vortex shedding generation in the wake region and as a result avoiding the VIV of the deck, because the complex process of separation of the wind flow from the deck edges, reattachments of them

### 3.5 Results of Vorticity and Kinetic Energy

and again separation of the flow to establish vortex shedding is dependable on many factors that arranges the better situation to avoid vortex shedding not only the streamlined shape of the deck itself only.

The results of the kinetic energy for all the three deck streamlined length cases proof energy dissipation in a harmonic form but in different rate. When the deck streamlined length is  $L = 0$  m, the kinetic energy starts to increase till 25 seconds from the wind flow simulation and it continues to be stable for 5 seconds, then it decreases in light oscillatory pattern indicating energy dissipation due to vortex shedding and vibration of the deck till the end of 100 seconds of the simulation. In the same way for the deck streamlined length  $L = 2$  m, but only after 30 seconds of the simulation the start of energy dissipation is taking place in a smaller rate than the previous case (see **Figure 3.25**). Furthermore, for the deck streamlined length case  $L = 1$  m, the kinetic energy starts to increase until 15 seconds from the simulation and continues to be stable for the next 5 seconds, after that the kinetic energy decreases in a semi smooth way showing greater energy dissipation than the previous two cases. This indicates that a certain streamlined shape of the deck is critical for earlier vortex shedding generation as a result earlier vibration of the deck.

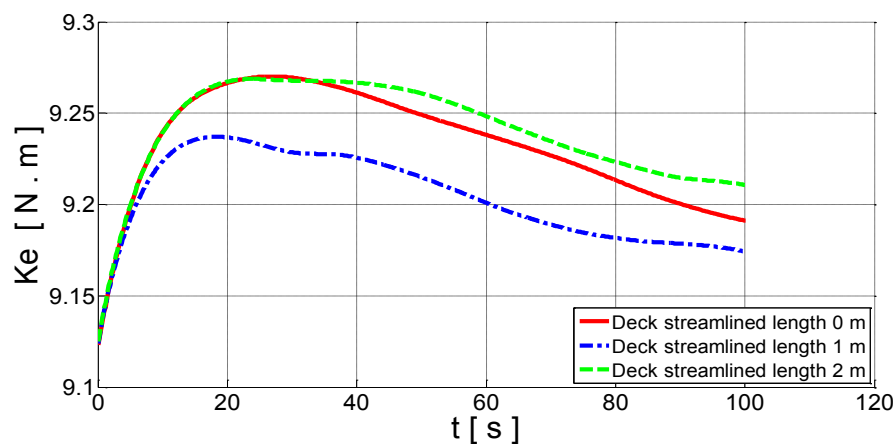


**Figure 3.25** Effect of deck streamlined length on the kinetic energy of the system

#### 3.5.3 Dynamic Viscosity of Air Effect

The input parameter **X3** is the dynamic viscosity of air. For a certain stable wind speed, the vortex shedding from the downstream of the deck is generated in an organized style and the asymmetric two rows of vortices. When this parameter increases, the vortices shape and pattern are affected with a very small rate which can be distinguished from the simulation results a little hardly as shown in **Figure 3.26**, **Figure 3.27** and **Figure 3.28**, where the style of the vortex shedding and the asymmetric shape of the vortices are not changed almost. This indicates that the vortex shedding is affected by this input parameter with a small amount.

### 3.5 Results of Vorticity and Kinetic Energy

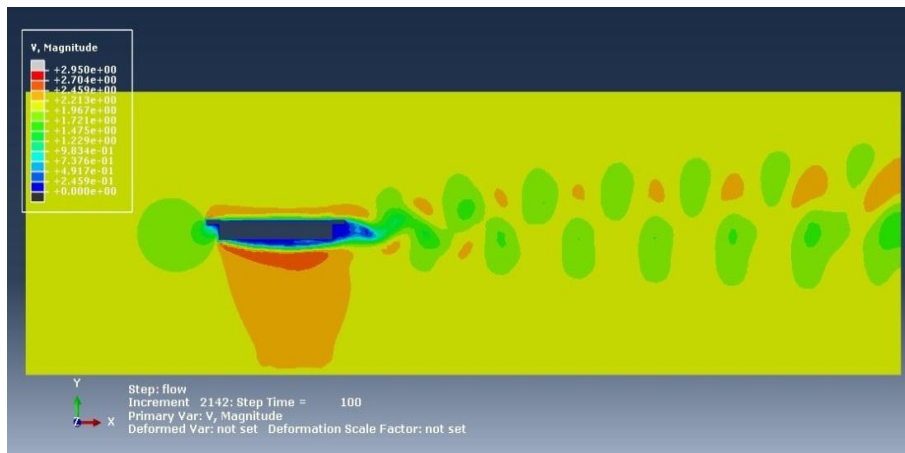


Figure 3.26 Vortex shedding – Velocity field – Air dynamic viscosity  $\mu=1.632E-5$

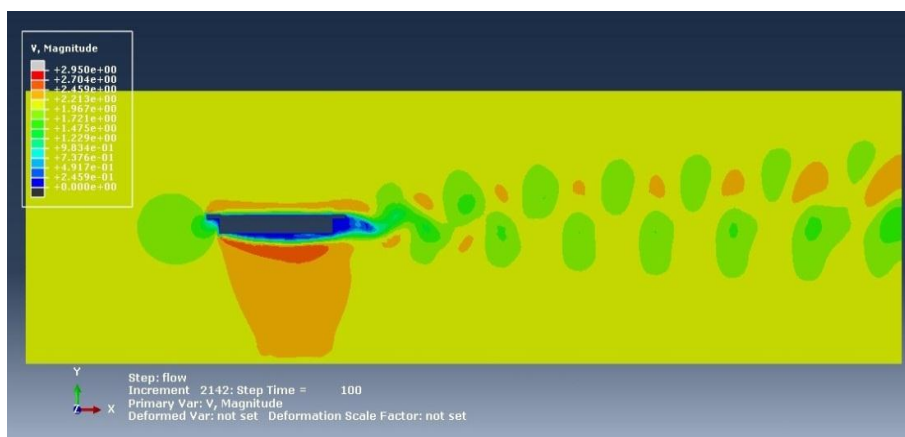


Figure 3.27 Vortex shedding – Velocity field – Air dynamic viscosity  $\mu=1.757E-5$

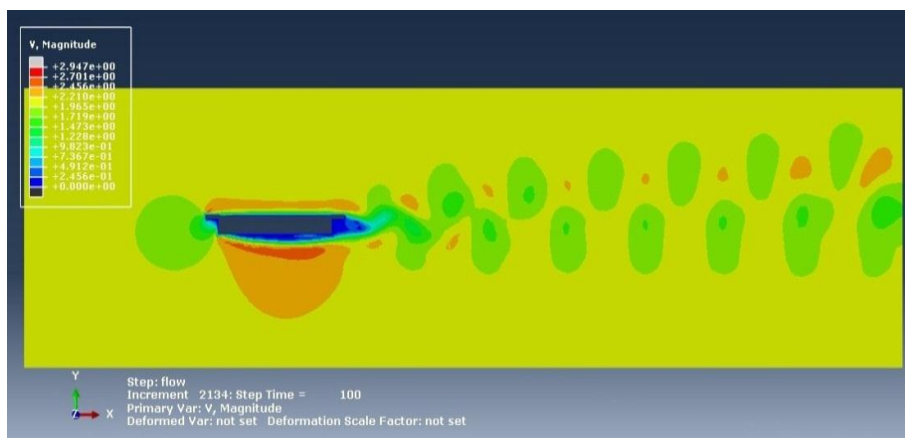
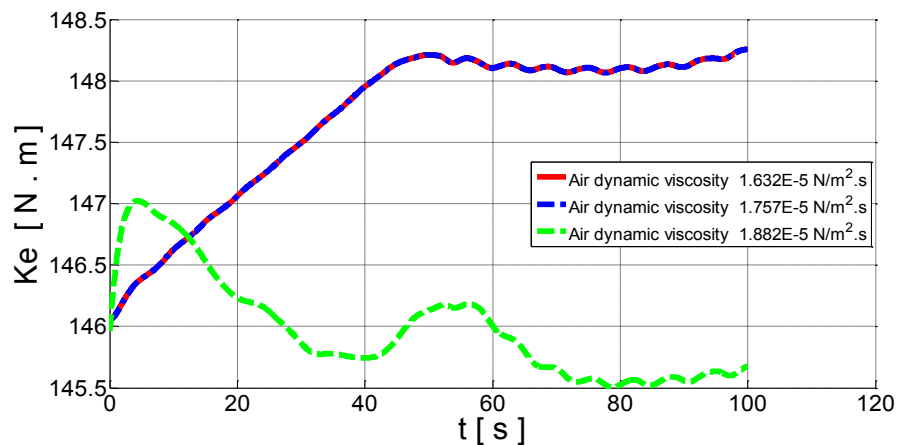


Figure 3.28 Vortex shedding – Velocity field – Air dynamic viscosity  $\mu =1.882E-5$

Considering kinetic energy of the system, the two cases of air dynamic viscosity  $\mu=1.632E-5$   $N/m^2.s$  and  $\mu=1.757E-5$   $N/m^2.s$  have the same effect on the vortex shedding from the deck where at the beginning of the wind flow simulation. The kinetic energy increases to higher values till 50 seconds and after that the kinetic energy values decreases and increases in an oscillatory pattern until the end of the simulation, this is an indication that the oscillation of

### 3.6 Validation of 2D - CFD Models

the deck starts after 50 seconds due to energy dissipation because of vortex shedding in the wake region and the kinetic energy becomes not stable. While in the case of air dynamic viscosity case  $\mu=1.882E-5$  N/m<sup>2</sup>.s, the kinetic energy of the system starts to increase till 5 seconds, but after that it begins to decrease in a simpler oscillatory non stable pattern but in a higher range (see **Figure 3.29**). This behavior means that the vortex shedding begins in earlier position but with the same pattern like the previous two cases for the same wind speed due to increase in the air dynamic viscosity but with higher vibration amplitudes. There is a nonlinear behavior of the deck vibration in relation with the air dynamic viscosity of the air.



**Figure 3.29** Effect of air dynamic viscosity on the kinetic energy of the system

### 3.6 Validation of 2D - CFD Models

The finite element models are validated through a comparison process against experimental data. The calculated results of the vortex shedding generated due to wind flow assignation in the 2D models of the segmental bridge decks are compared with two benchmarks results of the vortex shedding from the literature regarding the vortices shapes and patterns, where the generation of the vortices are indirectly associated with the kinetic energy of the system due to wind flow. Furthermore, the shape and pattern of the vortices are affected by the motion of the deck, and the wind speed strongly takes a main role in this process.

#### 3.6.1 Von Karman Benchmark

The axis of validation is the ratio of the distance between two rows of vortices and the distance between two vortices in the one row for a certain vortex trail. The value of this ratio in the vortex shedding for a bluff body stated by Von Karman is 0.282, where the same ratio value for the present 2D CFD model is between 0.291 and 0.296 considering five wind speed situations (5 m/s, 10 m/s, 15 m/s, 20 m/s and 25 m/s). There is a good agreement between the two results where the range of difference is narrow and falls between (0.009 –

### 3.6 Validation of 2D - CFD Models

0.014) see **Figure 3.30** and **Table 3.1**, where this ratio value in the CFD model is stable for many wind speed situations approximately.

**Table 3.1**

Validation with Von Karman benchmark

Wind speed m/s	CFD model hk / bk	Von Karman hk / bk
5	0.296	0.282
10	0.293	0.282
15	0.294	0.282
20	0.292	0.282
25	0.291	0.282

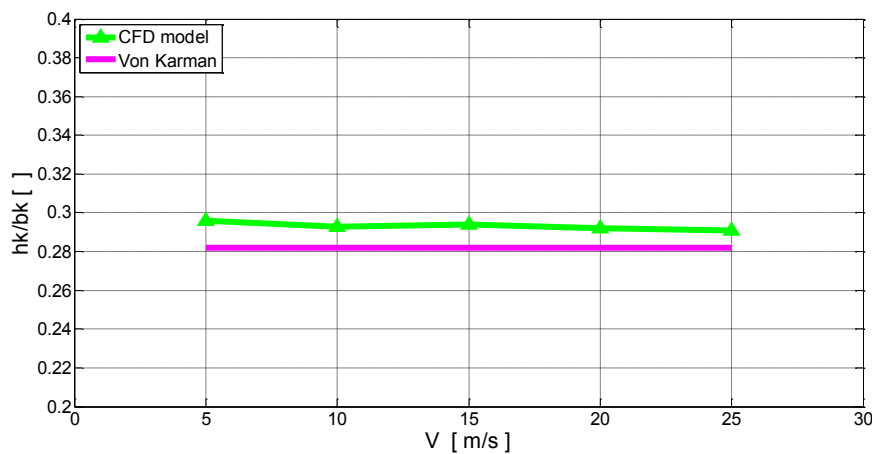


**Figure 3.30** Wind speed and ratio of two vortices rows central distance to one row vortices central distance validation

#### 3.6.2 Dyrbye and Hansen Benchmark

Another validation base is the distance between two vortices in the same row in the vortex trail. The results of this distance considering the present 2D CFD model for the previously mentioned five wind speed situations are between (11.22 – 11.31) m, while this distance is suggested by Dyrbye and Hansen to equal 4.3 times the height of the bluff body, and in this case equals to 11.18 m. It is quite obvious that there is a good agreement between the two results and the gap range is between (0.04 -0.13) m see **Figure 3.31** and **Table 3.2**. The results of this value are better validated for low wind speeds.

### 3.7 Sensitivity Analysis

**Table 3.2**

Validation with Dyrbye and Hansen benchmark

Wind speed m/s	CFD model bk	Dyrbye and Hansen bk
5	11.23	11.18
10	11.26	11.18
15	11.31	11.18
20	11.24	11.18
25	11.22	11.18

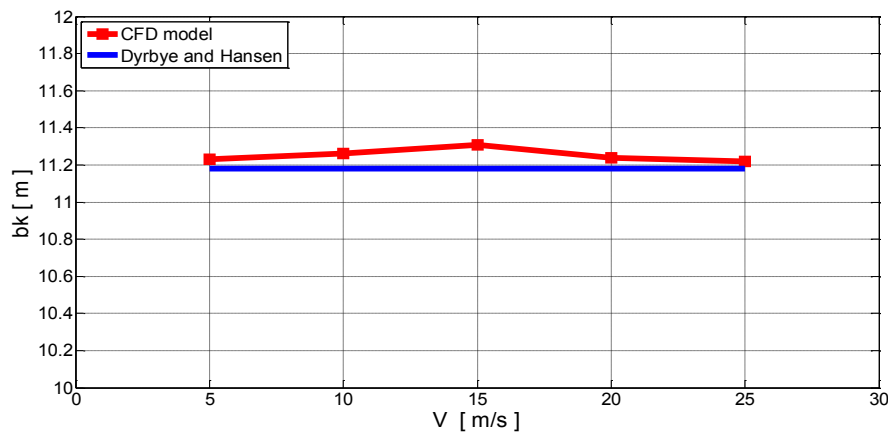


**Figure 3.31** Wind speed and one row vortices central distance validation

## 3.7 Sensitivity Analysis

Three input parameters (wind speed, deck streamlined length and dynamic viscosity of air) are being considered to undergo sensitivity analysis to calculate the sensitivity indices of each input parameter alone and with interaction terms, where the rational effects of each parameter are identified supporting on the surrogate models for two outputs (kinetic energy and lift force). Latin hypercube sampling method is dedicated in this process.

### 3.7.1 Latin Hypercube Sampling

Latin hypercube sampling is one of the popular methods of experimental design. [McKay *et al.*, 1979] suggested an alternative method of generating  $X^n$  that they called Latin hypercube

### 3.8 Surrogate Model Results and Discussion

---

sampling which is an extension of stratified sampling. Latin hypercube sampling ensures that each of the input variables has all of its range represented. Uniform sampling increases the realization efficiency while randomizing within the strata prevents the introduction of a bias and avoids the extreme value effect associated with simple stratified sampling. Let the range of each variable  $X_j, j = 1 \dots p$ , be simultaneously partitioned into  $n$  equally probable intervals. We note  $X_j^n$  the  $n$ -sample of the variable  $X_j$ . A Latin hypercube sampling of size  $n$  is obtained from a random selection of  $n$  values one per stratum for each  $X_j$ . Thus we obtain  $p$   $n$ -tuples that form the  $p$  columns of the  $n * p$  matrix of experiments  $X^n$  generated by Latin hypercube sampling: the  $i^{th}$  line of this matrix contains the  $p$  input variables and will correspond to the  $i^{th}$  code execution.

Mathematically, if  $X_1, \dots, X_p$  are mutually independent random variables with invertible continuous distribution functions  $F_j, j = 1, \dots, p$ , respectively, then the Latin hypercube sampling  $i^{th}$  sample for the  $j^{th}$  variable can be created as:

$$x_j^{(i)} = F_j^{-1} \left( \frac{\pi_j^{(i)} - \xi_j^{(i)}}{n} \right) \quad (3.6)$$

where the  $\pi_j$  is independent uniform random permutations of the integers  $\{1, 2, \dots, n\}$ , and the  $\xi_j^{(i)}$  are independent random numbers independent of the  $\pi_j$  [Petelet *et al.*, 2010; Pan *et al.*, 2011; Koziel *et al.*, 2011; Bakkiyaraj and Kumarappan, 2013].

### 3.8 Surrogate Model Results and Discussion

The regression coefficients were calculated for actual kinetic energy and lift force supporting on Latin hypercube sampling method, and in order to formulate the surrogate models for the predicted kinetic energy and lift force, 250 and 200 samples were used considering convergence process between the sensitivity indices respectively. Quadratic and interaction terms are used to construct the surrogate model for the case of kinetic energy for the system. The calculated coefficient of determination  $R^2$  between the actual and the predicted kinetic energy was 99.99% (see **Figure 3.32**) which is an excellent representation of the predicted kinetic energy, which means that just 0.01% of the system response still unexplained.

The response surface plots in **Figure 3.33**, **Figure 3.34** and **Figure 3.35** which have been generated using MATLAB codes, are the relation between each two aerodynamic parameters **X1X2**, **X1X3**, **X2X3** and the predicted kinetic energy of the system due to wind excitation and vortex shedding.



### 3.8 Surrogate Model Results and Discussion

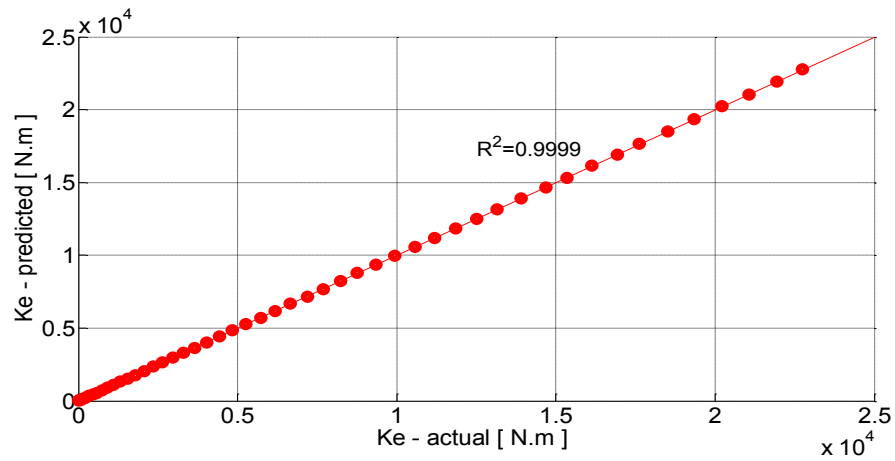


Figure 3.32 Coefficient of determination between actual and predicted kinetic energy

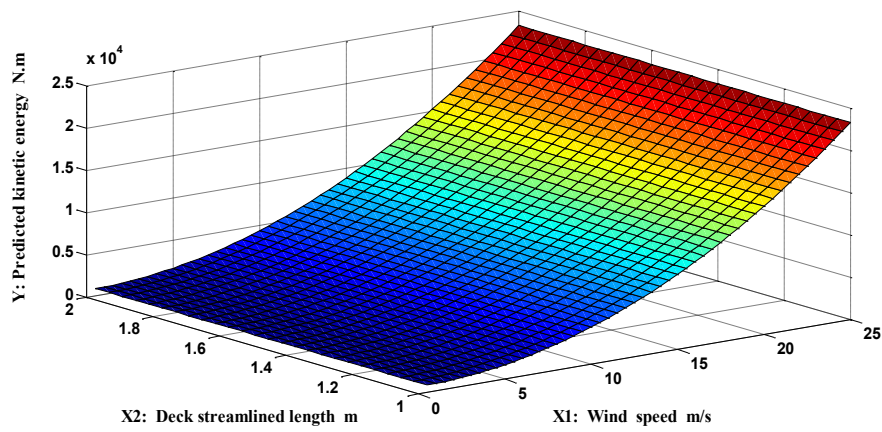


Figure 3.33 Response surface plot showing effect of X1 and X2 on the predicted kinetic energy

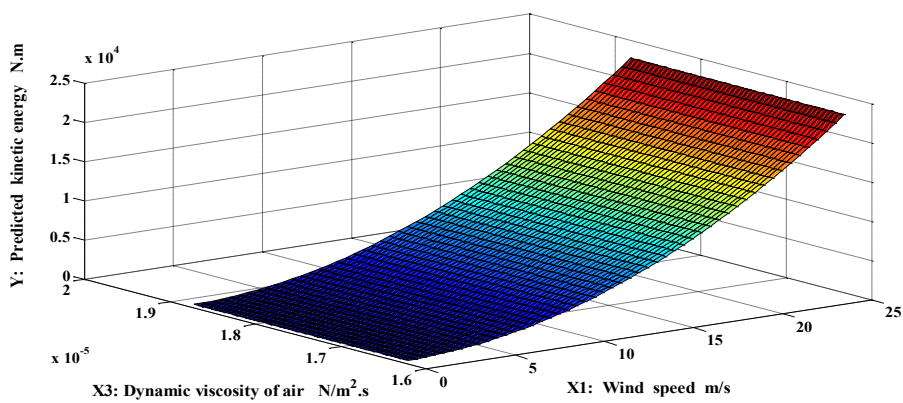
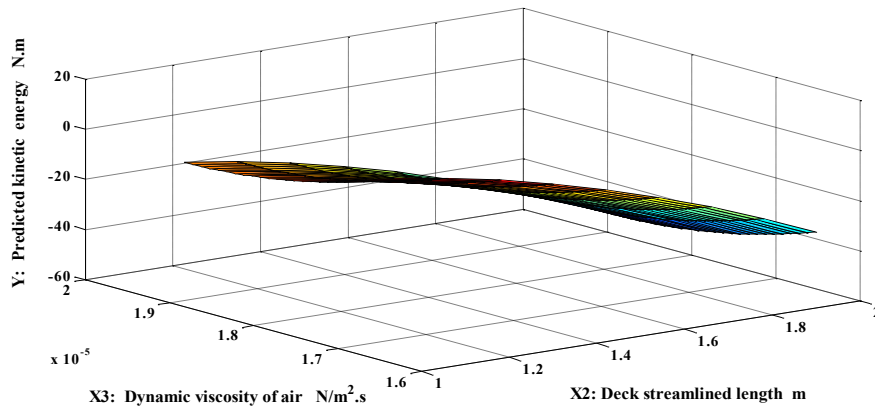


Figure 3.34 Response surface plot showing effect of X1 and X3 on the predicted kinetic energy

### 3.8 Surrogate Model Results and Discussion



**Figure 3.35** Response surface plot showing effect of **X2** and **X3** on the predicted kinetic energy

Quadratic and interaction terms are used to build the surrogate model to calculate the lift force generated in the deck. The coefficient of determination  $R^2$  calculated between the actual and the predicted lift force was  $R^2 = 99.99\%$  which is a very good approximation for the prediction of lift force where only 0.01% of the system response remains unexplained (see **Figure 3.36**).

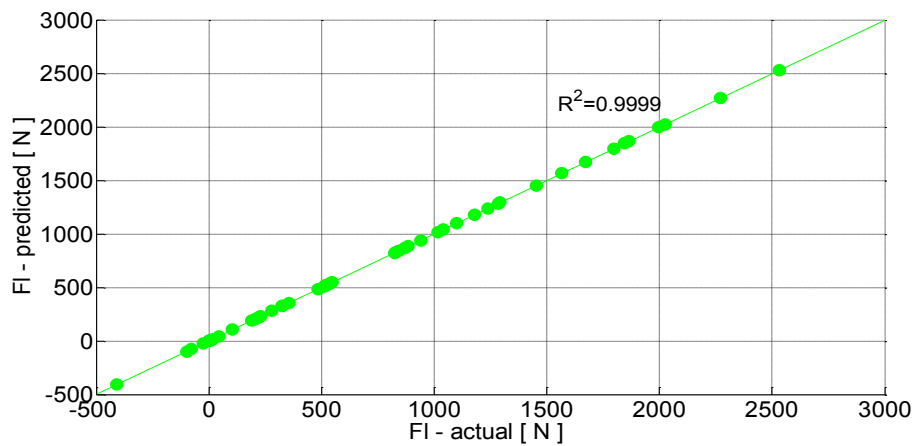


**Figure 3.36** Coefficient of determination between actual and predicted lift force

The next response surface plots express on the relation between each two aerodynamic parameters **X1X2**, **X1X3**, **X2X3** and the predicted lift force generated in the deck as shown in **Figure 3.37**, **Figure 3.38** and **Figure 3.39** which have been generated using MATLAB codes.

### 3.8 Surrogate Model Results and Discussion

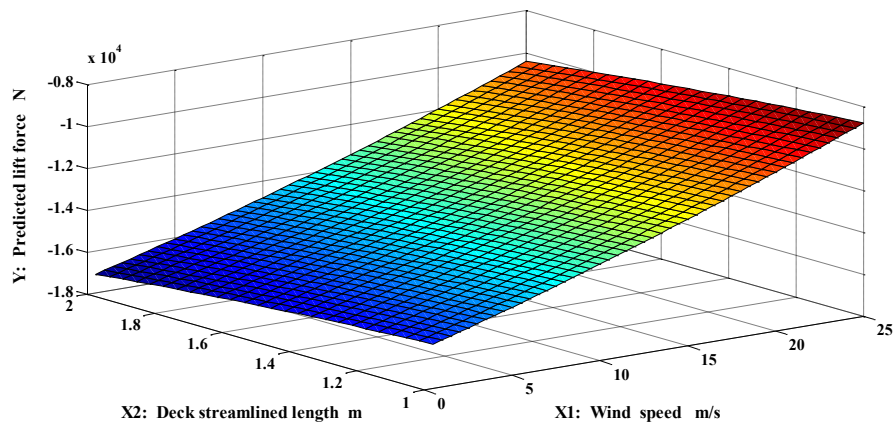


Figure 3.37 Response surface plot showing effect of X1 and X2 on the predicted lift force

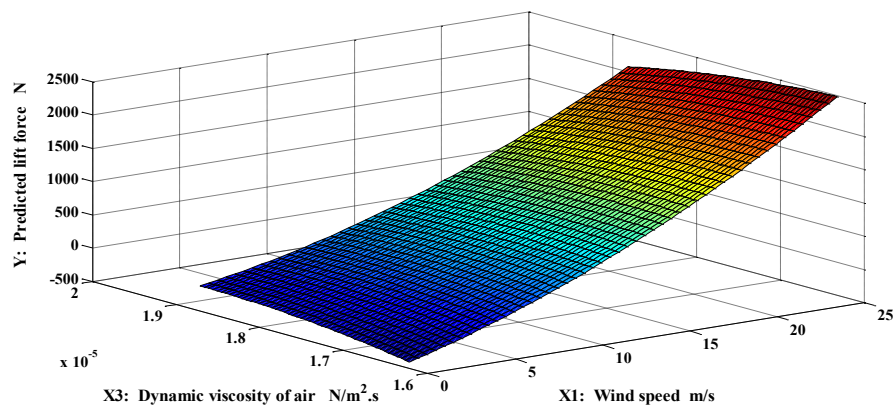


Figure 3.38 Response surface plot showing effect of X1 and X3 on the predicted lift force

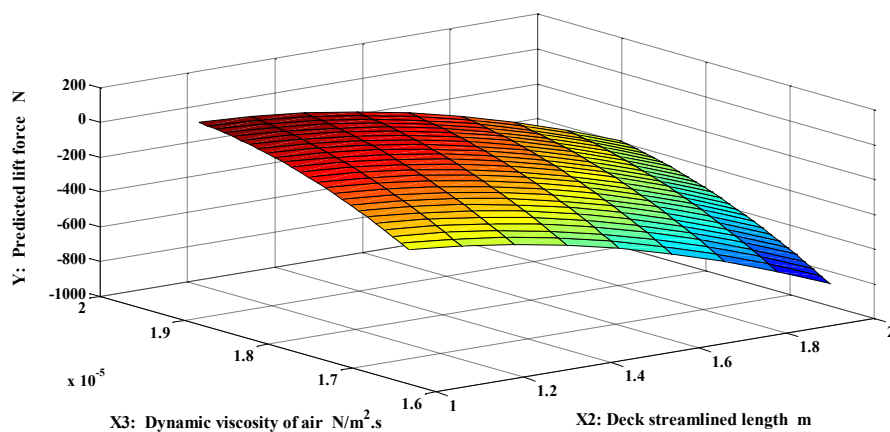


Figure 3.39 Response surface plot showing effect of X2 and X3 on the predicted lift force

## 3.9 Sensitivity Analysis Results and Discussion

The main orders of sensitivity indices for each aerodynamic parameter in addition to their interaction orders were calculated considering the convergence results which recommended using 250 samples to calculate the kinetic energy and 200 samples to calculate the lift force for VIV of the deck (see **Figure 3.40** and **Figure 3.41**). Supporting on the calculated results, the total sensitivity indices for each aerodynamic parameter have been calculated (see **Table 3.3**).

In relation with the kinetic energy, the total order sensitivity index of aerodynamic parameter (wind speed) is 0.9997, which is the biggest aerodynamic parameter, while the total order sensitivity index of **X2** is 0.0036. Furthermore, the total order sensitivity index of **X3** is 0.0040, this means that the kinetic energy of the system is 99.97% due to variation in the wind speed, and it is 0.36% due to the variation in the deck streamlined length. In the other hand, it is 0.40% due to the variation in the dynamic viscosity of the wind. While the interaction index between the aerodynamic parameters **X1** and **X2** is 0.0023 and between **X1** and **X3** is 0.0027, while between **X2** and **X3** is 0.0001, which means that there is a small interaction between the aerodynamic parameters taking part in the variation of the kinetic energy of the system due to vortex shedding.

While considering the lift force, the total order sensitivity index of **X1** is 0.8375, which is the biggest aerodynamic parameter, while the total order sensitivity index of **X2** is 0.1707. Furthermore, the total order sensitivity index of **X3** is 0.0294, this means that the lift force is dependable 83.75% on the wind speed variation, while it is 17.07% due to the deck streamlined length variation, and it is 2.94% due to the variation in the dynamic viscosity of the wind. While the interaction index between **X1** and **X2** is 0.0157 and between **X1** and **X3** is 0.0150, in the other hand, between **X2** and **X3** is 0.0012. This proves that the surrogate model is non-additive because there are small interactions between the aerodynamic parameters especially between wind speed and deck streamlined length once and between wind speed and dynamic viscosity of the wind in other side take part in the variation of the lift force generated in the deck, while not appreciable interaction between the deck streamlined length and the dynamic viscosity of the wind is seen to affect the lift force.

### 3.9.1 Convergence of The Results

The process of global sensitivity analysis supporting on Sobol's sensitivity indices requires sufficient samples of experiments to identify the predicted effect of the aerodynamic parameters on the VIV of the deck through two related outputs. The most efficient number of samples is being identified through the convergence of the sum of first orders and total

### 3.9 Sensitivity Analysis Results and Discussion

sensitivity indices of the aerodynamic parameters. All the sensitivity indices (first orders, interaction orders and total orders) for each aerodynamic parameter have been calculated using m MATLAB codes. Two outputs have been considered in the process of converges, the kinetic energy and the lift force. **Figure 3.40** and **Figure 3.41** show the relation between the number of samples and the sum of first orders sensitivity indices, in the same time between the number of samples and the sum of total sensitivity indices of the three aerodynamic parameters.

**Table 3.3**

Sensitivity indices

Sensitivity indices	Kinetic energy	Lift force
first order <b>X1</b>	0.9937	0.8039
first order <b>X2</b>	0.0001	0.1510
first order <b>X3</b>	0.0001	0.0104
<b>sum of first orders</b>	<b>0.9989</b>	<b>0.9971</b>
interaction between <b>X1</b> and <b>X2</b>	0.0023	0.0157
interaction between <b>X1</b> and <b>X3</b>	0.0027	0.0150
interaction between <b>X2</b> and <b>X3</b>	0.0001	0.0012
total order of <b>X1</b>	0.9997	0.8375
total order of <b>X2</b>	0.0036	0.1707
total order of <b>X3</b>	0.0040	0.0294
<b>sum of total orders</b>	<b>1.0073</b>	<b>1.0376</b>

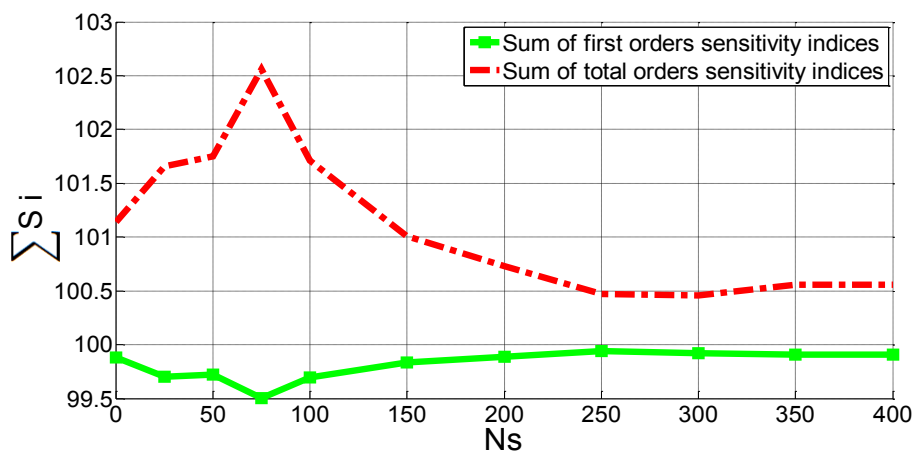


**Figure 3.40** Convergence of sensitivity indices – Kinetic energy

### 3.9 Sensitivity Analysis Results and Discussion

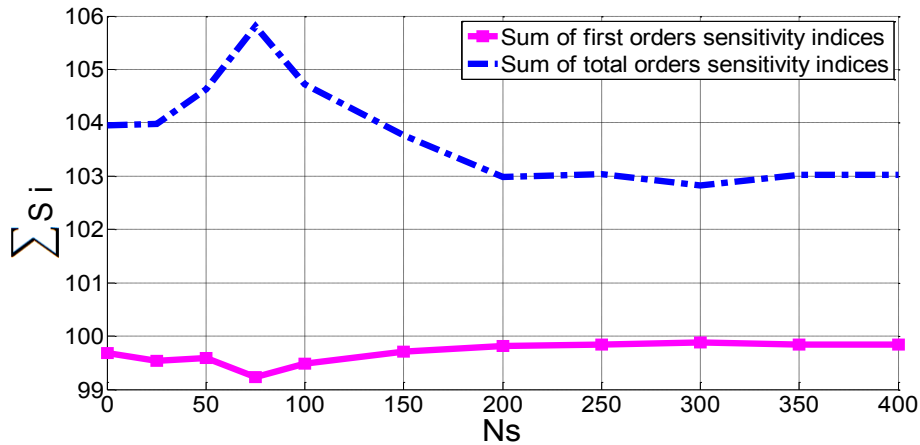


**Figure 3.41** Convergence of sensitivity indices – Lift force

For the case of kinetic energy (see **Figure 3.40**), the two curves of the sum of first orders and total orders of sensitivity indices at the beginning are starting without stability for coinciding to reach convergence, this situation continues till 250 samples. After this stage the two curves are starting to converge at the 250 number of samples, where the two curves continue to remain in a stable. In the same way, for the lift force (see **Figure 3.41**) the two curves are reaching convergence at 200 samples, and the coinciding pattern continues in a stable situation.

The convergence results of the two output cases predetermine utilizing 250 and 200 samples of experiments to efficiently calculate the predicted rational effects of each aerodynamic parameter on both the variation of the kinetic energy and lift force respectively.



# Chapter 4

## Fluid-Structure Interaction and Lock-in Phenomenon

### 4.1 Vortex Induced Vibration (VIV)

VIV can be known as the aerodynamic vibration which is caused by the alternate vortices generated from the interaction between the object and wind flow. Normally, the dimensionless constant called Strouhal number is used to evaluate the characteristic property of each bluff-body in wind flow by means of the phenomenon called the vortex shedding behind the object as shown in **Equation (4.1)** below.

$$S_t = \frac{f_s D}{U} \quad (4.1)$$

where the Strouhal number  $S_t$  depends on body geometry and the Reynolds number  $Re$ ,  $D$  is the across-wind dimension,  $U$  is the mean velocity and  $f_s$  is the primary frequency of the vortex shedding. When the vortices shed in the wake region is exciting an elastically supported body periodically, it will undergo a small response unless the Strouhal frequency reaches close to the across-flow frequency of the structure. The surface pressure generates in-line and across-flow forces with frequencies  $2f_s$  and  $f_s$  simultaneously, where a pitching moment has a frequency  $f_s$ . Here, the body interacts with the flow strongly. This frequency controls the vortex shedding even if the flow speed changes, which results in change of the Strouhal frequency away by a few percent from the natural frequency, this phenomenon is called lock-in [Dien, 1995; Kuroda, 1997; Larsen and Walther, 1997; Facchinetti *et al.*, 2004; Salvatori, 2007; Puckett *et al.*, 2011; Bourguet *et al.*, 2011; Tran, 2014]. It is known that the across-wind force increases until limited cycle of oscillation amplitude reached during synchronization. Also the along-structure correlation of force increases with oscillation amplitude. The most qualified models of the mathematical modeling of lock-in phenomenon are basing on coupled oscillators representing the structure and the wake [Diana *et al.*, 2006]. Practically, the models of the single degree of freedom are usually considered in the structural analysis, where a classical one is proposed by Simiu and Scanlan, 1996, through expressing the across-wind force as:



## 4.2 Fluid-Structure Interaction (FSI)

---

$$L_S = q[ C_{LS}(K)\sin(\omega t + \phi) + Y_1(K) \left(1 - \varepsilon(K) \frac{y^2}{D^2}\right) \frac{\dot{y}}{U} + Y_2(K) \frac{y}{D} ] \quad (4.2)$$

where  $C_{LS}$ ,  $Y_1$ ,  $Y_2$ , and  $\varepsilon$  are experimental parameters, functions of the Strouhal reduced frequency  $K_{st} = f_S D / U$ . In **Equation (4.2)**, three terms are distinguished: harmonic forcing term, a non-linear aerodynamic damping term, and an aerodynamic stiffness term. The harmonic term represents the alternating lift where lock-in does not occur due to vortex-shedding in the velocity ranges. The forcing term becomes negligible ( $C_{LS} \simeq 0$ ) in the region close to lock-in, and the other terms are controlling the synchronized oscillations. Using Van der Pol oscillator, the nonlinear damping term represents the self-limiting oscillations and the stiffness term holds the frequencies synchronized in the lock-in region [Zhang, 2003 and Salvatori, 2007].

Avoiding synchronization is suggested by Eurocode 1, but this phenomenon has been observed where the wind speed can range between wide limits, especially because a wide range of wind speeds result in the development of the phenomenon. Modifying the cross-section geometry of the bridge deck changes the vortex shedding behavior as a result changing the amplitude and the frequency of the oscillations but it does not development of the phenomenon [Andersson and Ahl, 2011].

## 4.2 Fluid-Structure Interaction (FSI)

Multi-physics cases are very difficult to being solved using analytical methods. They mostly should be solved by using numerical simulations or using experiments. The most advanced techniques and the reputed commercial software in CFD and CSD have made the numerical simulation possible. FSI within models created using finite element programs is mostly conducted by the use of a node to surface contact algorithm. Standard FSI algorithm has three steps, computing the surfaces and their normal, then conducting contact search between the nodes of the fluid that might contact with the surface and the last is applying penalty forces to the nodes of the fluid so that to prevent the fluid from penetrating the surfaces [Rabczuk *et al.*, 2010]. Exchange of the information is done at the interface between the two solvers, this is called the coupling which is of two types, the first is the one-way coupling and the second is the two-way coupling.

### 4.2.1 One-Way FSI

In one-way coupling, the motion of the fluid flow influences the solid structure but the reaction of the solid structure on the fluid flow is neglected. Also the two-way coupling can be possible. The calculation of the fluid flow is performed until reaching convergence. The

## 4.2 Fluid-Structure Interaction (FSI)

---

resulted forces at the interface from the fluid calculation are being interpolated to the structural mesh. Then the calculations of the structural dynamic are performed until meeting convergence criterion. The process is repeated until reaching the end time. Interaction between fluids and structures problems can be considered uncoupled problems within both separate domains. In these problems assumption is formulated that a domain is driven by another, but the driven domain has no feedback effect on the driving domain. CFD model simulation provides the pressure on the structure by the fluid, and they are applied like load condition or as a boundary for the finite element analysis simulation of the configuration, where no feedback is done by the deflection into the CFD, which is called one-way fluid structure interaction. Many civil structures are excited by dynamic wind loading which is an example of one-way fluid structure interaction. In these cases, the structural motion and displacement have no appreciable effect on the driving wind loads, where the structure can be separately analyzed, or by treating the structure as uncoupled from the driving wind under certain loads in the range of interest [Iliev *et al.*, 2004; Van Zuijlen *et al.*, 2006; Gale, 2008; Hassler, 2009; Schmucker *et al.*, 2010; Benra *et al.*, 2011; Hansen, 2013].

### 4.2.2 Two-Way FSI

In two-way coupling the motion of the fluid flow influences the solid structure and in the same time the fluid flow is influenced by the reaction of the structural solid. During the beginning of the time step, convergence solutions of the fluid calculation produce forces acting on the solid structure. Next, the forces are interpolated to the structural mesh the same as in the one-way coupling and the solutions from the structural solver is determined with the fluid forces as boundary conditions. As a result the mesh is deformed according to the response of the structure. The values of the displacements are interpolated to the fluid mesh which results in deforming the fluid domain. The process is repeated until reaching the convergence between the force and displacement values below the limit that was previously determined [Onate and Garcia, 2001 and Raja, 2012]. When both the fluid and the structure are interacting in a system of feedback in some practical applications in the engineering area, the structural displacements generated by the fluid motion enhance the fluid forces, and this is called two-way fluid structure interaction. In this case often the amplitude of the deflection of the structure is large. The wind power plant is one example of this type of analysis [Van Zuijlen *et al.*, 2006; Forster, 2007; Razzaq *et al.*, 2010; Benra *et al.*, 2011; Liaghat, 2014].

In the general form, the FSI can be represented by the coupling both the equation of the motion of the structure and the fluid. The equation of the motion of the structure can be expressed as:

$$\mathbf{M}_s \ddot{\mathbf{u}} + \mathbf{D}_s \dot{\mathbf{u}} + \mathbf{K}_s \mathbf{u} = \mathbf{F}_s \quad (4.3)$$

where  $\mathbf{M}_s$  is the structural mass matrix,  $\mathbf{D}_s$  the structural damping matrix,  $\mathbf{K}_s$  the structural stiffness matrix,  $\mathbf{F}_s$  the applied load vector, and  $\mathbf{u}$  the nodal displacement vector where the dot denotes the time derivative. When the stagnant fluid is surrounding the oscillating structure, the fluid effects on the structure should be accounted for. While the structure is oscillating, the close fluid to the surface of the structure is starting to undergo motion in such a way that the structure becomes affected by additional fluid force  $\mathbf{F}_s$ . As a result **Equation (4.3)** represents the forced oscillation form, where  $\mathbf{F}_s$  is the fluid reaction on the structural movement, and the decomposition of the force into three parts acting in-phase with the displacement  $\mathbf{u}$  vector, the velocity  $\dot{\mathbf{u}}$  vector and the acceleration  $\ddot{\mathbf{u}}$  vector of the structure is possible [Bonisch *et al.*, 2008; Von, 2012; Hengstler, 2013].

The accuracy of the two-way coupling is obvious, especially in large deflection cases where the structural deformation influences the fluid field strongly. In strong two-way coupling, solutions are of second order time accuracy, and they are more stable. In one-way coupling conservation of energy at the interface is not guaranteed, but in two-way coupling is. There is a benefit of one-way coupling simulations that ends with significant lower computational time. The second benefit is that the fluid mesh has deformations without need to be calculated, which result in producing a constant quality of the mesh. The effects of FSI for the cases of totally or partially submerged body in a fluid flow with a free surface can't be accurate predicted especially in cases related to civil engineering, offshore engineering and naval architecture [Onate and Garcia, 2001 and Schmucker *et al.*, 2010].

### 4.3 Finite Element Models

The models of the segmental bridge deck are generated in ABAQUS once in CFD and another in CSD. The CFD model is with a dimension 2.6 m height and total width of 22 m as shown in **Figure 4.1.a**. The thickness is 0.01 m (should be very small so as to be treated as a 2D model). The flow domain size is 140 m length and 40 m height, the position of the deck model in the flow domain should be in a position so that to facilitate a proper area to show the vortex shedding in the downstream in addition to an appropriate area above and under the deck model to show the boundary layers around the deck with the separation points (see **Figure 4.1.b**). Material properties for the CFD model are assigned where the air density is assigned 1.29 kg/m<sup>3</sup> and the dynamic viscosity of the air is assigned 1.8E-05 Pa.s.

### 4.3 Finite Element Models

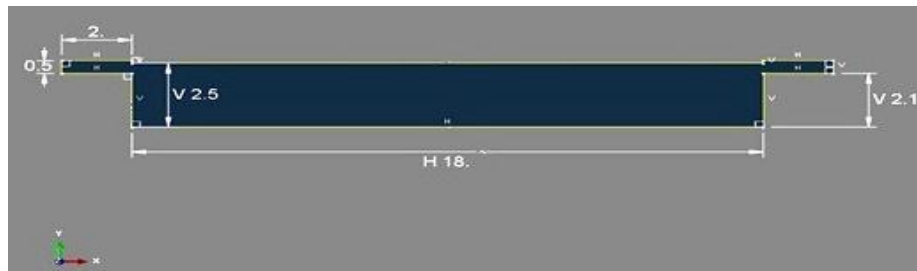


**Figure 4.1.a** Deck model dimensions

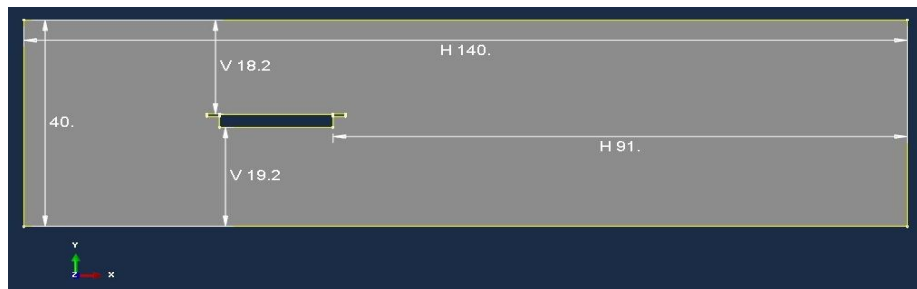


**Figure 4.1.b** Flow domain size



**Figure 4.1.c** The CSD model

The CFD model part is meshed using CFD element fluid family with FC3D8: A-8 node linear fluid brick. The deck wall assigned with 0.4 element size and the flow domain with 1 element size. The CSD model has the following material properties: concrete density is assigned  $2643 \text{ kg/m}^3$ , Young's modulus  $200\text{E}+08$  and the Poissons ratio 0.2 (see **Figure 4.1.c**). The role of the steel reinforcement is neglected for simplicity because the thickness of the CSD model is too small 0.01m and the reinforcement has no direct contact with the air. The CSD model part is meshed using 3D stress family with C3D8R: A-8 node linear brick reduced integration hourglass control.

A flow step with 100 seconds duration is created for the CFD model in addition to assigning predefined Spalarat-Allmaras model turbulence due to very large number of Reynolds number and or due to random oscillation of the time history curve of the kinetic energy dissipated, and

### 4.3 Finite Element Models

creating another dynamic implicit step with 100 seconds for the CSD model. The step time in each model must be the same, in addition to adding interaction with the same name in each model for the surfaces of interaction, also the important issue related to mesh generation is equality of the mesh size in each model. The job is created for the simulation of CFD model apart or one-way FSI approach, and another co-simulation job is generated for both the CFD and the CSD models together or two-way FSI approach.

#### 4.3.1 Boundary Conditions

Four boundary conditions are defined for the CFD and CSD models (**Figure 4.2**), fluid B.C for the inflow and far fields assigning the air speed value in the horizontal direction only (zero attack angle). The other two directions with zero magnitudes, fluid B.C for the outflow assigning zero pressure and fluid B.C for the front and back of the flow model with zero speed magnitude for the third direction perpendicular to the model (z-direction), and no-slip fluid B.C for the wall condition of the deck.

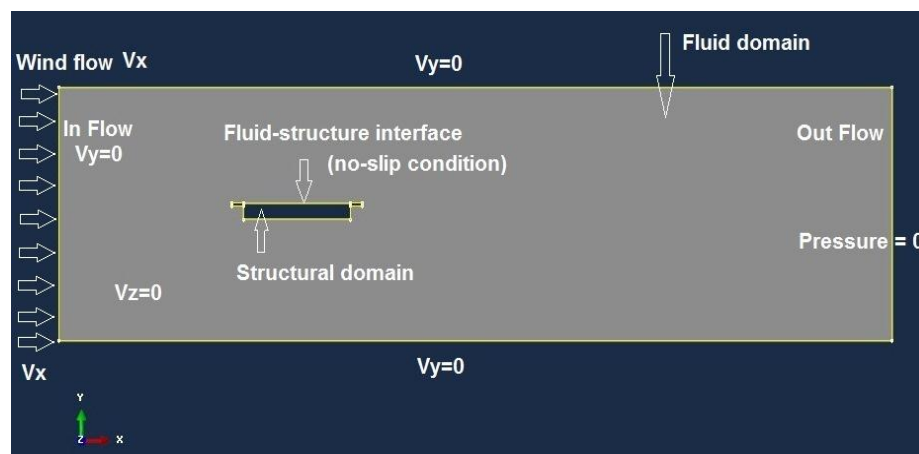


**Figure 4.2** Domains and fluid-structure interaction boundary conditions

A mesh size of 9943 elements would be utilized to mesh the CFD model. The mesh size of the deck in the structural domain should be the same as the mesh size of it in the flow domain at the interface so that to match or coincide. Depending on the desirable mesh size for the CFD model, the related mesh size of the CSD model was 357 elements (without refinement due to interface matching requirement (see **Figure 4.3.a** and **Figure 4.3.b**).

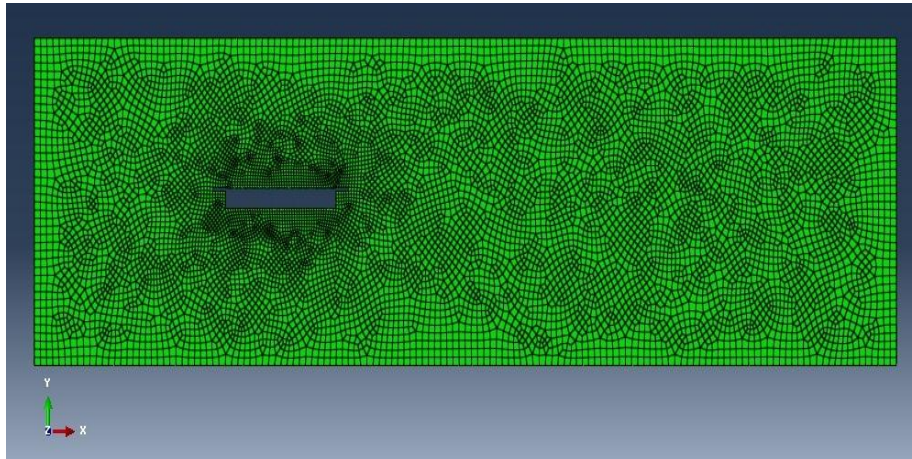


**Figure 4.3.a** CFD mesh size - 9943 elements

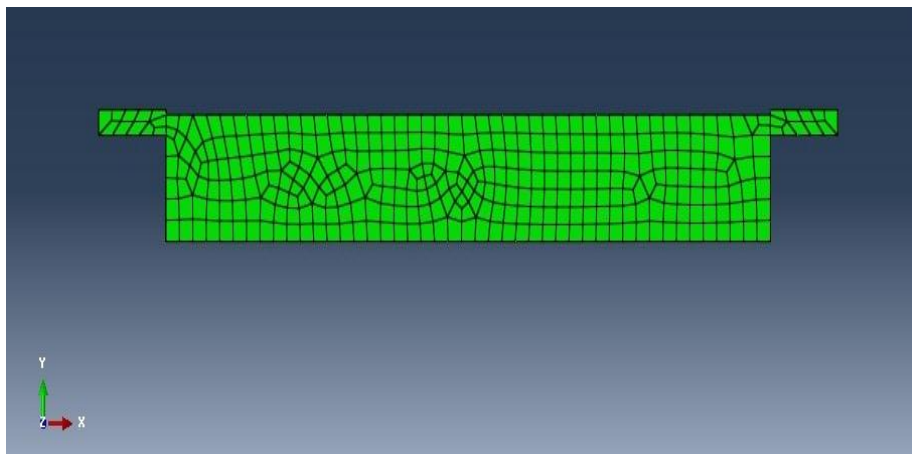


**Figure 4.3.b** CSD mesh size - 357 elements

## 4.4 Results and Discussion

### 4.4.1 Vortex Shedding Simulation

Generation of vortex shedding from the deck models exists with different patterns, and the simulations are considered at the time 100 seconds. When considering one-way FSI approach the vortex shedding for wind speed 1 m/s (see **Figure 4.4**) is generated and it is regular in periodic shedding from the tail of the deck, but for two-way FSI approach and for the same wind speed a simple vortex shedding exists with irregular shedding because the wind flow is affected by the feedback of the deck which disturbs the periodic shedding style of the vortices shed from the deck tail where the wind speed is not high (see **Figure 4.5**).

## 4.4 Results and Discussion

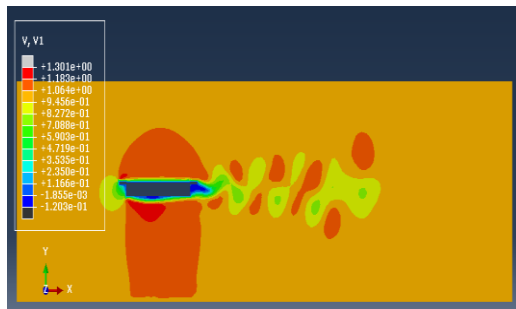


Figure 4.4 Vortex shedding one-way  $V=1$  m/s



Figure 4.5 Vortex shedding two-way  $V=1$  m/s

For wind speed 10 m/s a very good and efficient regular vortex shedding style from the deck exists for one-way FSI approach (see Figure 4.6) but for two-way FSI approach and for the same wind speed, the vortex shedding is generated with a different style which is an evidence of effect of the deck feedback (CSD simulation) on the surrounding wind flow, where increasing the wind speed increases the lift and drag forces as a result the disturbance in the vortices will be detected (see Figure 4.7).

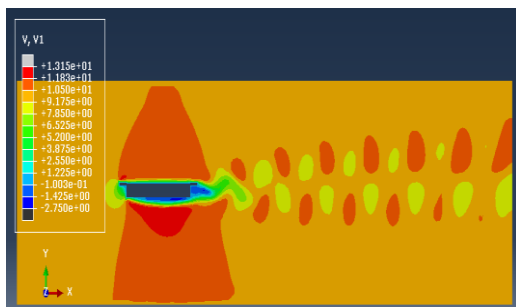


Figure 4.6 Vortex shedding one-way  $V=10$  m/s

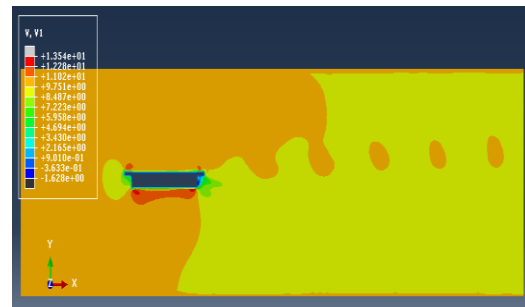


Figure 4.7 Vortex shedding two-way  $V=10$  m/s

While for wind speed 15 m/s another pattern of vortex shedding exists for one-way FSI approach which is affected by increasing the wind speed where it changes the shedding style and shape of the vortices (see Figure 4.8), but for two-way FSI approach and for the same wind speed the vortex shedding is generated but without a vanishing pattern, this happens because for higher wind velocities higher than the associated lock-in velocities leads to vanishing of the vortex shedding for a range velocities because the amplitudes of vibrations of the deck are increasing due to an increase in the lift and drag forces, hence the feedback of the deck on the wind flow increases (see Figure 4.9) and it is possible that the lock-in phenomenon and the vortex shedding generation restarts at higher wind velocities where this needs a very long duration simulation process and computationally is much costly.

## 4.4 Results and Discussion

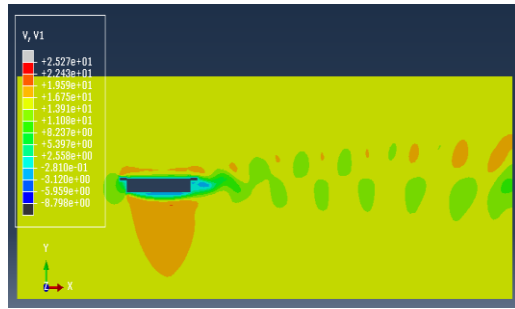


Figure 4.8 Vortex shedding one-way  $V=15$  m/s

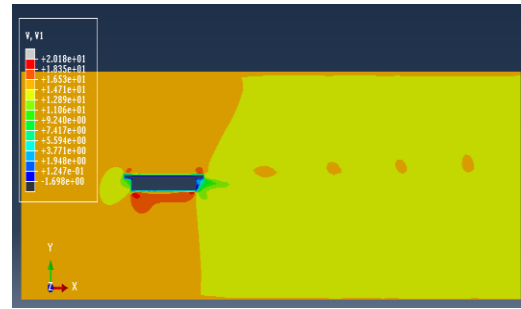


Figure 4.9 Vortex shedding two-way  $V=15$  m/s

### 4.4.2 Lift Forces

The lift forces are generated in the deck of the cable stayed bridge models with different values when assigning wind flow of multiple velocities (1 m/s, 5 m/s, 10 m/s and 15 m/s) first by considering one-way FSI approach in the simulation and the other by considering two-way FSI approach. Increasing the wind speed leads to increase in the lift forces generated in the deck models commonly in both approaches in a direct proportion. When the wind speed is 1 m/s, the time history of the lift forces in one-way FSI is showing a certain value with a stable situation without vertical periodic oscillation of the deck after 40 seconds, while for the same wind speed in two-way FSI, the lift forces have smaller values but showing a primary simple vertical periodic oscillation after 55 seconds (see Figure 4.10).

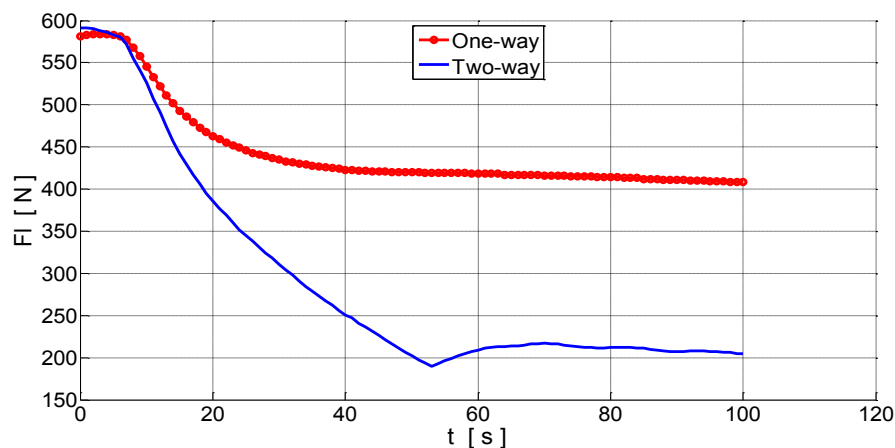
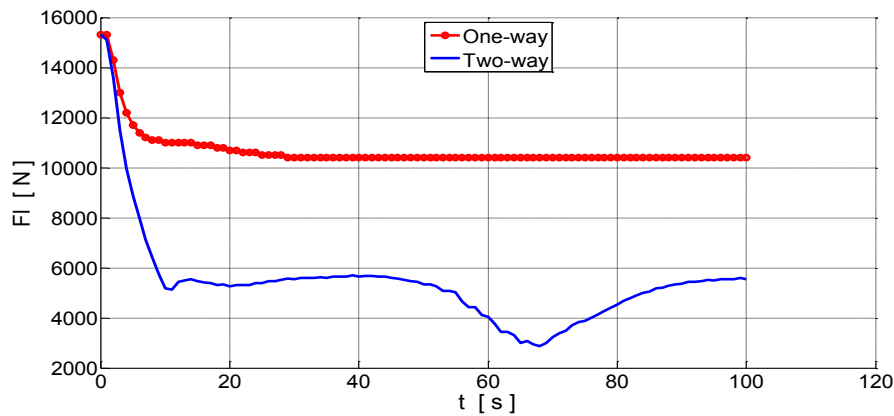


Figure 4.10 Time history of lift forces  $V=1$  m/s

When the wind speed increases to 5 m/s, the lift forces in one-way FSI increase in a high rate with a stable situation after 20 seconds without vertical periodic oscillation. For the same wind speed the lift forces are increasing with a high rate in two-way FSI with a better vertical periodic oscillation starting after 10 seconds (see Figure 4.11).



## 4.4 Results and Discussion



**Figure 4.11** Time history of lift forces  $V=5$  m/s

Increasing the wind speed to 10 m/s, the lift forces in one-way FSI are increasing with a high rate and the stability of the lift forces are obvious starting from 3 seconds without any vertical periodic oscillation, while for the same wind speed the lift forces in two-way FSI are increasing in a high rate too, but now the vertical periodic oscillatory behavior is much better seen starting from 5 seconds (see **Figure 4.12**).

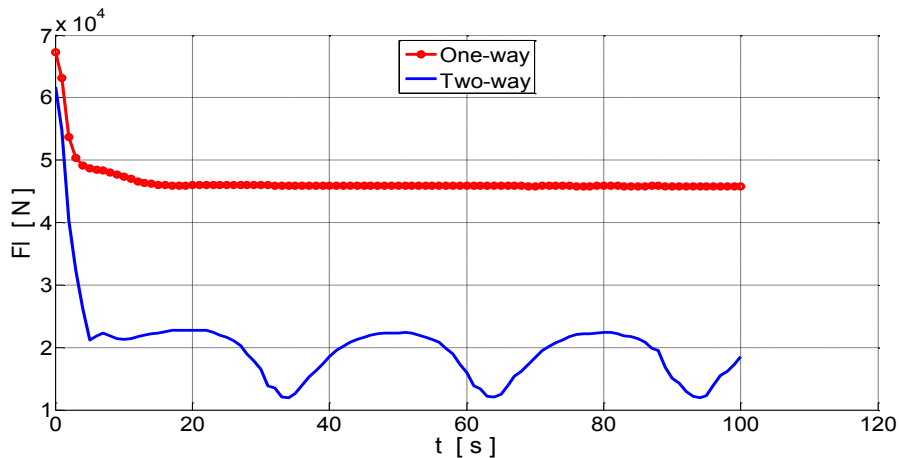


**Figure 4.12** Time history of lift forces  $V=10$  m/s

Now for the wind speed of 15 m/s, the lift forces for one-way FSI are increasing with a high rate and show stability without showing vertical periodic oscillation after 2 seconds, but in two-way FSI and for the same wind speed, the lift forces are increasing with a high rate exhibiting significant vertical periodic oscillation with bigger frequency after 3 seconds (see **Figure 4.13**).

## 4.4 Results and Discussion

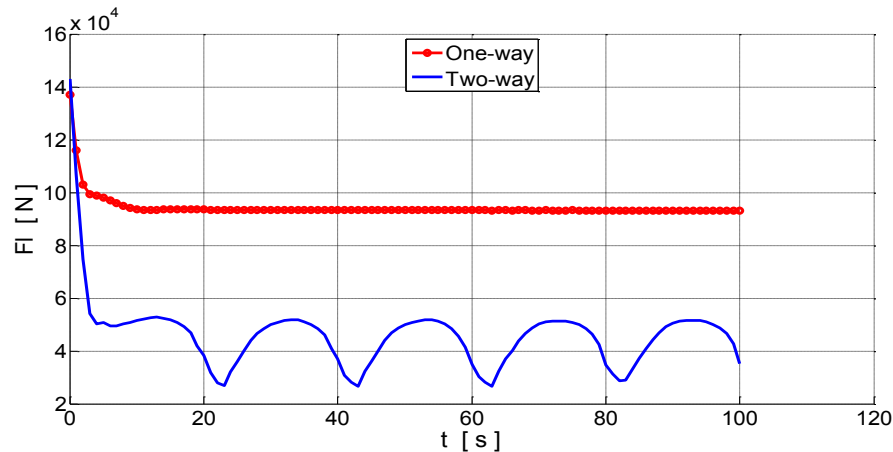


**Figure 4.13** Time history of lift forces  $V=15$  m/s

The difference in the lift forces between one-way and two-way approaches is due to kinetic energy dissipation in the latter approach which results in smaller values for lift forces. The results of the lift forces in one-way FSI is an evidence that this approach is not sufficient in detecting the actual VIV phenomenon, but the two-way FSI have a perfect ability in detecting it. This means that the amplitudes of the lift displacement in the deck are predicted with lower values of wind velocities, and thus the lock-in phenomenon is better predicted in earlier stages.

### 4.4.3 Drag Forces

For Drag forces, when one-way FSI approach is considered in the simulation process, the drag forces increase in a direct proportion but the pattern of the horizontal periodic vibration response of the deck models is not regular when the wind flow speed increases between (1 m/s to 15 m/s). When the wind speed value is 1 m/s, considering one-way FSI, the drag forces have a certain value with a stable horizontal periodic vibration starting after 5 seconds, but for two-way FSI and for the same wind speed, the drag forces have smaller values compared to previous approach, and the horizontal periodic vibration have a semi stable situation starting after 12 seconds and by time it is decreasing in a small rate (see **Figure 4.14**).

When the wind speed is increasing to 5 m/s, in one-way FSI, the drag forces are increasing in a large rate with a stable situation of horizontal periodic vibration but with a larger frequency for the amplitudes starting from the beginning of the wind excitation directly. While for two-way FSI and for the same wind speed, the drag forces are increasing with a high rate but still smaller than its values for the previous approach, in addition to creation of sudden changes in the amplitudes of the horizontal periodic vibration coinciding with the start of changes of vertical periodic vibrations after 45 seconds (see **Figure 4.15**), which means that the changes in

## 4.4 Results and Discussion

the frequency of the lift amplitudes leads to the change in the drag amplitudes in the same time.

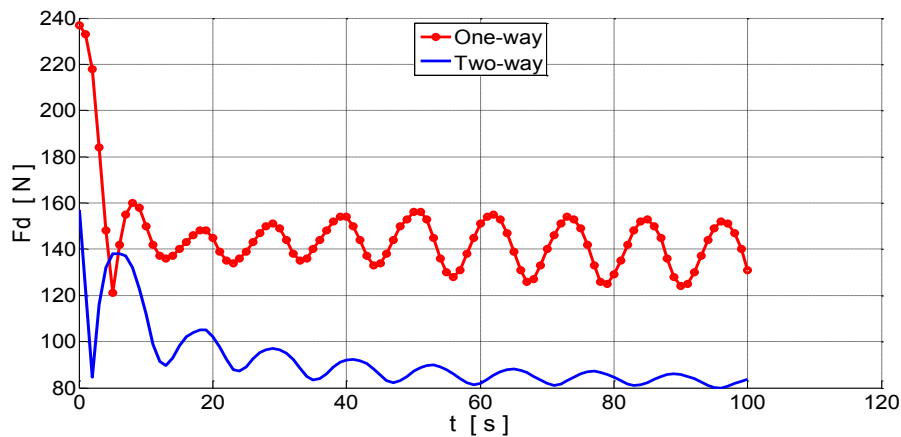


Figure 4.14 Time history of drag forces  $V=1$  m/s

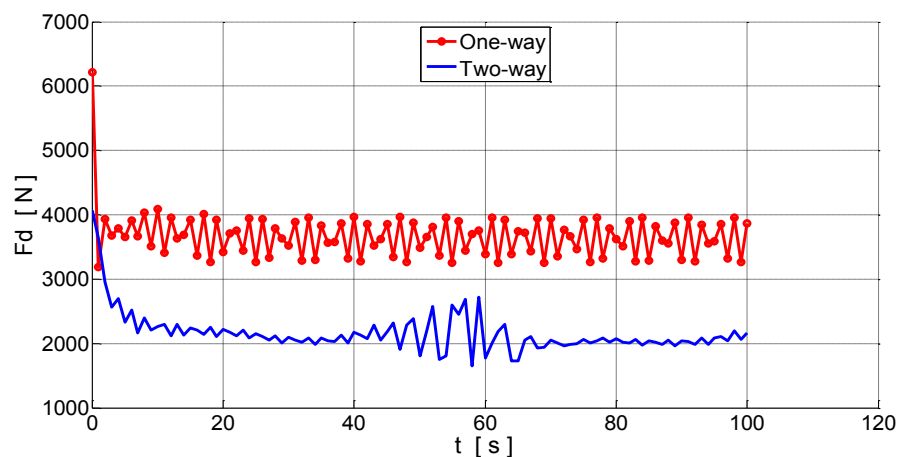
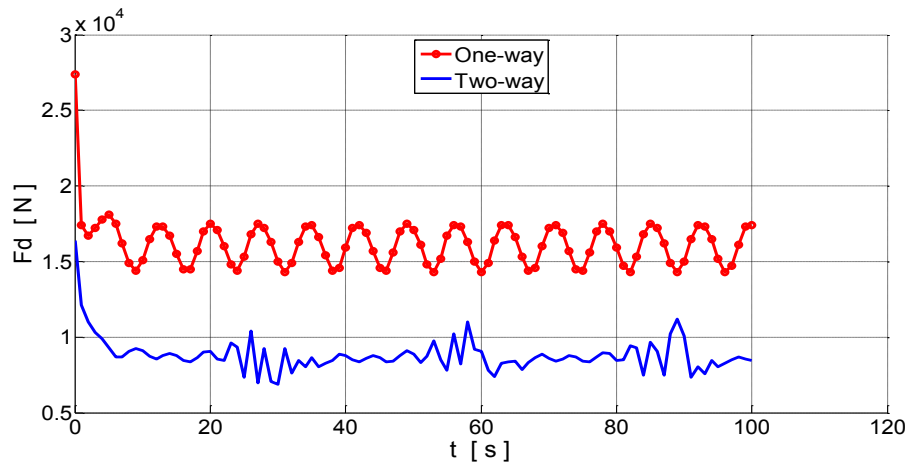


Figure 4.15 Time history of drag forces  $V=5$  m/s

Increasing the wind speed to 10 m/s, in one-way FSI, the drag forces are increasing in a large rate again with a stable situation of horizontal periodic vibration but with a smaller frequency for the amplitudes starting from the beginning of the wind excitation directly too. While for two-way FSI and for the same wind speed, the drag forces are increasing with a high rate but still smaller than its values for the one-way FSI approach, furthermore a creation of sudden changes in the amplitudes of the horizontal periodic vibration coinciding with the start of changes of vertical periodic vibrations after 25, 55 and 85 seconds (see **Figure 4.16**) which means that the changes in the frequency of the lift amplitudes leads to the change in the drag amplitudes in the same time, where in this case three times are obvious.

## 4.4 Results and Discussion



**Figure 4.16** Time history of drag forces  $V=10$  m/s

Continuous increase of wind speed to 15 m/s, and considering one-way FSI, the drag forces are increasing in a large rate again with a stable situation of horizontal periodic vibration but frequency for the amplitudes becomes bigger. While in two-way FSI and for the same wind speed, the drag forces are increasing with a high rate but still smaller than its values in one-way FSI approach, and it is worthy to mention that a creation of sudden changes in the amplitudes of the horizontal periodic vibration are coinciding with the start of changes of vertical periodic vibrations after 20, 40, 60, 80 and 100 seconds (see **Figure 4.17**) which means that the changes in the frequency of the lift amplitudes leads to the change in the drag amplitudes in the same time for five times along duration of 100 seconds of wind excitation.

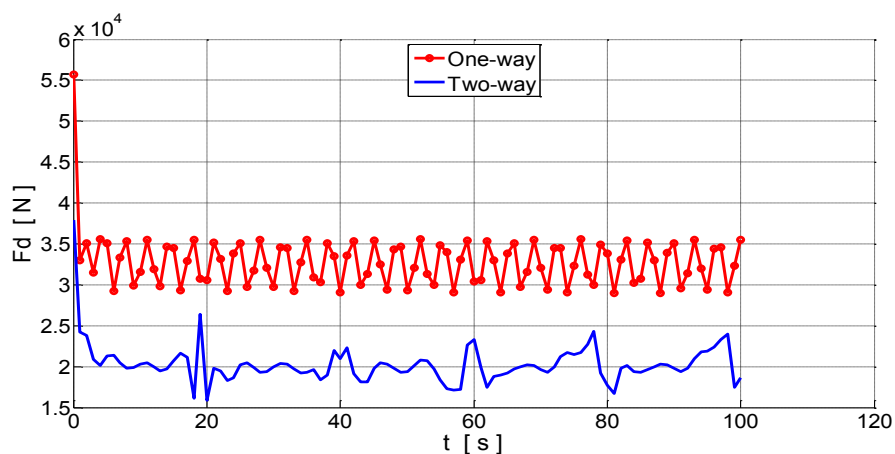


**Figure 4.17** Time history of drag forces  $V=15$  m/s

The difference in the drag forces between one-way and two-way approaches is due to kinetic energy dissipation in the latter approach which results in smaller values for drag forces. It is obvious that the lift forces value in one-way FSI approach is three times the drag forces value approximately for all the wind speed cases, compared to two-way FSI approach the lift forces

## 4.4 Results and Discussion

value is twice the drag forces value, the reason is the same which is related to the kinetic energy dissipation.

### 4.4.4 Kinetic Energy

The vibrational kinetic energy of the system is calculated from the simulation of vortex-induced vibration of the deck models of a long span bridge due to a wind excitation in ABAQUS for both the on-way and two-way FSI approaches. The results are for duration of 50 seconds. It is obvious that kinetic energy for the one-way approach is increasing from 4850 N.m to 4975 N.m and after this stage it becomes stable approximately till  $t = 20$  seconds, while for the two-way approach this value is not stable in the beginning 20 sec with a decreasing value from 4800 N.m and after that it becomes stable for the remain 30 seconds with a value of 4525 N.m (see **Figure 4.18**). This means that the kinetic energy of the vibrating system in one-way approach is still the same value approximately because the effect of the structural model of the deck on the surrounding wind has not been considered and no exchange of energy exists from the deck to the wind, so the overall kinetic energy remains high and stable compared to that in two-way approach, but due to exchange of kinetic energy between the deck and the wind together in two-way approach and large dissipation of the kinetic energy in this process, the overall kinetic energy is less than of it in the on-way approach.

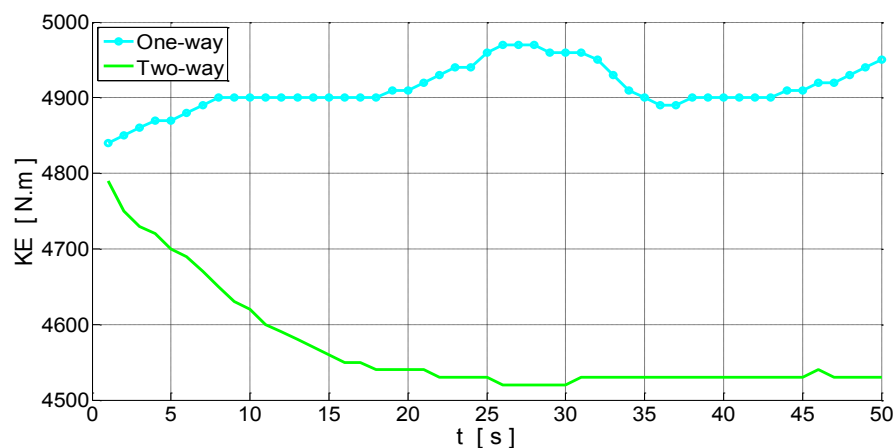


**Figure 4.18** Time history of the simulations kinetic energy

### 4.4.5 Lock-In Phenomenon

At lock-in region, the vortex shedding is generated more efficiently. For one-way FSI approach this phenomenon starts to appear clearly at wind speed of 11.5 m/s with regular periodic and stable shape of the vortices shedding from the tail of the deck. The simulations of the simulations are captured at the time histories 11.5 m/s, 11.7 m/s and 11.9 m/s. When

## 4.4 Results and Discussion

the two-way FSI approach is considered, the vortex shedding generates with irregular style due to the movement of the deck and its feedback on the surrounding wind flow for all wind speed cases. The similarity in vortex shedding style with respect to the shape of the vortices and the periodic pattern for all wind speed values for both the one-way and two-way approaches is an indication of the lock-in phenomenon where the frequency of vortex shedding remains constant approximately (see **Figure 4.19**).

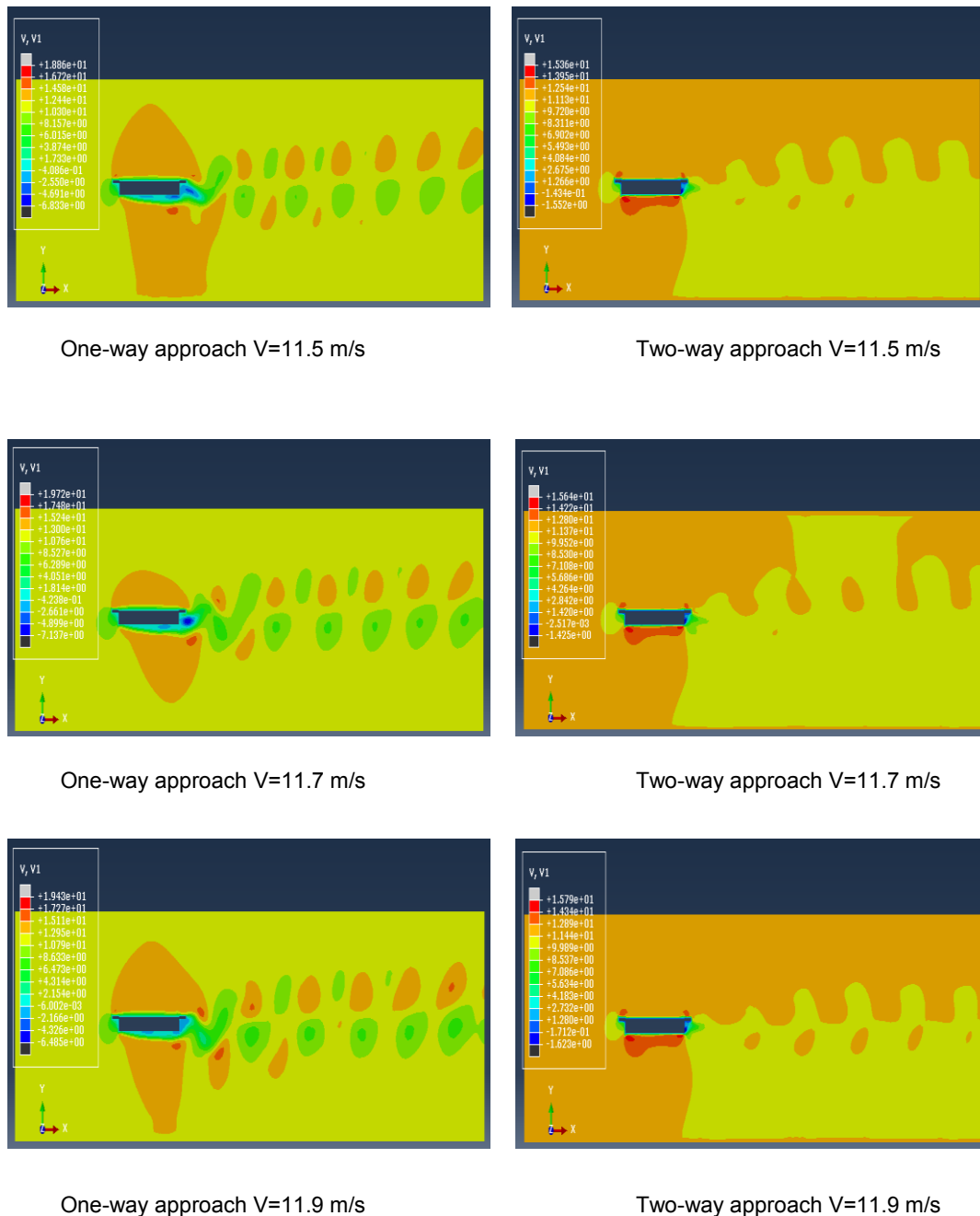


**Figure 4.19** Vortex shedding at Lock-in region

## 4.4 Results and Discussion

When only the one-way FSI approach is considered in the simulation, the lock-in phenomenon exists at the wind speed of 11.5 m/s approximately but it is not quite regular and the associated vortex shedding frequencies are near to 1.5 Hz till wind speed magnitude of 12 m/s, and after that range the vortex shedding frequency begins to increase in magnitude in a linear proportion with the wind speed as shown in **Figure 4.20**.

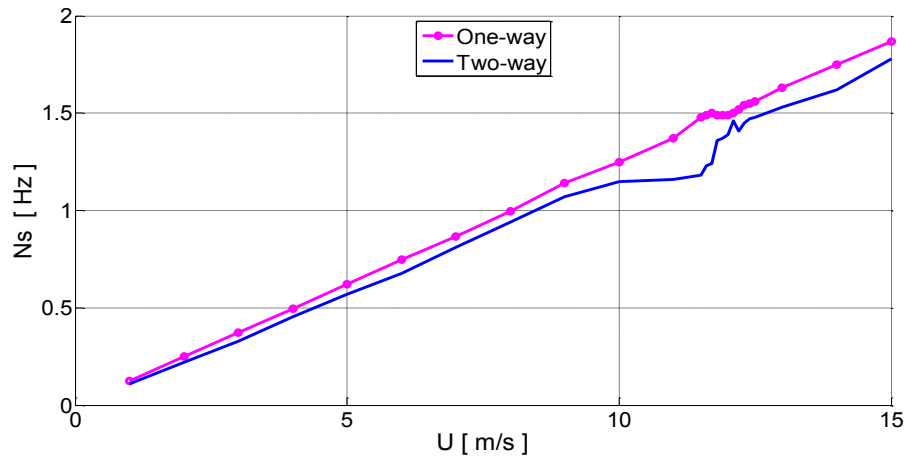


**Figure 4.20** Wind speed versus Vortex shedding frequency - Lock-In phenomenon

When considering the two-way FSI approach, the same phenomenon starts to appear at the wind speed magnitude of 10 m/s and ends at 11.5 m/s in a regular path compared to the previous approach, while the associated vortex shedding frequencies are 1.18 Hz. The vortex shedding frequency after the lock-in region increases rapidly to 1.45 Hz and starts to undertake a linear proportion approximately. This indicates that the FSI has an important and effective role in detecting the actual region where the lock-in phenomenon starts to generate and determines the associated shedding frequencies for lower natural frequencies of the system.

### 4.4.6 Lift Coefficient

The results of the relation between the Reynolds number  $Re$  and the lift coefficient  $C_l$  for the deck model when the wind speed changes from 1 m/s to 15 m/s when considering one-way FSI approach, the lift coefficient reaches a maximum value of 0.4 at Reynolds number value of  $0.75E+06$ , and the value of the lift coefficient is unstable until the Reynolds number magnitude  $0.9E+06$ , after that the relation becomes stable approximately for a lift coefficient value -0.4 without appreciable changes in the value of the lift coefficient (see **Figure 4.21**).

## 4.4 Results and Discussion

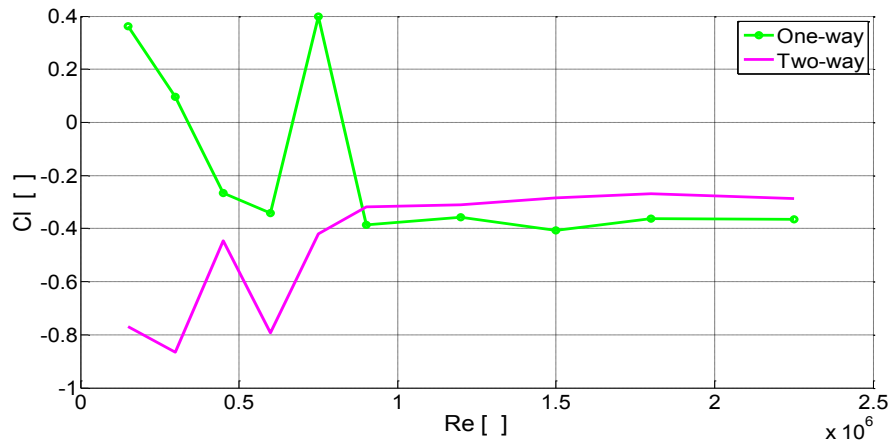


Figure 4.21 Reynolds number versus lift coefficient

The results of the relation between the Reynolds number and the lift coefficient when taking in account the two-way FSI approach, show that the maximum value of the lift coefficient is -0.3 begins from the Reynolds number value  $0.9E+06$  and in the same way as previous approach it is unstable until the latter value of the Reynolds number and becomes stable after that point.

### 4.4.7 Drag Coefficient

The results of the relation between the Reynolds number  $Re$  and the drag coefficient  $C_d$  for the deck model when the wind speed changes from 1 m/s to 15 m/s when considering one-way FSI approach, the drag coefficient reaches a maximum value of 0.023 at Reynolds number value of  $1.5 E+06$ , and the value of the drag coefficient is stable at 0.02 approximately (see Figure 4.22).

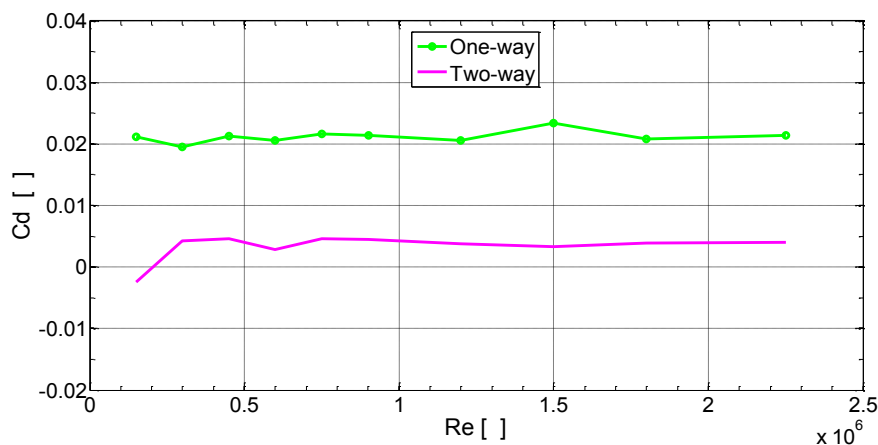


Figure 4.22 Reynolds number versus drag coefficient



## 4.4 Results and Discussion

While the relation between the Reynolds number and the drag coefficient when the two-way FSI approach is used, show that the maximum value of the lift coefficient is 0.005 begins from the Reynolds number value  $4.0E+05$  and it becomes stable starting from Reynolds number value  $0.8E+06$  approximately.

### 4.4.8 Reynolds Number

The Reynolds number  $Re$  calculations in each approach have been determined for multiple wind velocities supporting on the results of the simulations in ABAQUS in addition to lift and drag coefficients (see **Table 4.1**).

**Table 4.1**

Reynolds number versus lift and drag coefficients for multiple wind velocities

Wind speed m/s	Reynolds number one-way	Reynolds number two-way	Lift coefficient One-way	Lift coefficient two-way	Drag coefficient one-way	Drag coefficient two-way
1	1.50E+05	1.50E+05	0.3625	-0.77	0.0212	-0.0024
2	3.00E+05	3.00E+05	0.097	-0.866	0.01955	0.0042
3	4.50E+05	4.50E+05	-0.267	-0.445	0.0213	0.0046
4	6.00E+05	6.00E+05	-0.3405	-0.792	0.0206	0.00285
5	7.51E+05	7.51E+05	0.398	-0.419	0.0216	0.00455
6	9.01E+05	9.01E+05	-0.386	-0.317	0.0214	0.0045
8	1.20E+06	1.20E+06	-0.3585	-0.311	0.0206	0.0038
10	1.50E+06	1.50E+06	-0.4075	-0.285	0.02335	0.00325
12	1.80E+06	1.80E+06	-0.362	-0.269	0.0208	0.00385
15	2.25E+06	2.25E+06	-0.365	-0.288	0.0214	0.00405

### 4.4.9 Strouhal Number

The calculations of the Strouhal number  $S_t$  value for the deck models is between 0.322 and 0.324 for the one-way FSI approach, while for the two-way FSI approach this value is between 0.285 and 0.308 (see **Table 4.2**). The relation between the Reynolds number and the Strouhal number for the deck model when considering many cases of wind velocities for both approaches is stable and linear approximately for one-way FSI approach but it is not stable and nonlinear when adopting two-way FSI approach (see **Figure 4.23**).

#### 4.4 Results and Discussion

This result proves the fact that the Strouhal number is depending on the Reynolds number and it is nearly with a value of 0.2 for a large range of Reynolds number, and the FSI concept is better supporting this fact, this by comparing the results when considering two-way FSI approach, where the Strouhal number is between (0.28-0.29) approximately until Reynolds number value of (1E+06) but the Strouhal number value is constant at 0.32 until Reynolds number value of 2.3E+06 when considering one-way FSI approach.

**Table 4.2**

Strouhal number versus vortex shedding frequency for multiple wind velocities

Wind speed m/s	Shedding frequency one-way Hz	Shedding frequency two-way Hz	Strouhal number one-way	Strouhal number two-way
1	1.241E-01	1.105E-01	3.227E-01	2.873E-01
2	2.490E-01	2.208E-01	3.237E-01	2.870E-01
3	3.733E-01	3.292E-01	3.236E-01	2.853E-01
4	4.962E-01	4.549E-01	3.225E-01	2.957E-01
5	6.203E-01	5.712E-01	3.225E-01	2.970E-01
6	7.472E-01	6.758E-01	3.238E-01	2.928E-01
8	9.978E-01	9.415E-01	3.243E-01	3.060E-01
10	1.248E+00	1.154E+00	3.244E-01	3.000E-01
12	1.492E+00	1.386E+00	3.232E-01	3.003E-01
15	1.865E+00	1.777E+00	3.233E-01	3.080E-01

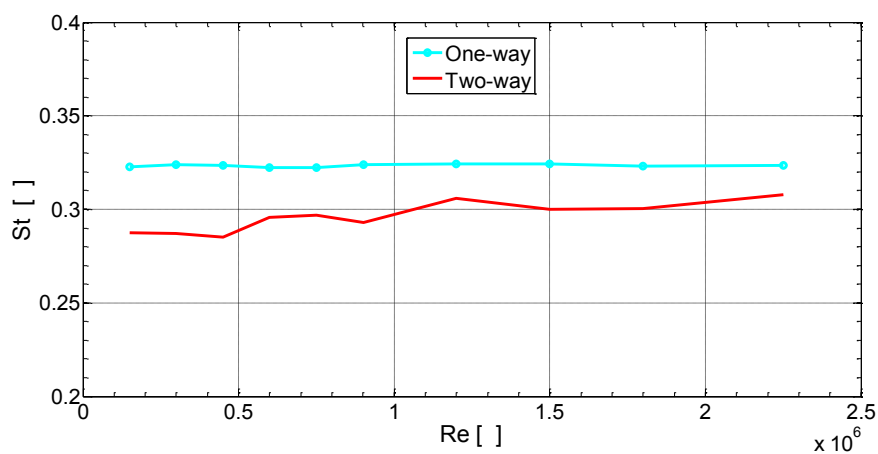


**Figure 4.23** Reynolds number versus Strouhal number

## 4.5 Validation of The FSI Models

It is essential to accurately simulate the FE models and this depends on verification of the numerical models through a comparison process against analytical solutions and or if it is possible to compare it against experimental data.

### 4.5.1 Simiu and Scanlan Benchmark

The results of the lock-in phenomenon determined from ABAQUS simulations in both one-way FSI approach and two-way FSI approach are compared with the compiled numerical results obtained by Simiu and Scanlan. The lock in phenomenon simulation using two-way FSI approach is better represents the actual phenomenon this by validation with the results obtained by Simiu and Scanlan (see **Figure 4.24**).

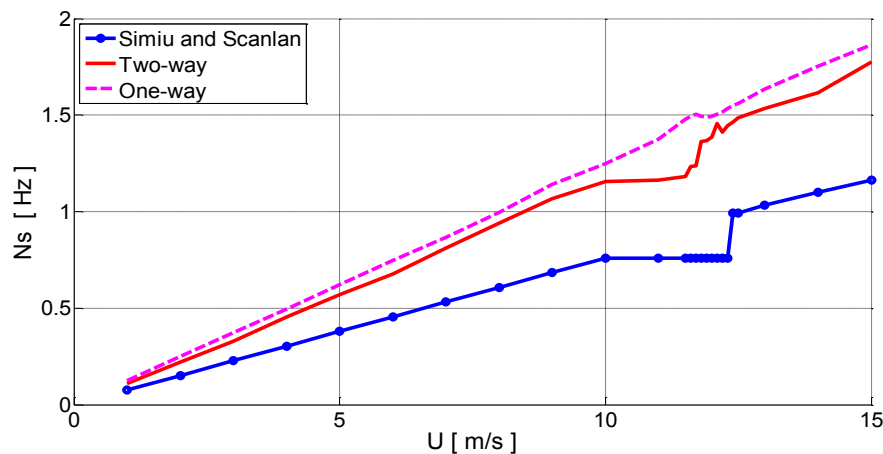


**Figure 4.24** Wind speed versus vortex shedding frequency- Lock-in phenomenon validation

Where the period of equal vortex shedding frequencies is greatly similar compared to the region of equal vortex shedding frequencies in the one-way FSI approach, where the start of the phenomenon in one-way approach is at wind speed 11.5 m/s till 12 m/s, but for two-way approach is starting from wind speed of 10 m/s till 11.5 m/s. This indicates the importance of the two-way FSI approach in simulating the generation of lock-in phenomenon as a result the vortex shedding induced vibration in the deck of the long span bridges can be determined more efficiently and predicted for earlier and wider range of wind velocities in addition to considering lower natural frequencies of the system which enhances the safety of the structure against the VIV.

### 4.5.2 Flat Plate Model (Munson and Co-authors) Benchmark

Another validation parameter is the drag coefficient  $C_d$  for the deck model for different Reynolds number values, where the main effective parameter is the wind speed changes from 1 m/s to 15 m/s. The benchmark of validation for  $C_d$  is the results of a flat plate model used by Munson and co-authors. The  $C_d$  results obtained in the flat plate model show that this value is unstable until Reynolds number of  $7.5E+05$  where  $C_d$  value is 0.08 and becomes stable in the region between 0.002 and 0.085 approximately but the  $C_d$  value is 0.02 for one-way FSI approach and it is 0.005 for two-way FSI approach, which means that there is a very good approximation between the results specifically between the benchmark and the two-way FSI approach (see **Figure 4.25**).

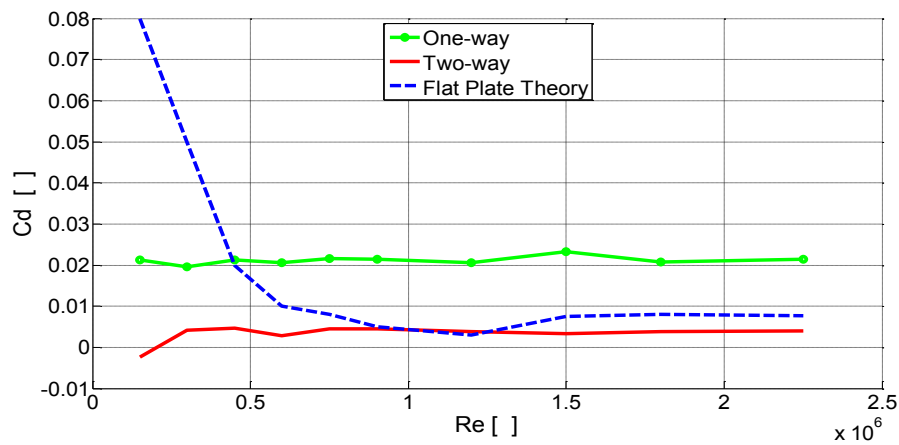


**Figure 4.25** Reynolds number versus drag coefficient validation



# Chapter 5

## Control Efficiency Optimization of Multiple Tuned Mass Dampers

### 5.1 Tuned Mass Damper (TMD)

The concept of TMD application dates back to the 1940s [Den Hartog, 1947]. This device is a linear dynamic vibration absorber system, consists of a secondary mass suspended via a viscous damper and a spring from a point on the main structure. It is tuned to a certain structural frequency of the structure such as a bridge in order to, when excited, the damper will resonate out of phase with the motion of the bridge, i.e., the TMD mass oscillates in the opposite direction of the main structure. Nowadays, establishment of this system succeeded in reducing wind-induced vibrations in many structural systems due to their particularity, where they need less construction and maintenance cost, in addition to that their operation is easy when used in the mechanical and civil engineering systems [Tang, 1997; Webster and Vaicaitis, 2003; Thamasungkeeti, 2009; Fujino *et al.*, 2010; Kumar, 2011; Miyata, 2003; Mishra, 2011; Shetty *et al.*, 2013; Wang *et al.*, 2014]. These devices are most effective when positioned at places of highest amplitudes. Therefore, considering this feature supplies the opportunity for energy dissipation through the damper inertia force acting on the main system. There are two main functions carried out by the TMD system, firstly it decreases the resonant response of the main structure, and secondly, increases the overall damping of the structure by the dashpot attached to, supplying additional source of energy dissipation. The modal damping is affected by the mass ratio within low frequency ratio range, and this effect almost finishes in high frequency ratio cases. The damping ratio has a great effect on the response of cable stayed bridges, and it is emphasized that under a particular combination of mass ratio, frequency ratio and the difference in the modal damping ratios, the effect of non-classical damping is highly important [Chen and Kareem, 2003; Huang, 2006; Abdel Raheem and Hayashikawa, 2008; Caruso *et al.*, 2009; Samani, 2010; Huang, 2011; Guo, 2012; Huang *et al.*, 2012; Casalotti *et al.*, 2013; Behrens *et al.*, 2013; Tran, 2014; Wen *et al.*, 2015].

## 5.2 Multiple Tuned Mass Dampers (MTMDs)

---

### 5.1.1 Energy Dissipation Mechanism

FSI between the exciting wind and the long span bridge generates aerodynamic instabilities. As a result the bridge deck would be prone to vertical and torsional vibrations. The deck motion is due to feeding energy into the bridge system by the the wind forces during one cycle of oscillation. The energy is exchanged by the phase shift between the vertical and the torsional vibrations and it counteracts the energy absorption by structural damping of the bridge. When the structural damping of the bridge is sufficiently low which can't dissipate these vibrations, the application of TMD becomes one of the solutions to suppress these vibrations and boost the structural damping of the bridge system [Tsai and Lin, 1993; Lin *et al.*, 2000; Gua *et al.*, 2002; Chen and Kareem, 2003; Chen and Cai, 2004]. The energy dissipation mechanism starts when the bridge deck vibrates, with the presence of the TMD, this device would be excited by the motion of the deck. When the mass of the damper moves in a certain direction, as the movement of the deck would be toward the opposite direction, hence the damping of the deck vibration is accomplished. The kinetic energy of the bridge structure transfers into the TMD system where its viscous damper absorbs it. In order to attain the most efficient energy absorbing rate, the natural period of the TMD is tuned to the natural period of the bridge system. This is why it is called (Tuned Mass Dampers), so the strategy of TMD application is attempting to dissipate the energy responsible of feeding the vibration. The viscous damper of the TMD should be adjusted to optimum value so that to maximize absorption of the energy [Zivanovic *et al.*, 2005; Feldmann and Heinemeyer, 2007; Andersson *et al.*, 2013; Xing *et al.*, 2014].

## 5.2 Multiple Tuned Mass Dampers (MTMDs)

The performance of TMD application in long span bridges is sensitive to the difference of frequency ratios between the TMD and the bridge structure, even when optimally designed, leads to serious performance deterioration this when the dynamic characteristics of the structure are different from those used to accomplish its optimum design. This can be overcome by the use of MTMDs. One of the important parameter for MTMDs is the mass distribution to reduce effectively the dynamic response of a main system. When the mass distribution is controlled along with other design parameters like damping ratio, frequency range, number of dampers, the control of the main system response is achieved. To increase the robustness of the vibration control system to various uncertainties in the structure, the use of more than one TMD is an effective solution, where MTMDs have distributed natural frequencies around the controlled mode of vibration [Lin *et al.*, 1999; Patil, 2010; Samani, 2010; Bandivadekar and Jangid, 2012; Wang *et al.*, 2014]. Adopting wide frequency band

### 5.3 Concept of TMD Using Two-Mass System

---

width makes it more robust and less sensitive to the change of the frequency ratio than using TMD [Igusa and Xu, 1994], in addition they are suggested to mitigate the vertical and torsional vibrations and to boost the aerodynamic stability of the long span bridges, which permits to control of more than one mode of a multi degree of freedom (MDOF) structure by tuning each TMD to the corresponding vibration mode of the main structure, or by tuning the TMDs to frequencies close to a certain mode of the system. Though, in spite of their higher effectiveness and robustness compared to single TMDs, the use of MTMDs encounters lack capabilities of real time retuning, consequently their adaptation to frequency varying excitation is very hard. The optimum TMD system for a certain structure is that one which minimizes the expected vibrations amplitudes. Practically, the design of a TMD begins by setting the value of the mass ratio, usually set within 1% to 10% [Warburton and Ayorinde, 1980]. The selection of this parameter value depends on the space availability to place the TMDs. Despite the fact that use of high mass ratio values aid to further decrease the vibration amplitudes, it may not be reasonable or economic because additional weight of the TMDs necessitates strengthening other structural elements. As soon as the value of the mass ratio has been elected, other design parameters such as frequency ratio and damping coefficients of the viscous dampers of the TMDs require to be assigned [Chen and Xiang, 1998; Gua *et al.*, 2001; Lin and Cheng, 2001; Lee and Li, 2005; Karmakar *et al.*, 2012; Estrad and Hong, 2015].

### 5.3 Concept of TMD Using Two-Mass System

The equation of motion for primary mass as shown in **Figure 5.1** is:

$$(1 - \mu)\ddot{u} + 2\xi\omega m\dot{u} + \omega^2 u = \frac{p}{m} - \mu\ddot{u}_d \quad (5.1)$$

$\mu$  is defined as the mass ratio, 
$$\mu = \frac{m_d}{m} \quad (5.2)$$

where  $m_d$  is the mass of the damper and  $m$  is the primary mass.

$$\omega^2 = \frac{k}{m} \quad (5.3)$$

$$c = 2\xi\omega m \quad (5.4)$$

$$c_d = 2\xi_d\omega_d m_d \quad (5.5)$$

where  $\dot{u}$  is the velocity,  $\ddot{u}$  is the acceleration,  $\xi_d$  is the damping ratio of the mass damper  $\omega_d$  is the natural frequency of the mass damper,  $\xi$ ,  $\omega$ ,  $c$ ,  $k$  are the damping ratio, natural frequency, damping coefficient and stiffness of the primary mass respectively.



### 5.3 Concept of TMD Using Two-Mass System

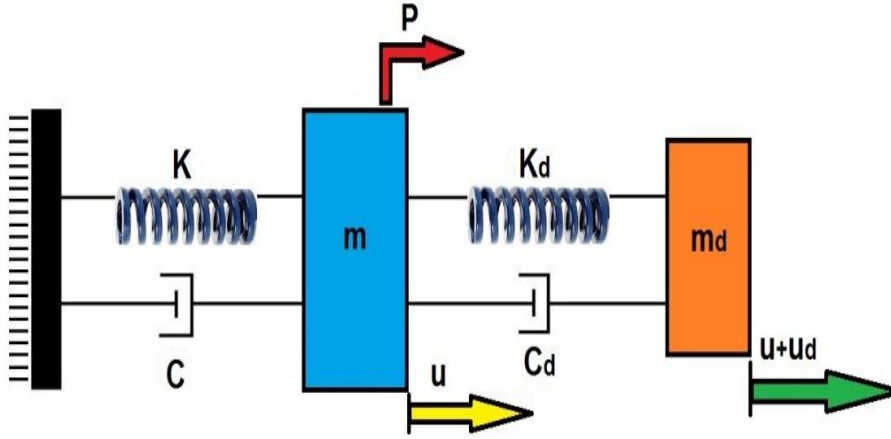


Figure 5.1 TMD attached to the primary mass

The equation of motion for tuned mass is given by:

$$\ddot{u}_d + 2\xi_d\omega_d\dot{u}_d + \omega_d^2u_d = -\ddot{u} \quad (5.6)$$

The purpose of adding the mass damper is to control the vibration of the structure when it is subjected to a particular excitation. The mass damper is having the parameters; the mass  $m_d$ , stiffness  $k_d$ , and damping coefficient  $c_d$ . The damper is tuned to the fundamental frequency of the structure such that:

$$\omega_d = \omega \quad (5.7)$$

$$k_d = \mu k \quad (5.8)$$

The primary mass is subjected to the following periodic sinusoidal excitation

$$p = \hat{p} \sin \omega t \quad (5.9)$$

then the response is given by

$$u = \hat{u} \sin(\omega t + \delta_1) \quad (5.10)$$

$$u_d = \hat{u}_d \sin(\omega t + \delta_1 + \delta_2) \quad (5.11)$$

where  $\hat{u}$ ,  $u$  and  $\delta$  denote the displacement amplitude, response and phase shift of the primary mass simultaneously,  $\hat{u}_d$ ,  $u_d$  are displacement amplitude and response of the damper respectively. The critical loading scenario is the resonant condition. The solution for this case has the following form:

## 5.4 Equation of Motion

---

$$\hat{u} = \frac{\hat{p}}{mk} \sqrt{\frac{1}{(1 + (2\xi/\mu + 1/2\xi_d)^2)}} \quad (5.12)$$

$$\hat{u}_d = (1 + 2\xi_d)\hat{u} \quad (5.13)$$

$$\tan \delta_1 = -\left(\frac{2\xi}{\mu} + \frac{1}{2\xi_d}\right) \quad (5.14)$$

$$\tan \delta_2 = -\frac{\pi}{2} \quad (5.15)$$

The above expression shows that the response of the tuned mass is 90° out of phase with the response of the primary mass. This difference in phase produces the energy dissipation contributed by the damper inertia:

$$\hat{u} = \frac{\hat{p}}{k} \left(\frac{1}{2\xi}\right) \quad (5.16)$$

$$\delta_1 = -\frac{\pi}{2} \quad (5.17)$$

To compare these two cases, we can express **Equation (5.12)** in terms of an equivalent damping ratio:

$$\hat{u} = \frac{\hat{p}}{k} \left(\frac{1}{2\xi_e}\right) \quad (5.18)$$

where

$$\xi_e = \frac{\mu}{2} \sqrt{\frac{1}{1 + (2\xi/\mu + 1/2\xi_d)^2}} \quad (5.19)$$

**Equation (5.19)** shows the relative contribution of the damper parameters to the total damping. Increasing the mass ratio magnifies the damping. However, since the added mass also increases, so there is a practical limit on it.

## 5.4 Equation of Motion

Based on the classical method of flutter analysis and relating to the vertical bending and torsion of a bridge, the frequencies of the TMDs are tuned to the neighborhood of the flutter frequency so as to increase the critical flutter wind speed as shown in **Figure 5.2**.

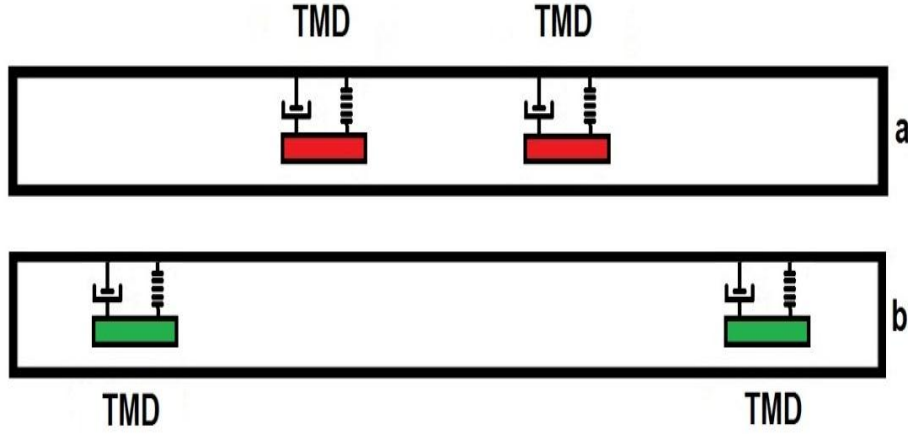


**Figure 5.2** Location of TMDs for suppressing a- Vertical vibration and b- Torsional vibration

The equation of motion of multi-degree of freedom structure TMDs which consists of structure, TMD1 and TMD2 motion attached to  $h^{th}$  and  $k^{th}$  degree of freedom subjected to wind load is given in **Equation (5.20)** besides **Equation (5.21)** presents the modal analysis expressions.

$$m\ddot{u} + c\dot{u} + ku = p \quad (5.20)$$

$$u = \begin{Bmatrix} u_s \\ u_{t1} \\ u_{t2} \end{Bmatrix} = Ax = \begin{bmatrix} \Phi_1 & \dots & \Phi_n & 0 & 0 \\ 0 & \dots & 0 & 1 & 0 \\ 0 & \dots & 0 & 0 & 1 \end{bmatrix} \begin{Bmatrix} x_s \\ x_{t1} \\ x_{t2} \end{Bmatrix} \quad (5.21)$$

where  $u_s$  is a vector of absolute displacement of the main structure;  $u_{t1}$  and  $u_{t2}$  are absolute displacement of TMD1 and TMD2 respectively;  $x_s$  is a vector of generalized-coordinate displacement of the main structure;  $x_{t1}$  and  $x_{t2}$  are generalized displacement of TMD1 and TMD2 respectively; and  $\Phi_n$  is an  $n^{th}$  natural mode shape of the main structure without TMD, normalizing such that modal mass = 1.

Substitute **Equation (5.21)** into **Equation (5.20)** and pre-multiply with transpose of  $A$  gives the equation of motion in modal coordinates, as shown in in **Equation (5.22)**.

$$M\ddot{x} + C\dot{x} + Kx = P \quad (5.22)$$

$$M = \begin{bmatrix} 1 & \dots & 0 & 0 & 0 \\ \vdots & \ddots & \vdots & \vdots & \vdots \\ 0 & \dots & 1_n & 0 & 0 \\ 0 & \dots & 0 & m_{t1} & 0 \\ 0 & \dots & 0 & 0 & m_{t2} \end{bmatrix} = diag(1,1, \dots, 1_n, m_{t1}m_{t2}) \quad (5.23)$$

## 5.4 Equation of Motion

$$C = A^T c A$$

$$= \begin{bmatrix} \Phi_1^T C_s \Phi_1 & \cdots & 0 & 0 & 0 \\ \vdots & \ddots & \vdots & \vdots & \vdots \\ 0 & \cdots & \Phi_n^T C_s \Phi_n & 0 & 0 \\ 0 & \cdots & 0 & 0 & 0 \\ 0 & \cdots & 0 & 0 & 0 \end{bmatrix} + C_{t1} \begin{bmatrix} \Phi_1 \Phi_{1h} & \cdots & 0 & 0 & 0 \\ \vdots & \ddots & \vdots & \vdots & \vdots \\ \Phi_{nh} \Phi_{nh} & \cdots & \Phi_{nh} \Phi_{nh} & -\Phi_{nh} & 0 \\ -\Phi_{nh} & \cdots & \Phi_{nh} & 1 & 0 \\ 0 & \cdots & 0 & 0 & 0 \end{bmatrix} + C_{t1} \begin{bmatrix} \Phi_{1k} \Phi_{1k} & \cdots & 0 & 0 & 0 \\ \vdots & \ddots & \vdots & \vdots & \vdots \\ \Phi_{nk} \Phi_{nk} & \cdots & \Phi_{nk} \Phi_{nk} & -\Phi_{nk} & 0 \\ 0 & \cdots & 0 & 0 & 0 \\ -\Phi_{nk} & \cdots & \Phi_{nk} & 1 & 0 \end{bmatrix} \quad (5.24)$$

$$K = A^T k A$$

$$= \begin{bmatrix} \Phi_1^T k_s \Phi_1 & \cdots & 0 & 0 & 0 \\ \vdots & \ddots & \vdots & \vdots & \vdots \\ 0 & \cdots & \Phi_n^T k_s \Phi_n & 0 & 0 \\ 0 & \cdots & 0 & 0 & 0 \\ 0 & \cdots & 0 & 0 & 0 \end{bmatrix} + k_{t1} \begin{bmatrix} \Phi_1 \Phi_{1h} & \cdots & 0 & 0 & 0 \\ \vdots & \ddots & \vdots & \vdots & \vdots \\ \Phi_{nh} \Phi_{nh} & \cdots & \Phi_{nh} \Phi_{nh} & -\Phi_{nh} & 0 \\ -\Phi_{1h} & \cdots & \Phi_{nh} & 1 & 0 \\ 0 & \cdots & 0 & 0 & 0 \end{bmatrix} + k_{t1} \begin{bmatrix} \Phi_{1k} \Phi_{1k} & \cdots & 0 & 0 & 0 \\ \vdots & \ddots & \vdots & \vdots & \vdots \\ \Phi_{nk} \Phi_{nk} & \cdots & \Phi_{nk} \Phi_{nk} & -\Phi_{nk} & 0 \\ 0 & \cdots & 0 & 0 & 0 \\ -\Phi_{nk} & \cdots & \Phi_{nk} & 1 & 0 \end{bmatrix} \quad (5.25)$$

where  $m_{ti}$ ,  $c_{ti}$ ,  $k_{ti}$  ( $i = 1,2$ ) represent mass, damping coefficient and stiffness of TMD1 and TMD2 respectively.

To achieve the most efficient response suppression of the bridge deck, the optimal damping ratio of TMD should be considered and to simplify the analysis, structural damping to be neglected. The optimum damping ratio and optimum frequency ratio parameters of randomly vibration can be calculated by **Equation (5.28)** and **Equation (5.29)** respectively [Warburton and Ayorinde, 1980], where  $\mu$  is ratio of TMD mass by structure mass **Equation (5.26)** and frequency ratio parameter **Equation (5.27)**.

$$\mu = \frac{m_d}{m} \quad (5.26)$$

$$f_{d,opt} = \frac{\omega_d}{\omega} \quad (5.27)$$

$$\xi_{d,opt} = \sqrt{\frac{\mu(3\mu + 4)}{8(\mu + 1)(\mu + 2)}} \quad (5.28)$$

$$f_{d,opt} = \sqrt{\frac{\mu + 2}{2(\mu + 1)^2}} \quad (5.29)$$

### 5.5 Finite Element Model of The TMD

The model of the TMD is created in ABAQUS as a steel mass structure having material properties of mass density 7800 kg/m<sup>3</sup> and elastic properties of Young's modulus 200+E9 Pa and Poisson's ratio 0.3, with a rectangular shape and dimensions (4\*4\*0.24) m. The TMDs are meshed with standard linear 3D stress C3D8R element type. They are installed and attached to the slab of the segmental deck of the cable stayed bridge inside the hollows, and they are connected to the bridge deck on both sides and in the center of the deck so as to provide both point-wise control forces and control torques. This distribution pattern allows controlling both the vertical and torsional motions. The TMD is attached to the slab of the deck by a spring with a variable stiffness and a dashpot having variable damping coefficient depending on the TMD design parameters (see **Figure 5.3**). The wind forces on TMDs are assumed to be negligible because the TMDs are installed inside the segmental deck. It is assumed that the mass ratio of the TMDs to the equivalent bridge mass is very small, therefore, the attachment of TMDs does not introduce a meaningful change to the static equilibrium of the bridge, and the structural mode shapes remain the same as those of the original cable stayed bridge without the TMDs.

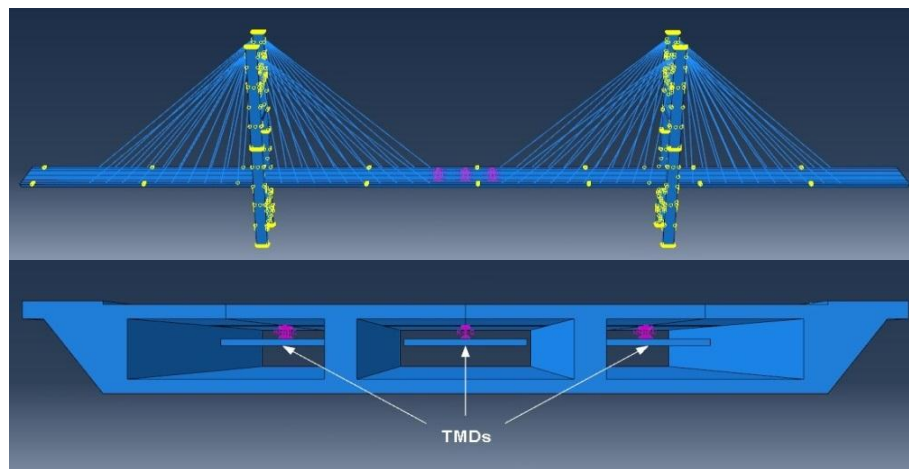


**Figure 5.3** Positioning the TMDs

A strong design wind speed used in all simulations which was 54 m/s and the frequency of the excitation is in such a way so that to produce a frequency matching higher mode shapes of vibrations in the cable stayed bridge model with coupling effects. The wind load assigned in the simulation is with duration of 30 seconds (see **Figure 5.4**).

## 5.5 Finite Element Model of The TMD

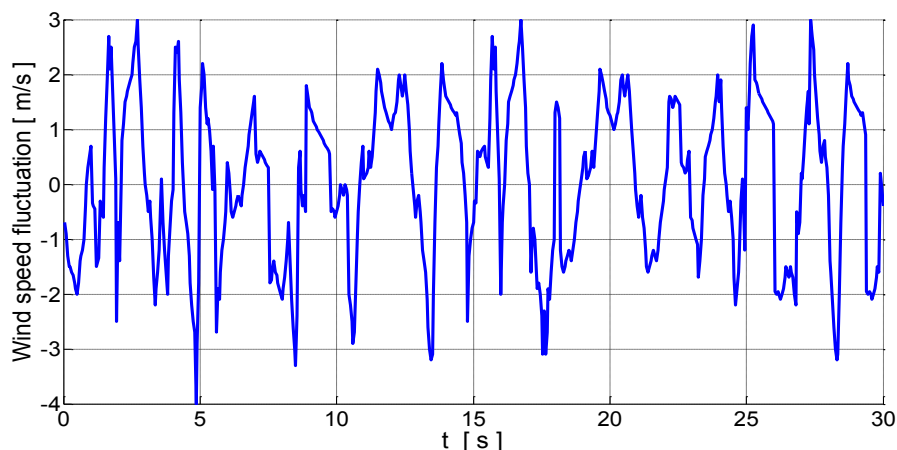


**Figure 5.4** Wind speed fluctuation profile

The wind attack angle is  $25^\circ$  perpendicular to the longitudinal axis of the cable stayed bridge. Frequency analysis has been undertaken to identify the first 20 mode shapes of vibrations for the model. In this work we concentrate on the vertical and the torsional vibrations only. The frequency magnitudes and the types of vibrations for eight mode shapes are available in **Table 5.1**.

**Table 5.1**

Vibration modes data

Mode shape	Type of vibration	Frequency ( Hz )
1	Vertical	0.242
3	Vertical	0.509
6	Vertical –Torsional	0.776
7	Torsional	0.789
9	Vertical	0.883
11	Lateral –Torsional	0.986
16	Vertical –Torsional	1.208
20	Vertical –Torsional	1.631

### 5.5.1 Mode Shapes Analysis

The process of designing the TMDs to control the vertical and torsional vibrations of the deck in the cable stayed bridge needs to investigate the frequency analysis to identify the

## 5.5 Finite Element Model of The TMD

mode shapes of vibrations, in particular the natural frequency of a certain mode shape that is equal or is near to the frequency of the exciting wind. The natural frequency of the dominant mode of vibration is considered in the design process to investigate the optimization of TMDs parameters. **Figure 5.5** shows eight mode shapes of vibrations.

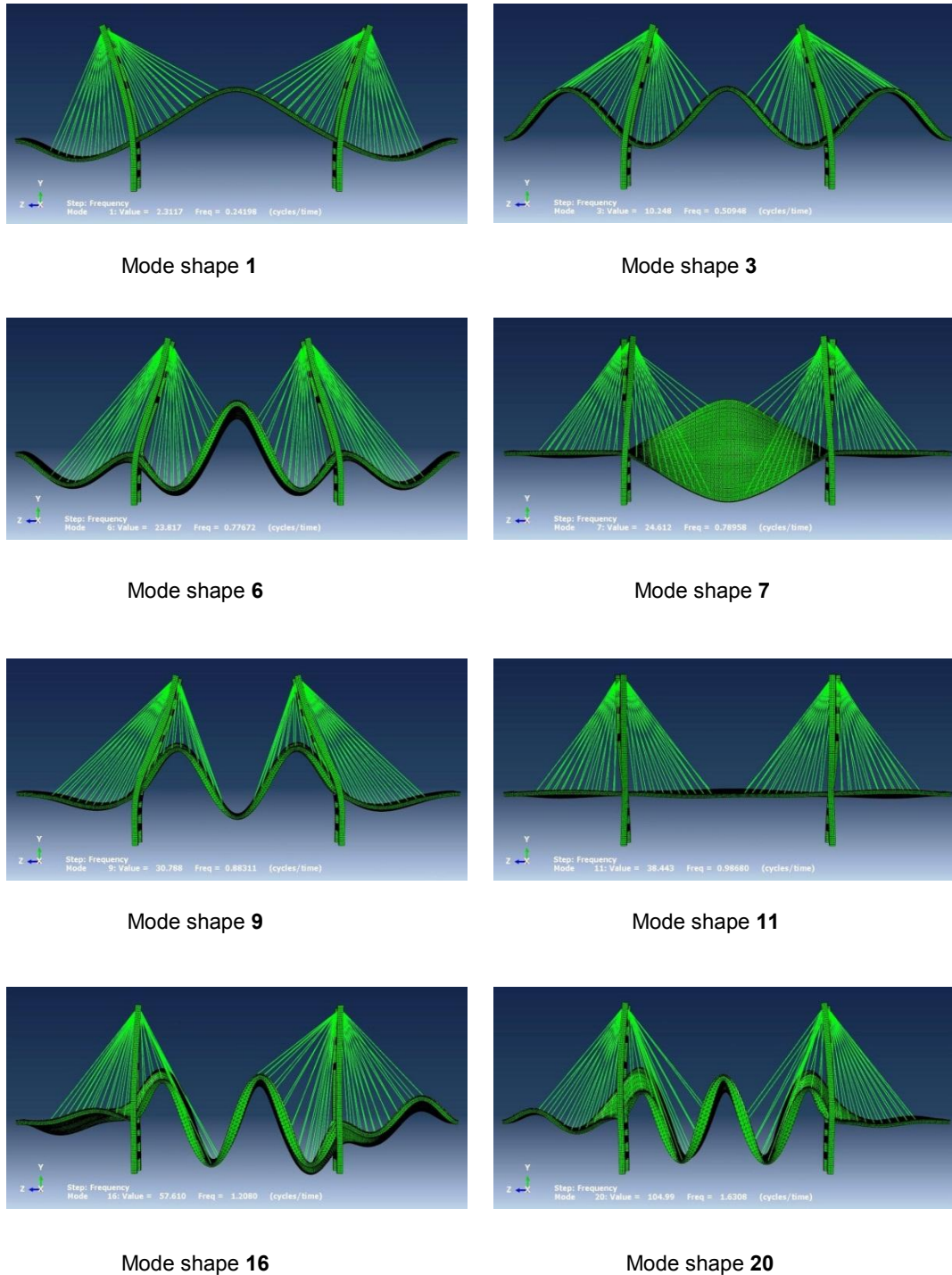
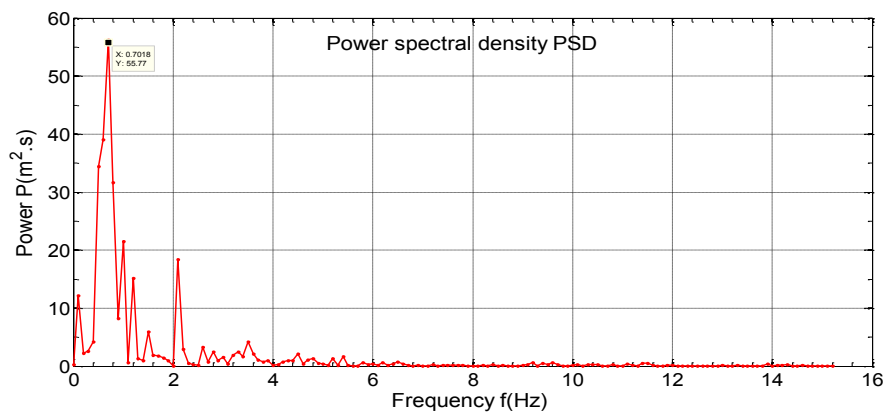


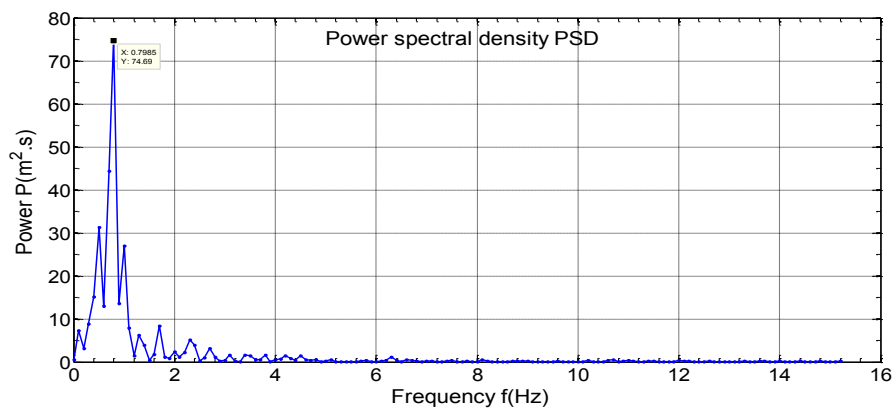
**Figure 5.5** Eight mode shapes of vibrations

## 5.5 Finite Element Model of The TMD

The vertical and torsional displacement time-histories at the mid span both for the center and the outer edge are transformed into frequency domain signals using the Fast Fourier Transform (FFT) technique by utilizing MATLAB codes, and the corresponding power spectral density (PSD) of each time-history is shown in **Figure 5.6**. The energy of the vertical vibrations of the bridge deck are concentrated on 0.7018 Hz, which is close to the sixth mode vibration natural frequency of the cable stayed model; and the energy of the torsional vibrations is centered on 0.7985 Hz, which is close to the seventh mode vibration natural frequency. Results indicate that the vertical responses of the cable stayed bridge model are dominated by the sixth mode, and the torsional responses are dominated by the seventh mode, and it is clear that the two dominant modes are similar in their natural frequencies to a big content. Thus, the sixth mode shape coupled (vertical-torsional) with natural frequency of 0.776 Hz would be the dominant vibration which would be based on to assign the TMDs design data so that to get the optimum effect in suppressing the vertical and torsional vibrations.



a- Vertical displacement



b- Torsional displacement

**Figure 5.6** Power spectral densities of vertical and torsional displacements at the mid span



## 5.6 Optimization of TMD Parameters

TMD parameters are found using minimax optimization technique proposed by Tsai and Lin. This technique to calculate the optimum values of frequency ratio and damping ratio for the specified mass ratio is an iterative numerical search. For a fixed value of frequency ratio, the maximum displacements for different values of damping ratios are found. Then the minimum values are selected from the maximum displacements of response, which is the minimax displacement for that value of frequency ratio. Then the above procedure is repeated for different values of frequency ratio to find the minimax value of each frequency ratio. Finally, the smallest minimizes are selected and corresponding frequency ratio and damping ratio are the optimum parameters of the system having specified mass ratio. The numerical simulations for all cases are implemented using ABAQUS finite element program.

### 5.6.1 Optimum Mass Ratio

When TMDs are designed, the mass ratio is an important parameter that is very sensitive to design the overall weight and the number of these TMDs in order to get the most optimized results for vibration mitigation. This parameter is the ratio of the TMDs total weight to the total weight of the cable stayed bridge. Five mass ratios are considered which are (0.25 %, 0.75 %, 1.25 %, 1.75 % and 2.25 %). The dimensions of each TMD are designed (4\*4\*0.24) m, they are distributed inside the three hollows of the segmental deck, and due to restriction of place availability they are positioned parallel along the center line of the cable stayed bridge model in a symmetrical pattern starting from the mid span region in the left and right directions, so every mass ratio situation will take a certain number of TMDs (3 numbers, 9 numbers, 15 numbers, 21 numbers and 27 numbers) respectively for each mass ratio case. **Table 5.2** details the design data of the TMDs considering the mode shape 6 with natural frequency of 0.776 Hz and constant frequency ratios of 1.0 and constant damping ratios of 0.05 which have been used in the simulations.

**Table 5.2**

Parameters of TMDs for multiple mass ratios

Mass ratio $\mu$	Frequency ratio $f$	TMD stiffness $K_d$ N/m	TMD damping coefficient $C_d$ N.s/m
0.25 %	1.0	54183	6982
0.75 %	1.0	162549	20947
1.25 %	1.0	270915	34912
1.75 %	1.0	379281	48876
2.25 %	1.0	487647	62841

## 5.6 Optimization of TMD Parameters

These situations are compared to the situation of the cable stayed bridge model excited by the wind without the application of TMDs so that to compare the result to get the effect of mass ratio on the vertical and torsional vibrations of the deck.

### 5.6.2 Results and Discussion

Considering the vertical vibration, the results confirm that the mass ratio of 2.25 % for designing the TMDs is the optimum case to control the vertical vibration in this model. The data is calculated for the point at the center above the deck at the mid span. Despite the fact that the TMDs are in the beginning of the wind excitation are increasing the vertical vibration, it needed approximately 10 seconds in order to start damping the vertical vibration (buffeting). This case has an obvious effect in reducing the vertical vibration that reached 34.76 % of its magnitude without adding TMDs (see **Figure 5.7**). The case of minimum mass ratio 0.25 % increased 33.20% of the vertical vibration, while the mass ratio of 0.75 % reduced 12.77 % of the vertical vibration, and the mass ratio 1.25 % increased 9.24 % of the vertical vibration. Finally the mass ratio 1.75 % has reduced the vertical vibration 15.12 % of the vertical vibration (see **Table 5.3**).

**Table 5.3**

Vertical vibration control efficiency-Mass ratio

Mass ratio $\mu$	Vertical vibration control efficiency %
0.25 %	-33.20
0.75 %	12.77
1.25 %	-9.24
1.75 %	15.12
2.25 %	34.76

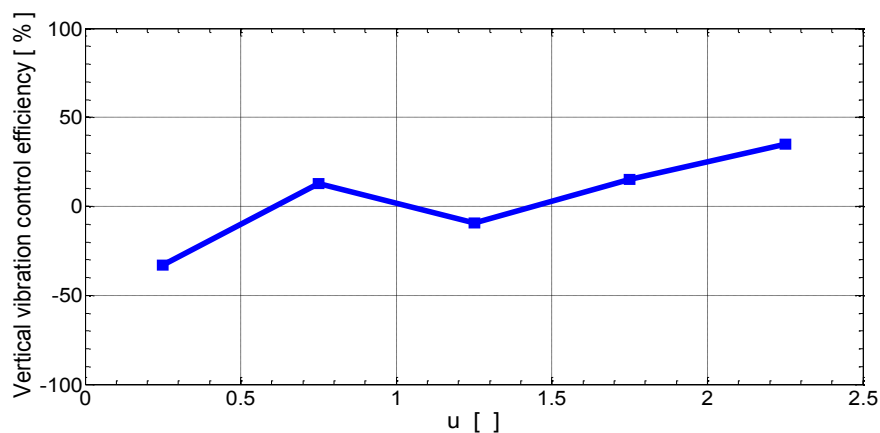


**Figure 5.7** TMD mass ratio effect on the vertical vibration

## 5.6 Optimization of TMD Parameters

This means that there is a nonlinear relation in the vertical vibration mitigation due to the increase of TMDs mass ratio, and due to lack of place availability inside the segmental deck and load effect in generating stresses due to the application of huge amounts of masses of the TMDs, the mass ratio application should be limited to a desired quantity.

Relating to the torsional vibration of the deck, it was detected that the increase of the TMDs mass ratio decreases the torsional (flutter) vibration to a significant amount as follows: for mass ratio 0.25 % decreased 13.72 % and for mass ratio 0.75 % decreased 33.80 %, and for mass ratio 1.25 % decreased 39.59 % while for mass ratio 1.75 % decreased 50.81% and finally for mass ratio 2.25 % decreased 58.47 %, (see **Figure 5.8** and **Table 5.4**). This is an indication that the weight of the TMDs helps to balance the torsional vibration because the TMDs are opposing the torsional vibration by their mass moments in the opposite direction. This means that increasing mass ratio has a significant effect in mitigating the torsional vibration of the deck.

**Table 5.4**

Torsional vibration control efficiency-Mass ratio

Mass ratio $\mu$	Torsional vibration control efficiency %
0.25 %	13.72
0.75 %	33.80
1.25 %	39.59
1.75 %	50.81
2.25 %	58.47

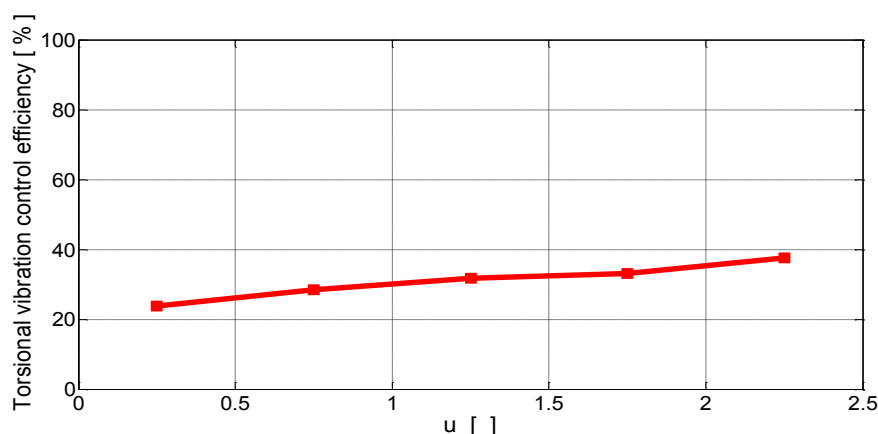


**Figure 5.8** TMD mass ratio effect on torsional vibration

From the results above, it is clear the importance of using TMDs with the mass ratio 2.25% to secure both the mitigation of the vertical vibration to 34.76% and the torsional vibration to 58.47%.

## 5.6 Optimization of TMD Parameters

### 5.6.3 Simulation of The Models

The mass ratio effect on the vertical and torsional vibrations of the cable stayed bridge is simulated in ABAQUS and the following simulations (see **Figure 5.9**) show the situations of vibrations due to wind excitation at time history of 30 seconds. The location of data collection is at the mid span of the deck first at the center point and the second at the right and left outer edges, where the first point is a reference to calculate the change in the vertical displacement in each case and the second two points are used to calculate the change in the torsional displacement.

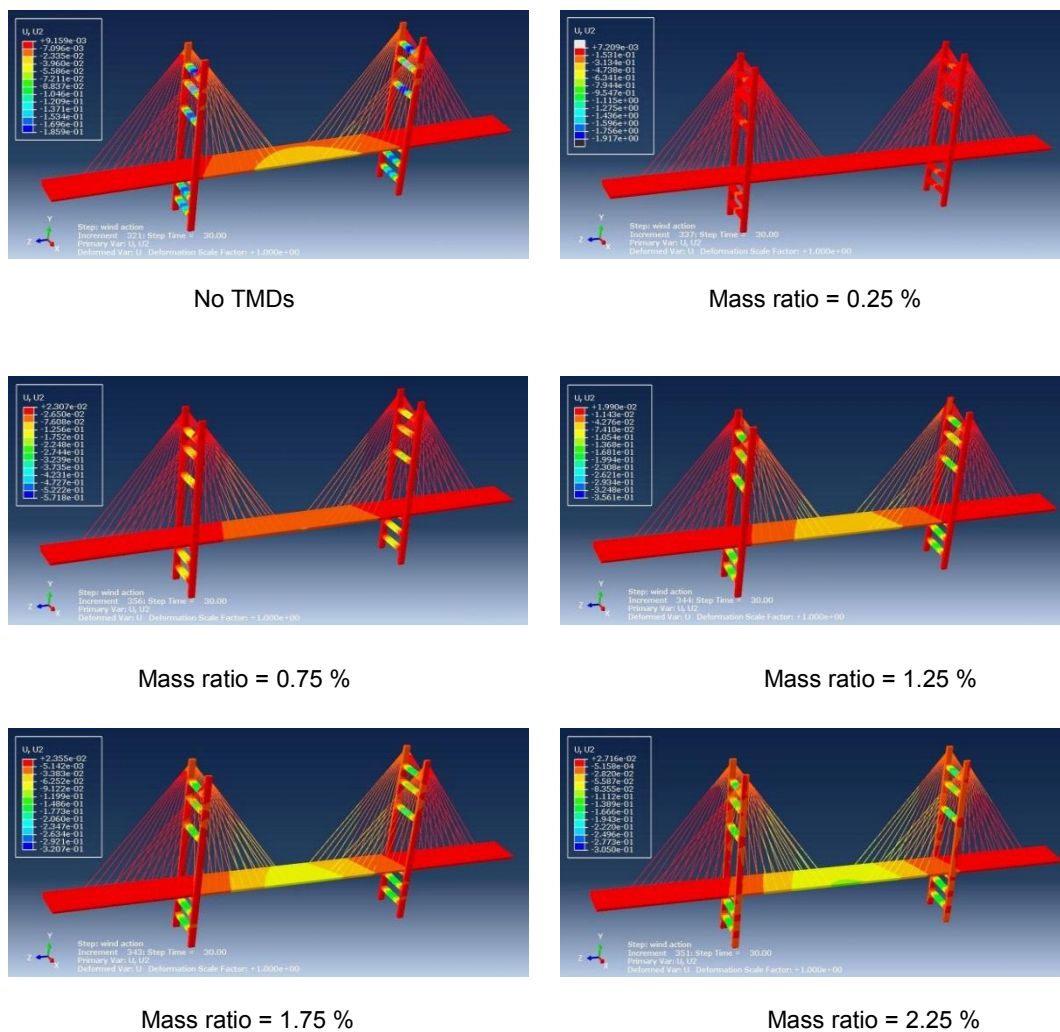


**Figure 5.9** TMDs mass ratio effect on vertical and torsional vibrations

### 5.6.4 Optimum Frequency Ratio

Another parameter of designing TMDs is the frequency ratio, which is the ratio of the TMD frequency and the natural frequency of the structure. The frequencies of the TMDs are tuned to the natural frequency of the cable stayed bridge or near this frequency that belongs to the

## 5.6 Optimization of TMD Parameters

dominant mode shape of vibration. As mentioned in previous section, the dominant mode of vibration is the mode shape 6, so the frequencies of the TMDs are tuned to 0.776 Hz which has been calculated from the frequency analysis. Five frequency ratios cases which are (0.8, 0.9, 1.0, 1.1 and 1.2) would be utilized to detect the optimum reduction of the vertical and torsional vibrations. **Table 5.5** shows the magnitudes of the stiffness and the damping coefficient of the TMDs for constant damping ratios of 0.05 and constant mass ratios of 2.25 % which was the best case to reduce the vertical and torsional vibrations.

**Table 5.5**

Parameters of the TMD for multiple frequency ratios

Frequency ratio $f$	Mass ratio $\mu$	TMD stiffness $K_d$ N/m	TMD damping coefficient $C_d$ N.s/m
0.8	2.25 %	312094	50273
0.9	2.25 %	394994	56557
1.0	2.25 %	487647	62841
1.1	2.25 %	590052	69125
1.2	2.25 %	702211	75409

### 5.6.5 Results and Discussion

To consider the vertical vibration, the TMDs in the beginning of the wind excitation are increasing the vertical vibration, and it needed approximately 10 seconds in order to start mitigating the vertical vibration. It was detected that the case of frequency ratio 1.2 has the largest effect in reducing the vertical vibration that reached 50.47% of its magnitude without applying TMDs (see **Figure 5.10**). The case of frequency ratio 0.8 increased 21.76% of the vertical vibration, while the frequency ratio of 0.9 decreased 6.16 % of the vertical vibration and the frequency ratio of 1.0 decreased 34.76 % of the vertical vibration, but in other hand the frequency ratio of 1.1 has decreased 46.18 % of the vertical vibration (see **Table 5.6**). There is linearity in the vertical vibration mitigation due to the change in frequency ratio design parameter till frequency ratio 1.0, after that the mitigation is less and tend to be stable or with a very small change. The reduction in the vertical vibration between the two frequency ratios 1.2 and 1.1 are near to each other, so the frequency ratio 1.1 can be considered the suitable ratio to assign the TMDs frequencies which is near to the natural frequency of the cable stayed bridge to optimize mitigating the vertical vibration of the deck.

## 5.6 Optimization of TMD Parameters

**Table 5.6**

Vertical vibration control efficiency-Frequency ratio

Frequency ratio $f$	Vertical vibration control efficiency %
0.8	-21.76
0.9	6.16
1.0	34.76
1.1	46.18
1.2	50.47

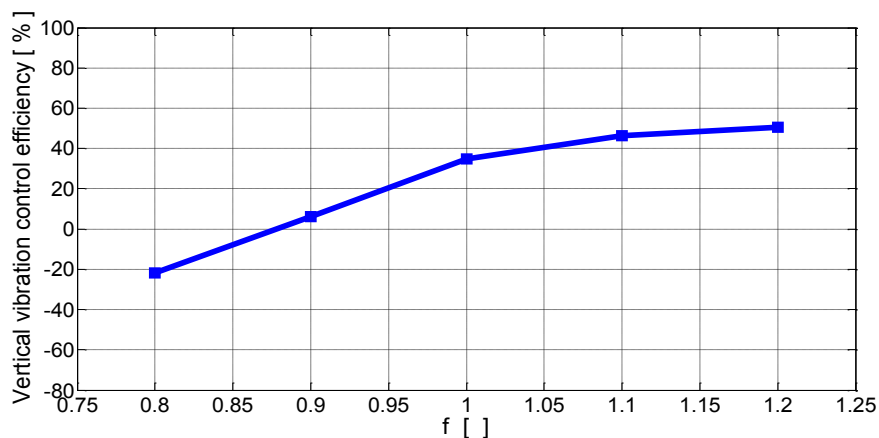


**Figure 5.10** TMD frequency ratio effect on the vertical vibration

Related to torsional vibration, all the frequency ratio cases have shown significant reduction of the torsional vibration of the deck (see **Figure 5.11** and **Table 5.7**). The change in the ratios has a very little effect on the results. Considering the frequency ratio 0.8, the torsional vibration was reduced to 58.74 % and for frequency ratio 0.9 decreased 58.25%, and for frequency ratio 1.0 decreased 58.47% while for frequency ratio 1.1 was decreased to 58.36 % and finally for frequency ratio 1.2 decreased 58.12%. This means that changing the frequency ratio of the TMDs has an appreciable effect in mitigating the torsional vibration of the deck in the cable stayed bridge till reaching the frequency ratio 1.0 or near the natural frequency of the cable stayed bridge but after that it has a small effect especially for large TMD mass ratios.

From the results discussed above, it is essential to use the frequency ratio 1.1 to tune the TMDs near to the natural frequency of the cable stayed bridge for the dominant mode shape 6 so that to control the vertical vibration to 46.18 % and to reduce the torsional vibration to 58.36%.

## 5.6 Optimization of TMD Parameters

**Table 5.7**

Torsional vibration control efficiency-Frequency ratio

Frequency ratio $f$	Torsional vibration control efficiency %
0.8	58.74
0.9	58.25
1.0	58.47
1.1	58.36
1.2	58.12

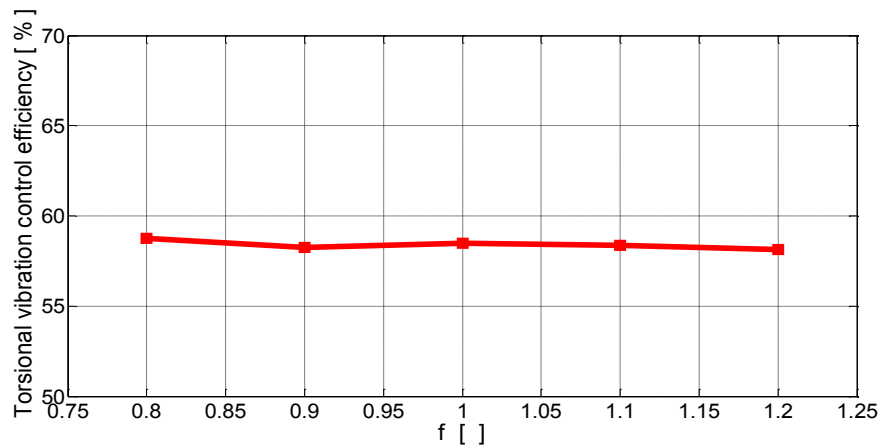


**Figure 5.11** TMD frequency ratio effect on torsional vibration

### 5.6.6 Optimum Damping Ratio

The damping ratio parameter is considered for designing TMDs in vibration control, and it is the ratio of the TMD damping coefficient to the critical damping coefficient of the main structure. Five damping ratios (0.01, 0.05, 0.1, 0.15 and 0.2) are used to calculate the optimum reduction in the vertical and torsional vibrations. **Table 5.8** shows the magnitudes of the stiffness and the damping coefficient of the TMDs considering these five damping ratio cases with constant frequency ratios of 1.0 and constant mass ratios of 2.25 %.

**Table 5.8**

Parameters of the TMD for multiple damping ratios

Damping ratio $\xi$	Mass ratio $\mu$	TMD stiffness $K_d$ N/m	TMD damping coefficient $C_d$ N.s/m
0.01	2.25 %	487647	12568
0.05	2.25 %	487647	62841
0.10	2.25 %	487647	125682
0.15	2.25 %	487647	188523
0.2	2.25 %	487647	251364

## 5.6 Optimization of TMD Parameters

### 5.6.7 Results and Discussion

Considering the vertical vibration, the results confirm that the damping ratio of 0.2 for designing the TMDs is the optimum case to control the vertical vibration in this model. The case of damping ratio 0.2 has the largest effect in reducing the vertical vibration which reached 46.00% of its magnitude without applying TMDs (see **Figure 5.12** and **Table 5.9**). The case of damping ratio 0.01 decreased 33.03 % of the vertical vibration, while the damping ratio of 0.05 decreased 34.76 % of the vertical vibration and the damping ratio of 0.1 decreased 38.93 % of the vertical vibration, but the damping ratio of 0.15 has decreased 43.74 % of the vertical vibration. Approximately a linear relation is apparent in the vertical vibration mitigation due to the change of damping ratio.

**Table 5.9**

Vertical vibration control efficiency-Damping ratio

Damping ratio $\xi$	Vertical vibration control efficiency %
0.01	33.03
0.05	34.76
0.10	38.93
0.15	43.74
0.2	46.00

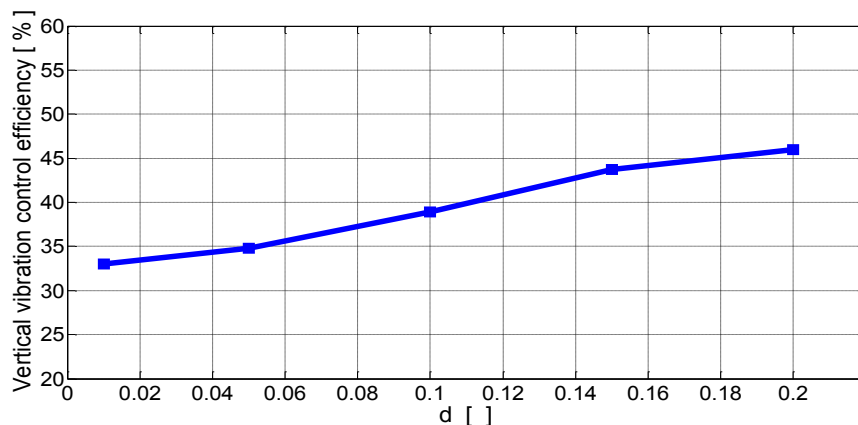


**Figure 5.12** TMD damping ratio effect on the vertical vibration

Considering the reduction of the torsional vibration of the deck (see **Figure 5.13** and **Table 5.10**). For damping ratio 0.01 the torsional vibration was reduced to 41.52% and for damping ratio 0.05 decreased 41.54%, and for damping ratio 0.1 decreased 41.52 % , and for damping ratio 0.15 was increased to 41.53 % and finally for damping ratio 0.2 decreased 41.56 %.



## 5.7 Validation of The TMDs Models

This means that changing the damping ratio of the TMDs has no effect on mitigating the torsional vibration of the deck in the cable stayed bridge for this range of damping ratios.

**Table 5.10**

Torsional vibration control efficiency-Damping ratio

Damping ratio $\xi$	Torsional vibration control efficiency %
0.01	41.52
0.05	41.54
0.10	41.52
0.15	41.53
0.2	41.56

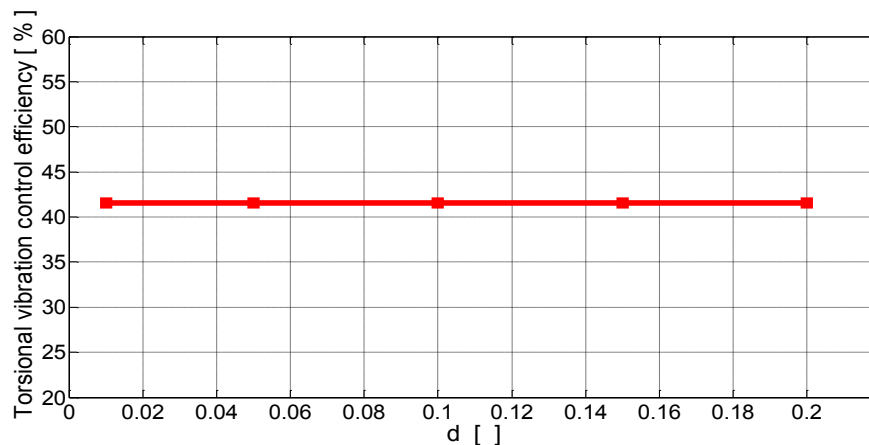


**Figure 5.13** TMD damping ratio effect on the torsional vibration

Through the evaluation of the results, it is recommended to use the damping ratio 0.2 for assigning TMDs damping coefficient so that to control the vertical vibration to 46.00% and to reduce the torsional vibration to 41.56%.

From the minimax optimization technique results done for the three design parameters, it was found that the use of TMDs with mass ratio 2.25%, frequency ratio of 1.1 and damping ratio 0.2 is the optimal case to guarantee the most efficient control of vertical and torsional vibrations of the deck.

## 5.7 Validation of The TMDs Models

The validation of the results for the TMDs design parameters is based on the comparison with the benchmarks from the literature which have been considered in the introduction section of this chapter. The first benchmark is the results obtained by Wang and co-authors

## 5.7 Validation of The TMDs Models

for two TMDs design parameters mass ratio and damping ratio effects on the vertical vibration of the deck for Sutong Bridge. The second benchmark is the results obtained by Lin and co-authors for TMDs mass ratio effect on the vertical and torsional vibrations of the deck.

### 5.7.1 Wang and Co-authors Benchmark

The following **Figure 5.14** is showing the curves of the results of the vertical vibration control efficiency considering mass ratio obtained by Wang and co-authors and the results obtained from the finite element model.

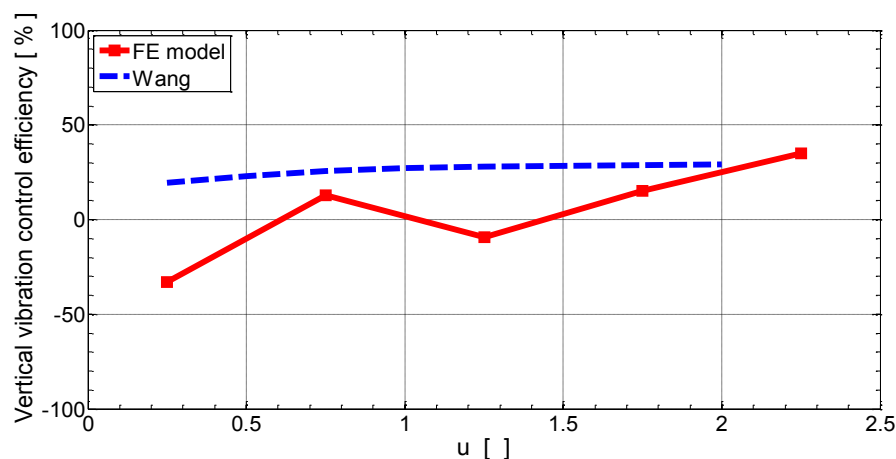


**Figure 5.14** Validation for TMDs mass ratio effect on the vertical vibration of the deck

The control efficiency of the vertical vibration obtained from the results of Wang and co-authors starts from 19.25% for mass ratio of 0.25% while it starts from -33.20% for the results obtained from the finite element model. The curve of results for the FE model reaches near the curve of the results of Wang and co-authors at mass ratio 0.75% with a control efficiency of 12.73% and 25% for the latter. The nearest position is at mass ratio 2% with a value of 25% and 29% for the latter. The results obtained from the FE model showed a good agreement with the results of Wang and co-authors at mass ratio range of (2% - 2.25%).

The curves of the results for the vertical vibration control efficiency considering the effect of damping ratio for both Wang and co-authors and the finite element model are shown in **Figure 5.15**. The control efficiency of the vertical vibration obtained by Wang and co-authors start with 26.70% for damping ratio of 0.01, while this output starts with 33.03% for the same damping ratio obtained from the finite element model and the two response curves are coinciding till the damping ratio 0.03. The control efficiency curve for Wang and co-authors ends with 22.25% for damping ratio 0.08 and the curve of the finite element model has a

## 5.8 Global Sensitivity Analysis

value of 36% at the same damping ratio. Supporting on the comparison between the two results, a good agreement exists between them in the damping ratio range (0.01-0.03).

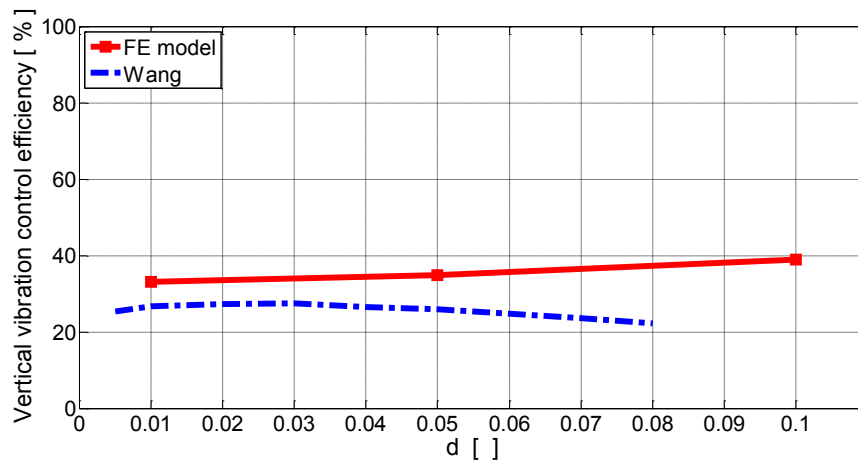


Figure 5.15 Validation for TMDs damping ratio effect on the vertical vibration of the deck

### 5.7.2 Lin and Co-authors Benchmark

Considering the aerodynamic coupling between the vertical and torsional vibrations for the dominant mode shape of vibration, and when the mass ratio of the TMDs is 2%, the control efficiency of the vertical vibration of the deck obtained from the results of the finite element model was 25%, and it was the same value 25% obtained from Lin and co-authors. This indicates that the two results have an excellent agreement, which pours to the validity of the obtained results from the finite element model.

## 5.8 Global Sensitivity Analysis

Global sensitivity analysis studies how the uncertainty in the output of a model numerical or otherwise can be apportioned to different sources of uncertainty in the model input. A good sensitivity analysis should run analyses over the full range of plausible values of key parameters and their interactions, to assess how impacts change in response to changes in key parameters. Global sensitivity analysis methods such as Sobol's sensitivity indices have been widely applied recently. Global sensitivity analysis explores the parameter space so that they provide robust sensitivity measures in the presence of nonlinearity and interactions among the parameters. Global sensitivity analysis, however, can be computationally intensive, since they require sampling parameter sets. Several approximation methods have been developed to

## 5.9 Box-Behnken Sampling Method

reduce the computational cost. Global sensitivity analysis can provide additional information for improving the system understanding.

Sobol sensitivity indices for the three design parameters (mass ratio, frequency ratio and damping ratio) are utilized to obtain the control efficiency of vertical and torsional vibrations of the deck after application of MTMDs.

## 5.9 Box-Behnken Sampling Method

Box-Behnken experimental design was based on to identify the relationship between the response functions (vertical vibration and torsional vibration) of the deck in the cable stayed bridge model and the three design variables of the TMDs (mass ratio, frequency ratio and damping ratio). Box-Behnken design is rotatable second-order designs based on three-level incomplete factorial designs. The special arrangement of the Box-Behnken design levels allows the number of design points to increase at the same rate as the number of polynomial coefficients. For three factors, for example, the design can be constructed as three blocks of four experiments consisting of a full two-factor factorial design with the level of the third factor set at zero.

Box-Behnken design requires an experiment number according to:

$$N = z^2 + z + c_p \quad (5.30)$$

where  $z$  is the factor number and  $c_p$  is the replicate number of the central point. Box-Behnken is a spherical, revolving design. Viewed as a cube (**Figure 5.16.a**), it consists of a central point and the middle points of the edges. However, it can also be viewed as consisting of three interlocking  $2^2$  factorial design and a central point (**Figure 5.16.b**). It has been applied for optimization of several chemical and physical processes.

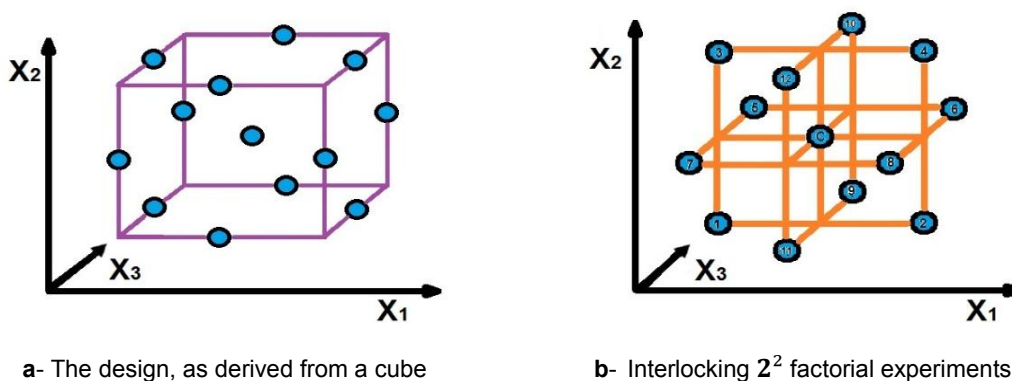


Figure 5.16 Box-Behnken experimental design

## 5.9 Box-Behnken Sampling Method

For the three-level three-factorial Box-Behnken experimental design, a total of 15 experimental runs shown in **Table 5.11** are needed. The model is of the following form:

$$y = \beta_0 + \beta_1 x_1 + \beta_2 x_2 + \beta_3 x_3 + \beta_{11} x_1^2 + \beta_{22} x_2^2 + \beta_{33} x_3^2 + \beta_{12} x_1 x_2 + \beta_{13} x_1 x_3 + \beta_{23} x_2 x_3 \quad (5.31)$$

where  $y$  is the predicted response,  $\beta_0$  model constant;  $x_1$ ,  $x_2$  and  $x_3$  independent variables;  $\beta_1$ ,  $\beta_2$  and  $\beta_3$  are linear coefficients;  $\beta_{12}$ ,  $\beta_{13}$  and  $\beta_{23}$  are cross product coefficients and  $\beta_{11}$ ,  $\beta_{22}$  and  $\beta_{33}$  are the quadratic coefficients. The coefficients, i.e. the main effect  $\beta_i$  and two factors interactions  $\beta_{ij}$  have been estimated from the experimental results by computer simulation programming applying least square method using MATLAB [Ferreira *et al.*, 2004; Rana *et al.*, 2004; Kannan *et al.*, 2004; Kincl *et al.*, 2005; Souza *et al.*, 2005; Ferreira *et al.*, 2007; Zhao and Tiede, 2011; Tekindal *et al.*, 2012; Karmakar *et al.*, 2012; Pasma *et al.*, 2013; Qiu *et al.*, 2014].

**Table 5.11**

The level of variables chosen for the Box-Behnken design

Variable	Symbol	Coded variable level		
		Low	Center	High
		-1	0	+1
Mass ratio	$X_1$	0.0025	0.0125	0.0225
Frequency ratio	$X_2$	0.8	1.0	1.2
Damping ratio	$X_3$	0.01	0.105	0.20

The following **Table 5.12** is showing both the coded and actual variable values that are related to the 15 runs of the simulation of wind excitation with application of TMDs to reduce the vertical and torsional responses of the deck utilizing variation in the three design parameters mentioned above.

## 5.9 Box-Behnken Sampling Method

**Table 5.12**

Box-Behnken design with coded and actual values for three size fractions

Run no.	Coded level of variables			Actual level of variables		
	$X_1$	$X_2$	$X_3$	Mass ratio	Frequency ratio	Damping ratio
1	-1	-1	0	0.0025	0.8	0.105
2	+1	-1	0	0.0225	0.8	0.105
3	-1	+1	0	0.0025	1.2	0.105
4	+1	+1	0	0.0225	1.2	0.105
5	-1	0	-1	0.0025	1.0	0.01
6	+1	0	-1	0.0225	1.0	0.01
7	-1	0	+1	0.0025	1.0	0.2
8	+1	0	+1	0.0225	1.0	0.2
9	0	-1	-1	0.0125	0.8	0.01
10	0	+1	-1	0.0125	1.2	0.01
11	0	-1	+1	0.0125	0.8	0.2
12	0	+1	+1	0.0125	1.2	0.2
13	0	0	0	0.0125	1.0	0.105
14	0	0	0	0.0125	1.0	0.105
15	0	0	0	0.0125	1.0	0.105

### 5.9.1 Surrogate Models Results

The regression coefficients calculated from the second-degree model both for vertical and torsional actual responses obtained using Box-Behnken method. Total of 15 runs are used to formulate the surrogate models for the predicted vertical and torsional vibrations control efficiency based on quadratic orders. The surrogate model for the case of vertical vibration control efficiency has a coefficient of determination  $R^2$  of 99.45% (see **Figure 5.17**) which is a very good representation of the predicted system response and just 0.55% of the system response still unexplained.

## 5.9 Box-Behnken Sampling Method

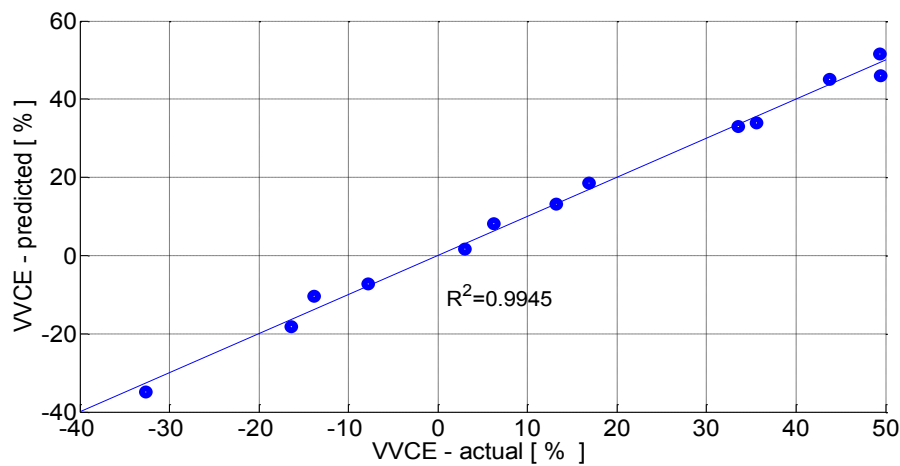


Figure 5.17 Coefficient of determination-Vertical vibration control efficiency

The surrogate model for the case of torsional vibration control efficiency has a coefficient of determination  $R^2$  of 99.99% (see Figure 5.18) which is an excellent approximation for the prediction of the system response and just 0.01% of the system response still unexplained.

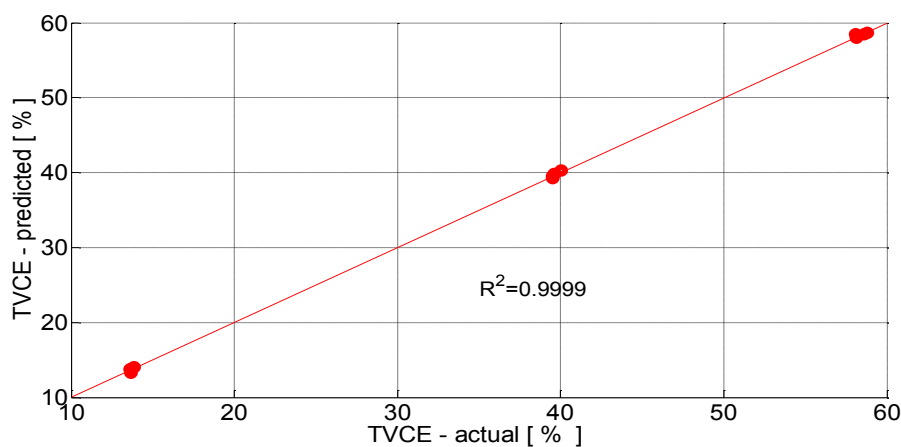


Figure 5.18 Coefficient of determination-Torsional vibration control efficiency

### 5.9.2 Sensitivity Indices Results and Discussion

The main orders of sensitivity indices for each design parameter in addition to their interaction orders were calculated considering the convergence process recommending the use of 250 samples to calculate the vertical vibration control efficiency (see Figure 5.19). Furthermore, the main and interaction orders of sensitivity indices for each design parameter were calculated supporting on 100 samples to calculate the torsional vibration control

## 5.9 Box-Behnken Sampling Method

efficiency (see **Figure 5.20**). Supporting on the calculated results, the total sensitivity indices for each design parameter have been calculated (see **Table 5.13**).

In relation with the vertical vibration control efficiency, the total order sensitivity index of design parameter mass ratio **X1** is 0.6979, this value is bigger than the total order sensitivity index of design parameter frequency ratio **X2** which is 0.2279, also it is much bigger than the total order sensitivity index of design parameter damping ratio **X3** which is 0.0883, this means that the vertical vibration control efficiency is 69.79% due to variation in mass ratio between the TMDs and the cable stayed bridge, and it is 22.79% due to the variation in frequency ratio between the natural frequencies of the TMDs and the cable stayed bridge, also it is 8.83% due to the variation in the damping ratio between them. While the interaction index between the design parameter **X1** and **X2** is 0.0091 and between **X1** and **X3** is 0.0030, while between **X2** and **X3** is 0.006, which means that there is a small interaction between the input factors taking part in the variation of the vertical vibration control efficiency.

**Table 5.13**

Sensitivity indices

Sensitivity indices	Vertical vibration control efficiency	Torsional vibration control efficiency
first order <b>X1</b>	0.6851	0.9997
first order <b>X2</b>	0.2176	0.0000
first order <b>X3</b>	0.0840	0.0001
<b>sum of first orders</b>	<b>0.999329</b>	<b>0.999961</b>
interaction between <b>X1</b> and <b>X2</b>	0.0091	0.0001
interaction between <b>X1</b> and <b>X3</b>	0.0030	0.0001
interaction between <b>X2</b> and <b>X3</b>	0.0006	0.0000
total order of <b>X1</b>	0.6979	0.9999
total order of <b>X2</b>	0.2279	0.0002
total order of <b>X3</b>	0.0883	0.0002
<b>sum of total orders</b>	<b>1.0141</b>	<b>1.0003</b>

While considering the torsional vibration control efficiency, the total order sensitivity index of **X1** is 0.9999, which can be named the controlling design parameter which is much bigger than the total order sensitivity index of **X2** which is 0.0002, also it is much bigger than the total order sensitivity index of **X3** which is 0.0002, this means that the torsional vibration control efficiency is dependable 99.99% on the mass ratio variation, while it is 0.02% due to the frequency ratio variation, and it is 0.02% due to the variation in damping ratio. While the interaction index between **X1** and **X2** is 0.0001 and between **X1** and **X3** is 0.0001, while between **X2** and **X3** is 0.0000, this proves that the surrogate model is additive approximately



## 5.9 Box-Behnken Sampling Method

which means that there is no interaction between design parameters take part in the variation of the torsional vibration control efficiency.

### 5.9.3 Convergence of The Results

The process of global sensitivity analysis supporting on Sobol's sensitivity indices requires certain or adequate samples of experiments to find out the predicted effect of the design parameters on the response of the system. The most efficient number of samples is being identified through the convergence of the sum of first orders and total sensitivity indices of the design parameters. All the sensitivity indices (first orders, interaction orders and total orders) for each design parameter have been calculated using m MATLAB codes. Two outputs have been utilized in the process of converges, the vertical vibration and torsional vibration control efficiency. **Figure 5.19** and **Figure 5.20** show the relation between the number of samples and the sum of first orders sensitivity indices, in the same time between the number of samples and the sum of total sensitivity indices of all design parameters.

For the case of vertical vibration control efficiency (see **Figure 5.19**), the two curves of the sum of first orders and total orders of sensitivity indices at the beginning are not coinciding to reach convergence till 250 samples. After this stage the two curves are starting to converge at the 250 number of samples, where the two curves continue to remain in a stable position after many times of changing the number of samples starting from 250 samples.

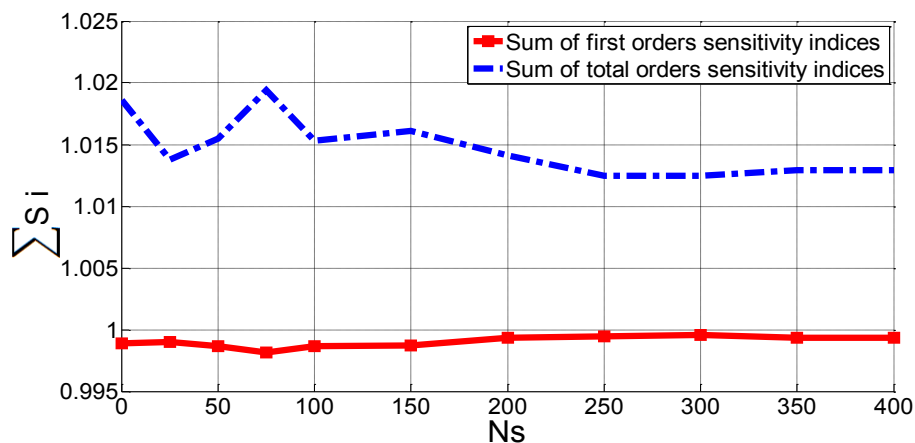


**Figure 5.19** Convergence of sensitivity indices-Vertical vibration control efficiency

While for the torsional vibration control efficiency (see **Figure 5.20**) the two curves are trying to reach convergence earlier than the previous case, the convergence starts at 100 number of samples and the process continues in the stability pattern.

## 5.9 Box-Behnken Sampling Method

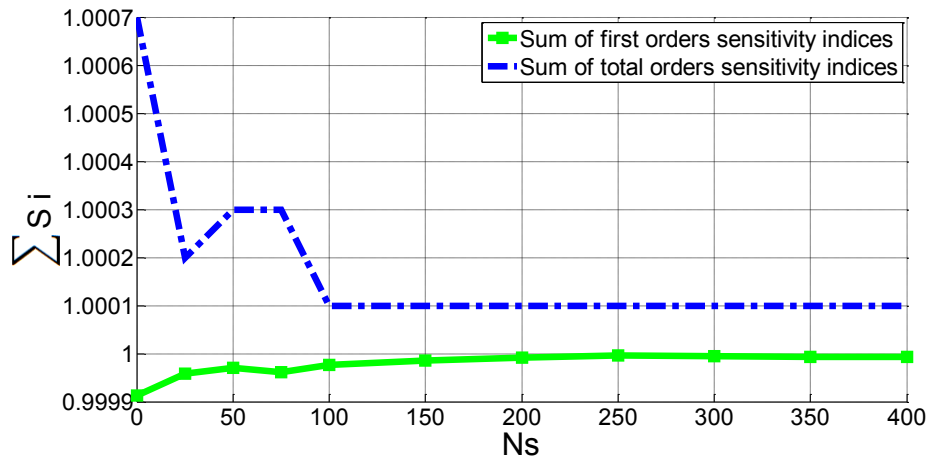


**Figure 5.20** Convergence of sensitivity indices-Torsional vibration control efficiency

The convergence results of the two cases necessitate utilizing 250 samples of experiments to efficiently get the predicted rational effects of each design parameter on the variation of the vertical vibration control efficiency, and to consider 100 samples to obtain the predicted rational effects of the design parameters on the variation of the torsional vibration control efficiency.



# Chapter 6

## Novel Structural Modification

### 6.1 Flutter Wind Speed

The flutter and buffeting response analysis of long span cable supported bridges exposed to a turbulent wind excitation is generally performed in the frequency domain based on the approach originally. The primary effect of the self-excited forces is to change the structural damping through the aerodynamic damping [Chen *et al.*, 2001 and Sato *et al.*, 2002]. The torsional-to-vertical frequency ratio is decisive for the critical flutter wind speed. In traditional bridge design, this means that the required torsional stiffness of the bridge deck is increased when the span goes up, which means that the mass of the bridge deck per unit length is increased. The principle of decreasing the torsional frequency to the level of the vertical frequency or below has been labeled the non-flutter design principle [Dyrbye and Hansen, 1997]. Dyrbye and Hansen, 1997 explained that for very long span suspension bridges, the torsional rigidity of a closed box girder is too small to resist flutter. In order to obtain large critical flutter wind speeds, they proposed a design in which the torsional and vertical frequencies deliberately were made identical. This concept was validated experimentally by [Bartoli *et al.*, 2008 and Andersen *et al.*, 2014].

### 6.2 Flutter Analysis

Identifying the flutter wind speed for the design of long span bridges, needs to perform wind tunnel analysis so that to calculate the flutter derivatives in addition to using frequency domain. A vibrating bridge deck under wind flow creates self-induced forces that depend on displacement vector  $\mathbf{y} = (v, w, \varphi_x)$  and its derivative, where  $v$  is horizontal,  $w$  is vertical and  $\varphi_x$  is the rotational degrees of freedom of the deck (see **Figure 6.1**).

The relationship between aeroelastic force  $\mathbf{f}_z$  and the displacement vector can be written employing flutter derivatives as formulated by [Simiu and Scanlan, 1986].

$$\begin{aligned}
 f_z = \begin{Bmatrix} D_z \\ L_z \\ M_z \end{Bmatrix} &= \frac{1}{2}\rho VKB \begin{pmatrix} P_1^* & -P_5^* & -BP_2^* \\ -H_5^* & H_1^* & BH_2^* \\ -BA_5^* & BA_1^* & B^2A_2^* \end{pmatrix} \begin{Bmatrix} \dot{v} \\ \dot{w} \\ \dot{\phi}_x \end{Bmatrix} \\
 &+ \frac{1}{2}\rho V^2 K^2 \begin{pmatrix} P_4^* & -P_6^* & -BP_3^* \\ -H_6^* & H_4^* & BH_3^* \\ -BA_6^* & BA_4^* & B^2A_3^* \end{pmatrix} \begin{Bmatrix} v \\ w \\ \phi_x \end{Bmatrix} \quad (6.1)
 \end{aligned}$$

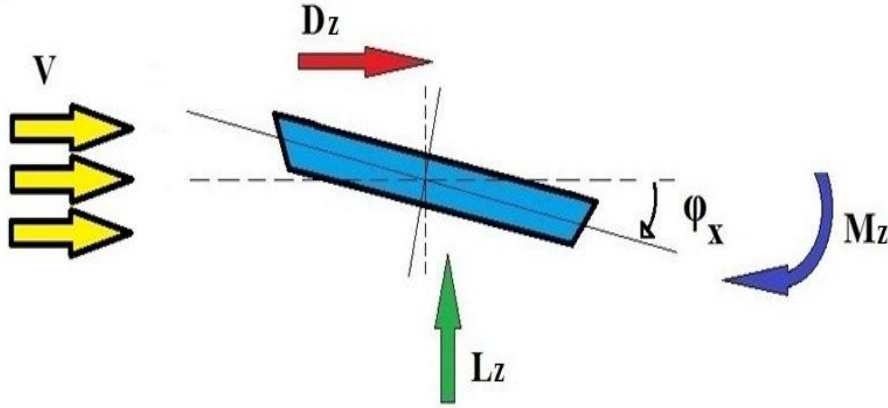


Figure 6.1 Wind induced forces (lift and drag) and moment in the deck

where  $B$  is the deck width,  $\rho$  is the air density,  $V$  is the acting wind speed,  $K = B\omega / V$  is the reduced frequency with  $\omega$  as the response frequency,  $A_i^*$ ,  $H_i^*$  and  $P_i^*$  ( $i = 1, \dots, 6$ ) are the flutter derivatives obtained experimentally. The multimodal flutter analysis is used to solve this problem. **Equation (6.1)** can be expressed in a matrix form as:

$$f_z = K_z y + C_z \dot{y} \quad (6.2)$$

where  $K_z$  and  $C_z$  are aeroelastic stiffness and damping matrices, while  $y$  represents a displacement vector of a node along the deck. The matrices  $K_z$  and  $C_z$  for the entire bridge, can be obtained by assembling the matrix of each bar element of the deck. The dimension of the matrices coincides with the total number of degree of freedom of the bridge deck. The system of equations that governs the dynamic behavior of the deck under aeroelastic forces is expressed as:

$$M\ddot{y} + C\dot{y} + Ky = f_z \quad (6.3)$$

where  $M$ ,  $C$ , and  $K$  are mass, damping, and stiffness matrices. By combining **Equation (6.2)** and **Equation (6.3)**, we get:

### 6.3 Finite Element Model After Modification

---

$$M\dot{\mathbf{y}} + (C - C_z)\dot{\mathbf{y}} + (K - K_z)\mathbf{y} = 0 \quad (6.4)$$

In order to solve the problem of **Equation (6.4)**, a modal analysis is performed. The displacement vector can be written as a function of the most relevant  $m$  mode shapes grouped by a modal matrix  $\Phi$ .

$$\mathbf{y} = \Phi G e^{\mu t} \quad (6.5)$$

where  $\mu$  and  $G$  are complex values. By plugging **Equation (6.5)** into **Equation (6.4)**, the system is transformed to:

$$(\mu^2 I G + \mu C_R G + K_R G) e^{\mu t} = 0 \quad (6.6)$$

$$\Phi^T M \Phi = I, \quad \Phi^T (C - C_z) \Phi = C_R, \quad \Phi^T (K - K_z) \Phi = K_R$$

**Equation (6.6)** becomes a nonlinear eigenvalue problem as:

$$(A - \mu I) G_\mu e^{\mu t} = 0 \quad (6.7)$$

$$A = \begin{pmatrix} -C_R & -K_R \\ I & 0 \end{pmatrix} \quad \text{and} \quad G_\mu = \begin{pmatrix} \mu G \\ G \end{pmatrix}$$

In order to solve this problem, we need mode shapes and natural frequencies of the bridge under study, which can be obtained by a finite element model. The solution to **Equation (6.7)** is expressed as  $\mu_{j=1, \dots, 2m} = \theta_j + i\gamma_j$  ( $j = 1, \dots, 2m$ ) where  $\theta$  is related to structural damping and  $\gamma$  is the damping frequency. Flutter is produced when  $\theta$  becomes null with increasing wind speed. This eigenvalue problem is solved to obtain flutter speed.

### 6.3 Finite Element Model After Modification

Two lateral steel beams 146 m length, 0.5 m thickness and 10 m width at the pylons and 5 m width at the middle part are added to the middle span tied with the deck and the pylons (see **Figure 6.2** and **Figure 6.3**). The lateral steel beams are modeled as (B31: A 2- node linear beam in space) elements. The mass density of the steel beam is 7800 Kg/m<sup>3</sup>, Young's modulus of elasticity is 2.0E+11 and Poisson's ratio is 0.3.

### 6.3 Finite Element Model After Modification

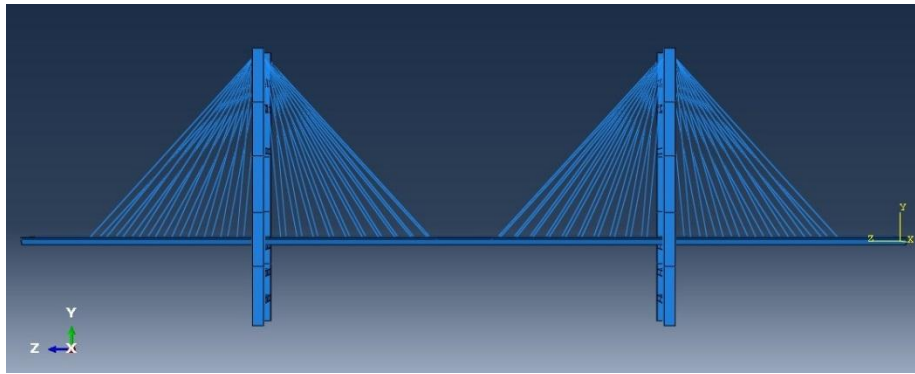


Figure 6.2 Finite element model before structural modification

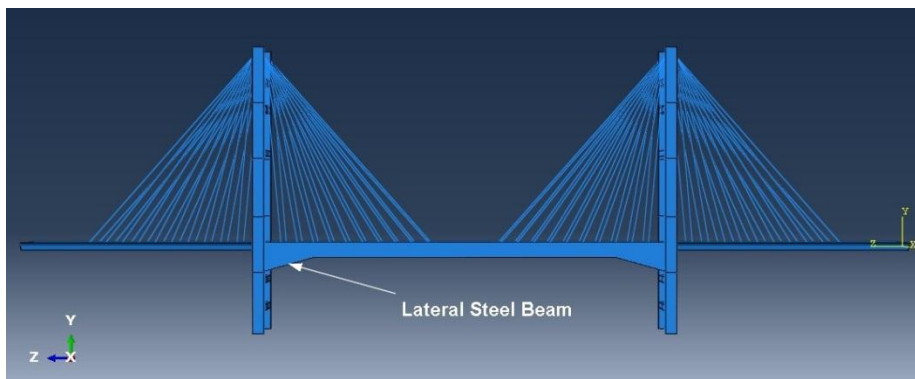


Figure 6.3 Finite element model after structural modification

A wind speed of 54 m/s has been dedicated in the numerical simulations, and the frequency of the excitation is arranged to produce a frequency falls in the frequency ranges of first eight mode shapes of vibrations of the cable stayed bridge model so that to include the vertical and torsional modes. The wind pressure assigned in the simulations is with duration of 30 seconds (see Figure 6.4).

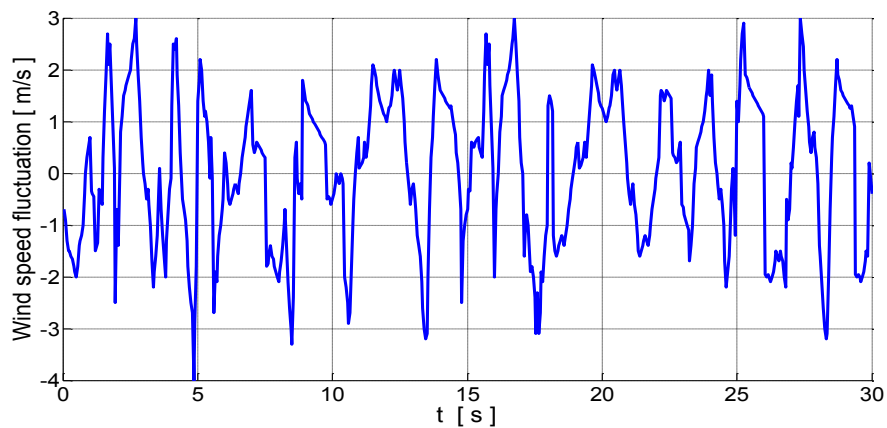


Figure 6.4 Wind speed fluctuation time history

### 6.3 Finite Element Model After Modification

The wind fluctuation data has been prepared depending on exact data from the literature in addition to modification of the excitation frequency [Wang *et al.*, 2010]. It is worthy to mention that after adding the two lateral steel beams, the level of wind pressure assignation would be modified because the wind will act on the new added structural member.

#### 6.3.1 Structural Modification and Mode Shapes

The first 8 mode shapes of vibrations have been obtained, the types of vibrations and the related frequency were determined for each mode shape. The first 4 mode shapes are vertical vibrations modes for the model before structural modification and their frequencies are 0.242 Hz, 0.347 Hz, 0.509 Hz and 0.613 Hz respectively. While for the model after modification, the first four mode shapes are vertical vibrations too, and their frequencies are 0.390 Hz, 0.450 Hz, 0.579 Hz and 0.752 Hz simultaneously (see **Table 6.1**).

**Table 6.1**

Mode shapes and frequencies

Mode shape	Type	Frequency ( Hz ) before modification	Type	Frequency ( Hz ) after modification
1	Vertical	0.242	Vertical	0.390
2	Vertical	0.347	Vertical	0.450
3	Vertical	0.509	Vertical	0.579
4	Vertical	0.613	Vertical	0.752
5	Lateral –Torsional	0.655	Lateral –Torsional	0.820
6	Vertical – Torsional	0.776	Vertical	0.856
7	Torsional	0.789	Lateral	0.960
8	Vertical	0.813	Torsional	0.986

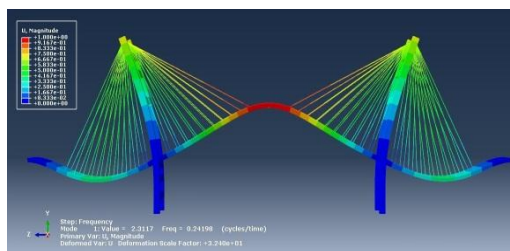
This means that no changes took place in the type of vibrations for the mentioned mode shapes but the magnitudes of frequencies have been increased to higher critical wind speeds with a difference range of (0.07-0.148) Hz between the two cases. The fifth and sixth mode shapes for the model before modification are coupled lateral torsional and vertical torsional vibrations with frequencies 0.655 Hz and 0.776 Hz respectively, and the same mode shapes for the model after modification are coupled lateral torsional vibrations with frequencies



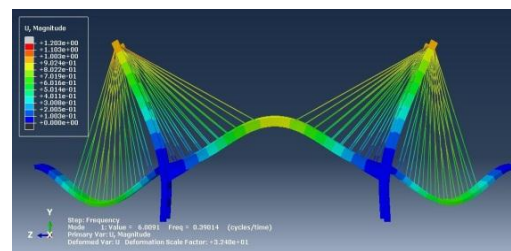
### 6.3 Finite Element Model After Modification

0.820 Hz and 0.856 Hz respectively. While the seventh and eighth mode shapes for the model before modification are torsional and vertical vibrations respectively with frequencies 0.789 Hz and 0.813 Hz respectively. In the other hand the same mode shapes for the model after modification are lateral and torsional vibrations with frequencies 0.960 Hz and 0.986 Hz respectively. This indicates that after structural modification the danger of coupling between the vertical and torsional vibrations has been removed and secured to remote region having natural frequency of 1.610Hz and safety against flutter instability has been increased widely.

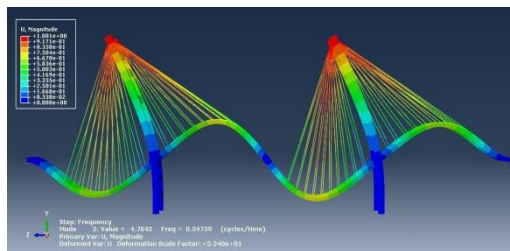
Simulation of frequency analysis for the first eight mode shapes of vibrations of the cable stayed bridge model before and after structural modification are shown in (Figure 6.5). The first 4 mode shapes of the model after structural modification have manifested appreciable decrease in the displacement for the same scale factor as shown by the amplitude of the displacement of the deck and the magnitude of the displacement represented by color.



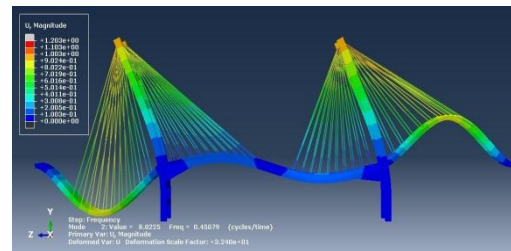
Mode shape 1 before modification



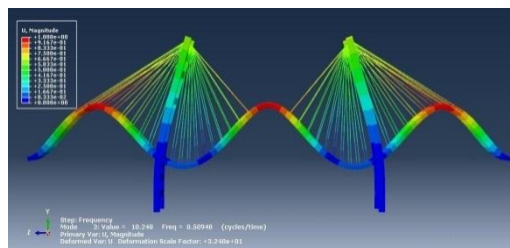
Mode shape 1 after modification



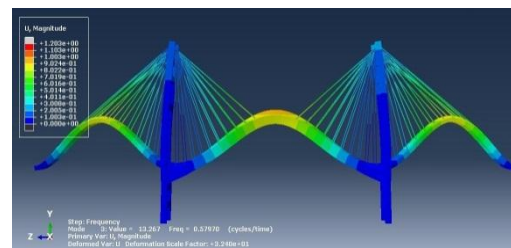
Mode shape 2 before modification



Mode shape 2 after modification



Mode shape 3 before modification



Mode shape 3 after modification

### 6.3 Finite Element Model After Modification

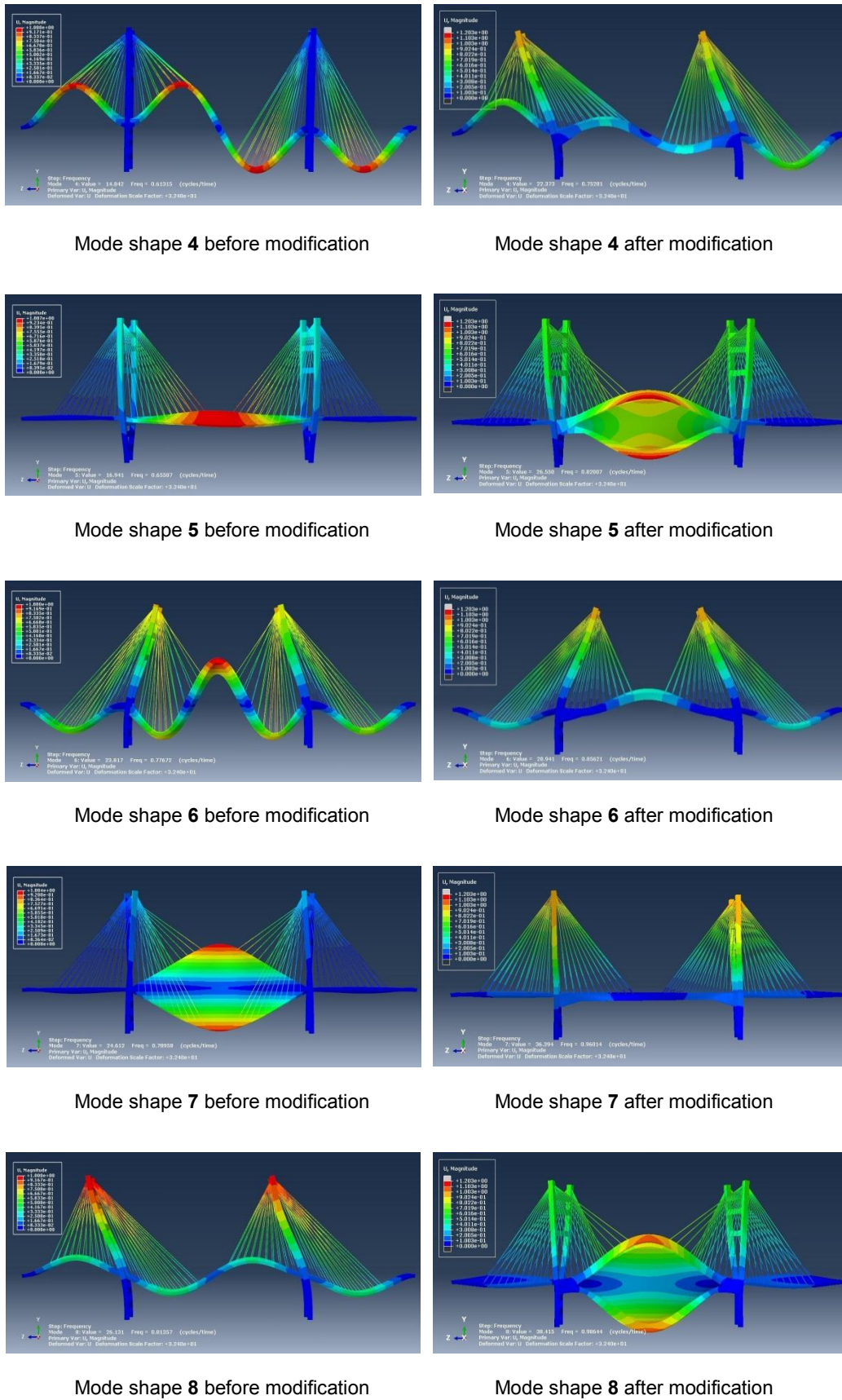


**Figure 6.5** Sixteen mode shapes of vibrations before and after structural modification

### 6.3 Finite Element Model After Modification

While for the mode shape 5, the lateral torsional vibration showed larger torsional displacement after modification. Furthermore, the mode shapes 6, 7 and 8 has been altered after the modification totally, where the types of vibrations have been changed and commonly the frequencies of all the 8 mode shapes have been increased indicating an increase in the bending and torsional stiffness.

#### 6.3.2 Results of Vertical Displacements

The magnitudes of vertical displacements at the center of the mid span during 30 seconds of wind excitation after modifying the model of the cable stayed bridge have decreased widely compared to the same situation before modification. It is worthy to mention that the amplitudes of vibrations are smaller and the frequency of deck vibration has increased (see **Figure 6.6**). The maximum displacement reached is 0.0175 m compared to the maximum displacement before modification is much smaller where it was 0.0325 m. These results indicate high suppression of vertical vibrations as a result, stiffer and safer structure.

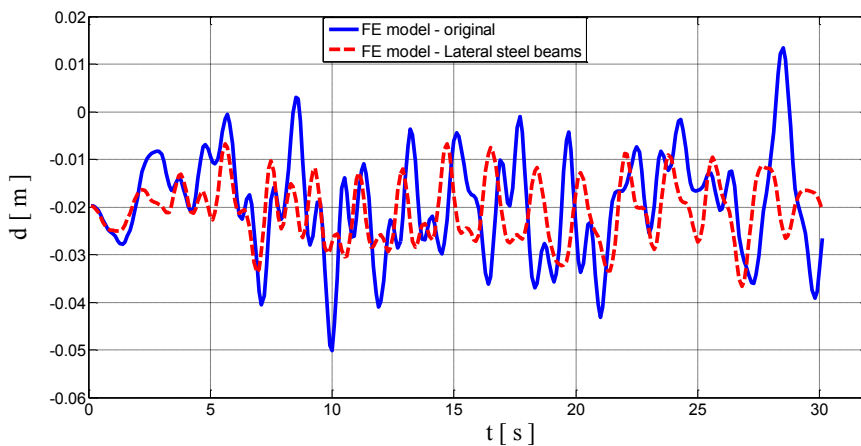


**Figure 6.6** Time history of vertical vibrations at center of the deck mid-span

#### 6.3.3 Results of Torsional Displacements

The torsional vibrations after the structural modification have decreased in wide range too. First the maximum torsional displacements reached 0.02 m and the frequency of fluttering has decreased very obviously till the end of the wind excitation. While the maximum torsional displacements was 0.035 m before the modification, as well as the fluttering rate was quicker (see **Figure 6.7**). This is a firm fact that the structural modification increased the torsional stiffness of the structure.

## 6.4 Results of Control Efficiency

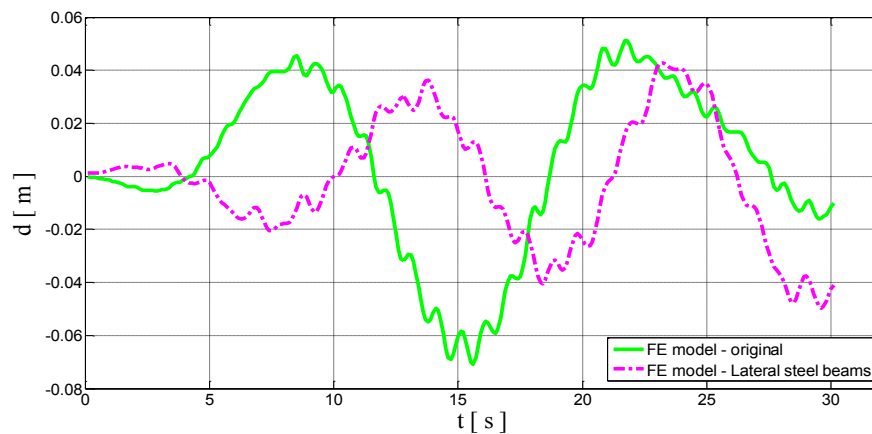


**Figure 6.7** Time history of torsional vibrations at outer edges of the deck mid-span

## 6.4 Results of Control Efficiency

Due to wind excitation for the duration of 30 seconds, the deck exhibited significant vertical and torsional vibrations. In order to control these vibrations, lateral steel beams to increase the structural stiffness of the system were adopted. The deck vibrations of the cable stayed bridge model after structural modification have decreased to a large limit. For vertical displacement at the mid span of the deck center, the displacement decreased in a wide range in such a way for the overall response the control efficiency reached 64.73% compared to the same response of the deck at the same point without structural modification. While the torsional displacement of the deck at the mid span point decreased too much, and the control efficiency for this case was 88.69% in comparison with the deck torsional response before structural modification. This means that this novel method have an efficient action in suppressing both the vertical and torsional vibrations of the deck.



# Chapter 7

## Thermal Fluid-Structure Interaction and Coupled Thermal-Stress Analysis Due to Fire

### 7.1 Standard Temperature-Time Fire Curve

Fire is one of the dangerous incidents for structures. Concrete is considered to resist the fire fairly compared to other materials such as steel and wood. When a high temperature of fire is exposed to concrete for a long time, mechanical properties of the concrete will be lost. When concrete is not protected, the experiments demonstrate that it would decrease its mechanical properties extremely above 300 °C. Standard ISO 834 fire curve is an international temperature-time curve which is used for heat-transfer analysis for structures (see **Figure 7.1**).

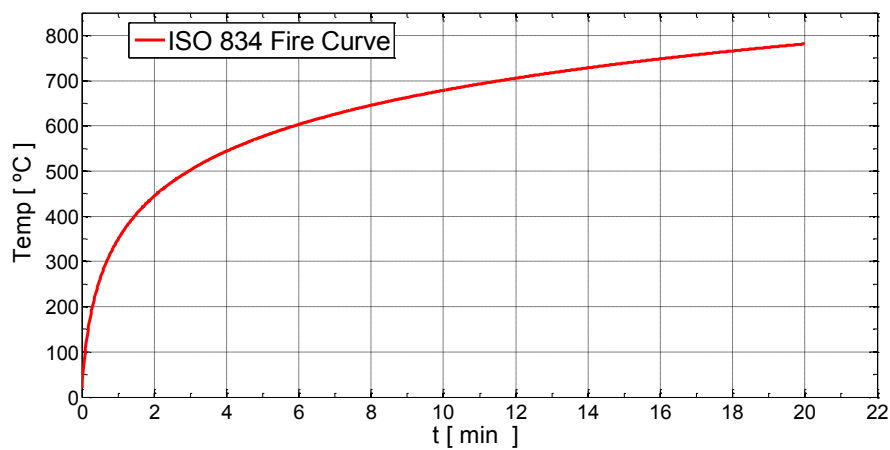


**Figure 7.1** ISO 834 Standard temp - Time fire curve

This name is originated due to the document number prepared at the International Standard Organization. The analysis of temperature is set for a specific time duration where the temperature is a function of time, and the temperature rises as a result of the increase in time, see **Equation (7.1)** [Carstensen, 2011; Sangluaia *et al.*, 2013; Palmklint and Svensson, 2016].

$$T_c = 20 + 345 * \log (8t + 1 ) \quad (7.1)$$

where  $T_c$  represents the temperature in degree Celsius and  $t$  is the time in minutes.

## 7.2 Heat-Transfer Analysis

The surface of any material element which is exposed to fire is subjected to heat-transfer by three modes; conduction, convection and radiation. The conduction is responsible of the internal heat-transfer through concrete structural members only. The temperature gradient drives heat-transfer from the hot to cold regions, which is called heat flux. Convection heat-transfer is due to change in the air density depending on the temperature, where this causes turbulence in the air leading to heat-transfer to nearby regions. Usually convection is ignored for the exposed surface of concrete because it is responsible of less than 10% of heat-transfer at the exposed area, but it is usually considered only for unexposed areas of the concrete surface. The radiation takes place when a structure is exposed directly to a fire, where the surface is heated through heat-transfer [Nakne, 2011; Allam *et al.*, 2013; Patade and Chakrabarti, 2013 and Ab Kadir, 2013].

The convective heat flux  $q_c$  is described by **Equation (7.2)** (EC 1991-1-2 2002).

$$q_c = h_c (T_s - T_a) \quad (7.2)$$

where  $h_c$  is convection coefficient, 25 W/m<sup>2</sup> K (EC 1991-1-2-2002),  $T_s$  is surface temperature (Kelvin) and  $T_a$  is ambient temperature (Kelvin).

Radiation differs from convection, for heat-transfer there is no need for a medium. It consists of electromagnetic waves from a region with high energy to a lower energy region. The emissivity factor is the dependable factor for radiation effect where the materials absorb radiated energy. The radiation heat flux  $q_r$  is described by **Equation (7.3)** (EC 1991-1-2 2002).

$$q_r = \phi * \epsilon_s * \epsilon_a * \sigma * (T_s^4 - T_a^4) \quad (7.3)$$

where  $\phi$  is shape factor, usually 1.0 when radiation to ambient temperature and no other surface (EC 1991-1-2-2002),  $\epsilon_s$  is emissivity of surface,  $\epsilon_a$  is emissivity of ambient, fire usually 1.0 (EC 1991-1-2-2002) and  $\sigma$  is Stephan-Boltzmann's constant,  $5.67*10^{-8}$  W/m<sup>2</sup> K<sup>4</sup>.

The net heat flux is described as the sum of **Equation (7.2)** and **Equation (7.3)**.

$$h_{net} = q_c + q_r \quad (7.4)$$

## 7.2 Heat-Transfer Analysis

The convective heat flux and radiation heat flux are depending on the temperature difference between the surface and ambient air. When the temperature is low, the main contribution to the total heat flux is from convection but when the temperature raises, the effect of radiation will govern.

### 7.2.1 Thermal Analysis of a Cable Stayed Bridge

Generally, the differences in the temperature in the longitudinal direction of bridges are not considered. Only one segmental section of the deck is appropriate to analyze the distribution of temperature due to fire exposition (see **Figure 7.2**). The process of heat-transfer in the segmental deck which is exposed to fire occurs through heat conduction, heat convection and thermal radiation. Where the heat conduction happens in the interior of the deck and it is governed by the Fourier heat-transfer equation. While heat convection takes place through energy exchange between the deck surface and the surrounding air which results in the diffusion and motion of the air. Furthermore, the radiation occurs via energy transfer from the fire to the deck and vice versa.

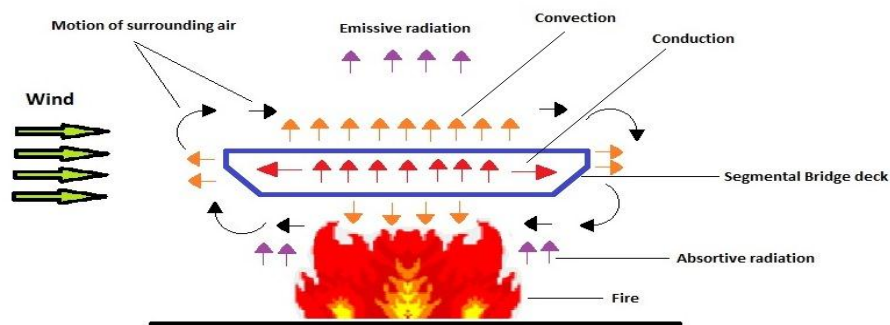


**Figure 7.2** The heat-transfer process of a segmental bridge deck exposed to fire

### 7.2.2 Heat-Transfer Theory

The temperature of a point in a bridge can be expressed as  $T_c = T_c(x, y, z, t)$  where  $x$ ,  $y$ , and  $z$  are Cartesian coordinates of the point and  $t$  = time. Heat-transfer theory is governed by the typical Fourier heat-transfer equation:

$$\rho c \frac{\partial T_c}{\partial t} = k \left( \frac{\partial^2 T_c}{\partial x^2} + \frac{\partial^2 T_c}{\partial y^2} + \frac{\partial^2 T_c}{\partial z^2} \right) \quad (7.5)$$

where  $k$  = isotropic thermal conductivity coefficient;  $\rho$  = density; and  $c$  = specific heat of the material. The temperature field of a structure at a specific time can be obtained by solving the preceding Fourier partial differential equation under initial and boundary conditions.



### 7.2.3 Thermal Boundary Conditions

There are three types of boundary conditions related to the structural thermal analysis. The first is that the structural boundary temperature is exactly known. The second is that the heat flux on the structural boundary is determinate. The third is that the heat flux on the structural boundary is proportional to the temperature difference between the bridge and the air. The boundary conditions associated with **Equation (7.5)** for the thermal analysis of a bridge can be written as a combination of types 2 and 3:

$$k \frac{\partial T_c}{\partial n} = h (T_a - T_s) + q \quad (7.6)$$

where  $n$  is normal to the surface and the heat-transfer coefficient is:  $h = h_c + h_r$  which is combining the heat-transfer coefficients of convection  $h_c$  and thermal irradiation  $h_r$  and its unit is  $W/m^2K$ .

$T_a$  is air temperature;  $T_s$  is structural surface temperature; and  $q$  is boundary heat exchange per unit area (heat fluxes, positive for inflow). The heat-transfer coefficient of convection  $h_c$  is related to wind speed. The wind blowing across the bridge surface significantly affects the heat-transfer convection coefficient and consequently influences the accuracy of the thermal analysis results. Previous studies on bridge thermal analysis used a constant value of wind speed for all structural surfaces. The heat-transfer coefficient of thermal radiation  $h_r$  depends on the structural material, surface temperature, and air temperature [Elbadry and Ghali, 1983; Lienhard and Lienhard, 2003; Choi *et al.*, 2012 and Zhou *et al.*, 2016].

## 7.3 Thermal Fluid-Structure Interaction

Thermal fluid-structure interaction (TFSI) happens in many engineering applications, for example in designing aircraft turbines, vehicle engines and in biomechanical fields. A full set of interaction phenomenon between the fluid and the solid is available in all mentioned applications. The interaction comprises the action of the fluid on the solid, also the solid acts on the fluid and additional heat-transfer exists in the whole system. In TFSI, a thermal field is considered in addition to the fluid and the structural fields. Considering the thermal field in the respective domain, flow and solid, describes a volume-coupled problem. The volume coupling to the thermal field is processed in each domain either with a partitioned approach or with a monolithic scheme, where surface coupling of the thermal field between the two domains is required. Therefore, the interaction of fluid, structure and thermo field leads to many different coupling processes. Reynolds-averaged Navier-Stokes is used to model the interaction phenomenon and the nonlinear Fourier heat conduction equations are used for the

## 7.3 Thermal Fluid-Structure Interaction

---

fluid and the solid phase, respectively. The thermal fluid-structure interaction investigates the heat exchange between a heated bridge deck and the air flow due to fire [Pironkov, 2010; Grilli *et al.*, 2012; Yin *et al.*, 2012; Gleim *et al.*, 2014; Birken *et al.*, 2015 and Talebi *et al.*, 2015].

### 7.3.1 Governing Equations

On a domain  $\Omega_1 \subset \mathbb{R}^d$  the physics is described by a fluid model, whereas on a domain  $\Omega_2 \subset \mathbb{R}^d$ , a different model describing a structure is used. The two domains are almost disjoint. The part of the interface where the fluid and the structure are supposed to interact is called the coupling interface. On this surface the coupling conditions are the temperature and the normal component of the heat flux which are both continuous across the interface.

### 7.3.2 Fluid Model

The fluid is modeled using the Reynolds-averaged Navier-Stokes equations, which are a second order system of conservation laws (mass, momentum, energy) modeling viscous compressible flow. We consider the two dimensional case, written in conservative variables density  $\rho$ , momentum  $m = \rho v$  and energy per unit volume  $E$ .

herein the following equation represents the viscous shear stress tensor

$$\tau_v = \eta (\nabla v + \nabla v^T) \quad (7.7)$$

and the heat flux is:

$$\mathbf{q} = -\lambda \nabla \theta \quad (7.8)$$

As the equation is dimensionless, the Reynolds number  $Re$  and the Prandtl number  $Pr$  appear. The equations are closed by the equation of state for the pressure:

$$p = (\gamma - 1) (\rho E - 0.5 |\mathbf{v}|^2) \quad (7.9)$$

## 7.4 Finite Element Model of TFSI

---

Furthermore, a Spalart-Allmaras one-equation model is used for the existing turbulence. The spatial discretization is done by a finite volume method whereas a Runge-Kutta method is used for the time integration.

$$\frac{\partial \rho}{\partial t} + \nabla \cdot (\rho \mathbf{v}) = 0 \quad (7.10)$$

$$\frac{\partial \rho \mathbf{v}}{\partial t} + \nabla \cdot (\rho \mathbf{v} \otimes \mathbf{v}) + \nabla p = \frac{1}{Re} \nabla \cdot \boldsymbol{\tau}_v \quad (7.11)$$

$$\frac{\partial \rho E}{\partial t} + \nabla \cdot (\mathbf{v} (\rho E + p)) = \frac{1}{Re} \left[ \nabla \cdot (T \mathbf{v}) - \frac{1}{Pr} \nabla \cdot \mathbf{q} \right] \quad (7.12)$$

### 7.3.3 Solid Model

The governing equations within the solid domain  $\Omega_2$  are given by the balance of heat energy and the Fourier law:

$$\rho \cdot h_s(\psi) \psi_r(x, t) = -div \mathbf{q}(x, t, \psi) - Q(x, t) \quad (7.13)$$

$$\mathbf{q}(x, t, \psi) = -\dot{H}(\psi) \nabla \psi(x, t) \quad (7.14)$$

here,  $\mathbf{q}$  is the heat flux vector,  $\psi_s$  the temperature of the solid,  $\psi_r$  the temperature rate,  $\rho$  the density,  $Q$  the heating source and  $\dot{H}(\psi)$  as well as  $h_s(\psi)$  are the temperature dependent conductivity and specific heat capacity. The Neumann boundary conditions are the forced convection  $\bar{c}$  of the fluid together with the thermal radiation  $\mathcal{E}(\psi) \sigma [\psi^4 - \psi_\infty^4]$  at the surface with the Stefan Boltzmann constant  $\sigma$ , the emissivity  $\mathcal{E}(\psi)$  and the bulk temperature is  $\psi_\infty^4$ .

## 7.4 Finite Element Model of TFSI

The finite element model of thermal fluid-structure-interaction between the fire heated segmental deck of a cable stayed bridge and the surrounding air due to heat-transfer when there is a wind flow in the same time by considering three fire scenarios is modeled as follows:

The model of the segmental bridge deck is generated in ABAQUS once in CFD and another in CSD. The CFD model is with a dimension 2.6 m height and total width of 22 m as shown in **Figure 7.3**. The thickness is 0.01 m. The flow domain size is 140 m length and 40 m height.

## 7.4 Finite Element Model of TFSI

Material properties for the CFD model are assigned where the air density is  $1.29 \text{ kg/m}^3$  and the dynamic viscosity of the air is  $(1.8\text{E-}05) \text{ Pa}\cdot\text{s}$ . The thermal conductivity of the air is  $0.0257 \text{ W/m}^2\text{K}$ , specific heat of air is  $1005.4 \text{ J/kg}\cdot\text{K}$  and the thermal expansion coefficient of air is  $0.00343 \text{ K}^{-1}$ .

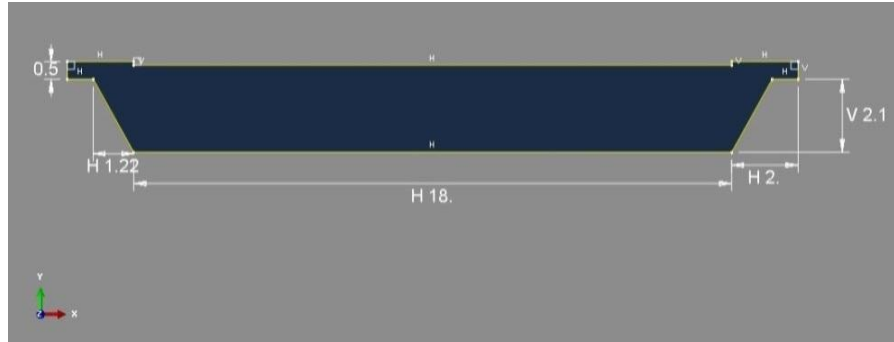


**Figure 7.3** Deck TFSI-model dimensions

The CFD model part is meshed using CFD element fluid family with FC3D8: A-8 node linear fluid brick. The deck wall assigned with 0.4 element size and the flow domain with 1 element size.

The CSD model have the following material properties concrete density is assigned  $2643 \text{ kg/m}^3$ , Youngs modulus  $200\text{E}+08$  and the Poissons ratio 0.2. The role of the steel reinforcement is neglected for simplicity because the thickness of the CSD model is too small 0.01m and the reinforcement has no direct contact with the air. The thermal conductivity, specific heat and the thermal expansion coefficient of the concrete are set with amplitudes supporting on temperature dependent data due to Eurocode EN 1994-1-2. The CSD model part is meshed using heat-transfer family with DC3D8: A-8 node linear heat-transfer brick.

A flow step with 100 seconds duration is created for the CFD model by activating the energy equation for temperature to enable the heat-transfer in the flow. An initial condition of fluid thermal energy is assigned for the whole model both the deck and the fluid domain to represent the ambient temperature of 293.15 K. Another transient heat-transfer step with 100 seconds is created for the CSD model. Also the same initial condition of temperature 293.15 K is assigned for the CSD model. The step time in each model must be the same, in addition to adding interaction with the same name in each model for the surfaces of interaction, also the important issue related to mesh generation is equality of the mesh size in each model. Four boundary conditions are defined for the CFD model, fluid B.C for the inflow and far fields assigning the air velocity value in the horizontal direction only (zero attack angle). The other two directions with zero magnitudes, fluid B.C for the outflow assigning zero pressure and fluid B.C for the front and back of the flow model with zero velocity magnitude for the

## 7.4 Finite Element Model of TFSI

third direction perpendicular to the model (z- direction), and no-slip fluid B.C for the wall condition of the deck.

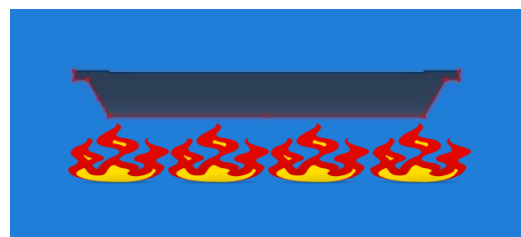
A temperature conduction boundary condition is defined for the surface of the CSD model supporting on three fire scenarios (above, under and beside) the deck by assigning time-temperature data amplitude due to ISO 834 fire curve. A heat flux load of  $100\,000\text{ W/m}^2$  (fire flames) is assigned to the surface of the CSD model three times (three fire scenarios). A convection interaction is assigned (three fire scenarios) with the film coefficient  $23.5\text{ W/m}^2\text{K}$  and sink temperature  $293.15\text{K}$ . A radiation interaction is assigned to the surfaces of the deck (three fire scenarios) with an emissivity of 0.85 for the concrete and ambient temperature  $293.15\text{ K}$  in addition the absolute zero temperature should be activated and assigned  $-273.15$  and the Stefan Boltzmann constant  $5.67\text{E-}08$ . A co-simulation job is generated for both the CFD and the CSD models together to enable transient heat-transfer type of thermal coupling between the two models.

### 7.4.1 Fire Scenarios

Three fire scenarios for 100 seconds duration are being considered to analyze the transient heat-transfer due to the difference in temperature between the surrounding air and the segmental deck where the incoming wind is cooler supporting on standard ISO 834 fire time-temperature curve. The first situation of the fire is above the segmental deck, the second scenario is under the segmental deck and the last scenario is beside the deck (see **Figure 7.4**).



a- Fire scenario-1



b- Fire scenario-2



c- Fire scenario-3

**Figure 7.4** Segmental deck exposed to fire scenarios

### 7.4.2 Results of TFSI-Models Simulations

The numerical simulation of the finite element model of the deck when exposed to three fire scenarios for 100 seconds duration which is considered a transient heat-transfer process is simulated in both the vorticity and temperature fields so that to explain the thermal effect of fire on the vortex shedding generated due to wind flow with a velocity of 6 m/s. The effect of the heat-transfer occurs due to conduction, convection and radiation methods, which have appreciable effect on the generated lift and drag forces in the deck.

Considering fire scenario 1, in the vorticity field the vortices are shed in a regular pattern from the tail of the deck in the lower region, but in the upper region the vortices tend to connect at the beginning of the shedding due to fire effect, but after a short distance the vortices start to separate generating vortex shedding. The connection of the vortices occurs again and becomes continuous. Regarding the temperature field, the thermal vortices are seen with a semi regular pattern with difference in the temperature. The temperature of the vortices is high in the start of the wake region reaching 658.8 °C while it decreases after shedding from the tail of the deck regularly till 459.3°C (see **Figure 7.5.a** and **Figure 7.5.b**).

Regarding scenario 2, in the vorticity field the vortices are shed in a regular pattern from the tail of the deck in the lower region, but in the upper region the vortices tend to connect at the beginning of the shedding and after a shortly the vortices separate in the same way as scenario1. The connection of the vortices occurs again and becomes continuous. While for the temperature field, the thermal vortices are seen with a vanishing pattern with difference in the temperature, which is high in the start of the wake region up to 658.8 °C while it decreases after shedding from the tail of the deck linearly till 592.3°C, where the vortices are being cooled slower than of the case in scenario 1 (see **Figure 7.5.c** and **Figure 7.5.d**). While in scenario 3, in the vorticity field the vortices are shed in a regular pattern from the tail of the deck in both the lower and upper regions. The vortices shed continuously with a better pattern of vortex shedding. While for the temperature field, the thermal vortices are seen with a continuous pattern with difference in the temperature. The temperature of the vortices is high in the start of the wake region up to 658.8 °C while it decreases after shedding from the tail of the deck linearly till 426.1°C which means that the vortices suffer from faster cooling during shedding compared to the cases of scenario 1 and scenario 2 (see **Figure 7.5.e** and **Figure 7.5.f**). To identify which fire scenario is critical for vortex induced vibration, analysis of generated lift and drag forces is a must, and it is detailed in the next sections.

## 7.4 Finite Element Model of TFSI

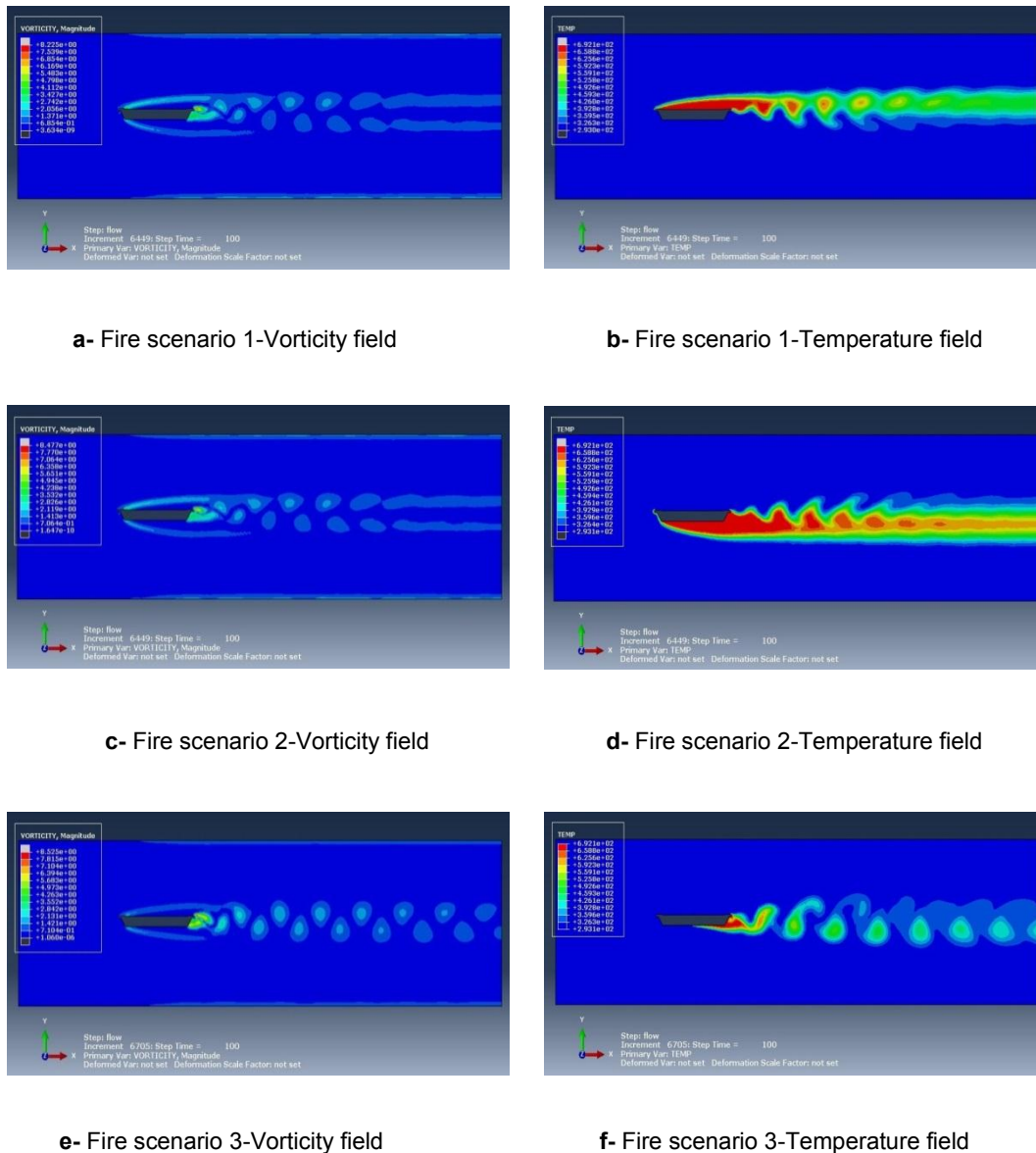


**Figure 7.5** TFSI-Models-Fire scenarios

### 7.4.3 Results of Lift and Drag Forces-FSI-Models

In order to identify the effect of thermal coupling of fluid-structure interaction due to wind flow for the deck of the cable stayed bridge during fire incident, analysis of the fire scenarios without thermal coupling is a valuable step so that to measure the difference in the behavior of the deck with respect of the vortex induced vibration. The generated lift and drag forces are other criteria of analysis, where the effect of fire is identified.

When there is no fire incident and just the fluid-structure interaction is considered, the lift forces amplitudes have a stable and regular frequency with range values (9000-19000) N. The drag forces have the same regular, stable frequency but lower amplitudes ranging between

## 7.4 Finite Element Model of TFSI

(3000-7000) N. The lift forces values are three times of the drag forces values approximately (see **Figure 7.6.a**).

Now fire scenarios are added to the numerical simulations to search the effect of transient heat-transfer without thermal coupling. In fire scenario 1, the fire region is above the deck. The lift forces values have a stable and regular frequency range of (50-80) N, where these values are much lower than the values of lift forces in the case of no fire scenario. While the drag forces have much lower amplitude values than the values of drag forces in the case of no fire scenario which are between (910-1330) N. The drag forces values are 18 times of the lift forces values approximately (see **Figure 7.6.b**). This is an indication that fire scenario 1 will decrease the lift and drag force in deck to a high ratio which is very significant in suppressing the vertical and horizontal vibration of the deck.

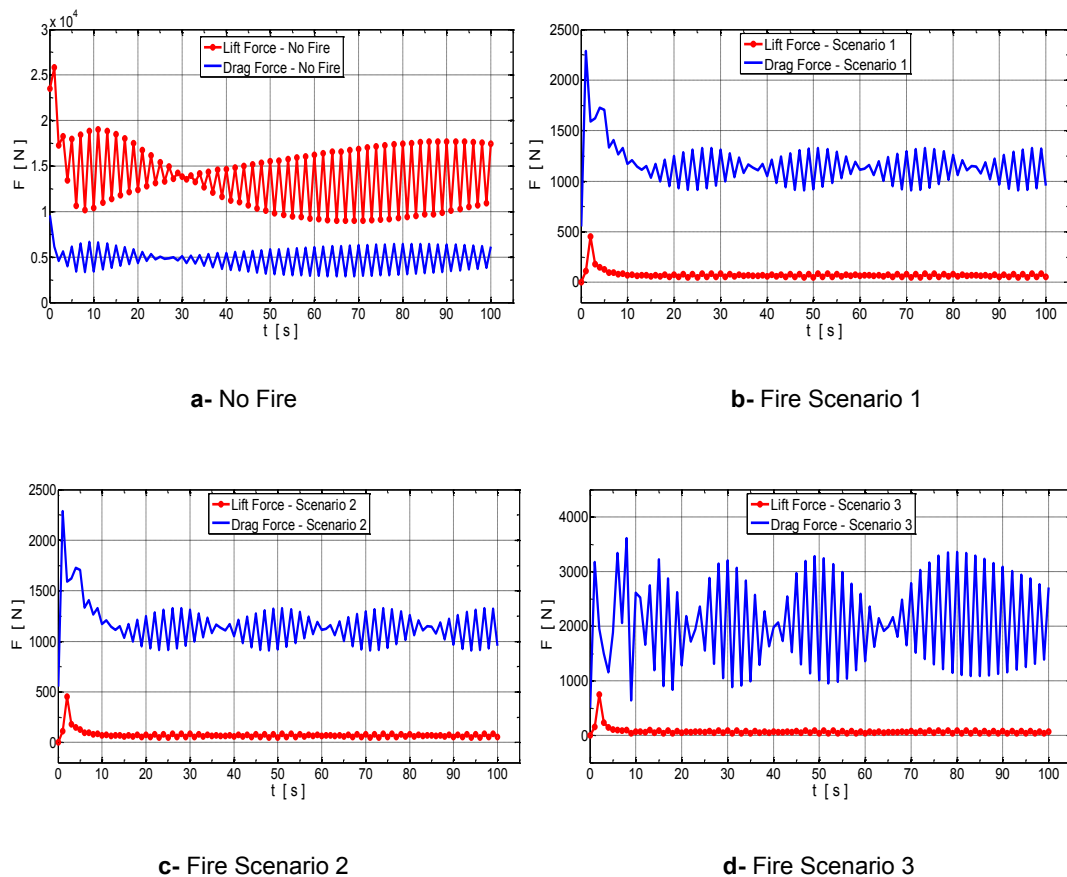


**Figure 7.6** Lift and drag forces-FSI models

In fire scenario 2, the fire region is under the deck. The lift forces values have a stable and regular frequency of (50-85) N the same as the scenario 1 without any change. The drag forces have amplitude values between (910-1330) N the same as scenario 1 without any change (see



## 7.4 Finite Element Model of TFSI

---

**Figure 7.6.c).** This is an indication that fire scenario 2 is very significant like the fire scenario 1 in suppressing the vertical and horizontal vibration of the deck to very high ranges.

In fire scenario 3, the fire region is under the deck but just at half of the region in one side only. The lift forces values have a stable and regular frequency of (35-90) N the same as the scenario 1 approximately. The drag forces have amplitude values between (640-3610) N different from scenario 1 and scenario 2, where the amplitude of the drag forces are much higher (see **Figure 7.6.d**). This is an indication that fire scenario 3 is more important in increasing the horizontal vibration of the deck, but it decreases the vertical vibration to a range which near to the range of its values in scenario 1 and scenario 2.

When no thermal coupling is considered, there is a nonlinear behavior of the deck under the fire scenarios with respect to both vertical and horizontal vibrations of the deck. So a special consideration should be given to each case supporting on the specifications of a certain design aims when considering transient heat-transfer due to fire.

### 7.4.4 Results of Lift and Drag Forces-TFSI-Models

Thermal coupling in the numerical simulations for the fire scenarios is utilized to search the effect of the of transient heat transfer on vortex induced vibration of the deck and behavior of the deck under the generated lift and drag forces. The case of no fire scenario available in the numerical simulation has been mentioned in the previous section, and here is considered only for comparison purpose so that to see the effect of thermal coupling on the behavior of the deck.

Fire scenarios are added to the numerical simulations to search the effect of transient heat-transfer with thermal coupling. In fire scenario 1, the lift forces values have a stable and regular frequency range of (4810-11620) N, where these values are lower than the values of lift forces in the case of no fire scenario up to half of their values approximately. While the drag forces have higher amplitude values than the values of drag forces in the case of no fire scenario but with regular repeated amplitudes relatively, and their values are between (2400-7160) N (see **Figure 7.7.b**). This is an indication that fire scenario 1 will decrease the lift forces to the half of its value and increase the amplitude of the drag force in deck. This behavior proves that a significant suppression in the vertical vibration will occur and negatively the horizontal vibration of the deck would be increased.

## 7.4 Finite Element Model of TFSI

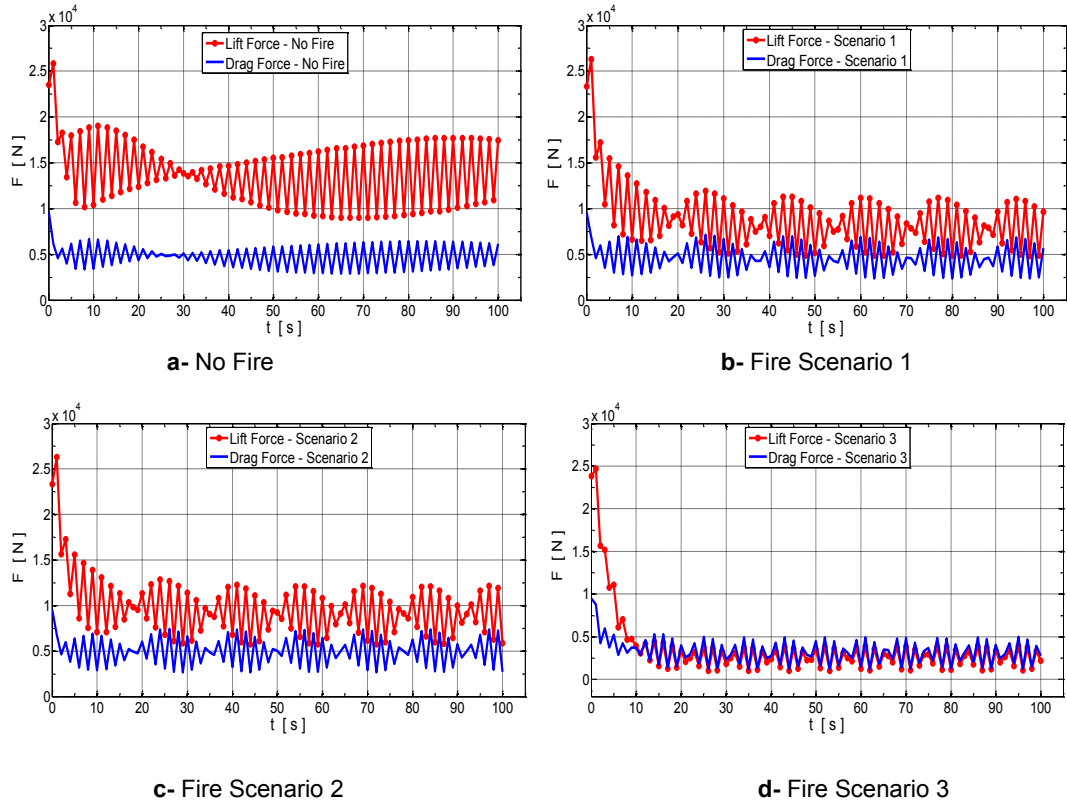


**Figure 7.7** Lift and drag forces-TFSI models

In fire scenario 2, the lift forces values have a stable and regular frequency of (4810-11620) N the same as the scenario 1 without any change. The drag forces have amplitude values between (2400-7160) N the same as scenario 1 without any change (see **Figure 7.7.c**). This is evidence that in fire scenario 2 the deck behaves like its behavior in the case of fire scenario 1 in suppressing the vertical vibration and increasing the horizontal vibration of the deck to a small range.

In fire scenario 3, the lift forces values have a stable and regular frequency of (1010-4420) N with a semi regular and stable frequency but much lower than the lift forces values in scenario 1 and scenario 2. The drag forces have amplitude values between (1210-5270) N which is much lower than its values in scenario 1 and scenario 2 (see **Figure 7.7.d**). This is an indication that fire scenario 3 is significant among the other scenarios in mitigating both the horizontal and vertical vibrations of the deck

When thermal coupling is adopted in the numerical simulations, there is a nonlinear behavior of the deck under fire scenario 1 and scenario 2 with respect to both vertical and horizontal vibrations of the deck. Furthermore, there is a significant behavior of the deck under fire

## 7.4 Finite Element Model of TFSI

---

scenario3 where both the horizontal and vertical vibrations are being suppressed to a good extent.

Finally, by comparing the behavior of the deck under fire scenarios in the FSI simulations and the TFSI simulations, a fact arises which is clear that considering TFSI will result in significant suppression of both horizontal and vertical vibrations in scenario 3 where the fire is under the deck at one side. The same suppression in vertical vibration occurs in both scenario 1 and scenario 2 but with a small increase in the horizontal vibration.

### 7.4.5 Results of Lock-in Phenomenon

To analyze the vortex shedding and generation of lock-in phenomenon, TFSI models are utilized supporting on the fire scenario 2 because the critical maximum lift and drag forces are generated in this scenario. Twenty five TFSI models and twenty five FSI models are utilized supporting on different wind flow velocities starting from 1 m/s to 15 m/s this after thorough investigations to identify the first lock-in region in advance before starting analysis. The first lock-in region for TFSI models was found to be between wind velocity (9-11.8) m/s and between (10-11.5) m/s for FSI models (see **Table 7.1**). Numerical simulations for all the models are utilized to identify the vortex shedding frequencies where lock-in regions are located (see **Figure 7.8**).

The vortex shedding frequency for TFSI models is starting from 0.122 Hz for the wind velocity 1 m/s and linearly continues till the wind velocity 8 m/s with shedding frequency of 0.979 Hz. After this point the vortex shedding frequency tends to reach a constant point of 1.059 Hz at wind velocity 9 m/s. The vortex shedding will remain constant approximately till wind velocity 11.8 m/s at shedding frequency of 1.122 Hz. The wind velocity region from 9 m/s to 11.8 m/s is called lock-in region. While for FSI models the vortex shedding frequency starts at 0.111 Hz where the wind velocity is 1 m/s and the curve continues to rise linearly till shedding frequency of 1.154 Hz for wind velocity 10 m/s. The shedding frequency becomes constant until shedding frequency 1.183 Hz at wind velocity 11.5 m/s. The constant region is the lock-in region for FSI model (see **Figure 7.8**).

In this region the amplitude of vibrations is independent from the shedding frequency despite of the increase in wind velocity, where resonance is expected to occur and serious damage, or may be failure of the structure to take place.

## 7.4 Finite Element Model of TFSI

**Table 7.1**

Lock-in data for TFSI and FSI models

	TFSI models	FSI models
Wind Velocity m/s	Vortex shedding frequency Hz	Vortex shedding frequency Hz
1	0.122	0.111
2	0.255	0.221
3	0.383	0.329
4	0.506	0.455
5	0.612	0.571
6	0.734	0.676
7	0.856	0.809
8	0.979	0.942
9	1.059	1.067
10	1.069	1.154
11	1.087	1.164
11.5	1.111	1.183
11.6	1.112	1.233
11.7	1.117	1.236
11.8	1.122	1.363
11.9	1.456	1.369
12	1.468	1.386
12.1	1.481	1.456
12.2	1.493	1.412
12.3	1.505	1.447
12.4	1.517	1.465
12.5	1.53	1.485
13	1.591	1.535
14	1.713	1.617
15	1.861	1.777

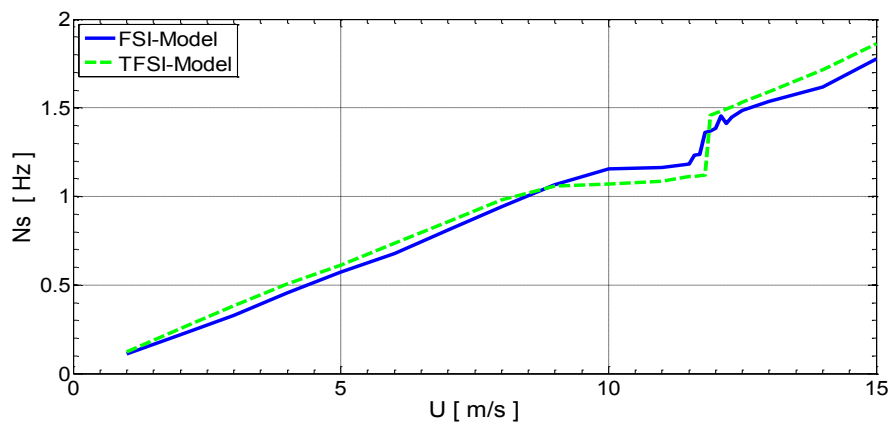


**Figure 7.8** Lock-in Phenomenon - TFSI and FSI models

## 7.5 Validation of TFSI-Models

The results of lock-in phenomenon calculated from the numerical simulations of TFSI models in addition to FSI models are validated with Simiu and Scanlan benchmark which are the numerical results of the lock-in obtained by them. The lock-in region of TFSI models starts from wind velocity 9 m/s and continues till wind velocity of 11.8 m/s, while for FSI models the wind velocity range in lock-in region is (10-11.5) m/s. When comparing the two results with the lock-in region by Simiu and Scanlan it is clear the two models are having the same shape and the same constant region of shedding frequencies approximately which is a very good agreement between all the results (see **Figure 7.9**). In the same time the comparison between the results of lock-in region of TFSI and FSI models, shows that the results of TFSI models has wider lock-in region or wider critical wind velocity range and earlier critical wind velocity is detectable in addition to lower natural frequency of the system for vibration at lock-in region which is very significant in the design of long span bridges regarding vibrations due to wind excitations.

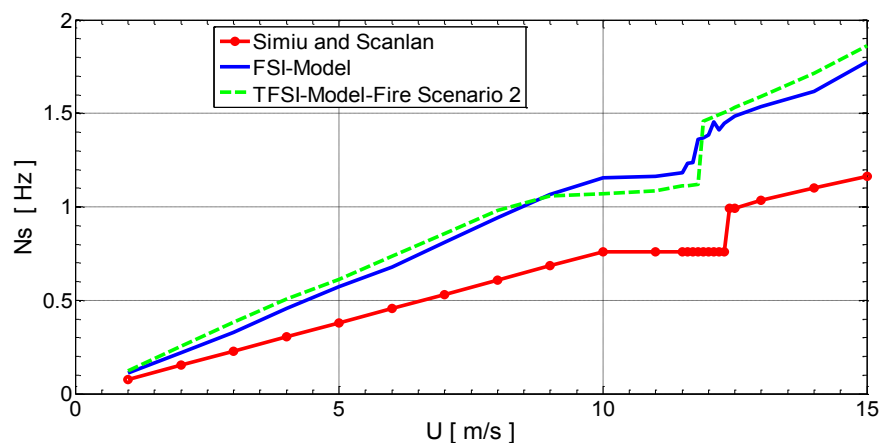


**Figure 7.9** Lock-in TFSI-models validation

## 7.6 Coupled Thermal-Stress Analysis

Coupled thermal-stress in bridges is a heat-transfer simulation which induces stresses through thermal expansion of the structure due to elevated temperature of the structure. The thermal effects on the bridges are expansion and deformations of the structure, stresses inducing cracks or spalling of the concrete depending on the duration of the heating source, in this analysis the source is three scenarios of fire incidents.

Modeling of thermal-stress analysis or coupled problems in general [Zhuang *et al.*, 2014] poses significant challenges on the computational methods, particularly when coupled with fluid-structure interaction and fracture. [Rabizadeh *et al.*, 2016] proposed an adaptive FE analysis for thermoelasticity problems in the context of the finite element method. Efficient approaches to fracture include meshfree methods [Rabczuk *et al.*, 2004; Rabczuk and Belytschko, 2005; Amiri *et al.*, 2014; Amiri *et al.*, 2016] the extended finite element method, phantom node methods [Rabczuk *et al.*, 2008; Chau-Dinh *et al.*, 2012; Vu-Bac *et al.*, 2013], extended meshfree methods [Rabczuk and Areias, 2000; Rabczuk and Belytschko, 2006; Rabczuk *et al.*, 2007; Zi *et al.*, 2007; Rabczuk and Zi, 2007; Rabczuk *et al.*, 2007; Bordas *et al.*, 2008; Rabczuk *et al.*, 2008; Rabczuk *et al.*, 2010; Amiri *et al.*, 2014], efficient remeshing techniques [Areias *et al.*, 2013; Areias *et al.*, 2013; Areias *et al.*, 2013; Areias *et al.*, 2015; Areias *et al.*, 2016], screen-Poisson models [Areias *et al.*, 2016 and Areias *et al.*, 2016], cracking particles methods [Rabczuk and Belytschko, 2004; Rabczuk and Areias, 2006; Rabczuk and Belytschko, 2007; Rabczuk *et al.*, 2007; Rabczuk and Samaniego, 2008; Rabczuk *et al.*, 2010], anisotropic softening elements [Areias *et al.*, 2014], extended IGA [Ghorashi *et al.*, 2015; Jia *et al.*, 2015; Nguyen-Thanh *et al.*, 2015; Quoc *et al.*, 2016], multiscale methods for fracture [Talebi *et al.*, 2013; Budarapu *et al.*, 2014; Silani *et al.*, 2014; Talebi *et al.*, 2014; Budarapu *et al.*, 2014; Talebi *et al.*, 2015; Silani *et al.*, 2016] and peridynamics or dual-horizon peridynamics formulations [Vu-Bac *et al.*, 2015; Amani *et al.*, 2016; Ren *et al.*, 2016; Vu-Bac *et al.*, 2016; Ren *et al.*, 2017 ], to name a few though IGA and XFEM has also been exploited for other applications [Nanthakumar *et al.*, 2013; Valizadeh *et al.*, 2015; Nguyen *et al.*, 2015; Anitescu *et al.*, 2015; Nanthakumar *et al.*, 2015; Ghasemi *et al.*, 2017; Chan *et al.*, 2017; Rabczuk and Ren, 2017; Hamdia *et al.*, 2017; Areias and Rabczuk, 2017 ]. Fluid-structure interaction driven fracture has been proposed for instance in [Rabczuk *et al.*, 2010]. However, a coupled thermal stress analysis involving fluid-structure interaction and fracture has not been carried out so far.

### 7.6.1 Thermal Cracking and Spalling of Concrete

Excessive differences in temperature within a concrete structure or its surrounding result in thermal cracking. This causes contract of the cool part more than the warmer part and consequently the contraction would be restrained. When the tensile stresses exceed the tensile strength of the concrete, the thermal cracks appear. When extreme temperature differences occur, thermal cracks with a random pattern appear on the concrete structural element. Spalling is another aspect of thermal stresses inducing thermal strains which end with the cracking and spalling of portions of concrete. The high temperature and intensity of the fire causes bursting pressure in the moisture trapped within the microstructure of the concrete. Due to unequal thermal expansion between the aggregates, cementitious paste and the steel

## 7.6 Coupled Thermal-Stress Analysis

bars can increase spalling of the concrete. In addition to material properties of the concrete, geometric parameters like section shape and size contribute to the spalling of concrete. Environmental parameters such as heating rate and profile, thermal restraint and temperature level also affect the occurrence of spalling [Stratford and Dhakal, 2008; Bo, 2011; Ervine, 2012; Chung *et al.*, 2013; Mueller and Kurama, 2014 and Klingsch, 2014].

Heating rates in the range of 20-32°C/min are significant for spalling to occur [Khoury, 2000]. The high heating rates occur in the early stages of the fire. Several researchers have identified critical temperature ranges for spalling to start regarding exposed surface to fire. [Akhtaruzzaman and Sullivan, 1970] have stated that exposed surface temperatures in the range of 375 - 425°C for normal weight concretes leads to spalling. [Choi and Shin, 2011] determined theoretically and experimentally the zone of spalling of a reinforced concrete beam exposed to ISO 834 fire where the location of the spalling is at the upper right and left of the external part of the beam.

### 7.6.2 Finite Element Model of Coupled Thermal-Stress

The full model of a cable stayed bridge is created in ABAQUS to undergo thermal stresses due to heat transfer from a fire source for a long duration of 20 minutes supporting on the standard ISO 834 Fire data. Three scenarios (the same as TFSI case) are dedicated to simulate the effect of the fire on the deformations, cracks and spalling of concrete. A cable stayed bridge model is created with 324 m length and 22 m width, the main parts of the bridge is the deck which consists of connected reinforced concrete deck segments with 2.6 m height. Four reinforced concrete pylons with square shapes 4\*4 m dimensions and 103 m height, and 80 stay cables are connecting the deck to the pylons in a fan shape arrangement, each cable with cross section area 0.00785 m<sup>2</sup> (see **Figure 7.10**).

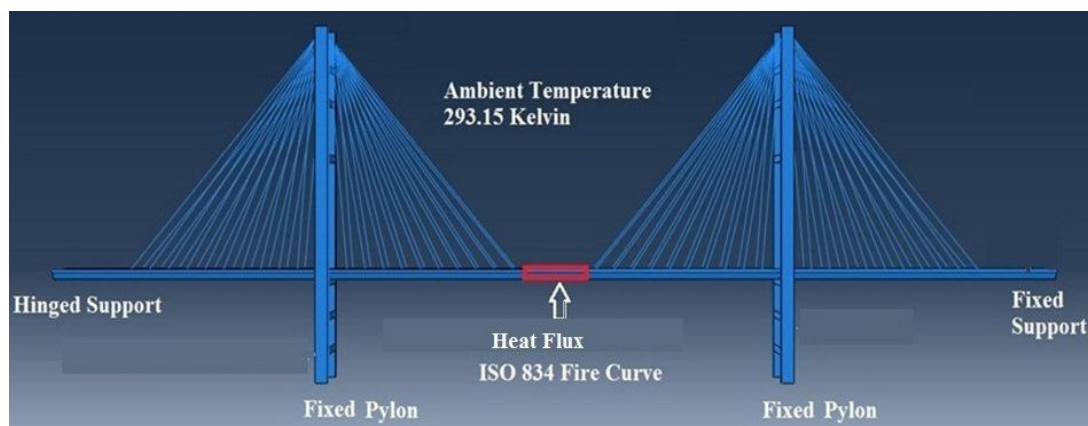


**Figure 7.10** Finite element 3D model of the cable stayed bridge

## 7.6 Coupled Thermal-Stress Analysis

The main steel bar diameter is 0.06 m and the diameter of the temperature steel bars in addition to the stirrups are 0.04 m. The boundary condition of the deck is fixed in one side and free for longitudinal translation in the other side. The pylons are fixed at the bottom and each two pylons are connected by six reinforced concrete ties with 4\*4 m dimensions and 22 m length. The stay cables equivalent Young's modulus of elasticity has been used to approximate the sagging occurrence in the cables because it was modeled as truss elements (see **Table 7.2**). An ambient temperature of 293.15 K is assigned to the whole model, and a static general step is created for duration of 1200 seconds. A predefined field (temperature type) is assigned in to the region where three fire scenarios are considered with amplitude of time dependent temperature (Standard ISO 834 Fire).

**Table 7.2**

Material properties

Material	Mass Density Kg/m <sup>3</sup>	Young's Modulus of Elasticity Pa	Poisson's Ratio	Thermal Conductivity W/m <sup>2</sup> K	Specific Heat J/kg.K
Concrete	2643	2.00E+10	0.20	2	890
Steel bar	7800	2.00E+11	0.30	20	490
Stay cable	9438	1.65E+11	0.30	21	460

To simulate the propagation of the cracks and the spalling in the concrete due to fire action, equivalent thermal stresses are added in the fired regions using XFEM approach for each fire scenario. Maximum principal stress is assigned in addition to the displacement at failure. The start of damage in the simulations is identified with a maximum principal stress generated at the temperature 400°C where the cracks and spalling in the concrete are prone to occur.

The deck is modeled as (C3D10: A10-quadratic tetrahedron) elements, pylons and ties are modeled as (C3D8R: An 8 node linear brick reduced integration hourglass control) elements, the reinforcing steel bars are modeled as (B31: A 2- node linear beam in space) elements and the stay cables are modeled as (T3D2: A 2- node linear 3D truss) elements.

### 7.6.3 Results of Deck Displacements

Three fire scenarios for the duration of 1200 seconds on the middle part of the cable stayed bridge in the region of (22\*20) m is considered and the results of the displacements for each case are calculated for a center point in the middle of the cable stayed bridge model.



## 7.6 Coupled Thermal-Stress Analysis

Considering the maximum horizontal displacements, this maximum value for scenario1 was low which is reached 0.7 cm upward at the end of the 1200 seconds. While for scenario 2, this maximum value was very low which is reached 0.02 cm upward at 172 seconds. Furthermore, the maximum value for scenario3 was high reaching 20.4 cm downward at the end of the 1200 seconds of the fire exposition (see **Figure 7.11**).

Relating to the maximum vertical displacements, all the scenario cases reached their maximum values at the end of the fire exposition after 1200 seconds. Scenario 1 showed very high maximum value of 44.2 cm upward. This maximum value for scenario2 was high reached 33.7 cm downward but it is less than of it in the previous scenario. While for scenario3, the maximum vertical displacement reached 18.1 cm downward which is less than all the scenario cases ( see **Figure 7.12**). Finally, with respect to the maximum angular displacements, all the scenarios reach the maximum value at the end of the 1200 seconds. In scenario 1, the maximum value was  $0.038^\circ$  which is considered very low which is not effective. In the other hand, this value for scenario 2 was  $0.064^\circ$  which is nearly twice the previous value but still not appreciable to induce stresses in the deck. While for scenario 3, the maximum value reached  $0.086^\circ$  which is greater than all the maximum values in scenario 1 and scenario2 and is three times of the maximum value in scenario 1 approximately and it is not an effective in producing stresses in the deck ( see **Figure 7.13**).

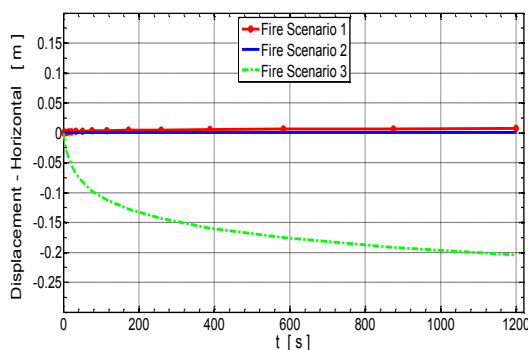


**Figure 7.11** Horizontal displacement

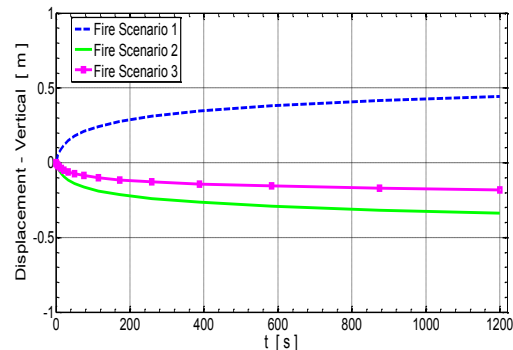


**Figure 7.12** Vertical displacement

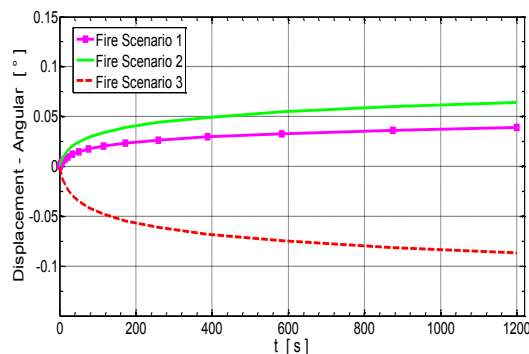


**Figure 7.13** Angular displacement

This is an indication that the horizontal displacement in scenario 3 where the fire is exposed on one side under the deck is the critical case in generating tension stresses in the fired side and compression stresses in the opposite sides of the deck. The vertical displacement in scenario 1 where the position of the fired region is above the deck is the critical case in inducing tension stresses that are the reason of propagation of cracks and spalling of the concrete above the deck whenever these stresses exceed the tensile strength of the concrete. While the angular displacement in scenario 3 is the critical case but it is too low which is not appreciated in the generation and propagation of cracks and spalling of concrete.

### 7.6.4 Extended Finite Element Method

The extended finite element method (XFEM) is a partition of unity based numerical method. It uses the partition of unity to describe the discontinuous displacement and uses the enrichment function to realize the displacement jump over the discontinuity, see **Equation (7.15)** which represents the discretization of the displacement field in 1D. The first term is the continuous displacement while the second term is the discontinuous displacement.

$$u^h(X) = \sum_{J \in \delta} N_J(X) u_J + \sum_{J \in \delta_c} N_J(X) H(f(X)) a_J \quad (7.15)$$

The classical finite element approximation is enhanced by means of enrichment functions. The enrichment procedure is employed on a local level for the XFEM. Thus, only nodes close to the crack tip, as well as the ones required for the correct localization of the crack, are enriched. In the XFEM, enrichment functions are added to additional nodes, in order to include information about discontinuities and singularities around the crack. These functions are the asymptotic near-tip solutions, which are sensitive to singularities, and the Jump function, which simulates the discontinuity when the crack opens. This evidently entails a tremendous computational advantage. The XFEM method was firstly introduced by [Belytschko and Black, 1999]. Their work, in which a method for enriching finite element approximation in such a way that crack growth problems can be solved with minimal remeshing, represents a milestone in the XFEM history. Later on, much more elegant formulations, including the asymptotic near-tip field and the Heaviside function in the enrichment scheme, have been proposed [Dolbow, 1999; Moes *et al.*, 1999; Dolbow *et al.*, 2000]. The XFEM method, furthermore, has been demonstrated to be well suited for three dimensional crack modelling [Sukumar *et al.*, 2000]. Let's assume we have a crack in element 2 between nodes 2 and 3. To capture the discontinuity, we multiply the FE shape function  $N_J$  with a so-called enrichment function. Since we know the displacement field is discontinuous, we use a discontinuous enrichment function such as the step function. The

## 7.6 Coupled Thermal-Stress Analysis

Figure 7.14 shows the enriched shape functions of node 2 and node 3 which can be seen that they are discontinuous across the crack.

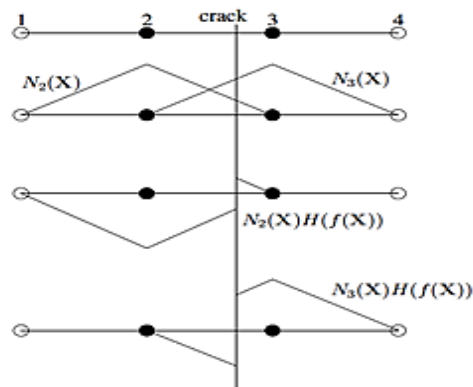


Figure 7.14 Enriching shape functions of node 2 and node 3

Regarding the XFEM discretization of the temperature field due to fire, we assume that the temperature is discontinuous across the crack and therefore we adopt the same enrichment strategy as for the displacement field.

The XFEM capabilities can be extended if employed in conjunction with the level set method (LSM) [Osher and Sethian, 1988; Stolarska *et al.*, 2001; Ventura *et al.*, 2003] which is a technique for describing a crack and tracking the motion of the crack. The first level set function describes the crack surface  $\Phi$  (phi), the second level set function is constructed so that the intersection of two level sets gives the crack front  $\Psi$  (psi). Such method permits to represent the 3D crack for both the position and the location of the crack tips (see Figure 7.15).

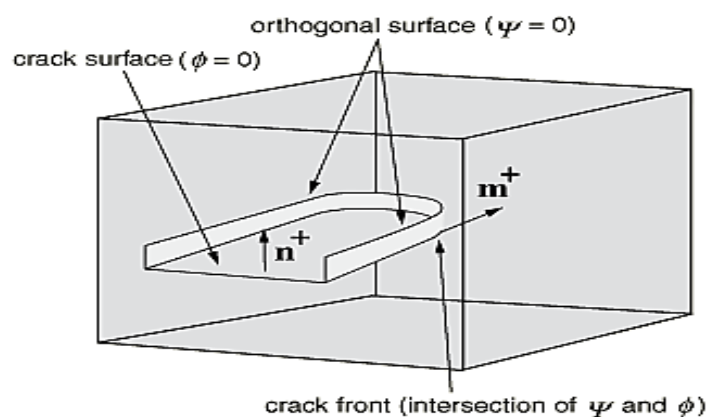


Figure 7.15 Crack in 3D by two level set functions  $\Phi$  and  $\Psi$

## 7.6 Coupled Thermal-Stress Analysis

### 7.6.5 Results of Cracking and Spalling of The Deck

To identify the damaged regions in the cable stayed bridge model, maximum principal stress values calculated in ABAQUS are used for damage detection with the support of XFEM to simulate the propagation of the cracks and occurrence of spalling in the concrete. In all fire scenarios the duration of the fire is 20 minutes supported on standard ISO 834 Fire data.

In fire scenario 1, the fired region is shown (see **Figure 7.16**). Cracks and spalling of concrete can be seen at the middle and external edges of deck (see **Figure 7.17**). The cracks propagated from the inner edges of the flange toward the external edges leading to occurrence of spalling. This is due to high vertical displacement upward and angular displacement of the deck caused by the thermal stresses which induced high tensile stresses in the concrete exceeded the tensile strength of the concrete.

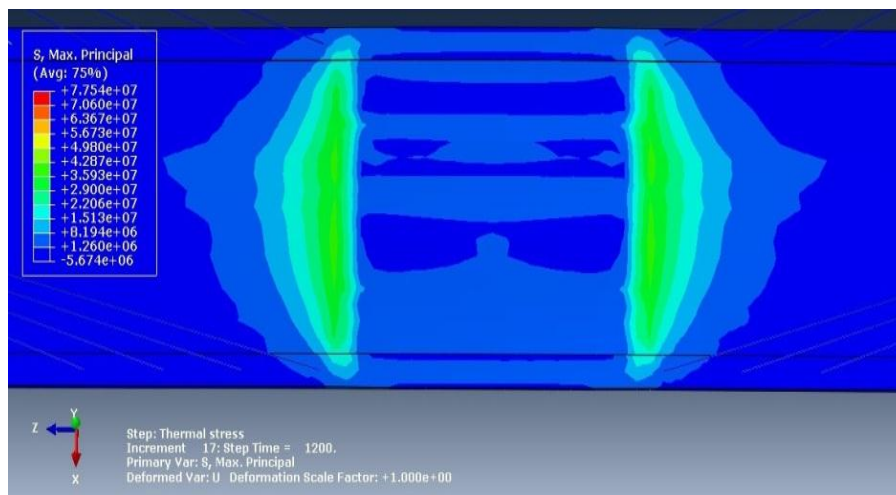


**Figure 7.16** Maximum principal stress - Fire scenario 1- Without XFEM damage simulation

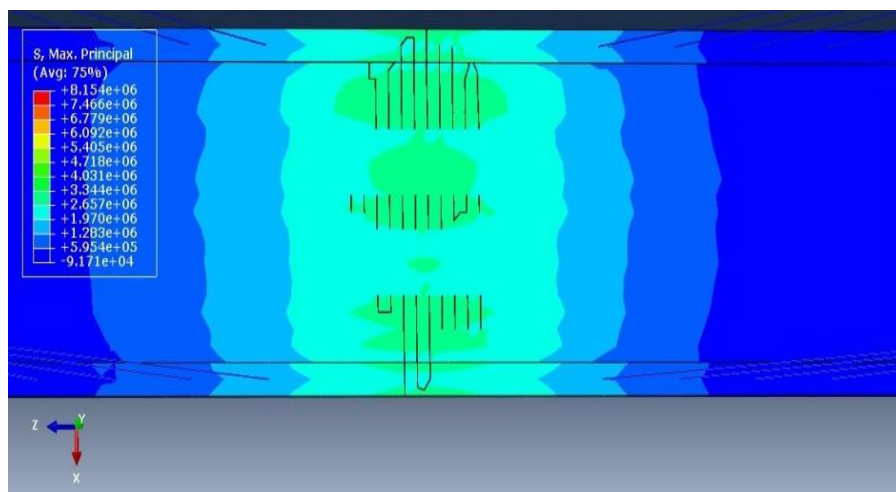


**Figure 7.17** Maximum principal stress - Fire scenario 1- With XFEM damage simulation

## 7.6 Coupled Thermal-Stress Analysis

Considering fire scenario 2, the fired region is shown in (Figure 7.18). Cracks are obvious in the web of the deck in addition to spalling of concrete at one side of the exterior edges (see Figure 7.19). The cracks appear first at the middle and the external edges of the web, then they propagate from the exterior edges toward middle part of the web and consequently spalling occurs. The thermal stresses generated high vertical displacement downward and relative higher angular displacement of the deck with respect to its value in scenario 1.

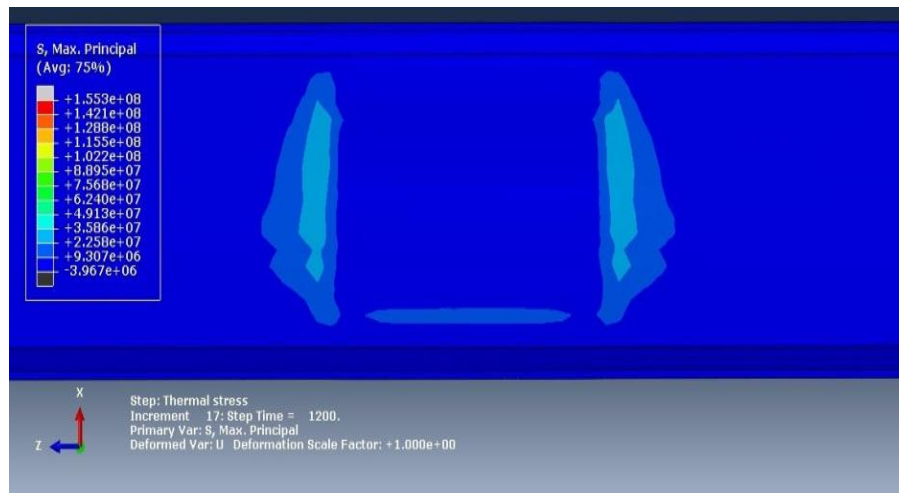


Figure 7.18 Maximum principal stress - Fire scenario 2- Without XFEM damage simulation

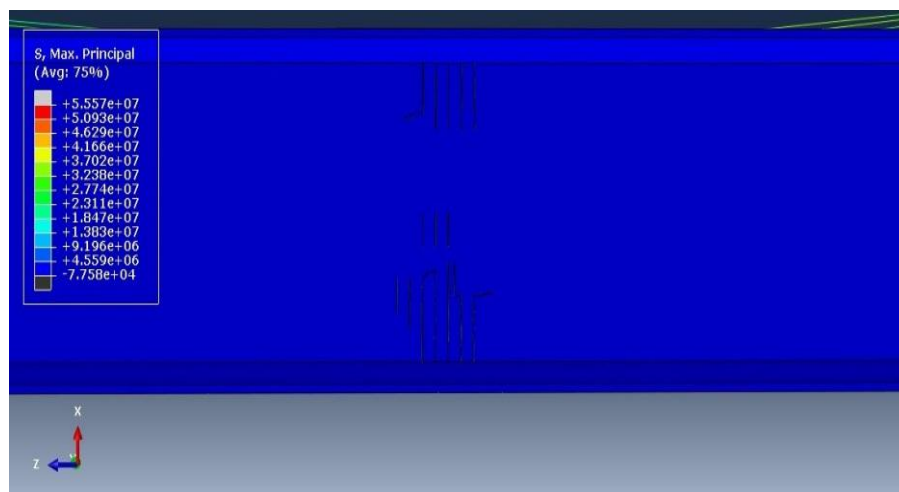
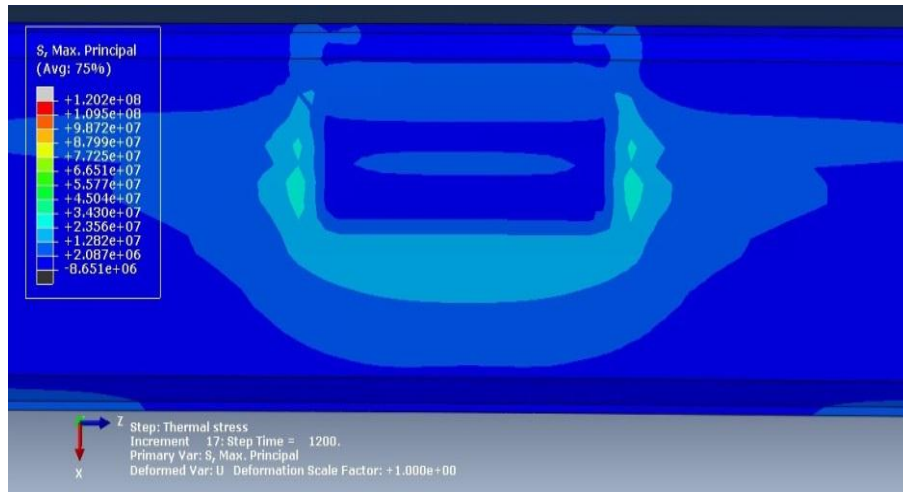


Figure 7.19 Maximum principal stress - Fire scenario 2- With XFEM damage simulation

While for fire scenario 3, the fired region is shown in (Figure 7.20). Cracks with spalling of concrete can be seen at one side of the exterior edges on the web (see Figure 7.21). The cracks start first at the fired side and then they propagate toward the middle of the web and as a result, spalling occurs.

## 7.6 Coupled Thermal-Stress Analysis



**Figure 7.20** Maximum principal stress - Fire scenario 3- Without XFEM damage simulation

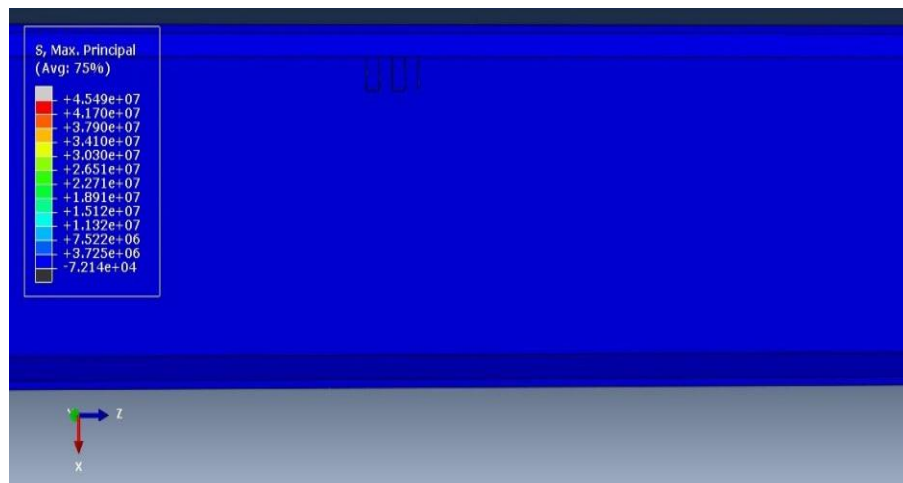


**Figure 7.21** Maximum principal stress - Fire scenario 3- With XFEM damage simulation

Cracks and spalling of concrete occur in all fire scenarios due to high temperature exposure of the deck. Consequently the highest damage in the deck of the cable stayed bridge takes place in the fire scenario 1 where the fire is above the deck because larger amounts of cracks and spalling appear in earlier time from the fire incident and the failure of the structure is more prone to occur compared to other two fire scenarios.

### 7.7 Validation of Coupled Thermal-Stress Models

Von Mises stress of the concrete is utilized as the criteria of failure detection in a concrete structure, which is used to visualize the location and magnitude of the deck crack and spalling due to fire exposition. To validate the models of the spalling and cracking of the deck, a benchmark of the spalling zone of the reinforced concrete beam by Choi and Shin, 2011 is dedicated. The zone of the cracks and spalling of concrete of the coupled thermal-stress models are in the upper external sides of the deck at the mid span of the cable stayed bridge model in all three fire scenarios. Comparing the two results indicates that there is a good agreement between the results of the coupled thermal-stress models and the results of the benchmark model.





# Chapter 8

## Conclusions and Recommendations for Further Researches

### 8.1 Conclusions

The application of ABAQUS finite element program to study the assessment of CSD, CFD and coupled models of wind-induced vibrations and control efficiency in long span cable supported bridges has shown great capabilities in identifying the predicted vertical and torsional vibrations and the associated critical wind speeds. The results confirmed the robustness of the approach in detecting the actual predicted VIV and lock-in phenomenon by utilizing the FSI concept. Another strength aspect of this work was optimizing the application of the MTMDs to suppress the vertical and torsional vibrations of the deck and the control efficiency of this method was high relatively compared to the previous results from the benchmarks in the literature. It is worthy to mention that employment of surrogate modeling supporting on many experimental sampling methods in addition to Sobol's global sensitivity indices method identified and detected the predicted roles and rational effects of eight certain and uncertain aerodynamic parameters which are considered the main sources of the aerodynamic stability of the long span cable supported bridges. Frequency analysis helped to identify the natural frequencies of the structure which are related to the vibration modes, in addition to recognizing the dangerous coupling between the vertical and the torsional vibrations. Structural modification was conducted and consequently, the vertical and torsional stiffness of the structure were increased. Also the danger of coupling was removed to higher natural frequencies which are rarely happen. Furthermore, a safer structural performance was obtained. The application of TFSI concept exhibited high accuracy and capability to simulate and analyze the effect of triple coupling between the wind and the deck domains in addition to the thermal boundary. It succeeded to predict the early generation of VIV and lock-in phenomena, also revealed the role of temperature field in the behavior of the cable stayed bridge during wind excitations and fire incidents together. The coupled thermal-stress analysis manifested very well in predicting the thermal deformations of the deck in addition to the damages detection regarding the generation of cracks and spalling of the concrete due to fire exposure with the support of XFEM analysis application.

## 8.1 Conclusions

---

All the mentioned results are formulating significant backgrounds to pave the way to the engineers in that field to insure preparing better design with a greater factor of safety against vibrations risks and the danger of structural failure in addition to wide region of modification solutions to control the early weakness in the behavior and performance of long span cable supported bridges under wind actions.

The following axes are the summary of the conclusions in details:

1- The numerical simulations in conjunction with frequency analysis confirmed the existence of vertical and torsional vibrations of the deck due to wind excitation which is being considered as a basic reference to understand the buffeting response and flutter instability of the cable stayed bridge, and the results of the vortex shedding from the deck of the long span bridge showed that the two-way FSI approach is more efficient than the one-way FSI approach in detecting the generation of earlier VIV and predicting lower critical wind velocities as a result detecting earlier lock-in phenomenon, which are indications for designers to avoid the VIV in the design stage by ensuring that the frequencies of the vortices generated are sufficiently separated from the natural frequencies of the long span bridge by altering the geometrical design of the deck or changing the natural frequencies of the system. The results of lift forces generated in the deck of the long span bridge in the two-way FSI approach is smaller than the same values for the one-way FSI approach, which means that the two-way approach determines the actual magnitude of the energy dissipation for the VIV of the deck and the vertical periodic oscillation of the deck is detected in lower wind velocities only by utilizing two-way FSI approach. Supporting on these results, the cable stayed bridge is designed safely through avoiding wrong estimation of late VIV where in some cases lead to resonant and dangerous events.

2- Eight certain and uncertain aerodynamic parameters have been optimally identified their values that are responsible of improving the aerostatic and aerodynamic instabilities of the cable stayed bridge. The wind attack angle and wind speed parameters were the most effective parameters that affected the buffeting response and the flutter instability in addition to generation of vortex shedding. The deck streamlined length parameter demonstrated a nonlinear effect for a certain deck shape which falls between a bluff shape and a streamlined shape which was an optimum case that supports the generation of vortex shedding and the oscillation of the deck. The dynamic viscosity of air parameter has a nonlinear effect on the vortex shedding and the vertical oscillations of the deck, where increasing this parameter to high values will enhance the generation of the vortex shedding due to energy dissipation mechanism. The viscous damping of the stay cable parameter showed a nonlinear relation with the vertical vibration of the deck. When this parameter is increased, the displacement at the

## 8.1 Conclusions

---

center of the deck mid-span decreased in a small range with irregular pattern. While for torsional vibration of the deck, a very small non appreciable effect on the flutter displacement of the deck was seen. The mass ratio parameter that is related to the TMDs has a nonlinear effect on the vertical vibration control efficiency and linear effect on the torsional vibration control efficiency. Commonly increasing this ratio to a limited range will decrease both the vertical and torsional vibrations of the deck in an appreciable amount. The frequency ratio parameter has a semi linear effect on the vertical vibration control efficiency and linear effect on the torsional vibration control efficiency. Where increasing this parameter value in a bound limit, will decrease the vertical vibration of the deck in acceptable rate. While increasing this parameter value has a nonappreciable effect on the torsional vibration. Finally the damping ratio parameter has a linear effect on the vertical vibration control efficiency and linear effect on the torsional vibration control efficiency. Where increasing this parameter value in a bound limit, will decrease the vertical vibration of the deck with a small rate, and has a very small effect on the torsional vibration which can be neglected.

3- Global sensitivity analysis for the aerodynamic parameters formulated surrogate models which were supported on Monte Carlo sampling method to predict the buffeting response and flutter instability of the cable stayed bridge so that to dedicate suitable plans and solutions for each vibration case thoroughly. Latin hypercube sampling method established efficient surrogate models to calculate the predicted kinetic energy of the system and the lift forces that are the background data to analyze and control the generation of VIV. Box-Behnken experimental method formulated excellent surrogate models representing the actual response of the system to efficiently calculate the performance of the MTMDs in suppressing both the vertical and torsional vibrations of the deck.

4- The sensitivity indices revealed the rational effect and role of each aerodynamic parameter on the aerodynamic instability of the structure which are considered important data to identify the priorities in the design procedure so that to optimize the response of the system against vertical and torsional vibrations of the deck which are resulting due to strong critical wind excitations. The role and the rational effects of wind attack angle parameter were very high on both the vertical and torsional vibrations of the deck. The uncertainty of this parameter has been identified to a good range which is responsible directly on the aerodynamic instability of the structure. While the role and the rational effects of the deck streamlined length parameter was not important related to the kinetic energy of the system, while it was effective on the generation of lift forces due to VIV and buffeting response. Consequently a good consideration should be given to this parameter. Related to the rational effects of the stay cables viscous damping parameter, it is clear that this parameter has a fair effect on the vertical vibration and a good effect on the torsional vibration, as a result the uncertainties of

## 8.1 Conclusions

---

this parameter are well studied. The role and the rational effects of wind speed parameter were very high on the kinetic energy of the system and the lift forces and this parameter should be considered for uncertainties in the generation of vortex shedding and oscillation of the deck due to VIV and flutter instability. In the other hand, the dynamic viscosity of air parameter has a non appreciable rational effect on the kinetic energy of the system, and has a small rational effect on the lift forces, hence the uncertainties related to this parameter on the vortex shedding and oscillation of the deck is very small. Furthermore, the rational effect of the mass ratio on the vertical vibration was high and on the torsional vibration was too much high, where this parameter can be considered the source of torsional control efficiency. While the rational effect of the frequency ratio parameter on the vertical vibration was low and no effect at all on the torsional vibration. Moreover, the rational effect of the damping ratio parameter on the vertical vibration was too much low and no effect on the torsional vibration.

5- The novel structural modification of the cable stayed bridge model succeeded to increase the bending and torsional stiffness of the structure to a wide range in such a way that showed larger efficiency as vibrations suppressor compared to other approaches that have been adopted for vibrations control in long span bridges such as TMDs, Sealed tuned liquid column gas dampers and electromechanical actuator. The natural frequencies of the system were modified positively, where the flutter wind speed has been modified to larger magnitudes, and it insured the safety of the structure against a dangerous coupling between the vertical and torsional mode shapes of vibrations by altering the coupling mode shape to much higher natural frequencies after structural modification, which is an indication that the safety of the structure against vertical and torsional vibrations and the coupling between them has been guaranteed to a large factor of safety.

6- When TFSI numerical simulations are adopted, nonlinear behavior is detected for the deck under fire scenario 1 and fire scenario 2 regarding the horizontal and vertical vibrations of the deck which imposes special analysis for each case up to the design needs and specifications of safety against vibrations. While for fire scenario 3 a significant suppression of both horizontal and vertical vibrations to a good level has been identified. This fact can be further utilized to use heating sources to invent new devices for the suppressing vibrations in long span bridges where the lower temperature that enhances that target is lower than 100°C supporting on the results of lift and drag forces for fire scenario 3 and the standard ISO 834 fire curve. An earlier critical wind velocity is discovered for the TFSI simulations in the same time lower vortex shedding frequencies for fire scenario 2 where the fire is under the deck, which enhances the generation of earlier VIV and earlier lock-in phenomenon which is a serious matter related to the service ability and safety of the cable stayed bridge due to vibrations and failure. As a result a special attention should be dedicated to prevent

## 8.2 Recommendations for Further Researches

---

heating of the deck (above part) especially in hot countries where the source of heating from the environment helps this situation. Using both coupled thermal-stress and XFEM simulations, all fire scenarios generated thermal stresses in the deck due to very high temperature, consequently deformations and damage of the concrete comprising cracks and spalling of the concrete, especially fire scenario 1 where larger amounts of cracks and spalling appear earlier which is considered critical for the safety of the structure compared to fire scenario 2 and fire scenario 3.

## 8.2 Recommendations for Further Researches

Supporting on the conclusions and the capability of model assessment by the finite element method and the sensitivity analysis approach, it is recommended to further widening the scope of the researches in this area by conducting the following investigations:

1- Using different models for the segmental decks such as circular and trapezoidal shapes so that to investigate the buffeting response and flutter instability of the long span cable supported bridge, where certain structural shapes are highly decisive in generating vibrations.

2- Considering higher wind speeds for CFD simulations more than 25 m/s so that to discover higher critical wind speeds which are responsible of higher shedding frequencies related to far lock-in regions, where the computational efforts and cost are higher compared to lower winds speeds cases. This helps to secure placing the design of the deck away from vortex induced vibration in very strong winds situations.

3- Designing the MTMDs with various shapes and dimensions in addition to positioning them in different places in the deck so that to optimize their effects on controlling both the vertical and torsional vibrations of the deck. Also a combination of both MTMDs and viscous dampers is recommended, where this method in certain cases might be effective in enhancing the suppression of the vibrations.

4- Modeling the stay cables with other shapes of distributions, such as semi fan shapes and harp shapes to search the robustness of the structural modification for damping consideration, where the local and the global responses even the coupled responses of the long span cable supported bridges are associated with the motions and the quasi static motions of the stay cables.

5- Investigating other uncertain parameters such as horizontal skewedness of the wind effect on the buffeting response and flutter instability of the structure, in addition to its effect on the vortex shedding and lock-in phenomenon, where in most of research studies this parameter is not considered due to complexity of modeling the wind profile in finite element method.

## **8.2 Recommendations for Further Researches**

---

6- Adopting different sampling methods like (LP-TAU) to search the results of the surrogate models of the predicted response of the structure for vibrations control, and supporting on other sensitivity analysis methods such as analysis of variance (ANOVA) and Fourier Amplitude Sensitivity Test (FAST) to calculate the effect of the parameters on the aerostatic and aerodynamic stability of the structure, in addition to comparison process between these methods to identify the most critical method in that direction.

7- Starting global sensitivity analysis in thermal fluid-structure interaction simulations utilizing transient heat-transfer of a fire considering input parameters such as heating rate, heat flux, concrete density, ambient temperature and wind speed so that to identify the role and rational effect of each parameter on the behavior of the deck during fire incidents.

# Appendix A

## A.1 Mesh Convergence

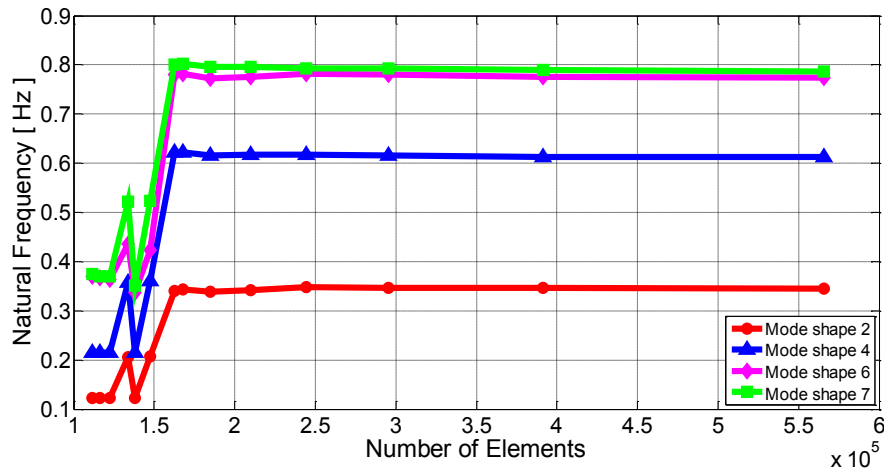


Figure A.1 Mesh convergence for mode shapes of vibrations

## A.2 Surrogate Models Equations for Vertical and Torsional Responses (MATLAB Codes)

$$\begin{aligned}
 Y_v = & -0.020883722 + 0.00010033145755 * x_1 * 1 - \\
 & 0.004164325912621 * x_2 * 1 + 0.349777764990117 * x_3 * 1 - \\
 & 0.000001157304765 * x_1.^2 + 0.000496530180774 * x_2.^2 - \\
 & 40.802891600598 * x_3.^2 + 0.00002158455372 * x_1 * x_2 - \\
 & 0.007290619361827 * x_1 * x_3 + 0.375075585195514 * x_2 * x_3
 \end{aligned} \tag{A.2-1}$$

$$\begin{aligned}
 Y_t = & 0.00066213 + 0.000071351888482 * x_1 * 1 - \\
 & 0.000614461247787 * x_2 * 1 + 0.429585797605989 * x_3 * 1 - \\
 & 0.000001098266034 * x_1.^2 + 0.000214156053979 * x_2.^2 - \\
 & 12.998644305948 * x_3.^2 + 0.000013018552105 * x_1 * x_2 - \\
 & 0.006775003312961 * x_1 * x_3 - 0.047574577127205 * x_2 * x_3
 \end{aligned} \tag{A.2-2}$$

A.3 Lift Force and Aerodynamic Parameters

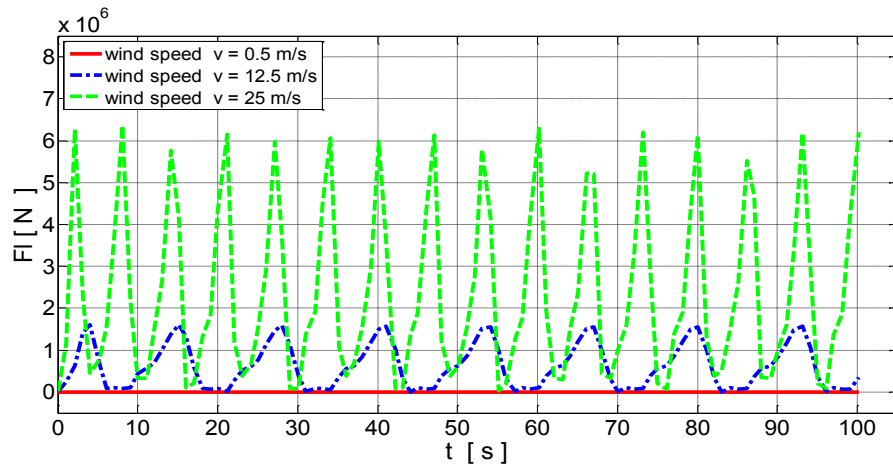


Figure A.3.1 Effect of wind speed on the generated lift force in the deck

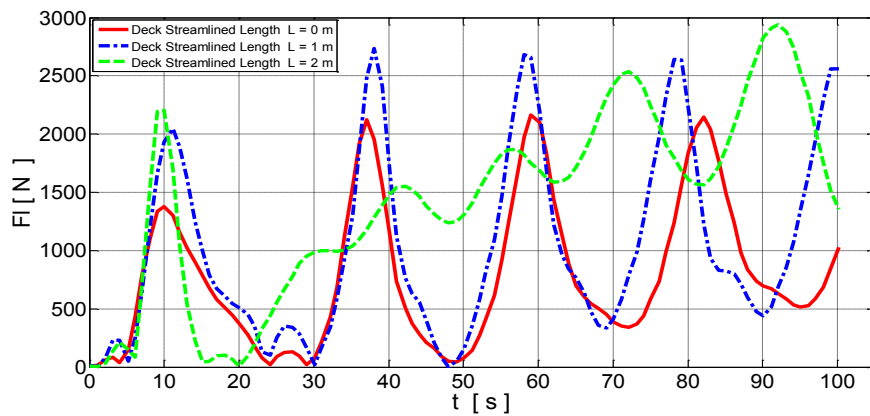


Figure A.3.2 Effect of deck streamlined length on the generated lift force in the deck

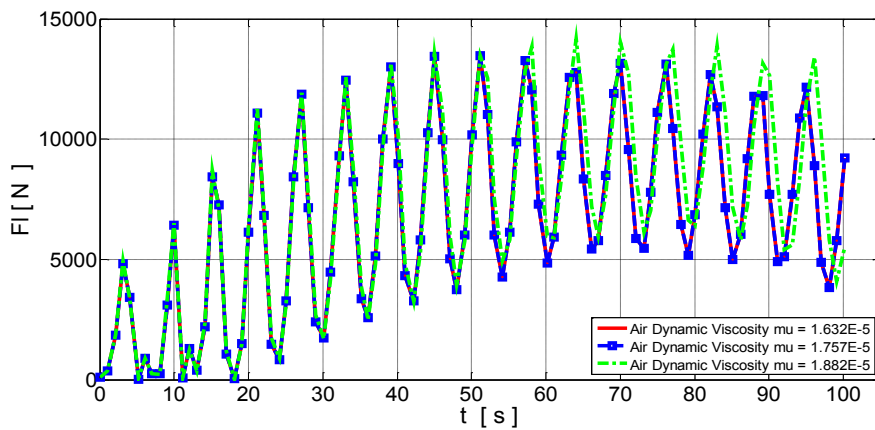


Figure A.3.3 Effect of air dynamic viscosity on the generated lift force in the deck



**A.4 Surrogate Models Equations for Kinetic Energy and Lift Force (MATLAB Codes)**

$$Y_{ke} = 909.283 - 18.142 * X1 + 18.548 * X2 - 96380686.352 * X3 + 36.486 * X1.^2 - 26.663 * X2.^2 + 2537569337783.03 * X3.^2 + 2.891 * X1 * X2 + 954150.697 * X1 * X3 + 615868.57 * X2 * X3 \quad (A.4-1)$$

$$Y_{fl} = -15665.09 + 256 * X1 + 135.69 * X2 + 1631247932.54 * X3 + 2 * X1.^2 - 457.43 * X2.^2 - 43018934785069.2 * X3.^2 - 16.9 * X1 * X2 - 11417513.33 * X1 * X3 + 36495311.07 * X2 * X3 \quad (A.4-2)$$

**A.5 Effect of TMD's Design Parameters on Vertical and Torsional Responses**

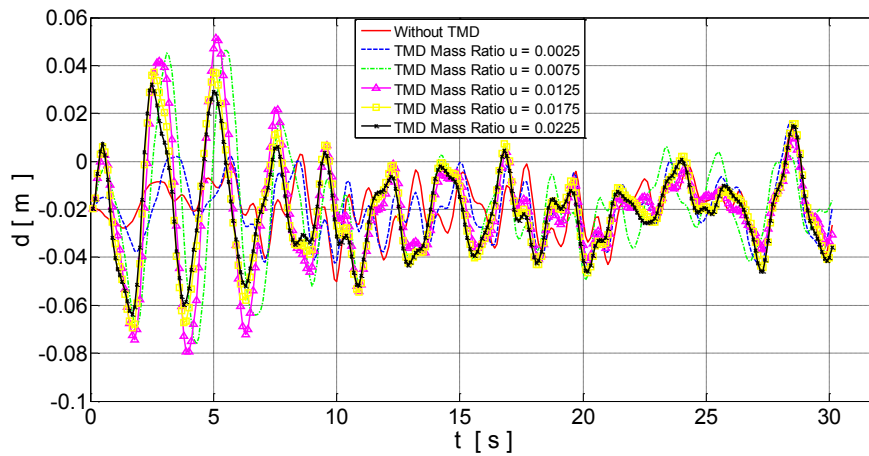


**Figure A.5.1** Effect of TMD mass ratio on the vertical vibration of the deck

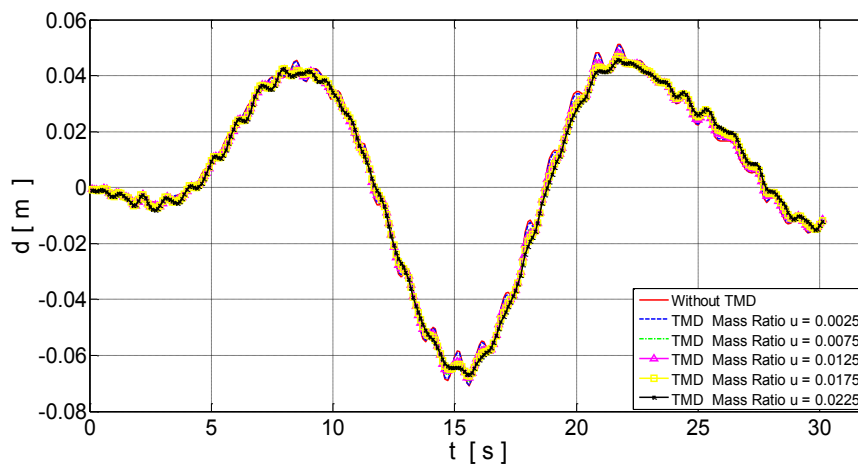


**Figure A.5.2** Effect of TMD mass ratio on the torsional vibration of the deck

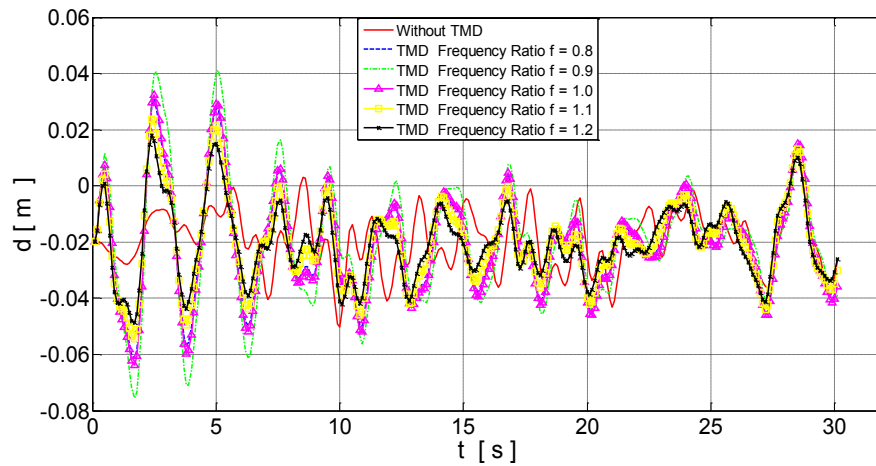


Figure A.5.3 Effect of TMD frequency ratio on the vertical vibration of the deck

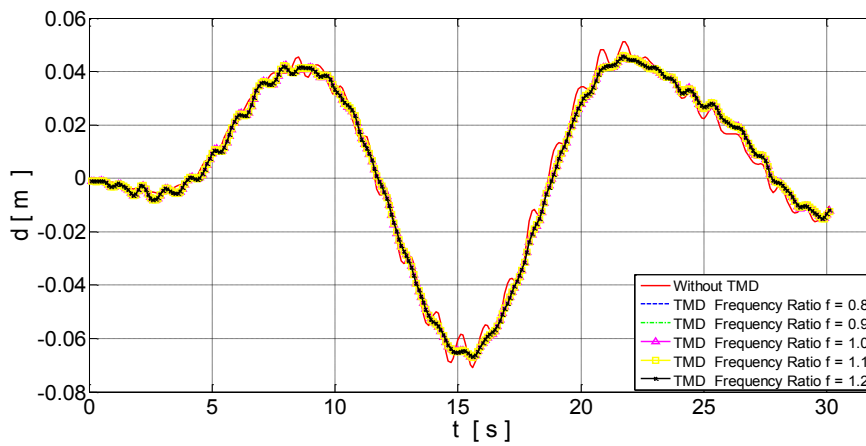


Figure A.5.4 Effect of TMD frequency ratio on the torsional vibration of the deck

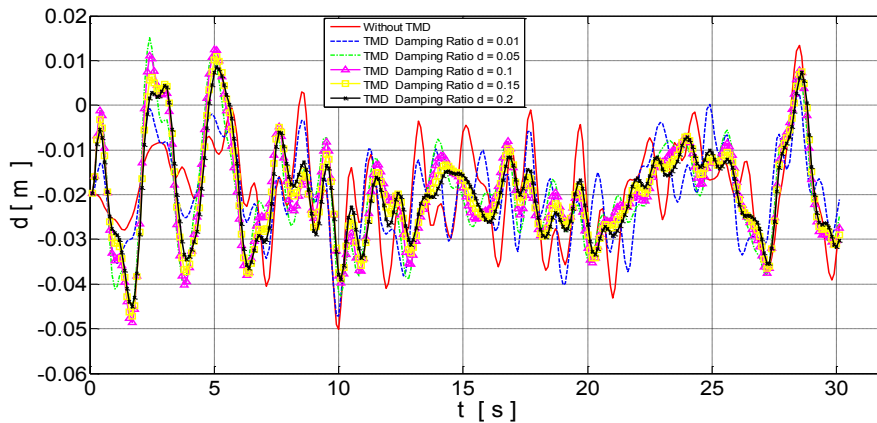


Figure A.5.5 Effect of TMD damping ratio on the vertical vibration of the deck

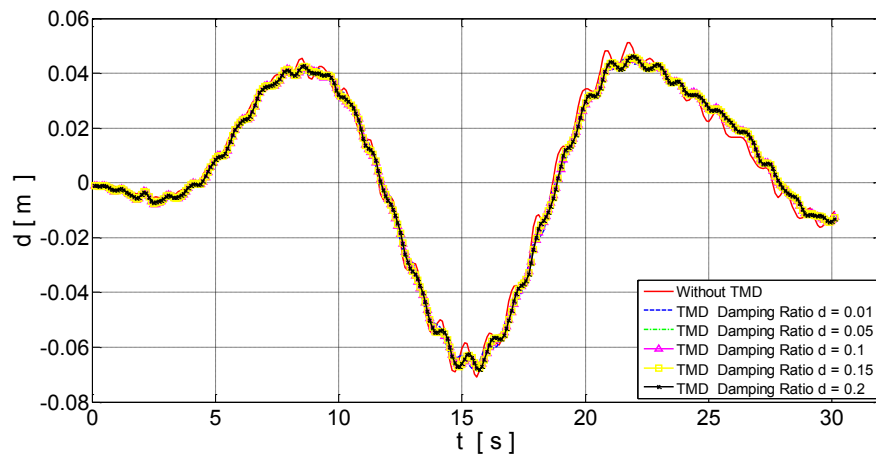


Figure A.5.6 Effect of TMD damping ratio on the torsional vibration of the deck

### A.6 Surrogate Models Equations for Vertical and Torsional Control Efficiencies (MATLAB Codes)

$$\begin{aligned}
 Y_{vce} = & -89.6379207064 + 1615.7368421052 * x_1 * 1 + 92.6646381579 * x_2 * 1 - \\
 & 193.0342797784 * x_3 * 1 - 104900 * x_1.^2 - \\
 & 26.1875 * x_2.^2 + 1401.3850415513 * x_3.^2 + 3353.7500000001 * x_1 * x_2 + 2576.31578947 \\
 & 36 * x_1 * x_3 - 75.5263157895 * x_2 * x_3 \quad (A.6-1)
 \end{aligned}$$

$$\begin{aligned}
 Y_{tce} = & 9.02947974379 + 3243.90789473678 * x_1 * 1 - 6.21513157902 * x_2 * 1 - \\
 & 5.48476454295 * x_3 * 1 - \\
 & 35449.9999999983 * x_1.^2 + 3.25000000004 * x_2.^2 + 0.55401662052 * x_3.^2 - \\
 & 109.999999999999 * x_1 * x_2 - 115.78947368418 * x_1 * x_3 + 5.26315789474 * x_2 * x_3 \quad (A.6-2)
 \end{aligned}$$

# References

- Ab Kadir M. A.** (2013). *Fire Resistance of Earthquake Damaged Reinforced Concrete Frames*. PhD Thesis - The University of Edinburgh, Edinburgh, UK.
- Abdel Raheem S. E. and Hayashikawa T.** (2008). Vibration and Damping Characteristics of Cable-Stayed Bridges Tower Control. *International Association for Bridge and Structural Engineering*, 8, 30 - 37.
- Abdel-Aziz A. and Attia W. A.** (2008). Aeroelastic Investigation of Different Deck Sections for Suspension Bridges by Numerical Analysis. *International Journal of Engineering and Innovative Technology (IJEIT)*, 4(12), 49 - 57.
- Abdi I. A., Abdulrahim A., Haser S., Uzol O. and Kurc O.** (2012). Experimental and Numerical Investigation of Wind Effects on Long Span Bridge Decks. *10th International Congress on Advances in Civil Engineering*, Ankara, Turkey. 17-19 October 2012.
- Agar T. T. A.** (1989). Aerodynamic Flutter Analysis of Suspension Bridges by a Modal Technique. *Engineering Structures*, 11, 75 - 82.
- Akhtaruzzaman, A. A. and Sullivan P. J.** (1970). Explosive Spalling of Concrete Exposed to High Temperature. *Concrete Structures and Technology Research Report*. London, Imperial.
- Al-Assaf A.** (2006). *Flutter Analysis of Open-Truss Stiffened Suspension Bridges Using Synthesized Aerodynamic Derivatives*. PhD Thesis - Department of Civil and Environmental Engineering, Washington State University, Washington, USA.
- Allam S. M., Elbakry H. M. F. and Rabeai A. G.** (2013). Behavior of One-Way Reinforced Concrete Slabs Subjected to Fire. *Alexandria Engineering Journal*. 52, 749 - 761.
- Alos-Moya J., Paya-Zaforteza I., Garlock M., Loma-Ossorio E., Schiffner D. and Hospitaler A.** (2014). Analysis of a Bridge Failure Due to Fire Using Computational Fluid Dynamics and Finite Element Models. *Engineering Structures*, 68, 96 - 110.
- Amani J., Oterkus E., Areias P. M. A., Zi G., Nguyen-Thoi T. and Rabczuk T.** (2016). A non-ordinary state-based peridynamics formulation for thermoplastic fracture. *International Journal of Impact Engineering*, 87, 83 - 94.
- Amenaghawon N.A., Nwaru K. I., Aisien F. A., Ogbeide S. E. and Okieimen C. O.** (2013). Application of Box-Behnken Design for the Optimization of Citric Acid Production from Corn Starch Using *Aspergillus Niger*. *British Biotechnology Journal*, 3(3), 236 - 245.

## References

---

- Amiri F., Anitescu C., Arroyo M., Bordas S. and Rabczuk T.** (2014). XLME interpolants, a seamless bridge between XFEM and enriched meshless methods. *Computational Mechanics*, 53(1), 45 - 57.
- Amiri F., Millan D., Arroyo M., Silani M. and Rabczuk T.** (2016). Fourth order phase-field model for local max-ent approximants applied to crack propagation. *Computer Methods in Applied Mechanics and Engineering*, 312(C), 254 - 275.
- Amiri F., Millán D., Shen Y., Rabczuk T. and Arroyo M.** (2014). Phase-field modeling of fracture in linear thin shells. *Theoretical and Applied Fracture Mechanics*, 69, 102 - 109.
- Andersen M. S., Sahin E., Laustsen B., Lenius M. and Læso Jesper R.** (2014). Implementation of the Non-Flutter Design Principle. *XIII Conference of the Italian Association for Wind Engineering INVENTO 2014*, Genova, Italy. 22-25 June 2014.
- Andersson A., Connor A. O. and Karoumi R.** (2013). External Damping of Stay Cables Using Adaptive and Semi-Active Vibration Control. *8th International Cable Supported Bridge Operators Conference*, Edinburgh, UK. 3-5 June 2013.
- Andersson C. and Ahl D.** (2011). *Fluid Structure Interaction Evaluation of Two Coupling Techniques*. M.Sc Dissertation - School of Information Science, Computer and Electrical Engineering, Halmstad University, Halmstad, Germany.
- Andrienne T.** (2012). *Experimental and Numerical Investigations of the Aeroelastic Stability of Bluff Structures*. PhD Thesis - Department of Aerospace and Mechanics, University of Liege, Liege, Belgium.
- Anitescu C., Jia Y., Zhang Y. and Rabczuk T.** (2015). An isogeometric collocation method using superconvergent points. *Computer Methods in Applied Mechanics and Engineering*, 284, 1073 -1097.
- Annadurai G., Sung S. S. and Lee D. L.** (2004). Optimisation of Floc characteristics for Treatment of Highly Turbid Water. *Separation Science and Technology*, 39(1), 19 - 42.
- Areias P. and Rabczuk T.** (2013). Finite strain fracture of plates and shells with configurational forces and edge rotation. *International Journal for Numerical Methods in Engineering*, 94(12), 1099 - 1122.
- Areias P. and Rabczuk T.** (2017). Steiner-point free edge cutting of tetrahedral meshes with applications in fracture. *Finite Elements in Analysis and Design*, 132, 27 - 41.
- Areias P. M. A., Rabczuk T. and Camanho P. P.** (2014). Finite strain fracture of 2D problems with injected anisotropic softening elements. *Theoretical and Applied Fracture Mechanics*, 72, 50 - 63.
- Areias P., Msekh M. A. and Rabczuk T.** (2016). Damage and fracture algorithm using the screened Poisson equation and local remeshing. *Engineering Fracture Mechanics*, 158, 116 - 143.
- Areias P., Rabczuk T. and Camanho P. P.** (2013). Initially rigid cohesive laws and fracture based on edge rotations. *Computational Mechanics*, 52(4), 931 - 947.

## References

---

- Areias P., Rabczuk T. and De Sá J. C.** (2016). A novel two-stage discrete crack method based on the screened Poisson equation and local mesh refinement. *Computational Mechanics*, 58(6), 1003 - 1018.
- Areias P., Rabczuk T. and Dias-da-Costa D.** (2013). Element-wise fracture algorithm based on rotation of edges. *Engineering Fracture Mechanics*, 110, 113 - 137.
- Areias P., Rabczuk T. and Msekh M.** (2016). Phase-field analysis of finite-strain plates and shells including element subdivision. *Computer Methods in Applied Mechanics and Engineering*, 312(C), 322 - 350.
- Areias P., Reinoso J., Camanho P. and Rabczuk T.** (2015). A constitutive-based element-by-element crack propagation algorithm with local mesh refinement. *Computational Mechanics*, 56(2), 291 - 315.
- Aslan N. and Cebeci Y.** (2007). Application of Box-Behnken Design and Response Surface methodology for modeling of some Turkish coals. *Fuel*, 86(1 - 2), 90 - 97.
- Asyikin M. T.** (2012). *CFD Simulation of Vortex Induced Vibration of a Cylindrical Structure*. M.Sc. Dissertation - Department of Civil and Transport Engineering, Norwegian University of Science and Technology, Trondheim, Norway.
- Baba S., Kajita T. and Ninomiya K.** (1988). Fire Under a Long Span Bridge. *13 th International Association for Bridge and Structural Engineering (IABSE) congress*, Helsinki. 6-10 June 1988.
- Badia S. and Codina R.** (2007). On Some Fluid Structure Iterative Algorithms Using Pressure Segregation Methods: Application to Aeroelasticity. *International Journal for Numerical Methods in Engineering*, 72, 46 - 71.
- Bakis K. N., Massaro M., Williams M. S. and Limebeer D. J. N.** (2016). Aeroelastic Control of Long-Span Suspension Bridges with Controllable Winglets. *Journal of Structural Control and Health Monitoring*, DOI: 10.1002/stc.1839.
- Bakkiyaraj R. A. and Kumarappan N.** (2013). Reliability Evaluation of Composite Electric Power System Based On Latin Hypercube Sampling. *International Journal of Electrical, Robotics, Electronics and Communications Engineering*, 7(4), 245 - 250.
- Bandivadekar T. P. and Jangid R. S.** (2012). Mass Distribution of Multiple Tuned Mass Dampers for Vibration Control of Structures. *International Journal of Civil and Structural Engineering*, 3(1), 70 - 84.
- Baroni G. and Tarantola S.** (2014). A General Probabilistic Framework for Uncertainty and Global Sensitivity Analysis of Deterministic Models: A Hydrological Case Study. *Environmental Modelling and Software*, 51, 26 - 34.

## References

---

- Bartoli, G., Asdia, P., Febo, S., Pasto, C. and Procino, L.** (2008). Innovative Solutions for Long-Span Suspension Bridges. *BBAA VI International Colloquium on: Bluff Bodies Aerodynamics and Applications*. Milano, Italy. 20-24 July 2008.
- Behrens B. A., Krimm R. and Hasselbusch T.** (2013). Tuned Mass Damper With Piezoelectrically Tunable Damping. *20th International Congress on Sound and Vibration (ICSV20)*, Bangkok, Thailand. 7-11 July 2013.
- Belloli M., Fossati F., Giappino S. and Muggiasca S.** (2014). Vortex Induced Vibrations of a Bridge Deck: Dynamic Response and Surface Pressure Distribution. *Journal of Wind Engineering and Industrial Aerodynamics*, 133, 160 - 168.
- Belytschko T. and Black T.** (1999). Elastic crack growth in finite elements with minimal remeshing. *International Journal for Numerical Methods in Engineering*, 45(5), 601 - 620.
- Bennetts I. and Moinuddin K.** (2009). Evaluation of the Impact of Potential Fire Scenarios on Structural Elements of a Cable-Stayed Bridge. *Journal of Fire Protection Engineering*, 19(4), 85 - 106.
- Benra F. K., Dohmen H. J., Pei J., Schuster S. and Wan B.** (2011). A Comparison of One-Way and Two-Way Coupling Methods for Numerical Analysis of Fluid-Structure Interactions. *Journal of Applied Mathematics*, 853560, 1 - 16.
- Bienkiewicz, B.** (1987). Wind Tunnel Study of Effects of Geometry Modification on Aerodynamics of a Cable Stayed Bridge Deck. *Journal of Wind Engineering and Industrial Aerodynamic*, 26(3), 325 - 339.
- Birken P., Gleim T, Kuhl D. and Meister A.** (2015). Fast Solvers for Unsteady Thermal Fluid Structure Interaction. *International Journal for Numerical Methods in Fluids*, 79(1), 16 - 29.
- Blackburn H. and Henderson R.** (1996). Lock-in Behavior in Simulated Vortex –Induced Vibration. *Journal of Experimental Thermal and Fluid Science*, 12, 184 - 189.
- Bo S.** (2011). *Finite Element Simulation of Fire Induced Spalling in High Strength Concrete Slabs*. M.Sc. Dissertation - Department of Civil and Environmental Engineering, Lehigh University, Pennsylvania, USA.
- Bonisch S., Dunne T. and Rannacher R.** (2008). Numerics of Fluid-Structure Interaction. *Hemodynamical Flows, Modeling, Analysis and Simulation*, 37, 333 - 378.
- Bordas S., Rabczuk T. and Zi G.** (2008). Three-dimensional crack initiation, propagation, branching and junction in non-linear materials by an extended meshfree methods without asymptotic enrichment. *Engineering Fracture Mechanics*, 75(5), 943 - 960.

## References

---

- Borna A., Habashi W. G., McClure G. and Nadarajah S. K.** (2013). CFD-FSI Simulation of Vortex-Induced Vibrations of a Circular Cylinder with Low Mass-Damping. *Journal of Wind and Structures*, 16(5), 411 - 431.
- Bosch H. R. and Dhall T.** (2008). Aerodynamic Investigation of Generic Bridges Deck Section Models. *BBAA VI International Colloquium on: Bluff Bodies Aerodynamics & Applications*, Milano, Italy. 20-24 July 2008.
- Bosman E.** (2012). *Wind induced Vibration of fr UHSC Bridge Decks*. M.Sc. Dissertation - Faculty of Civil Engineering and Geosciences, Delft University of Technology, Delft, Netherland.
- Bourdier S.** (2008). *Vortex-Induced Vibrations of a Non-Linearly Supported Rigid Cylinder*. PhD Thesis - School of Civil Engineering and the Environment, University of Southampton, Southampton, UK.
- Bourguet R., Karniadakis G. E. and Triantafyllou M. S.** (2011). Lock-In of the Vortex-Induced Vibrations of a Long Tensioned Beam in Shear Flow. *Journal of Fluids and Structures*, 27, 838 - 847.
- Braxtan N. L., Wang Q., Whitney R. and Koch G.** (2015). Numerical Analysis of a Composite Steel Box Girder Bridge in Fire. *Applications of Structural Fire Engineering*, Dubrovnic, Croatia. 15-16 October 2015.
- Braxtan N. L., Whitney R., Wang Q. and Koch G.** (2015). Preliminary Investigation of Composite Steel Box Girder Bridges in Fire. *Bridge Structures*, 11, 105 - 114.
- Budarapu P., Gracie R., Bordas S. and Rabczuk T.** (2014). An adaptive multiscale method for quasi-static crack growth. *Computational Mechanics*, 53(6), 1129 - 1148.
- Budarapu P., Gracie R., Yang S. W., Zhuang X. and Rabczuk T.** (2014). Efficient coarse graining in multiscale modeling of fracture. *Theoretical and Applied Fracture Mechanics*, 69, 126 - 143.
- Burhenne S., Jacob D. and Henze G. P.** (2011). Sampling Based on Sobol Sequences for Monte Carlo Techniques Applied to Building Simulations. *12th Conference of International Building Performance Simulation Association*, Sydney. 14-16 November 2011.
- Carstensen J. V.** (2011). *Material Modelling of Reinforced Concrete at Elevated Temperatures*. M.Sc. Dissertation - Department of Civil Engineering, Technical University of Denmark. Lyngby, Denmark.
- Caruso G, Mekki O. B. and Bourquin F.** (2009). Modeling and Experimental Validation of a New Electromechanical Damping Device. *Journal of Vibroengineering*, 11(4), 1 - 9.
- Casalotti A., Arena A. and Lacarbonara W.** (2013). Flutter Suppression in Long-Span Suspension Bridges by Arrays of Hysteretic Tuned Mass Dampers. *XXI AIMETA Congress of Theoretical and Applied Mechanics*, Torino, Italy. 17-20 September 2013.



## References

---

- Chakrabarti S. K.** (2005). *Physical Modelling of Offshore Structures. Handbook of Offshore Engineering. Offshore Structure Analysis.* Inc., Plainfield, IL, USA, 2005. Chapter 13, 1001 - 1054.
- Chan C. L., Anitescu C. and Rabczuk T.** (2017). Volumetric parametrization from a level set boundary representation with a PHT-splines. *Computer Aided Design*, 82, 29 - 41.
- Chau-Dinh T., Zi G., Lee P. S., Rabczuk T. and Song J. H.** (2012). Phantom-node method for shell models with arbitrary cracks. *Computers & Structures*, (92 - 93), 242 - 256.
- Chen A., Ma R. and Wang D.** (2009). Aerodynamic Problems of Cable Stayed Bridges Spanning Over One Thousand Meters. *Engineering Sciences*, 7(3), 16 - 22.
- Chen Q. and Xiang H.** (1998). The Vibration Suppressing Performance of the Multiple Tuned Mass Damper (MTMD) and its Control Over the Buffeting of Bridges. *Journal of Tongji University Natural Science*, 28(2), 125 - 133.
- Chen S.** (2004). *Dynamic Performance of Bridges and Vehicles Under Strong Wind.* PhD Thesis - Department of Civil and Environmental Engineering, Louisiana State University, Louisiana, USA.
- Chen S. R. and Cai C. S.** (2003). Control of Wind-Induced Coupled Vibration of Long-span Bridges with Tuned Mass Dampers. *11th International Wind Engineering Conferences*, Lubbock, Texas, USA, 853 - 860.
- Chen S. R. and Cai C. S.** (2004). Coupled Vibration Control With Tuned Mass Damper for Long-Span Bridges. *Journal of Sound and Vibration*, 278, 449 - 459.
- Chen S. R., Cai C. S., Chang C. C. and Gu M.** (2004). Modal Coupling Assessment and Approximated Prediction of Coupled Multimode Wind Vibration of Long-Span Bridges. *Journal of Wind Engineering and Industrial Aerodynamic*, 92, 393 - 412.
- Chen W. L., Li H. and Hu H.** (2014). An Experimental Study on the Unsteady Vortices and Turbulent Flow Structures Around Twin-Box-Girder Bridge Deck Models With Different Gap Ratios. *Journal of Wind Engineering and Industrial Aerodynamics*, 132, 27 - 36.
- Chen X.** (2006). Analysis of Long Span Bridge Response to Winds: Building Nexus between Flutter and Buffeting. *Journal of Structural Engineering*, 132(12), 2006 - 2017.
- Chen X.** (2010). *Optimization and Estimation Routine for Tuned Mass Damper.* M.Sc. Dissertation - Department of Mechanical Engineering. Blekinge Institute of Technology, Karlskrona, Sweden.
- Chen X.** (2012). Prediction of Buffeting Response of Long Span Bridges to Transient Non Stationary Winds. *The Seventh International Colloquium on Bluff Body Aerodynamics and Applications (BBAA7)*. Shanghai, China. 2-6 September 2012.
- Chen X. and Kareem A.** (2003). Efficacy of Tuned Mass Dampers for Bridge Flutter Control. *Journal of Structural Engineering ASCE*, 129(10), 1291 - 1300.

## References

---

- Chen X., Kareem A. and Matsumoto M.** (2001). Multimode Coupled Flutter and Buffeting Analysis of Long Span Bridges. *Journal of Wind Engineering and Industrial Aerodynamics*, 89(7-8), 649 - 664.
- Chen X., Matsumoto M. and Kareem A.** (2000). Aerodynamic Coupling Effects on Flutter and Buffeting of Bridges. *Journal of Engineering Mechanics, ASCE*, 126(1), 17 - 26.
- Chen Z. Q., Han Y., Hua X. G., and Luo Y. Z.** (2009). Investigation on Influence Factors of Buffeting Response of Bridges and its Aeroelastic Model Verification for Xiaoguan Bridg. *Engineering Structures*, 31(2), 417 - 431.
- Cheng S.** (1999). *Structural and Aerodynamic Stability Analysis of Long Span Cable Stayed Bridges*. PhD Thesis - Department of Civil and Environmental Engineering, Carleton University, Ottawa, Canada.
- Choi E. G. and Shin Y. S.** (2011). The Structural Behavior and Simplified Thermal Analysis of Normal-Strength and High-Strength Concrete Beams Under Fire. *Engineering Structures*, 33(4), 1123 - 1132.
- Choi J.** (2008). *Concurrent Fire Dynamics Models and Thermo-Mechanical Analysis of Steel and Concrete Structures*. PhD Thesis - School of Civil and Environmental Engineering, Georgia Institute of Technology, Georgia, USA.
- Choi J., Haj-Ali R. and Kim H. S.** (2012). Integrated Fire Dynamic and Thermo-Mechanical Modeling of a Bridge Under Fire. *Structural Engineering and Mechanics*. 42(5), 815 - 829.
- Chowdhury A. G.** (2004). *Identification of Frequency Domain and Time Domain Aeroelastic Parameters for Flutter Analysis of Flexible Structures*. PhD Thesis - Department of Aerospace Engineering, Iowa State University, Iowa, USA.
- Chung C. H., Im C. R. and Park J.** (2013). Structural Test and Analysis of RC Slab After Fire Loading. *Nuclear Engineering and Technology*, 45(2), 223 - 236.
- Chunhua L. and Haifan X.** (2000). Simulation of Buffeting Response History for Long Span Bridges. *8th ASCE Specialty Conference on Probabilistic Mechanics and Structural Reliability*. Notre Dame, Indiana, USA. 24-26 July 2000.
- Confalonieri R., Bregaglio S. and Acutis M.** (2010). A Proposal of an Indicator for Quantifying Model Robustness Based on the Relationship Between Variability of Errors and of Explored Conditions. *Ecological Modelling*, 221, 960 - 964.
- Corriols A. S. and Morgenthal G.** (2012). Computational Analysis of VIV Observed on Existing Bridges. *The Seventh International Colloquium on Bluff Body Aerodynamics and Applications (BBAA7)*, Shanghai, China. 2-6 September 2012.

## References

---

- Dahl K.** (2013). *Aeroelastic Behavior of Very Long Span Suspension Bridges*. M.Sc.Dissertation - Department of Structural Engineering and Materials Science, University of Stavanger, Stavanger, Norway.
- Diana G., Belloli M. and Rocchi D.** (2006). On the Vortex Shedding Forcing on Suspension Bridge Deck. *Journal of Wind Engineering and Industrial Aerodynamics*, 94(5), 341 - 363.
- Diana G., Zasso A., Vigevano L. and Formaggia L.** (2006). Flow-Structure Interaction of the Oscillating Circular Cylinder in the Lock-in Region: Computational Versus Experimental Approach Comparison. *The Fourth International Symposium on Computational Wind Engineering (CWE2006)*, Yokohama, Japan. 16-19 July 2006.
- Diana, G., Bruni, S., Collina, A., and Zasso, A.** (1998). Aerodynamic Challenges in Super Long Span Bridges Design. *Proceedings of International Symposium on Advances in Bridge Aerodynamics*, Copenhagen, Denmark.
- Dien J. P. V.** (1995). *Fatigue Resistant Design of Cantilevered Sign, Signal, and Luminaire Support Structures*. M.Sc. Dissertation - Lehigh University, Pennsylvania, USA.
- Ding Q. and Lee P. K. K.** (2000). Computer Simulation of Buffeting Actions of Suspension Bridges Under Turbulent Wind. *Computers and Structures*, 76, 787 - 797.
- Ding Q., Lee P. K. K. and Lo S. H.** (2000). Time Domain Buffeting Analysis of Suspension Bridges Subjected to Turbulent Wind With Effective Attack Angle. *Journal of Sound and Vibration* , 233(2), 311 - 327.
- Dol S. S., Kopp G. A. and Martinuzzi R. J.** (2008). The Suppression of Periodic Vortex Shedding From a Rotating Circular Cylinder. *Journal of Wind Engineering and Industrial Aerodynamics*, 96, 1164 - 1184.
- Dolbow J.** (1999). *An extended finite element method with discontinuous enrichment for applied mechanics*. PhD Thesis - Northwestern University, Illinois, USA.
- Dolbow J., Moes N. and Belytschko T.** (2000). Discontinuous enrichment infinite elements with a partition of unity method. *Finite Elements in Analysis and Design*, 36(3 - 4), 235 - 260.
- Dotreppe, J. C., Majkut, S. and Franssen, J. M.** (2006). Failure of a Tied-Arch Bridge Submitted to a Severe Localized Fire. *Structures and Extreme Events, IABSE Symposium*, Budapest, Hungary. 92, 272 - 273, September 2006.
- Dowell E. H. and Hall K. C.** (2001). Modeling of Fluid-Structure Interaction. *Annual Review of Fluid Mechanics*, 33(1), 445 - 490.
- Dyrbye C. and Hansen O. S.** (1997). *Wind Loads on Structures*. John Wiley and Sons Ltd, New York, USA.

## References

---

- Dyrbye, C. and Hansen O. S.** (1999), *Wind Loads on Structures*. John Wiley and Sons Ltd. New York, USA.
- Edvardsen K. I.** (2010). *Numerical Analysis of Vortex Shedding*. M.Sc Dissertation - Faculty of Science and Technology, University of Stavanger, Stavanger, Norway.
- Elbadry M. M. and Ghali A.** (1983). Temperature Variations in Concrete Bridges. *Journal of Structural Engineering*, 109(10), 2355 - 2374.
- Ervine A.** (2012). *Damaged Reinforced Concrete Structures in Fire*. PhD Thesis - Department of Civil Engineering, University of Edinburgh, Edinburgh, UK.
- Estrada P. A. and Hong H. P.** (2015). Sensitivity Analysis of the Effectiveness of Tuned Mass Dampers to Reduce The Wind-Induced Torsional Responses. *Latin American Journal of Solids and Structures*, 12, 2520 - 2538.
- Facchinetti M L, Langre E. D. and Biolley F.** (2004). Vortex-Induced Travelling Waves along a Cable. *European Journal of Mechanics B/Fluids*, 23, 199 - 208.
- Fariduzzaman. Leonardo G., Lavi R. Z. and Amrinsyah N.** (2008). Low Wind Speed Heaving Resonance. *3rd International Symposium on Advanced Fluid/Solid Science and Technology in Experimental Mechanics*, Tainan, Taiwan. 7-10 December 2008.
- Farshidianfar A. and Zanganeh H.** (2009). The Lock-in Phenomenon in VIV Using A Modified Wake Oscillator Model for both High and Low Mass-Damping Ratio. *Iranian Journal of Mechanical Engineering*, 10(2), 5 - 28.
- Feldmann M. and Heinemeyer C.** (2007). *Human Induced Vibration of Steel Structures*, Design of Foot Bridges. HIVOSS, RFS2-CT-00033.
- Ferreira S. L. C., Bruns R. E., da Silva E. G. P., dos Santos W. N. L. , Quintella C. M. , David J. M. , de Andrade J. B., Breikreitz M. C. , Jardim I. C. S. F. and Neto B. B.** (2007). Statistical Designs and Response Surface Techniques for the Optimization of Chromatographic Systems. *Journal of Chromatography A*, 1158, 2 - 14.
- Ferreira S. L. C., Santos W. N. L., Quintella C. M., Neto B. B. and Boque S. J. M.** (2004). Doehlert Matrix: A Chemometric Tool for Analytical Chemistry Review. *Talanta*, 63(4), 1061 - 1067.
- Flamand O., De Oliveira F., Vlamis A. S., Papanikolas P. and Panagis A.** (2014). Using Non Continuous Records From Full Scale Monitoring System for Fatigue Assessment. *7th European Workshop on Structural Health Monitoring*, La Cite, Nantes, France. 8-11 July 2014.
- Flamand O., De Oliveira F., Vlamis A. S. and Papanikolas P.** (2013). Conditions for Occurrence of Vortex Shedding on a Large Cable Stayed Bridge; Full Scale Data From Monitoring System. *6th European and African Conference on Wind Engineering*, Robinson, CamBridge. 7-13 July 2013.

## References

---

- Forster C.** (2007). *Robust Methods for Fluid-Structure Interaction With Stabilized Finite Elements*. PhD Thesis - Institute of Structural Mechanics, University of Stuttgart, Stuttgart, Germany.
- Frandsen J. B.** (2004). Numerical Bridge Deck Studies Using Finite Elements Part I: Flutter. *Journal of Fluids and Structures*, 19, 171 - 191.
- Fransos D.** (2008). *Stochastic Numerical Models for Wind Engineering*. PhD Thesis - Polytechnic University of Turin, Torino, Italy.
- Fujino Y. and Siringoringo D.** (2013). Vibration Mechanisms and Controls of Long-Span Bridges: A Review. *Structural Engineering International*, 23(3), 248 - 268.
- Fujino Y., Siringoringo D. M., Nagayama T. and Su D.** (2010). Control, Simulation and Monitoring of Bridge Vibration – Japan’s Recent Development and Practice. *IABSE-JSCE Joint Conference on Advances in Bridge Engineering-II*, Dhaka, Bangladesh. 8-10 August 2010.
- Gale J.** (2008). *Fluid-Structure Interaction for Simulations of Fast Transients*. PhD Thesis - Faculty of Mathematics and Physics, University of Ljubljana, Ljubljana, Slovenia.
- Garlock M., Paya-Zaforteza I., Kodur V. and Gu L.** (2012). Fire Hazard in Bridges: Review, Assessment and Repair Strategies. *Engineering Structures*, 35, 89 - 98.
- Ge Y. J. and Xiang H. F.** (2008). Bluff Body Aerodynamics Application in Challenging Bridge Span Length. *BBAA VI International Colloquium on: Bluff Bodies Aerodynamics and Applications*, Milano, Italy. 20-24 July 2008.
- Ge Y. J. and Xiang H. F.** (2009). Aerodynamic Stabilization for Box-Girder Suspension Bridges with Super-Long Span. *5th European and African Conference on Wind Engineering, EACWE 5*. Florence, Italy. 19-23 July 2009.
- Ghasemi H., Park H. S. and Rabczuk T.** (2017). A level-set based IGA formulation for topology optimization of exoelectric materials. *Computer Methods in Applied Mechanics and Engineering*, 313, 239 - 258.
- Ghorashi S., Valizadeh N., Mohammadi S. and Rabczuk T.** (2015). T-spline based XIGA for fracture analysis of orthotropic media. *Computers & Structures*, 147, 138 - 146.
- Giuliani L., Crosti C. and Gentili F.** (2012) *Vulnerability of Bridges to Fire*, *Proceedings of the 6th International Conference on Bridge Maintenance, Safety and Management (IABMAS)*, Stresa, Lake Maggiore, Italy. 8-12 July 2012.
- Gleim T., Birken P., Weiland M., Kuhl D., Meister A. and Wunsch O.** (2014). Thermal Fluid-Structure-Interaction - Experimental and Numerical Analysis. *Proceedings of the International Conference on Numerical Analysis and Applied Mathematics (ICNAAM)*, Rhodes, Greece. 22-28 September 2014.

## References

---

- Glen G. and Isaacs K.** (2012). Estimating Sobol Sensitivity Indices Using Correlations. *Journal of Environmental Modelling and Software*, 37, 157 - 166.
- Gosteev Y. A., Obuhovskiy A. D. and Salenko S. D.** (2014). Influence of the Shape on Aerodynamic Characteristics of Girder Bridges. *Magazine of Civil Engineering*, 5(49), 63 - 72.
- Grilli M., Hickel S. and Adams N. A.** (2012). An Innovative Approach to Thermo-Fluid-Structure Interaction Based on an Immersed Interface Method and a Monolithic Thermo-Structure Interaction Algorithm. *42nd AIAA Fluid Dynamics Conference and Exhibit*. Louisiana, USA. 25-28 June 2012.
- Grouthier C., Michelin S., Bourguet R., Sadeghi Y. M. and de Langre E.** (2014). On the Efficiency of Energy Harvesting using Vortex-Induced Vibrations of Cables. *Journal of Fluids and Structures*, 49, 427 - 440.
- Gu M., Chang, C. C., Wu W. and Xiang H. F.** (1998). Increase of Critical Flutter Wind Speed of Long-Span Bridges using Tuned Mass Dampers. *Journal of Wind Engineering and Industrial Aerodynamics*, 73, 111 - 123.
- Gua M., Chena S. R. and Chang C. C.** (2002). Control of Wind-Induced Vibrations of Long-Span Bridges by Semi-Active Lever-Type TMD. *Journal of Wind Engineering and Industrial Aerodynamics*, 90, 111 - 126.
- Gua Ming, Chena S. R. and Chang C. C.** (2001). Parametric Study on Multiple Tuned Mass Dampers for Buffeting Control of Yangpu Bridge. *Journal of Wind Engineering and Industrial Aerodynamics*, 89, 987 - 1000.
- Gunaraj V and Murugan N.** (1999). Application of Response Surface Methodologies for Predicting Weld Base Quality in Submerged Arc Welding of Pipes. *Journal of Materials Processing Technology*, 88(1 - 3), 266 - 275.
- Guo P.** (2012). *Damping System Designs using Nonlinear Frequency Analysis Approach*. PhD Thesis - Department of Automatic Control and Systems Engineering, University of Sheffield, Sheffield, UK.
- Haan F. L.** (2000). *The Effects of Turbulence on the Aerodynamics of Long Span Bridges*. PhD Thesis - Department of Aerospace and Mechanical Engineering, University of Notre Dame, Notre Dame, Indiana, USA.
- Hamdia K., Silani M., Zhuang X., He P. and Rabczuk T.** (2017). Stochastic analysis of the fracture toughness of polymeric nanoparticle composites using polynomial chaos expansions. *International Journal of Fracture*, 206(2), 215 - 227.
- Hansen M. S.** (2013). *Boundary Conditions for 3D Fluid-Structure Interaction Simulations of Compliant Vessels*. M.Sc. Dissertation - Department of Structural Engineering, Norwegian University of Science and Technology, Trondheim, Norway.

## References

---

- Hansen S. O., Srouji R. G., Isaksen B. and Berntsen K.** (2013). Vortex-Induced Vibrations of Streamlined Single Box Girder Bridge Decks. *14 TH International Conference on Wind Engineering ICWE 2014*, Robinson, CamBridge. 21-26 June 2013.
- Haque M. N.** (2015). *Shaping Effects on Aerodynamics of Long-Span Cable-Supported Bridge Deck by Unsteady RANS*. PhD Thesis - Department of Civil Engineering, Yokohama National University, Louisiana, USA.
- Haque M. N., Katsuchi H., Yamada H. and Nishio M.** (2016). Flow Field Analysis of a Pentagonal-Shaped Bridge Deck by Unsteady RANS. *Engineering Applications of Computational Fluid Mechanics*, 10(1), 1 - 16.
- Hassler M.** (2009). *Quasi-Static Fluid-Structure Interactions Based on a Geometric Description of Fluids*. PhD Thesis - Faculty of Civil Engineering, Geo-and Environmental Sciences, Karlsruhe Institute of Technology, Karlsruhe, Germany.
- He X. Moaveni B., Conte J. P. and Elgamal A.** (2008). Modal Identification Study of Vincent Thomas Bridge Using Simulated Wind-Induced Ambient Vibration Data. *Computer-Aided Civil and Infrastructure Engineering*, 23(5), 373 - 388.
- Hengstler J. A. N.** (2013). *Influence of the Fluid-Structure Interaction on the Vibrations of Structures*. PhD Thesis - Faculty of Engineering, ETH Zurich, Zurich, Switherland.
- Homma T and Saltelli A.** (1996). Importance Measures in Global Sensitivity Analysis of Model Output. *Reliability Engineering and System Safety*, 52(1), 1 - 17.
- Huang L.** (2011). *Experimental Study on Bridge Stay Cable Vibration Mitigation Using External Viscous Damper*. M.Sc. Dissertation - Department of Civil and Environmental Engineering, University of Windsor, Windsor, Canada.
- Huang M. H.** (2006). *Dynamic Characteristics of Slender Suspension FootBridges*. PhD Thesis - Faculty of Built Environmental and Engineering, Queensland University of Technology, Brisbane, Australia.
- Huang M. H., Lin Y. Y. and Weng M. X.** (2012). Flutter and Buffeting Analysis of Bridges Subjected to Skew Wind. *Journal of Applied Science and Engineering*, 15(4), 401 - 413.
- Igusa T. and Xu K.** (1994). Vibration Control Using Multiple Tuned Mass Damper. *Journal of Sound and Vibration*, 175(4), 491 - 503.
- Iliev O., Mikelic A., Turek S. and Popov P.** (2004). Fluid Structure Interaction Problems in Deformable Porous Media: Toward Permeability of Deformable Porous Media. *Fraunhofer-Institut für Techno- und Wirtschaftsmathematik ITWM*, 65, 1 - 39.

## References

---

- Irwin P. A.** (2008). Bluff Body Aerodynamics in Wind Engineering. *Journal of Fluids and Structures*, 96, 701 - 712.
- Jain A., Jones, N. P. and Scanlan, R. H.** (1996). Coupled Flutter and Buffeting Analysis of Long-Span Bridges. *Journal of Structural Engineering*, ASCE, 122(7), 716 - 725.
- Janjic D.** (2010). *Aspects of Wind Buffeting Response and Non-Linear Structural Analysis for Cable Stayed Bridges*. TDV Consulting GmbH, Dorian Janjic & Partner, Graz, Austria.
- Jia Y., Anitescu C., Ghorashi S. and Rabczuk T.** (2015). Extended isogeometric analysis for material interface problems. *IMA Journal of Applied Mathematics*, 80(3), 608 - 633.
- Jones N. P. and Spartz C. A.** (1990). Structural Damping Estimation for Long-Span Bridges. *Journal of Engineering Mechanics*, 116(11), 2414 - 2433.
- Jurado J. A., Sanchez R., Hernandez S., Nieto F. and Kusano I.** (2012). A Review of Cases of Vortex Shedding Excitation in Bridges: Sectional Models Testing. *The Seventh International Colloquium on Bluff Body Aerodynamics and Applications (BBAA7)*, Shanghai, China. 2-6 September 2012.
- Kannan N., Rajakumar A. and Rengasamy G.** (2004). Optimization of Process Parameters for Adsorption of Metal Ions on Straw Carbon by Using Response Surface Methodology. *Environmental Technology*, 25(5), 513 - 522.
- Karmakar D., Chaudhuri S. R. and Shinozuka M.** (2012). Conditional Simulation of Non-Gaussian Wind Velocity Profiles: Application to Buffeting Response of Vincent Thomas Suspension Bridge. *Probabilistic Engineering Mechanics*, 29, 167 - 175.
- Katsuchi, H., Jones, N. P., and Scanlan, R. H.** (1999). Multimode Coupled Flutter and Buffeting Analysis of The Akashi-Kaikyo Bridge. *Journal of Structural Engineering*, ASCE, 125(1), 60 - 70.
- Kazutoshi M., Masafumi T. and Tooru I.** (2007). Reynolds Number Effects on the Steady and Unsteady Aerodynamic Forces Acting on the Bridge Deck Sections of Long-Span Suspension Bridge. *IHI Engineering Review*, 40(1), 12 - 26.
- Keerthana M., Jaya K. P., Rajan S. Selvi, Clemons H. and Sankar R. Ravi.** (2011). Numerical Studies on Evaluation of Aerodynamic Force Coefficients of Cable-Stayed Bridge Deck. *Journal of wind and Engineering*, 8(2), 19 - 29.
- Keitel H., Karaki G., Lahmer T., Nikulla S. and Zabel V.** (2011). Evaluation of Coupled Partial Models in Structural Engineering Using Graph Theory and Sensitivity Analysis. *Engineering structures*, 33, 3726 - 3736.
- Khoury, G. A.** (2000). Effect of Fire on Concrete and Concrete Structures. *Progress in Structural Engineering and Materials*, 2(4), 429 - 447.



## References

---

- Kincl M., Turk S. and Vrecer F.** (2005). Application of Experimental Design Methodology in Development and Optimization of Drug Release Method. *International Journal of Pharmaceutics*, 291(1 - 2), 39 - 49.
- Kiviluoma R.** (2001). *Frequency-Domain Approach for Calculating Wind-Induced Vibration and Aeroelastic Stability Characteristics of Long-Span Bridges*. PhD Thesis - Helsinki University of Technology, Espoo, Finland.
- Klingsch E. W. H.** (2014). *Explosive Spalling of Concrete in Fire*. PhD Thesis - Institute of Structural Engineering, ETH Zurich, Zurich, Switzerland.
- Kodur V. K. and Agrawal A.** (2016). Critical Factors Governing the Residual Response of Reinforced Concrete Beams Exposed to Fire. *Fire Technology*. 52, 967 - 993.
- Kodur V., Aziz E. and Dwaikat M.** (2013). Evaluating Fire Resistance of Steel Girders in Bridges. *Journal of Bridge Engineering*, 18(7), 633 - 643.
- Koziel S., Ciaurri D. E. and Leifsson L.** (2011). *Computational Optimization, Methods and Algorithms, Surrogate-Based Methods*, SCI 356, Springer-Verlag Berlin, Heidelberg, 2011, 33 - 59.
- Kubo Y.** (2004). Prospects for the Suppression of Aeroelastic Vibrations of a Long-Span Bridge Using Boundary Layer Control. *Journal of Vibration and Control*, 10(9), 1359 - 1373.
- Kumar A.** (2011). *Investigation of the Dynamic Performance of a Cable Stayed Foot Bridge*. PhD Thesis - School of Civil Engineering and Mechanical Structural Systems, University of Trento, Italy.
- Kuroda S.** (1997). Numerical Simulation of Flow Around a Box Girder of a Long Span Suspension Bridge. *Journal of wind engineering*, 67&68, 239 - 252.
- Kusano I.** (2015). *Reliability Based Design Optimization of Long Span Bridges Under Flutter Constraint*. PhD Thesis - Universidade Da Coruna, La Coruna, Spain.
- Kusano I., Baldomir A., Jurado J. A. and Hernandez S.** (2014). Reliability Based Design Optimization of Long Span Bridges Considering Flutter. *Journal of Wind Engineering and Industrial Aerodynamics*, 135, 149 - 162.
- Kvamstad T. H.** (2011). *Assessment of the Flutter Stability Limit of The Hålogaland Bridge Using a Probabilistic Approach*. M.Sc. Dissertation - Department of Structural Engineering. Norwegian University of Science and Technology NTNU, Trondheim, Norway.
- Kwak J. S.** (2005). Application of Taguchi and Response Surface Methodologies For Geometric Error in Surface Grinding Process. *International Journal of Machine Tools and Manufacture*, 45(3), 327 - 334.

## References

---

- Kwon S. D.** (2010). Uncertainty of Bridge Flutter Velocity Measured at Wind Tunnel Tests. *The Fifth International Symposium on Computational Wind Engineering (CWE2010)*, Chapel Hill, North Carolina, USA. 23-27 May 2010.
- Larsen A. and Walther J. H.** (1997). Aeroelastic Analysis of Bridge Girder Sections Based on Discrete Vortex Simulations. *Journal of Wind Engineering*, 67&68, 253 - 265.
- Larsen A. and Walther J. H.** (1998). Discrete Vortex Simulation of Flow Around Five Generic Bridge Deck Sections. *Journal of Wind Engineering and Industrial Aerodynamics*, 77&78, 591 - 602.
- Lee C. and Li Q. S.** (2005). Evaluation of The Lever-Type Multiple Tuned Mass Dampers for Mitigating Harmonically Forced Vibration. *International Journal of Structural Stability and Dynamics*, 5(4), 641 - 664.
- Liaghat T.** (2014). *Two Way Fluid Structure Coupling Vibration and Damping Analysis of an Oscillating Hydrofoil*. M.Sc. Dissertation - Department of Mechanical Engineering, Polytechnic School of Montreal, Montreal, Canada.
- Liaw K. F.** (2005). *Simulation of Flow Around Bluff Bodies and Bridge Deck Sections using CFD*. PhD Thesis - School of Civil Engineering, University of Nottingham, Nottingham, UK.
- Lienhard, J. and Lienhard, J.** (2003). *A Heat Transfer Textbook*, 3rd Ed., Phlogiston Press, Cambridge, MA.
- Lin Y. Y. and Cheng C. M.** (2001). Performance of Multiple Tuned Mass Dampers for Suppressing Buffeting Response and Increasing Flutter Speed of Long Span Bridges. *Journal of the Chinese Institute of Engineers*, 24(3), 273 - 288.
- Lin Y. Y., Cheng C. M. and Lee C. H.** (1999). Multiple Tuned Mass Dampers for Controlling Coupled Buffeting and Flutter of Long Span Bridges. *Wind and Structures*, 2(4), 267 - 284.
- Lin Y. Y., Cheng C. M. and Lee C. H.** (2000). A Tuned Mass Damper for Suppressing the Coupled Flexural and Torsional Buffeting Response of Long-Span Bridges. *Engineering Structures*, 22, 1195 - 1204.
- Lin Y. Y., Cheng C. M. and Sun D.** (2000). Wind Induced Vibration Control of Long Span Bridges by Multiple Tuned Mass Dampers. *Tamkang Journal of Science and Engineering*, 3(1), 1 - 13.
- Lin Y. Y., Cheng C. Ming, Wu J. C., Lan T. L. and Wu K. T.** (2005). Effects of Deck Shape and Oncoming Turbulence on Bridge Aerodynamics. *Tamkang Journal of Science and Engineering*, 8(1), 43 - 56.
- Liu M. Y. and Wang P. H.** (2012). *Finite Element Analysis of Cable-Stayed Bridges with Appropriate Initial Shapes Under Seismic Excitations Focusing on Deck-Stay Interaction*. Department of Civil Engineering, Chung Yuan Christian University, Jhongli city, Taiwan. Chapter 9, 231 - 256.

## References

---

- Liu M. Y., Lin L. C. and Wang P. H.** (2012). Investigation on Deck-Stay Interaction of Cable-Stayed Bridges With Appropriate Initial Shapes. *Structural Engineering and Mechanics*, 43(5), 691 - 709.
- Lopes A. V., Cunha A. and Luis M. C. S.** (2006). CFD based Evaluation of the Lock-in Phenomenon of a Bridge under Wind. *III European Conference on Computational Mechanics, Solids, Structures and Coupled Problems in Engineering*, Lisbon, Portugal. 5-8 June 2006.
- Ma C. M., Liao H. and Tao Q.** (2010). Wind Tunnel Test on the Wind-Resistant Behavior of a Long-Span Cable-Stayed Bridge during Erection. *Journal of Southwest Jiaotong University*, 18(2), 112 - 117.
- Maguire J. R and Wyatt T.** (2002). *Dynamics: An Introduction for Civil and Structural Engineers*. Thomas Telford Publishing, Thomas Telford Ltd, London.
- Man S. K.** (2004). *Lateral and Torsional Vibration Control of Long Span Bridge Deck Using Novel Tuned Liquid Column Dampers*. PhD Thesis - Department of Civil and Structural Engineering, The Hong Kong Polytechnic University, Kowloon, Hong Kong.
- Marin D. A. A.** (2003). *Stochastic Structural Control of Bridges Subject to Wind-Induced Vibrations Using Separated Surfaces*. M.Sc.Dissertation - Faculty of Engineering, National University of Colombia, Colombia.
- Matsumoto M., Niihara, Y., Kobayashi, Y., Shirato, H., and Hamasaki, H.** (1995). Flutter Mechanism and its Stabilization of Bluff Bodies. *Proceeding of 9th ICWE*, New Delhi, India. 827 - 838.
- McKay, M. D., Conover W. J. and Beckman R. J.** (1979). A Comparison of Three Methods for Selecting Values of Input Variables in the Analysis of Output from a Computer Code. *Technometrics* 21, 239 - 245.
- Meinhardt C., Yin X., Luo Y. and Gao X.** (2014). Enhancement of the Chong Qi Bridge Project Girder sections to Reduce Vortex Shedding Induced Oscillations by Applying Passive Tuned Mass Damper Systems. *Proceedings of the 9th International Conference on Structural Dynamics, EURO DYN 2014*, Porto, Portugal. 30 June - 2 July 2014.
- Mishra R.** (2011). *Application of Tuned Mass Damper for Vibration Control of Frame Structures Under Seismic Excitations*. M.Sc. Dissertation - Department of Civil Engineering, National Institute of Technology, Rourkela, India.
- Miyata T.** (2003). Historical View of Long-Span Bridge Aerodynamics. *Journal of Wind Engineering and Industrial Aerodynamics*, 91(12 - 15), 1393 - 1410.
- Moes N., Dolbow J. and Belytschko T.** (1999). A finite element method for crack growth without remeshing. *International Journal for Numerical Methods in Engineering*, 46, 131 - 150.

## References

---

- Mohammadi M. S.** (2013). *Wind Loads on Bridges Analysis of a Three Span Bridge Based on Theoretical Methods and Eurocode 1*. M.Sc. Dissertation - Department of Civil and Architectural Engineering, Royal Institute of Technology (KTH), Stockholm, Sweden.
- Mueller K. A. and Kurama Y. C.** (2014). Through-Thickness Thermal Behavior of Two RC Bearing Walls under Fire. *Structures Congress 2014*, 1159 - 1169.
- Munson B. R., Young D. F. and Okiishi T. H.** (2002). *Fundamentals of Fluid Mechanics*. 4th edition, New York: John Wiley & Sons, Inc., 578 - 584.
- Nagao F., Utsunomiya H., Oryu T. and Manabe, S.** (1993). Aerodynamic Efficiency of Triangular Fairing on Box Girder Bridge. *Journal of Wind Engineering and Industrial Aerodynamics*, 49(1 - 3), 565 - 574.
- Nakne J. K. D.** (2011). *FE-Analysis of a Beam-Column Connection in Composite Structures Exposed to Fire*. M.Sc. Dissertation - Department of Civil and Environmental Engineering, Chalmers University of Technology. Chalmers, Sweden.
- Nanthakumar S. S., Lahmer T. and Rabczuk T.** (2013). Detection of flaws in piezoelectric structures using extended FEM. *International Journal for Numerical Methods in Engineering*, 96(6), 373 - 389.
- Nanthakumar S., Valizadeh N., Park H. and Rabczuk T.** (2015). Surface effects on shape and topology optimization of nanostructures. *Computational Mechanics*, 56(1), 97 - 112.
- Nelson R. S.** (2011). *Experimental Investigation of Wind Effects on Long-Span Slender Bridges with Stochastic Traffic Flow*. M.Sc. Dissertation - Department of Civil and Environmental Engineering, Colorado State University, Fort Collins, Colorado, USA.
- Nguyen V. P., Anitescu C., Bordas S. P. A. and Rabczuk T.** (2015). Isogeometric analysis: An overview and computer implementation aspects. *Mathematics and Computers in Simulations*, 117, art. no. 4190, 89 - 116.
- Nguyen-Thanh N., Valizadeh N., Nguyen M. N., Nguyen-Xuan H., Zhuang X., Arcias P., Zi G., Bazilevs Y., De Lorenzis L. and Rabczuk T.** (2015). An extended isogeometric thin shell analysis based on Kirchhoff-Love theory. *Computer Methods in Applied Mechanics and Engineering*, 284, 265 - 291.
- Nicoli J. M.T.** (2008). *Different Mechanisms of Vortex Induced Vibration of Bridges*. PhD Thesis - Department of Mechanical and Hydraulic Engineering Structures, University of Granada, Granada, Spain.
- Nobuto J., Fujino Y. and Ito M.** (1988). A Study on the Effectiveness of TMD to Suppress a Coupled Flutter of Bridge Deck. *Proceedings of The Japan Society of Civil Engineers JSCE*, 398(1 - 10), 413 - 416.

## References

---

- Noda T., Kubo Y., Kimura K., Kato K., Okubo K. and Yoshida K.** (2009). The Effects of Lower Flange Slope on The Aerodynamic Stability of a Pentagonal Cross-Section Girder. *Journal of Civil Engineering (JSCE)*, 65(3), 797 - 807.
- Nossent J., Elsen P. and Bauwens W.** (2011). Sobol Sensitivity Analysis of a Complex Environmental Model. *Journal of Environmental Modelling and Software*, 26, 1515 - 1525.
- Odden T. H. and Skyvulstad H.** (2012). *Wind-induced Dynamic Response and Aeroelastic Stability of a Suspension Bridge crossing Sognefjorden*. M.Sc. Dissertation - Department of Structural Engineering, Norwegian University of Science and Technology, Trondheim, Norway.
- Onate E. and Garcia J.** (2001). A Finite Element Method for Fluid-Structure Interaction with Surface Waves Using A Finite Calculus Formulation. *International Centre for Numerical Methods in Engineering, Universidad Politecnica de Cataluna*, PI208, 1 - 34.
- Osher S. and Sethian J.** (1988). Fronts propagating with curvature dependent speed: algorithms based on Hamilton-Jacobi formulations. *Journal of Computational Physics*, 79(1), 12 - 49.
- Pacheco B., Fujino Y. and Sulekh A.** (1993). Estimation Curve for Modal Damping in Stay Cables with Viscous Damper. *Journal of Structural Engineering*, 119(6), 1961 - 1979.
- Palmklint E. and Svensson M.** (2016). *Thermal and Mechanical Response of Composite Slabs Exposed to Travelling Fire*. M.Sc. Dissertation - Department of Civil, Environmental and Natural Resources Engineering, Lulea University of Technology, Lulea, Sweden.
- Pan F., Zhu J., Ye M., Pachepsky Y. A. and Wue Y. S.** (2011). Sensitivity Analysis of Unsaturated Flow and Contaminant Transport with Correlated Parameters. *Journal of Hydrology*, 397(3 - 4), 238 - 249.
- Pasma S. A., Daik R., Maskat M. Y. and Hassan O.** (2013). Application of Box-Behnken Design in Optimization of Glucose Production from Oil Palm Empty Fruit Bunch Cellulose. *International Journal of Polymer Science*, 104502, 1 - 8.
- Patade H. K. and Chakrabarti M. A.** (2013). Thermal Stress Analysis of Beam Subjected To Fire. *Journal of Engineering Research and Applications*, 3(5), 420 - 424.
- Patil A. S.** (2010). *Mitigation of Vortex Induced Response in Long Span Bridges*. M.Sc Dissertation - Department of Civil and Environmental Engineering, The Florida State University, Florida, USA.
- Paya-Zaforteza I. and Garlock M.** (2012). A Numerical Investigation on the Fire Response of a Steel Girder Bridge. *Journal of Constructional Steel Research*. 75, 93 - 103.
- Peng J. and Chen G. S.** (2012). Flow Oscillating Structure Interactions and the Applications to Propulsion and Energy Harvest. *Journal of Applied Physics Research*, 4(2), 1 - 14.

## References

---

- Peris-Sayol G., Paya-Zaforteza I. and Alos-Moya J.** (2014). Analysis of The Response of a Steel Girder Bridge to Different Tanker Fires Depending on its Structural Boundary Conditions. *8th International Conference on Structures in Fire*, Shanghai, China. 11-13 June 2014.
- Petelet M., Iooss B., Asserin O. and Loredo A.** (2010). Latin Hypercube Sampling with Inequality Constraints. *Advances in Statistical Analysis*, 94, 325 - 339.
- Petersen C.** (2001). *Schwingungsdämpfer im Ingenieurbau*, Ed. Maurer Söhne GmbH and Co.KG, Munich.
- Phan D. H. and Nguyen N. T.** (2013). Flutter and Buffeting Control of Long-Span Suspension Bridge by Passive Flaps: Experiment and Numerical Simulation. *International Journal of Aeronautical and Space Science*, 14(1), 46 - 57.
- Pironkov P.** (2010). *Numerical Simulation of Thermal Fluid-Structure-Interaction*. PhD Thesis - Department of Mechanical Engineering, Technische Universität Darmstadt, Darmstadt, Germany.
- Potgieter I. C. and Gamble W. L.** (1989). Nonlinear Temperature Distributions in Bridges at Different Locations in the United States. *PCI Journal*, 34(4), 80 - 103.
- Pourzeynali S. and Esteki S.** (2009). Optimization of the TMD Parameters to Suppress the Vertical Vibrations of Suspension Bridges Subjected to Earthquake Excitations. *International Journal of Engineering, Transactions B: Applications*, 22(1), 23 - 34.
- Preumont A., Voltan M., Sangiovanni A., Bastaits R., Mokrani B. and Alaluf D.** (2015). An Investigation of the Active Damping of Suspension Bridges. *Mathematics and Mechanics of Complex Systems*, 3(4), 385 - 406.
- Puckett J., Johnson R. and Barker M.** (2011). *Study of the Effects of Wind Power and Vortex-Induced Vibrations to Establish Fatigue Design Criteria for High-Mast Poles*. Department of Transportation, University Transportation Centers Program, University of Wyoming, Wyoming, USA.
- Qin H., Liao H., Li M. and Sun Y.** (2013). Vortex-Induced Vibration of Continuous Beam Bridge and its Mitigation. *The Eighth Asia-Pacific Conference on Wind Engineering*, Chennai, India. 10-14 December 2013.
- Qiu P., Cui M., Kang K., Park B., Son Y., Khim E., Jang M. and Khim J.** (2014). Application of Box-Behnken Design With Response Surface Methodology for Modeling and Optimizing Ultrasonic Oxidation of Arsenite With H<sub>2</sub>O<sub>2</sub>. *Central European Journal of Chemistry*, 12(2), 164 - 172.
- Quoc T. T., Rabczuk T., Bazilevs Y. and Meschke G.** (2016). A higher-order stress-based gradient-enhanced damage model based on isogeometric analysis. *Computer Methods in Applied Mechanics and Engineering*, 304, 584 - 604.

## References

---

- Rabczuk T. and Areias P. M. A.** (2000). A meshfree thin shell for arbitrary evolving cracks based on an external enrichment. *CMES-Computer Modeling in Engineering and Sciences*, 1(1), 11 - 26.
- Rabczuk T. and Areias P. M. A.** (2006). A new approach for modelling slip lines in geological materials with cohesive models. *International Journal for Numerical and Analytical Methods in Engineering*, 30(11), 1159 - 1172.
- Rabczuk T. and Belytschko T.** (2004). Cracking particles: a simplified meshfree method for arbitrary evolving cracks. *International Journal for Numerical Methods in Engineering*, 61(13), 2316 - 2343.
- Rabczuk T. and Belytschko T.** (2005). Adaptivity for structured meshfree particle methods in 2D and 3D. *International Journal for Numerical Methods in Engineering*, 63(11), 1559 - 1582.
- Rabczuk T. and Belytschko T.** (2006). Application of particle methods to static fracture of reinforced concrete structures. *International Journal of Fracture*, 137(1 - 4), 19 - 49.
- Rabczuk T. and Belytschko T.** (2007). A three dimensional large deformation meshfree method for arbitrary evolving cracks. *Computer Methods in Applied Mechanics and Engineering*, 196(29 - 30), 2777 - 2799.
- Rabczuk T. and Ren H.** (2017). A peridynamics formulation for quasi-static fracture and contact in rock. *Engineering Geology*, 225, 42 - 48.
- Rabczuk T. and Samaniego E.** (2008). Discontinuous modelling of shear bands using adaptive meshfree methods. *Computer Methods in Applied Mechanics and Engineering*, 197(6 - 8), 641 - 658.
- Rabczuk T. and Zi G.** (2007). A meshfree method based on the local partition of unity for cohesive cracks. *Computational Mechanics*, 39(6), 743 - 760.
- Rabczuk T., Areias P. M. A. and Belytschko T.** (2007). A meshfree thin shell method for nonlinear dynamic fracture. *International Journal for Numerical Methods in Engineering*, 72(5), 524 - 548.
- Rabczuk T., Areias P. M. A. and Belytschko T.** (2007). A simplified meshfree method for shear bands with cohesive surfaces. *International Journal for Numerical Methods in Engineering*, 69(5), 993 - 1021.
- Rabczuk T., Belytschko T. and Xiao S. P.** (2004). Stable particle methods based on Lagrangian kernels. *Computer Methods in Applied Mechanics and Engineering*, 193(12 - 14), 1035 - 1063.
- Rabczuk T., Bordas S. and Zi G.** (2007). A three-dimensional meshfree method for continuous multiple-crack initiation, propagation and junction in statics and dynamics. *Computational Mechanics*, 40(3), 473 - 495.
- Rabczuk T., Bordas S. and Zi G.** (2010). On three-dimensional modelling of crack growth using partition of unity methods. *Computers & Structures*, 88(23 - 24), 1391 - 1411.

## References

---

- Rabczuk T., Gracie R., Song J. H. and Belytschko T.** (2010). Immersed particle method for fluid-structure interaction. *International Journal for Numerical Methods in Engineering*, 81(1), 48 - 71.
- Rabczuk T., Robert G., Jeong H. S. and Ted B.** (2010). Immersed Particle Method for Fluid-Structure Interaction. *International Journal for Numerical Methods in Engineering*, 81(1), 48 - 71.
- Rabczuk T., Zi G., Bordas S. and Nguyen-Xuan H.** (2008). A geometrically non-linear three dimensional cohesive crack method for reinforced concrete structures. *Engineering Fracture Mechanics*, 75(16), 4740 - 4758.
- Rabczuk T., Zi G., Bordas S. and Nguyen-Xuan H.** (2010). A simple and robust three dimensional cracking-particle method without enrichment. *Computer Methods in Applied Mechanics and Engineering*, 199(37 - 40), 2437 - 2455.
- Rabczuk T., Zi G., Gerstenberger A. and Wall W. A.** (2008). A new crack tip element for the phantom node method with arbitrary cohesive cracks. *International Journal for Numerical Methods in Engineering*, 75(5), 577 - 599.
- Rabizadeh E., Bagherzadeh A. S. and Rabczuk T.** (2016). Goal-oriented error estimation and adaptive mesh refinement in dynamic coupled thermoelasticity. *Computers & Structures*, 173, 187 - 211.
- Raja R. S.** (2012). *Coupled Fluid Structure Interaction Analysis on a Cylinder Exposed to Ocean Wave Loading*. M.Sc. Dissertation - Department of Applied Mechanics, Chalmers University of Technology, Goteborg.
- Rana P., Mohan N. and Rajagopal C.** (2004). Electrochemical Removal of Chromium From Wastewater by Using Carbon Aerogel Electrodes. *Water Research*, 38(12), 2811 - 2820.
- Raychaudhuri S.** (2008). Introduction to Monte Carlo Simulation. *Proceedings of the 2008 Winter Simulation Conference*, Miami, Florida. 7-10 December 2008.
- Razzaq M., Tsotskas C., Turek S., Hron J., Kipouros T. and Savill M.** (2010). Insight into Fluid Structure Interaction Benchmarking Through Multi-Objective Optimization. *Wiley Inter Science*, 2, 1 - 25.
- Ren H., Zhuang X. and Rabczuk T.** (2017). Dual-horizon peridynamics: a stable solution to varying horizons. *Computer Methods in Applied Mechanics and Engineering*, 318, 762 - 782.
- Ren H., Zhuang X., Cai Y. and Rabczuk T.** (2016). Dual-Horizon Peridynamics. *International Journal for Numerical Methods in Engineering*, 108(12), 1451 - 1476.
- Ricciardelli F., Grenet E. T. d. and Hangan H.** (2002). Pressure Distribution, Aerodynamic Forces and Dynamic Response of Box Sections. *Journal of Wind Engineering and Industrial Aerodynamics*, 90(10), 1135 - 1150.



## References

---

- Saltelli A and Tarantola S.** (2002). On the Relative Importance of Input Factors in Mathematical Models: Mafety Assessment for Nuclear Waste Disposal. *Journal of American Statistical Association* 97, 702 - 709.
- Saltelli A.** (2004). *Global Sensitivity Analysis: An Introduction*. European Commission, Joint Research Centre of Ispra, Italy.
- Saltelli A. and Annoni P.** (2010). How to Avoid a Perfunctory Sensitivity Analysis. *Environmental Modelling and Software*, 25(12), 1508 - 1517.
- Saltelli A., Chan K. K., and Scott M.** (2000). *Sensitivity Analysis*. John Wiley & Sons publishers, New York, USA.
- Saltelli A., Ratto M., Andres T., Campolongo F., Cariboni J. and Gatelli D.** (2008). *Global Sensitivity Analysis: The Primer*. John Wiley & Sons Ltd, New York, USA.
- Salvatori L.** (2007). *Assessment and Mitigation of Wind Risk of Suspended-Span Bridges*. PhD Thesis - Faculty of Architecture, Civil Engineering and Environmental Sciences, University of Braunschweig and Faculty of Engineering, University of Florence, Braunschweig and Florence, Germany and Italy.
- Samani F. S.** (2010). *Vibration Reduction on Beams Subjected to Traveling Loads Using Linear and Nonlinear Dynamic Absorbers*. PhD Thesis - Department of Mechanical Engineering, Shahid Bahonar University of Kerman, Kerman, Iran.
- Sangluaia C., Haridharan M. K., Natarajan C. and Rajaraman A.** (2013). Behaviour of Reinforced Concrete Slab Subjected To Fire. *International Journal of Computational Engineering Research*, 3(1), 195 - 206.
- Sardesai M. V. and Desai A. K.** (2013). Investigation In to Cable-Structure Interaction for Extra-Dosed Bridge. *International Journal of Engineering Research and Applications (IJERA)*, 3(4), 1424 - 1429.
- Sarkic A.** (2014). *Validated Numerical Simulation of Fluid-Structure Interactions of Bridge Girders in Turbulent Wind Fields*. PhD Thesis - Faculty of Civil and Environmental Engineering, Ruhr-Universität Bochum, Bochum, Germany.
- Sarwar M. W. and Ishihara T.** (2010). Numerical Study on Suppression of Vortex-Induced Vibrations of Box Girder Bridge Section by Aerodynamic Counter Measures. *Journal of wind Engineering and Industrial Aerodynamics*, 98(12), 701 - 711.
- Sato H., Hirahara N., Fumoto K., Hirano S. and Kusuhara S.** (2002). Full Aeroelastic Model Test of a Super Long-span Bridge with Slotted Box Girder. *Journal of Wind Engineering and Industrial Aerodynamics*, 90, 2023 - 2032.
- Scanlan R. H.** (1977). Motion of Suspended Bridge Spans Under Gusty Wind. *Journal of the Structural Division*, 103(9), 1867 - 1883.

## References

---

- Schewe G. and Larsen A.** (1998). Reynolds Number Effects in The Flow Around a Bluff Bridge Deck Cross Section. *Journal of Wind Engineering and Industrial Aerodynamics*, (74 - 76), 829 - 838.
- Schmucker H., Flemming F. and Coulson S.** (2010). Two-Way Coupled Fluid-Structure Interaction Simulation of a Propeller Turbine. *International Journal of Fluid Machinery and Systems*, , 3(4), 342 - 351.
- Schumacher J.** (2016). *Assessment of Bridge-Structures Under Fired Impact: A Case Study Approach*. M.Sc. Dissertation - Department of Civil and Environmental Engineering, University of Rhode Island, Kingston, USA.
- Selvam R. P., Tarini M. J. and Larsen A.** (1998). Computer Modelling of Flow Around Bridges Using LES and FEM. *Journal of Wind Engineering*, 77&78, 643 - 651.
- Shetty R. S., Prashanth. M. H, Channappa. T. M. and Ravikumar. C. M.** (2013). Vibration Suppression of Steel Truss Railway Bridge Using Tuned Mass Dampers. *International Journal of Civil and Structural Engineering*, 4(1), 63 - 71.
- Shin Y. B., Sin S. H., Kim Y. M. and Hwang J. S.** (2014). Performance Evaluation of Linear Active Mass Damper for Bridges Through Wind Tunnel Test. *Proceedings of the 9th International Conference on Structural Dynamics, EUROLYN 2014*, Porto, Portugal. 30 June-2 July 2014.
- Shuxian H.** (2009). Time Domain Buffeting Analysis of Large Span Cable-stayed Bridge. M.Sc. Dissertation - Faculty of Engineering. Norwegian University of Porto, Porto, Portugal.
- Silani M., Talebi H., Hamouda A. S. and Rabczuk T.** (2016). Nonlocal damage modelling in clay/epoxy nanocomposites using a multiscale approach. *Journal of Computational Science*, 15, 18 - 23.
- Silani M., Ziaei-Rad S., Talebi H. and Rabczuk T.** (2014). A semi-concurrent multiscale approach for modeling damage in nanocomposites. *Theoretical and Applied Fracture Mechanics*, 74, 30 - 38.
- Simiu E. and Scanlan R. H.** (1986). *Wind Effects on Structures*. Second Edition. John Wiley and Sons. New York, USA.
- Simiu E. and Scanlan R. H.** (1996). *Wind Effects on Structures*. Third Edition, John Wiley and Sons. New York, USA.
- Soltane S., Mekki O. B., Montassar S. and Auricchio F.** (2010). Damping Stay Cable Transverse Vibration Using Shape Memory Alloys and Magneto Rheological Dampers. *Advances in Geomaterials and Structures*, 9, 135 - 140.
- Souza A. S., dos Santos. W. N. L. and Ferreira S. L. C.** (2005). Application of Box–Behnken Design in The Optimization of An On-Line Pre-Concentration System Using Knotted Reactor For Cadmium

## References

---

- Determination by Flame Atomic Absorption Spectrometry. *Spectrochimica Acta Part B: Atomic Spectroscopy*, 60(5), 737 - 742.
- Stærdahl J. W., Sorensen N. and Nielsen S. R. K.** (2008). Aeroelastic Stability of Suspension Bridges using CFD. *Proceedings of International Symposium of the International Association for Shell and Spatial Structures (IASS), Structural Architecture - Towards the Future Looking to The Past*, Venice, Italy. 3-6 December 2008.
- Starossek U. and Aslan H.** (2007). A Novel Aero-Elastic Damper for Long-Span Bridges. *12th International Conference on Wind Engineering*, Cairns, Australia. 1-6 July 2007.
- Starossek U. and Aslan H.** (2008). Passive Control of Bridge Deck Flutter Using Tuned Mass Dampers and Control Surfaces. *7th European Conference on Structural Dynamics (EURODYN 2008)*, Southampton, UK. 7-9 July 2008.
- Stevens R. and Simonsen K.** (2008). *Investigation on Long Span Suspension Bridges During Erection, The Great Belt East Bridge*. M.Sc. Dissertation - Department of Civil Engineering, Aalborg University, Aalborg, Denmark.
- Stolarska M., Chopp D. L., Moes N. and Belytschko T.** (2001). Modeling crack growth by level sets in the extended finite element method. *International Journal for Numerical Methods in Engineering*, 51(8), 943 - 960.
- Storlie C. B. and Helton J. C.** (2008). Multiple Predictor Smoothing Methods for Sensitivity Analysis: Description of Techniques. *Journal of Reliability Engineering and System Safety*, 93(1), 28 - 54.
- Stratford T. and Dhakal R. P.** (2008). Spalling of Concrete: Implications for Structural Performance in Fire. *20th Australasian Conference on Mechanics of Structure and Materials*, Toowoomba, Australia. 2-5 December 2008.
- Su C., Han D. J., Yan Q. S., Au F. T. K., Tham L. G., Lee P. K. K., Lam K. M. and Wong K. Y.** (2003). Wind-Induced Vibration Analysis of The Hong Kong Ting Kau Bridge. *Proceedings of The Institution of Civil Engineers Structures and Buildings*, 156(3), 263 - 272.
- Sukumar N., Moes N., Moran B. and Belytschko T.** (2000). Extended finite element method for three dimensional crack modeling. *International Journal for Numerical Methods in Engineering*, 48, 1549 - 1570.
- Sutardi S.** (2014). The Rate of Turbulent Kinetic Energy Dissipation in a Turbulent Boundary Layer on a Flat Plate. *IPTEK, Journal of Proceeding Series*, 1, 63 - 66.
- Talebi E., Tahir M. M., Zahmatkesh F. and Kueh A. B. H.** (2015). Fire Response of a 3D Multi-Storey Building With Buckling Restrained Braces. *Latin American Journal of Solids and Structures*, 12(11), 2118 - 2142.

## References

---

- Talebi H., Silani M. and Rabczuk T.** (2015). Concurrent multiscale modelling of three dimensional crack and dislocation propagation. *Advances in Engineering Software*, 80, 82 - 92.
- Talebi H., Silani M., Bordas S. P. A., Kerfriden P. and Rabczuk T.** (2013). Molecular dynamics/XFEM coupling by a three-dimensional extended bridging domain with applications to dynamic brittle fracture. *International Journal for Multiscale Computational Engineering*, 11(6), 527 - 541.
- Talebi H., Silani M., Bordas S., Kerfriden P. and Rabczuk T.** (2014). A computational library for multiscale modelling of material failure. *Computational Mechanics*, 53(5), 1047 - 1071.
- Tang J., Viieru D. and Shyy W.** (2008). Effects of Reynolds Number and Flapping Kinematics on Hovering Aerodynamics. *American Institute of Aeronautics and Astronautics Journal*, 46(4), 967 - 976.
- Tang K. H.** (1997). *Tuned Mass Dampers for Flutter and Buffeting Control of Long-Span Suspension Bridges*. M.Sc. Dissertation - Department of Mechanical Engineering, Hong Kong University of Science and Technology, Hong Kong.
- Tekindal M. A, Bayrak H., Ozkaya B. and Genc Y.** (2012). Box Behnken Experimental Design in Factorial Experiments: The Importance of Bread for Nutrition and Health. *Turkish Journal of Field Crops*, 17(2), 115 - 123.
- Thamasungkeeti W.** (2009). *Suppression of Aerodynamic Responses of IRR Cable-Stayed Bridge by Tuned Mass Dampers and Aerodynamic Appendages*. M.Sc. Dissertation - Department of Civil Engineering. Thammasat University, Bangkok, Thailand.
- Tong, C.** (2010). Self validated Variance based Methods for Sensitivity Analysis of Model Outputs. *Reliability Engineering & System Safety*, 95(3), 301 - 309.
- Tran D. A.** (2014). *Numerical Investigation into the Suppression Mechanism of Vortex-Induced Vibration for Box Girder in the Presence of Flap*. PhD Thesis - Urban Innovation Faculty, Yokohama National University, Kanagawa, Japan.
- Tsai H. C. and Lin G. C.** (1993). Optimum Tuned Mass Damper for Minimizing Steady State Response of Support-Excited and Damped System. *Journal of Earthquake Engineering and Structural Dynamics*, 22, 957 - 973.
- Ubertini F, Comanducci G. and Laflamme S.** (2015). A Parametric Study on Reliability Based Tuned Mass Damper Design Against Bridge Flutter. *Journal of Vibration and Control*, 1 - 22.
- Ubertini F.** (2008). *Wind Effects on Bridges: Response, Stability and Control*. PhD Thesis - School of Civil Engineering University of Pavia, Pavia, Italy.

## References

---

- Vairo G.** (2010). A Simple Analytical Approach to the Aeroelastic Stability Problem of Long Span Cable Stayed Bridges. *International Journal for Computational Methods in Engineering Science and Mechanics*, 11(1), 1 - 19.
- Valdebenito G. E. and Aparicio A. C.** (2006). Seismic Behaviour of Cable Stayed Bridges: A State of the Art Review. *4th International Conference on Earthquake Engineering*, Taipei, Taiwan. 12-13 October 2006.
- Valizadeh N., Bazilevs Y., Chen J. S. and Rabczuk T.** (2015). A coupled IGA-meshfree discretization of arbitrary order of accuracy and without global geometry parameterization. *Computer Methods in Applied Mechanics and Engineering*, 293, 20 - 37.
- Van Vu T., Lee H. Y., Chun N. H., Oh S. T., Kim Y. M. and Lee H. E.** (2011). Flutter Analysis of Bridges Through Use of State Space Method. *Proceedings of the 8<sup>th</sup> International Conference on Structural Dynamics, EURO-DYN 2011*, Leuven, Belgium. 4-6 July 2011.
- Van Zuijlen A. H., Bosscher S. and Bijl H.** (2006). Two Level Algorithms for Partitioned Fluid-Structure Interaction Computations. *European Conference on Computational Fluid Dynamics*, Delft, Netherland. 5-8 September 2006.
- Vazquez J. G. V.** (2007). *Nonlinear Analysis of Orthotropic Membrane and Shell Structures Including Fluid-Structure Interaction*. PhD Thesis - Department of Resistance of Materials and Structures and Engineering, Universitat Politecnica de Catalunya, Barcelona, Spain.
- Ventura G., Budyn E. and Belytschko T.** (2003). Vector level sets for description of propagating crack in finite elements. *International Journal for Numerical Methods in Engineering*, 58(10), 1571 - 1592.
- Von V.** (2012). *Fluid-Structure Interaction Induced Oscillation of Flexible Structures in Uniform Flows*. PhD Thesis - Faculty of Engineering, Universitat Erlangen-Nurnberg, Erlangen, Germany.
- Vu-Bac N., Lahmer T., Zhuang X., Nguyen-Thoi T. and Rabczuk T.** (2016). A software framework for probabilistic sensitivity analysis for computationally expensive models. *Advances in Engineering Software*, 100, 19 - 31.
- Vu-Bac N., Nguyen-Xuan H., Chen L., Lee C. K., Zi G., Zhuang X., Liu G. R. and Rabczuk T.** (2013). A phantom-node method with edge-based strain smoothing for linear elastic fracture mechanics. *Journal of Applied Mathematics*, 978026.
- Vu-Bac N., Rafiee R., Zhuang X., Lahmer T. and Rabczuk T.** (2015). Uncertainty quantification for multiscale modeling of polymer nanocomposites with correlated parameters. *Composites. Part B, Engineering*, 68, 446 - 464.
- Wainwright H. M., Finsterle S, Jung Y, Zhou Q. and Birkholzer J. T.** (2014). Making Sense of Global Sensitivity Analyses. *Computers and Geosciences*, 65, 84 - 94.

## References

---

- Wang H, Li A, Zong Z, Tong T. and Zhou R.** (2013). *Damper Optimization for Long-Span Suspension Bridges: Formulations and Applications*. IGI global, Pennsylvania.
- Wang H, Tao T, Cheng H. and He X.** (2014). Simulation Study on Train-Induced Vibration Control of a Long-Span Steel Truss Girder Bridge by Tuned Mass Dampers. *Hindawi Publishing Corporation, Mathematical Problems in Engineering*, 1 - 12.
- Wang H, Tao T., Cheng H.. and Li A. Q.** (2014). A Simulation Study on The Optimal Control of Buffeting Displacement for The Sutong Bridge with Multiple Tuned Mass Dampers. *Journal of Zhejiang University - Science A: Applied Physics and Engineering*, 15(10), 798 - 812.
- Wang H., Li A., Zhao G. and Li J.** (2010). Non-Linear Buffeting Response Analysis of Long-Span Suspension Bridges with Central Buckle. *Earthquake Engineering and Engineering Vibration*, 9(2), 259 - 270.
- Warburton G. B. and Ayorinde E. O.** (1980). Optimum Absorber Parameters for Simple Systems. *Earthquake Engineering and Structural Dynamics*, 8(3), 197 - 217.
- Wardlaw R. L., Tanaka H. Utsunomiya H.** (1983). Wind Tunnel Experiments on the Effects of Turbulence on the Aerodynamic Behavior of Bridge Road Decks. *Journal of Wind Engineering and Industrial Aerodynamics*, 14(1 - 3), 247 - 257.
- Webster A. C. and Vaicaitis R.** (2003). Application of Tuned Mass Dampers to Control Vibrations of Composite Floor Systems. *Engineering Journal - American Institute of Steel Construction*, 116 - 124.
- Wen Q., Hua X. G. and Chen Z. Q.** (2015). Field Validation on Vibration Control of a Cable-Stayed Footbridge with Tuned Mass Dampers. *11th International Workshop on Advanced Smart Materials and Smart Structures Technology*, University of Illinois, Urbana-Champaign, USA. 1-2 August 2015.
- Wilde K. and Fujino Y.** (1998). Aerodynamic Control of Bridge Deck Flutter by Active Surfaces. *Journal of Engineering Mechanics, ASCE*, 124(7), 718 - 727.
- Wright W., Lattimer B., Woodworth M. Nahid M. and Sotelino E.** (2013) *Highway Bridge Fire Hazard Assessment*, Blacksburg, VA, USA: Virginia Polytechnic Institute and State University.
- Wu T. and Kareem A.** (2012). An Overview of Vortex-Induced Vibration (VIV) of Bridge decks. *Frontiers of Structural and Civil Engineering-Springer*, 6(4), 335 - 347.
- Xavier O., David. and Dvid W.** (2015). Forces and Moments on Flat Plates of Small Aspect Ratio with Application to PV Wind Loads and Small Wind Turbine Blades. *Journal of Energies*, 8(4), 2438 - 2453.
- Xiao Y. Q., Hu G., Tu M. Q. and Zheng R. Q.** (2012). The Influence of Turbulence Integral Scale to Buffeting of Long-Span Bridge. *Applied Mechanics and Materials*, (105 - 107), 9 - 12.

## References

---

- Xie F. F., Deng J. and Zheng Y.** (2011). Multi-Mode Vortex Induced Vibrations of Flexible Circular Cylinder. *Journal of Hydrodynamics, Ser. B*, 23(4), 483 - 490.
- Xie X., Xiaozhang L. and Yonggang S.** (2014). Static and Dynamic Characteristics of a Long Span Cable Stayed Bridge with CFRP Cables. *Materials*, 7(6), 4854 - 4877.
- Xing C., Wang H., Li A. and Xu Y.** (2014). Study on Wind Induced Vibration Control of a Long Span Cable Stayed Bridge Using TMD Type Counterweight. *Journal of Bridge Engineering*, 19(1), 141 - 148.
- Xiong L., Liao H. L. and Li M. S.** (2014). The Flutter Performance Study for a Suspension Bridge Based on Numerical Analysis and Wind-Tunnel Test. *The 2014 World Congress on Advances in Civil, Environmental and Materials Research (ACEM14)* , Busan, Korea. 24-28 August 2014.
- Xu Y. L.** (2013). *Wind Effects on Cable Supported Bridges*. John Wiley & Sons Singapore Pte. Ltd.
- Xu Y. L., Hu L., and Kareem A.** (2014). Conditional Simulation of Nonstationary Fluctuating Wind Speeds for Long-Span Bridges. *Journal of Engineering Mechanics*, 140(1), 61 - 73.
- Yang F.** (2008). *Optimal Vibration Suppression of Beam-Type Structures Using Passive and Semi-Active Tuned Mass Dampers*. PhD Thesis - Department of Mechanical and Industrial Engineering, Concordia University, Montreal, Canada.
- Yin L., Jiang J. and Chen L.** (2012). A Monolithic Solution Procedure for a Thermal Fluid- Structure Interaction System of Thermal Shock. *Procedia Engineering*, 31, 1131 - 1139.
- Zhan C. S., Song X. M., Xia J. and Tong C.** (2013). An Efficient Integrated Approach for Global Sensitivity Analysis of Hydrological Model Parameters. *Environmental Modelling and Software* , 41 , 39 - 52.
- Zhang M. M., Cheng L. and Zhou Y.** (2004). Closed-Loop-Controlled Vortex Shedding and Vibration of a Flexibly Supported Square Cylinder Under Different Schemes. *Physics of Fluids*, 16(5), 1439 - 1448.
- Zhang W.** (2012). *Fatigue Performance of Exciting Bridges Under Dynamic Loads From Winds and Vehicles*. PhD Thesis - Department of Civil and Environmental Engineering, Louisiana State University, Louisiana, USA.
- Zhang X.** (2003). *Aeroelastic Analysis of Super Long Cable-Supported Bridges*. PhD Thesis - School of Civil and Environmental Engineering, Nanyang Technological University, Nanyang, Singapore.
- Zhang X.** (2012). *Wind Effect on Long Span Bridge*. M.Sc. Dissertation - Department of Civil and Environmental Engineering, Massachusetts Institute of Technology, Massachusetts, USA.

## References

---

- Zhang X. Y., Trame M. N., Lesko L. J. and Schmidt S.** (2015). Sobol Sensitivity Analysis: A Tool to Guide the Development and Evaluation of Systems Pharmacology Models. *CPT: Pharmacometrics and Systems Pharmacology*, 4(2), 69 - 79.
- Zhang Z. Q., Ding Y. L. and Geng F. F.** (2016). Investigation of Influence Factors of Wind-Induced Buffeting Response of a Six-Tower Cable-Stayed Bridge. *Shock and Vibration*, ID 6274985, 1 - 16.
- Zhao J. and Tiede C.** (2011). Using a Variance Based Sensitivity Analysis for Analyzing the Relation Between Measurements and Unknown Parameters of a Physical Model. *Nonlinear Processes in Geophysics*, 18, 269 - 276.
- Zhou G. D. and Yi T. H.** (2013). Thermal Load in Large-Scale Bridges: A State-of-the-Art Review. *International Journal of Distributed Sensor Networks*, 2013, ID 217983, 1 - 17.
- Zhou L., Xia Y., Brownjohn J. M. W. and Koo K. Y.** (2016). Temperature Analysis of a Long-Span Suspension Bridge Based on Field Monitoring and Numerical Simulation. *Journal of Bridge Engineering*, 21(1), 04015027, 1 - 10.
- Zhuang X., Huang R., Liang C. and Rabczuk T.** (2014). A coupled thermo-hydro-mechanical model of jointed hard rock for compressed air energy storage. *Mathematical Problems in Engineering*, 179169.
- Zi G., Rabczuk T. and Wall W. A.** (2007). Extended meshfree methods without branch enrichment for cohesive cracks. *Computational Mechanics*, 40(2), 367 - 382.
- Ziegler F. and Amiri A. K.** (2013). Bridge Vibrations Effectively Damped By Means of Tuned Liquid Column Gas Dampers. *Asian Journal of Civil Engineering (BHRC)*, 14(1), 1 - 16.
- Zivanovic S., Pavic A. and Reynolds P.** (2005). Vibration Serviceability of Foot Bridges Under Human-Induced Excitation: a Literature Review. *Journal of Sound and Vibration*, 279(1 - 2), 1 - 74.





# Curriculum Vitae

## Personal Information:

**Name:** Dr.-Ing. Nazim Abdul Nariman

**Occupation:** Researcher and Consultant Structural Engineer

**Date of Birth:** 15. Feb.1971

**Marital Status:** Married

**Mobile Tel.:** 004915226164226 / 009647702210546

**E-mail:** kakarevi@yahoo.com      nazim.nariman@uni-weimar.de

**Address:** Am Herrenrodchen 1C, 99427 - Weimar , Germany



## Language Skills:

1- English    2- Kurdish    3- Arabic    4- Persian

## Education:

- 1- Dr.-Ing. in Structural Mechanics (2012-2017)  
Bauhaus Universitat Weimar  
Germany
- 2- M.Sc. in Structural Engineering (2009-2010)  
Universiti Sains Malaysia  
Malaysia
- 3- B.Sc. in Civil Engineering (1988-1992)  
Salahaddin University  
Iraq

## Engineering Software Skills:

- 1- AUTO CAD
- 2- ETABS
- 3- ABAQUS
- 4- ANSYS
- 5- LUSAS
- 6- MATLAB
- 7- PYTHON
- 9- C++

## Professional Qualifications:

- 1-Methods of Teaching at Garmian University-Iraq (2014)

- 2-American USAID Certificate in Project Management-(2008)
- 3-TOEFL Certificate with Score of (517) in (2007)
- 4-English Language Proficiency Exam Certificate from Sulaimani University-Iraq (2006)
- 5-Computer Proficiency Exam Certificate from Sulaimani University-Iraq (2006)

### **Affiliation and Membership:**

- 1- Member of American Society of Civil Engineers ASCE (2015)
- 2- Member of German Bauhaus Research School (2012)
- 3- Member of Iraqi Society of Professionals ISOP (2010)
- 4- Consultant Civil and Structural Engineer at KEU-Iraq (1993)
- 5- Member of Iraqi Syndicate of Civil Engineers-Iraq (1992)

### **Research Interests:**

- Model Assessment and Sensitivity Analysis of Structures
- Uncertainty Quantification of Structural Damage and Failure
- Surrogate Modeling and Structural Response Prediction
- Fluid-Structure Interaction (FSI)
- Thermal Fluid-Structure Interaction (TFSI)
- Finite Element Method (FEM)
- Extended Finite Element Method (XFEM)
- Fire Effects on Structures
- Wind Effects on Structures
- Earthquake Effects on Structures

### **Journals Reviewer:**

- 1- Journal of Civil Engineering and Science (JCES).
- 2- International Journal of Civil Engineering and Geo Environmental of University Malaysia Pahang (IJCEG).
- 3- NED, University Journal of Research (NEDUJR).
- 4- Scientific Journal of Koya University (ARO).
- 5- Journal of Sustainable Architecture and Civil Engineering of Kaunas University of Technology (JSACE).
- 6- Frontiers of Structural and Civil Engineering (FSCE)-Springer.
- 7- Open Journal of Civil Engineering (OJCE)
- 8- Engineering Geology-Elsevier.
- 9- International Journal of Mechanical Sciences-Elsevier

### **List of Publications:**

- 1- Nariman N. A. (2017). **Thermal Fluid-Structure Interaction and Coupled Thermal-Stress Analysis in a Cable Stayed Bridge Exposed to Fire.** *Frontiers of Structural and Civil Engineering*, doi:10.1007/s11709-017-0452-4.
- 2- Nariman N. A., Lahmer, T., Karampour P. (2017). **Uncertainty Quantification of Stability and Damage Detection Parameters of Coupled Hydrodynamic-Ground Motion in Concrete Gravity Dams.** *Frontiers of Structural and Civil Engineering*, a special issue in modeling of multi-field problems (accepted).

- 3- Nariman N. A. (2017). **Kinetic Energy Based Model Assessment and Sensitivity Analysis of Vortex Induced Vibration of Segmental Bridge Decks.** *Frontiers of Structural and Civil Engineering*, 11(4), 480-501.
- 4- Nariman N. A. (2017). **Aerodynamic Stability Parameters Optimization and Global Sensitivity Analysis for a Cable Stayed Bridge.** *KSCE Journal of Civil Engineering*, 21(5), 1866-1881.
- 5- Nariman N. A. (2017). **Control Efficiency Optimization and Sobol's Sensitivity Indices of MTMDs Design Parameters for Buffeting and Flutter Vibrations in a Cable Stayed Bridge.** *Frontiers of Structural and Civil Engineering*, 11(1), 66-89.
- 6- Nariman N. A. (2017). **A Novel Structural Modification to Eliminate the Early Coupling between Bending and Torsional Mode Shapes in a Cable Stayed Bridge.** *Frontiers of Structural and Civil Engineering*, 11(2), 131-142.
- 7- Nariman N. A. (2016). **Influence of Fluid-Structure Interaction on Vortex Induced Vibration and Lock-in Phenomena in Long Span Bridges.** *Frontiers of Structural and Civil Engineering*, 10(4), 363-384.
- 8- Nariman N. A. (2014). *Earthquake Response Analysis of a Concrete Gravity Dam.* Amazon Books.
- 9- Nariman N. A. (2014). *Vibration and Mode Shapes Analysis of Cable Stayed Bridges Considering Different Structural Parameters.* GRIN Verlag GmbH, V267379.
- 10- Nariman N. A. (2014). *Nonlinear Structural Design Optimization of Cable Stayed Bridges.* Lap-Lambert Academic Publishing.
- 11- Nariman N. A. (2013). *Twisting Feature in High Rise Structures.* Amazon Books.

## Work History:

- 1- Consultant Civil Engineer at Ministry of Health - Kurdistan Region - Iraq (2001-2017)
- 2- Project Manager at Kurdistan Health Foundation KHF - Kurdistan Region - Iraq (1999-2001)
- 3- Project Manager at QANDIL Swedish NGO - Kurdistan Region - Iraq (1997-1999)
- 4- Supervisor Engineer at Ministry of Works and Rehabilitation - Kurdistan Region - Iraq (1993-1997)

## References:

1- Prof. Dr.-Ing. Timon Rabczuk  
 Bauhaus Universitat-Weimar  
 timon.rabczuk@uni-weimar.de

Tel: 00493643584511

2- Assoc. Prof. Dr. Choong Kok Keong  
 University Sains Malaysia  
 cekkc@usm.my

Tel: 006045996225